

AD-A245 427



AVSCOM TR-90-C-004
ME-TSPC-TR-90-11

2

An Investigation of the Three-Dimensional Flow Field in a Centrifugal Compressor

John R. Fagan, Jr. and Sanford Fleeter

Prepared For
U.S. ARMY AVIATION
SYSTEMS COMMAND

NATIONAL AERONAUTICS AND SPACE
ADMINISTRATION
NASA LEWIS RESEARCH CENTER
Grant NSG-3285

This document has been approved
for public release and sale; its
distribution is unlimited.

Thermal Sciences and Propulsion Center
School of Mechanical Engineering
Purdue University
1003 Chaffee Hall
West Lafayette, Indiana 47907-1003

92-01441



92 1 16 023

AVSCOM TR-90-C-004

**AN INVESTIGATION OF THE THREE-DIMENSIONAL FLOW
FIELD IN A CENTRIFUGAL COMPRESSOR**

John Robert Fagan, Jr. and Sanford Fleeter

Prepared For

U.S. ARMY AVIATION SYSTEMS COMMAND

**NATIONAL AERONAUTICS AND SPACE ADMINISTRATION
NASA LEWIS RESEARCH CENTER
GRANT NSG-3285**

May 1990

**Thermal Sciences and Propulsion Center
School of Mechanical Engineering
Purdue University
West Lafayette, Indiana 47907**

Statement A per telecon
Larry Schumann, AVSCOM/ Code 0300
Cleveland, OH 44135
NWW 1-29-92

Accession For	
NTIS CRA&I	<input checked="checked" type="checkbox"/>
DTIC TAB	<input type="checkbox"/>
Unannounced	<input type="checkbox"/>
Justification	
By	
Distribution/	
Availability Codes	
Dist	Availability or Special
A-1	



ABSTRACT

A series of experiments was performed to provide three-dimensional flow field data in centrifugal compressor passages and to describe the characteristic flow phenomena at the point of incipient rotating stall. These experiments entailed the acquisition and analysis of one-dimensional LDV data in the impeller passages of the Purdue Research Centrifugal Compressor at two compressor operating points: (1) the design operating point and (2) the incipient stall operating point. Additionally, the nature of compressor rotating stall was quantified by the acquisition and analysis of unsteady pressure data at the impeller inlet and exit. Finally, predictions at the design operating point from contemporary internal flow models were used for comparison with the LDV data.

The LDV data taken at both operating points show the traditional jet-wake structure observed in many centrifugal compressors. At the design point, the wake was observed along the shroud 70% of the length from the pressure to suction surface. At the incipient stall point, the wake was located in the shroud suction corner.

The unsteady pressure data show three distinct modes of rotating stall in the compressor, depending upon the mass flow rate. One mode is characterized by two stall patterns rotating concurrently with relative rotational speeds below 15% of the impeller rotational speed. This mode occurs at the highest mass flow rate and is strongest at the impeller inlet. The other two rotating stall modes occur at reduced mass flow rates and are characterized by single rotating stall patterns. The patterns in both modes rotate with relative speeds exceeding 90% of the impeller rotational speed, with the patterns strongest at the diffuser inlet.

The inviscid flow model did not successfully predict the compressor flow field. The viscous flow model achieved better success. It predicted the major phenomena in the flow field, specifically the wake structure near the end of the passage. However, the viscous model shows poor correlation with the data, predicting that the wake was located in the shroud suction corner different from the LDV results at the design operating point.

TABLE OF CONTENTS

	Page
LIST OF TABLES	
LIST OF FIGURES	
LIST OF SYMBOLS	
CHAPTER 1 - INTRODUCTION	1
1.1 Research Objectives	4
1.2 Review of Impeller Flow Studies	5
1.3 Technical Approachs	7
CHAPTER 2 - PURDUE RESEARCH CENTRIFUGAL COMPRESSOR	10
CHAPTER 3 - DATA ACQUISITION AND ANALYSIS	15
3.1 Laser Doppler Velocimetry	15
3.2 Unsteady Pressure Measurements	44
CHAPTER 4 - IMPELLER FLOW FIELD MODELING	47
4.1 Inviscid Model	49
4.2 Viscous Model	51
CHAPTER 5 - RESULTS	55
5.1 LDV Measurements	55
5.2 Unsteady Pressure Measurements	112
5.3 Flow Field Predictions	141

	Page
CHAPTER 6 - SUMMARY AND CONCLUSIONS	164
LIST OF REFERENCES	167
APPENDICES	
Appendix A - Ray Tracing	169
Appendix B - Error Estimation	175
Appendix C - L2F Evaluation	182

LIST OF TABLES

Table	Page
2.1 Research Compressor Facility Parameters	12
3.1 LDV Probe Volume Dimensions	18
3.2 Traversing System Positioning Limits and Precision	32
3.3 LDV Measurement Parameters	34
5.1 Vorticity Contour Levels	73
5.2 Turbulence Intensity and Enthalpy Contour Levels	89
5.3 Centrifugal Compressor Rotating Stall Modes	115
Appendix	
Table	
B.1 Experimental Parameters and Results	176
B.2 Experimental Uncertainty Due to Individual Sources	179
B.3 Measurement Direction Uncertainty	180
C.1 LDV and L2F Comparison	183

LIST OF FIGURES

Figure	Page
1.1 Centrifugal Compressor Components	2
1.2 Centrifugal Compressor Flow Phenomena	3
2.1 Centrifugal Compressor Flow Path	11
2.2 Impeller with Plexiglass Shroud	13
2.3 Optical Access to Compressor Flow Path	14
3.1 Dual Beam Laser Doppler Velocimeter	16
3.2 Bragg Cell Operation	22
3.3 Correction of Directional Ambiguity by Frequency Shifting	25
3.4 LDV Preliminary Optics	28
3.5 LDV Final Optics Assembly	29
3.6 Instrumentation for LDV Measurements in the Centrifugal Compressor	31
3.7 Scatter and Mean Frequency Plots (Low Turbulence)	36
3.8 Scatter and Mean Frequency Plots (Moderate Turbulence)	37
3.9 Orthogonal Coordinate System Orientation	40
3.10 Frequency Histogram Plot (Low Turbulence)	42
3.11 Frequency Histogram Plot (Moderate Turbulence)	43
3.12 Impeller Measurement Locations - Plane 4	45
3.13 Microphone Locations in Centrifugal Compressor	46
5.1 Measurement Plane Locations	56
5.2 Impeller Passage Flow Work	58
5.3 Throughflow Velocity Plot - LDV Data Design Point - Plane 1	59
5.4 Throughflow Velocity Plot - LDV Data Design Point - Plane 2	60
5.5 Throughflow Velocity Plot - LDV Data Design Point - Plane 3	61

Figure		Page
5.6	Throughflow Velocity Plot - LDV Data Design Point - Plane 4	62
5.7	Throughflow Velocity Plot - LDV Data Design Point - Plane 5	63
5.8	Throughflow Velocity Plot (Rotated View) - LDV Data Design Point - Plane 3	64
5.9	Throughflow Velocity Plot (Rotated View) - LDV Data Design Point - Plane 4	65
5.10	Throughflow Velocity Plot (Rotated View) - LDV Data Design Point - Plane 5	66
5.11	Secondary Velocity Vector and Vorticity Contour Plot - LDV Data Design Point - Plane 1	68
5.12	Secondary Velocity Vector and Vorticity Contour Plot - LDV Data Design Point - Plane 2	69
5.13	Secondary Velocity Vector and Vorticity Contour Plot - LDV Data Design Point - Plane 3	70
5.14	Secondary Velocity Vector and Vorticity Contour Plot - LDV Data Design Point - Plane 4	71
5.15	Secondary Velocity Vector and Vorticity Contour Plot - LDV Data Design Point - Plane 5	72
5.16	Throughflow Velocity Plot - LDV Data Incipient Stall Point - Plane 1	75
5.17	Throughflow Velocity Plot - LDV Data Incipient Stall Point - Plane 2	76
5.18	Throughflow Velocity Plot - LDV Data Incipient Stall Point - Plane 3	77
5.19	Throughflow Velocity Plot - LDV Data Incipient Stall Point - Plane 4	78
5.20	Throughflow Velocity Plot - LDV Data Incipient Stall Point - Plane 5	79
5.21	Throughflow Velocity Plot (Rotated View) - LDV Data Incipient Stall Point - Plane 3	80
5.22	Throughflow Velocity Plot (Rotated View) - LDV Data Incipient Stall Point - Plane 4	81
5.23	Throughflow Velocity Plot (Rotated View) - LDV Data Incipient Stall Point - Plane 5	82
5.24	Secondary Velocity Vector and Vorticity Contour Plot - LDV Data Incipient Stall Point - Plane 1	83
5.25	Secondary Velocity Vector and Vorticity Contour Plot - LDV Data Incipient Stall Point - Plane 2	84
5.26	Secondary Velocity Vector and Vorticity Contour Plot - LDV Data Incipient Stall Point - Plane 3	85

Figure		Page
5.27	Secondary Velocity Vector and Vorticity Contour Plot - LDV Data Incipient Stall Point - Plane 4	86
5.28	Secondary Velocity Vector and Vorticity Contour Plot - LDV Data Incipient Stall Point - Plane 5	87
5.29	Turbulence Intensity Contour Plot - LDV Data Design Point - Plane 1	91
5.30	Turbulence Intensity Contour Plot - LDV Data Design Point - Plane 2	92
5.31	Turbulence Intensity Contour Plot - LDV Data Design Point - Plane 3	93
5.32	Turbulence Intensity Contour Plot - LDV Data Design Point - Plane 4	94
5.33	Turbulence Intensity Contour Plot - LDV Data Design Point - Plane 5	95
5.34	Turbulence Intensity Contour Plot - LDV Data Incipient Stall Point - Plane 1	96
5.35	Turbulence Intensity Contour Plot - LDV Data Incipient Stall Point - Plane 2	97
5.36	Turbulence Intensity Contour Plot - LDV Data Incipient Stall Point - Plane 3	98
5.37	Turbulence Intensity Contour Plot - LDV Data Incipient Stall Point - Plane 4	99
5.38	Turbulence Intensity Contour Plot - LDV Data Incipient Stall Point - Plane 5	100
5.39	Enthalpy Contour Plot - LDV Data Design Point - Plane 1	101
5.40	Enthalpy Contour Plot - LDV Data Design Point - Plane 2	102
5.41	Enthalpy Contour Plot - LDV Data Design Point - Plane 3	103
5.42	Enthalpy Contour Plot - LDV Data Design Point - Plane 4	104
5.43	Enthalpy Contour Plot - LDV Data Design Point - Plane 5	105
5.44	Enthalpy Contour Plot - LDV Data Incipient Stall Point - Plane 1	107
5.45	Enthalpy Contour Plot - LDV Data Incipient Stall Point - Plane 2	108
5.46	Enthalpy Contour Plot - LDV Data Incipient Stall Point - Plane 3	109
5.47	Enthalpy Contour Plot - LDV Data Incipient Stall Point - Plane 4	110

Figure		Page
5.48	Enthalpy Contour Plot - LDV Data Incipient Stall Point - Plane 5	111
5.49	Constant Speed Operating Line for the Centrifugal Compressor	114
5.50	Unfiltered and Filtered Unsteady Pressure Signal - Baseline (Microphone 3)	116
5.51	Unfiltered and Filtered Unsteady Pressure Signal - Baseline (Microphone 4)	117
5.52	Fourier Analysis of Unsteady Pressure Signal - Baseline (Microphone 3)	118
5.53	Fourier Analysis of Unsteady Pressure Signal - Baseline (Microphone 4)	119
5.54	Unfiltered and Filtered Unsteady Pressure Signal - Stall Onset (Microphone 3)	121
5.55	Unfiltered and Filtered Unsteady Pressure Signal - Stall Onset (Microphone 4)	122
5.56	Fourier Analysis of Unsteady Pressure Signal - Stall Onset (Microphone 3)	123
5.57	Fourier Analysis of Unsteady Pressure Signal - Stall Onset (Microphone 4)	124
5.58	Rotating Stall Pattern - Three Cells	125
5.59	Unfiltered and Filtered Unsteady Pressure Signal - Mode 1 (Microphone 3)	126
5.60	Unfiltered and Filtered Unsteady Pressure Signal - Mode 1 (Microphone 4)	127
5.61	Fourier Analysis of Unsteady Pressure Signal - Mode 1 (Microphone 3)	128
5.62	Fourier Analysis of Unsteady Pressure Signal - Mode 1 (Microphone 4)	129
5.63	Unfiltered and Filtered Unsteady Pressure Signal - Mode 2 (Microphone 3)	131
5.64	Unfiltered and Filtered Unsteady Pressure Signal - Mode 2 (Microphone 4)	132
5.65	Fourier Analysis of Unsteady Pressure Signal - Mode 2 (Microphone 3)	133
5.66	Fourier Analysis of Unsteady Pressure Signal - Mode 2 (Microphone 4)	134
5.67	Unfiltered and Filtered Unsteady Pressure Signal - Mode 3 (Microphone 3)	136
5.68	Unfiltered and Filtered Unsteady Pressure Signal - Mode 3 (Microphone 4)	137

Figure		Page
5.69	Fourier Analysis of Unsteady Pressure Signal - Mode 3 (Microphone 3)	138
5.70	Fourier Analysis of Unsteady Pressure Signal - Mode 3 (Microphone 4)	139
5.71	Throughflow Velocity Plot - Inviscid Prediction Design Point - Plane 1	142
5.72	Throughflow Velocity Plot - Inviscid Prediction Design Point - Plane 2	143
5.73	Throughflow Velocity Plot - Inviscid Prediction Design Point - Plane 3	144
5.74	Throughflow Velocity Plot - Inviscid Prediction Design Point - Plane 4	145
5.75	Throughflow Velocity Plot - Inviscid Prediction Design Point - Plane 5	146
5.76	Secondary Velocity Vector Plot - Inviscid Prediction Design Point - Plane 1	147
5.77	Secondary Velocity Vector Plot - Inviscid Prediction Design Point - Plane 2	148
5.78	Secondary Velocity Vector Plot - Inviscid Prediction Design Point - Plane 3	149
5.79	Secondary Velocity Vector Plot - Inviscid Prediction Design Point - Plane 4	150
5.80	Secondary Velocity Vector Plot - Inviscid Prediction Design Point - Plane 5	151
5.81	Throughflow Velocity Plot - Viscous Prediction Design Point - Plane 1	153
5.82	Throughflow Velocity Plot - Viscous Prediction Design Point - Plane 2	154
5.83	Throughflow Velocity Plot - Viscous Prediction Design Point - Plane 3	155
5.84	Throughflow Velocity Plot - Viscous Prediction Design Point - Plane 4	156
5.85	Throughflow Velocity Plot - Viscous Prediction Design Point - Plane 5	157
5.86	Secondary Velocity Vector Plot - Viscous Prediction Design Point - Plane 1	158
5.87	Secondary Velocity Vector Plot - Viscous Prediction Design Point - Plane 2	159
5.88	Secondary Velocity Vector Plot - Viscous Prediction Design Point - Plane 3	160
5.89	Secondary Velocity Vector Plot - Viscous Prediction Design Point - Plane 4	161

Figure	Page
5.90 Secondary Velocity Vector Plot - Viscous Prediction Design Point - Plane 5	162
Appendix	
Figure	
A.1 Ray Trace Angle Conventions	170
A.2 Ray Trace Impeller Shroud Model	172
A.3 Ray Trace Through the Impeller Shroud	174
C.1 L2F Optical Path	184
C.2 L2F Measurement Access	186
C.3 Optical Correction Geometry	188
C.4 Impeller Inlet Flow Field	189
C.5 LDV and L2F Throughflow Velocity Data (z=3.8 cm)	191
C.6 Inviscid and Viscous Prediction of Throughflow Velocity (z=3.8 cm)	192
C.7 LDV and L2F Throughflow Velocity Data (z=6.7 cm)	193
C.8 Inviscid and Viscous Prediction of Throughflow Velocity (z=6.7 cm)	194

LIST OF SYMBOLS

<u>Symbol</u>	<u>Description</u>
d_m	Probe Volume Diameter
D_{e-2}	Illumination Beam Diameter
f	Focal Length
h	Enthalpy
k	Half Angle
l_m	Probe Volume Length
n	Number of Samples
N_{cr}	Number of Cycles for LDV Measurement
N_{fr}	Number of Fringes
P	Power
U	Velocity
w	Weighting Function
α	Measurement Direction Angle
λ	Wavelength
ν	Frequency
Subscripts	
1	Impeller Inlet
2	Impeller Exit
a	Measurement Direction
D	Doppler
i	Coordinate Direction
s	Shift
t	Tangential

CHAPTER 1 - INTRODUCTION

Centrifugal compressors are used in small gas turbine engines, turbochargers, refrigeration units and a variety of other industrial applications. The compressor is the first component in the basic gas turbine cycle and is responsible for "compressing" or raising the pressure of large volumes of flowing air. The components of a typical centrifugal compressor are shown in Figure 1.1. The compression process is accomplished in the impeller and diffuser sections. In the impeller, the kinetic energy of the fluid is increased, with work done on the fluid by the rotating impeller blades. The diffuser converts this kinetic energy to pressure energy, increasing the static pressure of the fluid. The inlet section can have prewhirl vanes with the limitation that the leading edge of the impeller blade must be oriented for smooth flow at the inlet flow angle. The diffuser section is also often vaned to reduce the volume required to decelerate the flow.

The design process for these compressors optimizes performance and efficiency, while emphasizing safety and reliability over operating range. Thus, centrifugal compressor design systems are dependent upon a complete understanding of the internal fluid mechanics. However, due to the complex three-dimensional flows associated with centrifugal machinery, general analytical and computational tools are inadequate for the modelling of the relevant flow physics, with experimental studies primarily having focused on overall design point performance. In this day when fractional percentage increases in compressor efficiency convert to significant performance gains and savings in fuel cost, the ability to characterize and subsequently predict flow phenomena such as flow separation and the strong secondary flows in turbomachinery blade rows, Figure 1.2, is an essential part of the design process.

The operating envelope for centrifugal machinery often necessitates the operation of the compressor at off-design points. This can result in flow phenomena not encountered near the compressor design point. Of particular importance are the

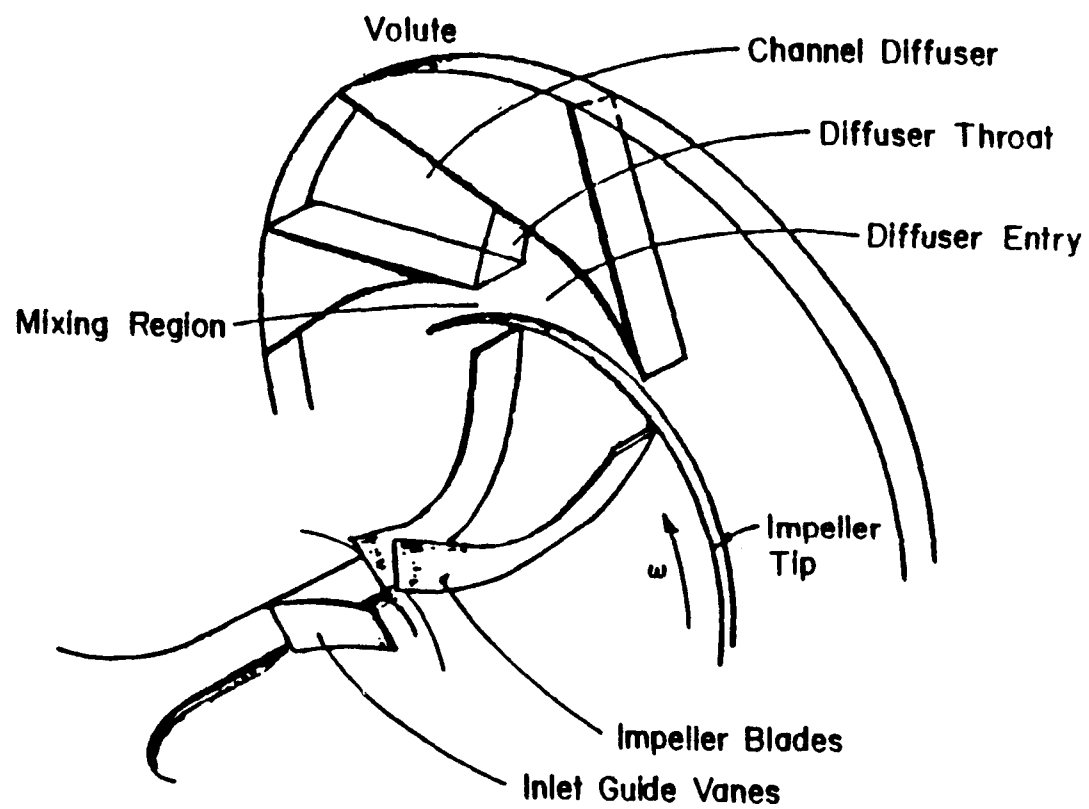


Figure 1.1 Centrifugal Compressor Components

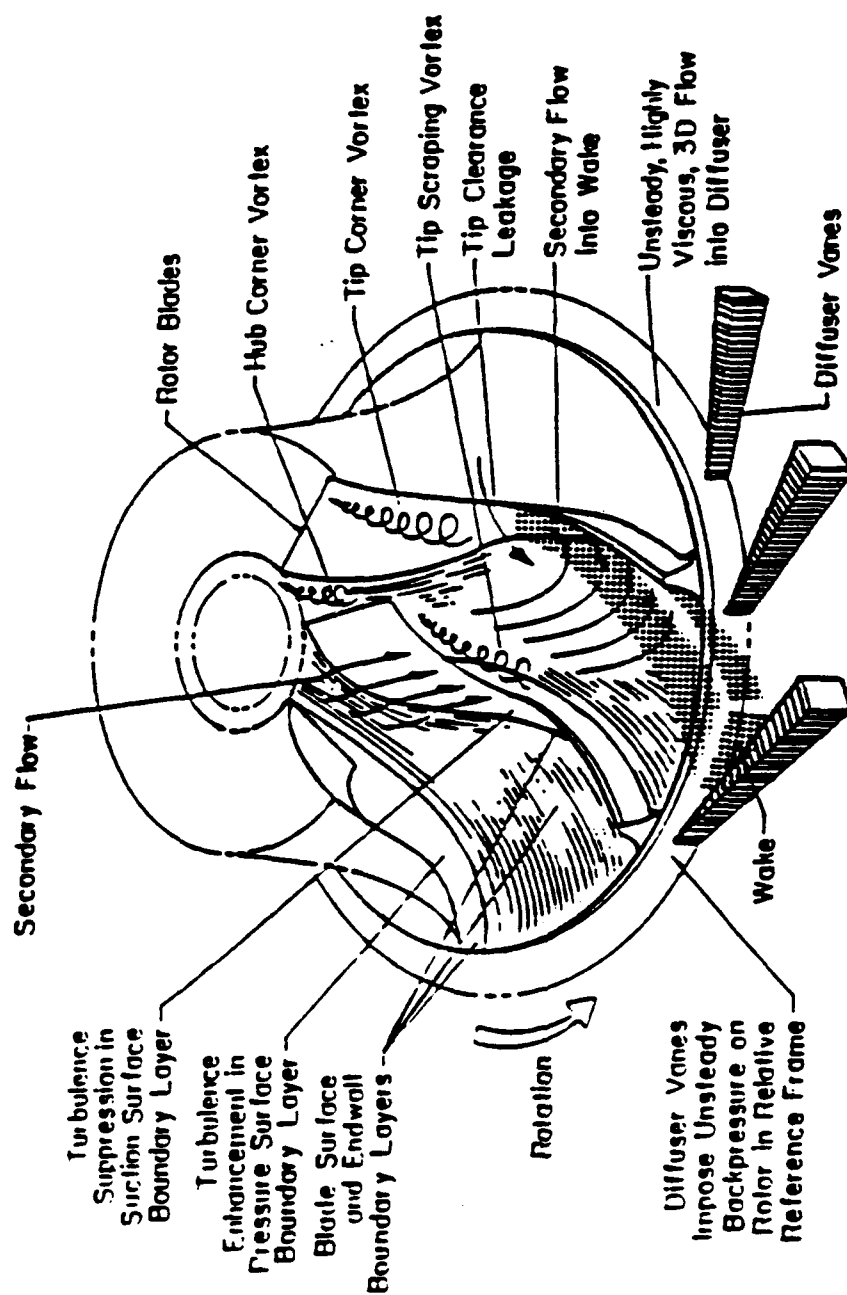


Figure 1.2 Centrifugal Compressor Flow Phenomena

self-excited flow oscillations that can occur at low mass flow rates. The most violent is surge, characterized by low frequency flow oscillations throughout the entire compression system. Surge results in a fluctuation of the net flow rate. In many systems a less violent phenomena, rotating stall, precedes surge as the mass flow rate is reduced. Rotating stall is characterized by the occurrence of rotating velocity fluctuations attributed as originating in one component of the compression system. Unlike surge, rotating stall does not cause an oscillation of the net flow rate through the system. However, both phenomena are sources of mechanical vibration which can be severe in high compression ratio machines. Since rotating stall generally precedes surge, the point of incipient rotating stall is considered the operating limit for the machine.

1.1 Research Objectives

The overall objectives of this research program are: (1) to provide internal three-dimensional centrifugal compressor flow field data at the machine design point and at the point of incipient rotating stall; (2) to define the nature of the rotating stall, i.e., the number of stall cells and their rotational speed. The velocity data will be used to define and study the fluid mechanic phenomena characteristic of compressor operation at the design point and in the regime near the onset of self-excited flow oscillations. The data will also be suitable to verify existing mathematical models and direct the development of advanced models. These objectives will be accomplished through a series of experiments performed in the Purdue Research Centrifugal Compressor.

Specific research objectives include: (1) quantification of the three-dimensional mean flow through the rotating impeller blade passages at the design point and at the point of incipient rotating stall by the acquisition and analysis of laser Doppler velocimetry data; (2) quantification of the nature of the rotating stall accomplished by the acquisition and analysis of unsteady pressure data at the impeller inlet and at circumferentially distributed locations at the impeller exit; and (3) evaluation of contemporary internal flow codes at the compressor design point for application to these complex flow fields.

1.2 Review Of Impeller Flow Studies

The turbomachinery literature applicable to this research can be grouped into two general categories: (1) optical measurements of the compressor flow field; and (2) the analysis of rotating stall in turbomachinery.

The first category includes the measurement of both the mean flow field in the rotating passages of the impeller and the impeller exit periodic unsteady flow field. The flow in both regions is highly three-dimensional, viscous dominated, and affected by separation of the flow from the blade surface. These flow field data are of fundamental interest because the ability of the impeller to do work on the fluid is directly related to the stage pressure ratio and efficiency. Relevant literature is described in the following.

A number of excellent summary articles of research in this category have been presented as part of the von Karman Institute lecture series on flow in centrifugal compressors. Krain [1] emphasized the flow field mapping done at the DFVLR-Institut für Luftstrahlantriebe with a laser two-focus velocimeter (L2F). The research performed by Eckardt and Krain have helped to qualify the differences in the flow field due to variations in impeller geometry by making measurements in a radial blade impeller, a backswept blade impeller, and an impeller with splitter blades. All three were high speed impellers with similar performance. The original investigation by Eckardt [2] provided the first flow field data inside the impeller passages of a high speed compressor. However, the L2F data only provide two components of the three-dimensional velocity vector. Elder and Forster [3] give an historical perspective, describing a series of investigations in a variety of facilities including low speed and high speed impellers. Of the investigations described by Elder and Forster, only Johnson and Moore [4] measured the three-dimensional flow field in the impeller passages. They measured the velocities with pressure probes that were traversed in the rotating passages. In addition to the limitations of introducing a physical probe into the passage, the measurements were made in a high speed impeller operating at very low speed (500 RPM).

Adler and Levy [5] used a single component laser Doppler velocimeter (LDV) to study the flow through an impeller with ten straight backswept blades. They found the impeller flow to be stable and attached, in contrast to the flow in many radial exit impellers. This work is particularly interesting because the laser Doppler velocimetry measurements were made through a window rotating with a velocity similar to that of the rotating shroud on the impeller of the centrifugal compressor to be used in this research.

Durao, Goulas, and Whitelaw [6] used a single component laser Doppler velocimeter to measure the circumferential and radial velocity components and the rms values of the corresponding fluctuating components in a 16 bladed centrifugal impeller. Their investigation, aimed at determining the nature of the secondary flow in the blade passages, revealed the existence of two vortices of unequal strength with opposite directions of rotation. The smaller of the two vortices and the associated wake region is located immediately behind the suction surface of the blades.

The second literature review category is the study of rotating stall. An introduction to the basic concepts of rotating stall is given by Stenning [7]. The majority of the experiments involve unsteady pressure and velocity measurements and flow visualization to identify the rotational velocity and the structure of rotating stall cells. An additional body of literature exists in which stall cells are modeled, with the models used to predict the onset and the rotational speed of rotating stall.

A summary of rotating stall investigations was also presented as part of the von Karman Institute lecture series on centrifugal compressors. Van Den Braembussche [8] describes the development of the current understanding of rotating stall. Several investigations cited by Van Den Braembussche are worthy of note. Senoo [9] presented a stability criterion based upon the inlet flow angle with which to predict the onset of rotating stall. Frigne and Van Den Braembussche [10] systematically studied the differences between impeller and diffuser rotating stall. They found rotating stall in the diffuser was characterized by stall cells with relative rotational speeds less than 20% of the rotational speed of the impeller. Also, different types of impeller rotating stall occurred with both low and high relative rotational speeds.

Kammer and Rautenberg [11] made measurements in a moderate speed compressor (12,000 - 14,000 RPM). They found the stall cells were characterized by a reverse flow region extending the length of the impeller near the shroud. Further work on the same experimental rig was reported by Haupt, Chen, and Rautenberg [12]. They confirmed that the reverse flow extended the height of the passage and was strongest near the shroud. Additionally, they found that the fluid in the stall cell originated on the pressure side of one passage and returned on the suction side of the next passage. Also, the reverse flow region is separated from the blade suction surface by a separation bubble near the outlet of the passage.

Mizuki, Hattori, Ariga, and Watanabe [13] made intra-passage flow field measurements in a low-speed compressor (4,150 RPM) on which a four-port yaw probe could be mounted at various locations in the impeller hub. Their results quantify the flow field and the total pressure loss distribution in the passages.

Current models for rotating stall in centrifugal impellers are limited to diffuser stall in a vaneless diffuser. Early work by Jansen [14] and Abdelhamid [15] assumed an unsteady small perturbation flow superimposed on a steady potential flow in a vaneless diffuser with parallel walls. Moore [16] considered non-parallel diffuser walls and developed a more complete small perturbation disturbance solution. This model predicts both a slow and a fast rotating stall which are compared to experimental observations of diffuser and impeller rotating stall, respectively. This suggests that it is inappropriate to describe an origin of the stall cells.

1.3 Technical Approach

The technical approach requires the quantification of the internal three-dimensional flow field in the Purdue Research Centrifugal Compressor at its design point and at the point of incipient rotating stall. This is accomplished by making measurements with a one-dimensional laser Doppler velocimeter. Additionally, unsteady pressure data will be acquired at the impeller inlet and at circumferentially distributed

locations at the impeller exit to determine the nature of the rotating stall. Finally, the flow field data taken at the compressor design point will be correlated with predictions obtained from contemporary inviscid and viscous turbomachinery flow models.

1.3.1 Flow Field Measurements

The flow field measurements are made with a laser Doppler velocimeter. The non-intrusive nature of optical flow measurement techniques such as laser Doppler velocimetry (LDV) have had a great effect on experimental fluid dynamics research. Specific to turbomachinery studies, they have allowed direct measurement of the velocity field in a rotating blade row. As with any measurement technique, there are inherent limitations with laser Doppler velocimetry. These include: (1) the light scattering particles entrained in the flow must be sufficiently small to follow the fluctuations of the flow; (2) the experimental environment may not be compatible with the controlled conditions required for the optics; (3) differentiation of the Doppler signal from noise due to stray reflections and electronic equipment is often difficult; and (4) the measurements are subject to velocity bias. Consequently, the LDV signal-to-noise ratio is usually small, especially in backscatter mode, and there are locations in the flow field where measurements are not possible.

The use of optical flow measurement techniques introduces unique difficulties. However, it has been demonstrated that they can be sufficiently eliminated or corrected, thereby enabling valid measurements in many environments. Thus, for many measurements, the advantages of a non-intrusive system outweigh the liabilities. Specifically, the measurements of the flow field in the rotating passage of turbomachinery could not be made by inserting probes into the flow field.

1.3.2 Unsteady Pressure Measurements

The unsteady pressure measurements are made with high response pressure transducers. The acquisition of time dependent pressure data depends upon a transducer system and data acquisition hardware with sufficient frequency response to measure the highest frequency component of interest. The frequency of the self-excited flow

oscillations are of the order of the impeller rotational frequency. State-of-the-art high frequency transducers and data acquisition systems have a frequency response 5 orders of magnitude higher than the rotational frequency of the Purdue Research Centrifugal Compressor impeller. Consequently, instrumentation limitations are not a factor in making these measurements.

CHAPTER 2 - PURDUE RESEARCH CENTRIFUGAL COMPRESSOR

The Purdue Research Centrifugal Compressor is a large scale, low speed turbomachine which features a mixed-flow impeller with 23 backswept blades and a vaned radial diffuser driven by a 29.8 kW (40 hp) electric motor. The shrouded impeller has an axial inlet, with the air exiting the impeller at an angle of approximately 85 degrees from the axial direction. The compressor is operated at a constant speed of 1,790 rpm, with the mass flow rate controlled by a butterfly valve on the discharge piping. The facility is described by Bryan and Fleeter [17]. A cross-section of the flow path is shown in Figure 2.1, with important facility parameters given in Table 2.1.

Optical access to the impeller flow passages is accomplished with a plexiglass shroud, Figure 2.2. This requires seals at both the leading and trailing edges of the impeller. The seal at the leading edge is a labyrinth seal, with a rotating face seal used at the trailing edge.

Optical access is also provided to the compressor diffuser flow path, including the vaneless space and the vaned diffuser. This is accomplished with a window which is approximately 30.5 cm (12 in) long and covers three diffuser vane passages. It extends to within 2.5 cm (1 in) of the impeller outlet to allow measurement near the outlet as well as in the diffuser vane regions. The optical access to the compressor is shown in Figure 2.3.

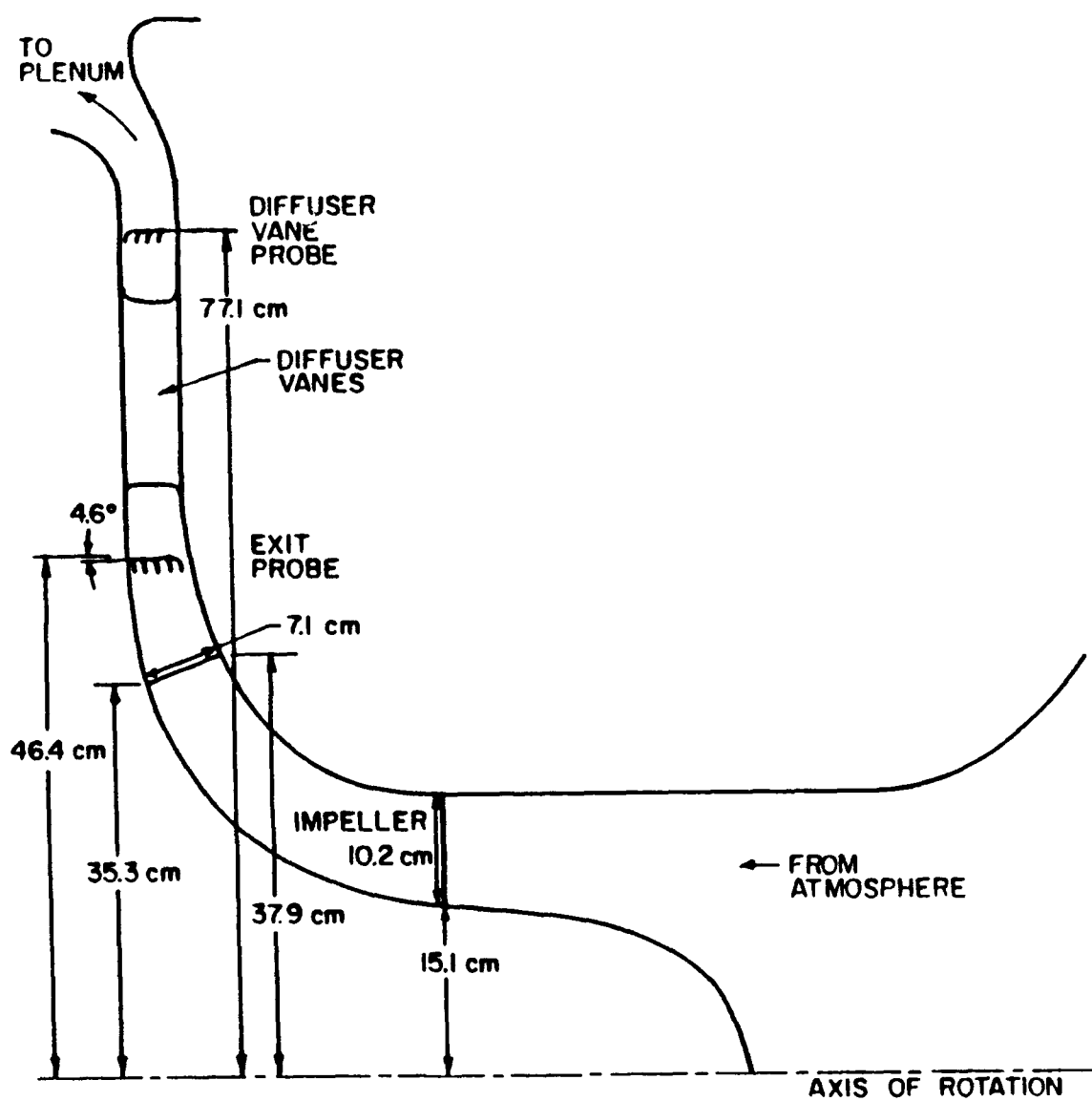


Figure 2.1 Centrifugal Compressor Flow Path

Table 2.1 Research Compressor Facility Parameters

Mean Radius Inlet: 20.3 cm
 Exit: 36.8 cm

Number of Blades: 23

Mixed-Flow

Backswept Blades

	Design	Incipient Stall
Mass Flow (kg/s)	3.33	2.18
Flow Coefficient	.253	.165
Rotational Speed (rpm)	1789	1792
Power (kW)	9.6	6.6



Figure 2.2 Impeller with Plexiglass Shroud

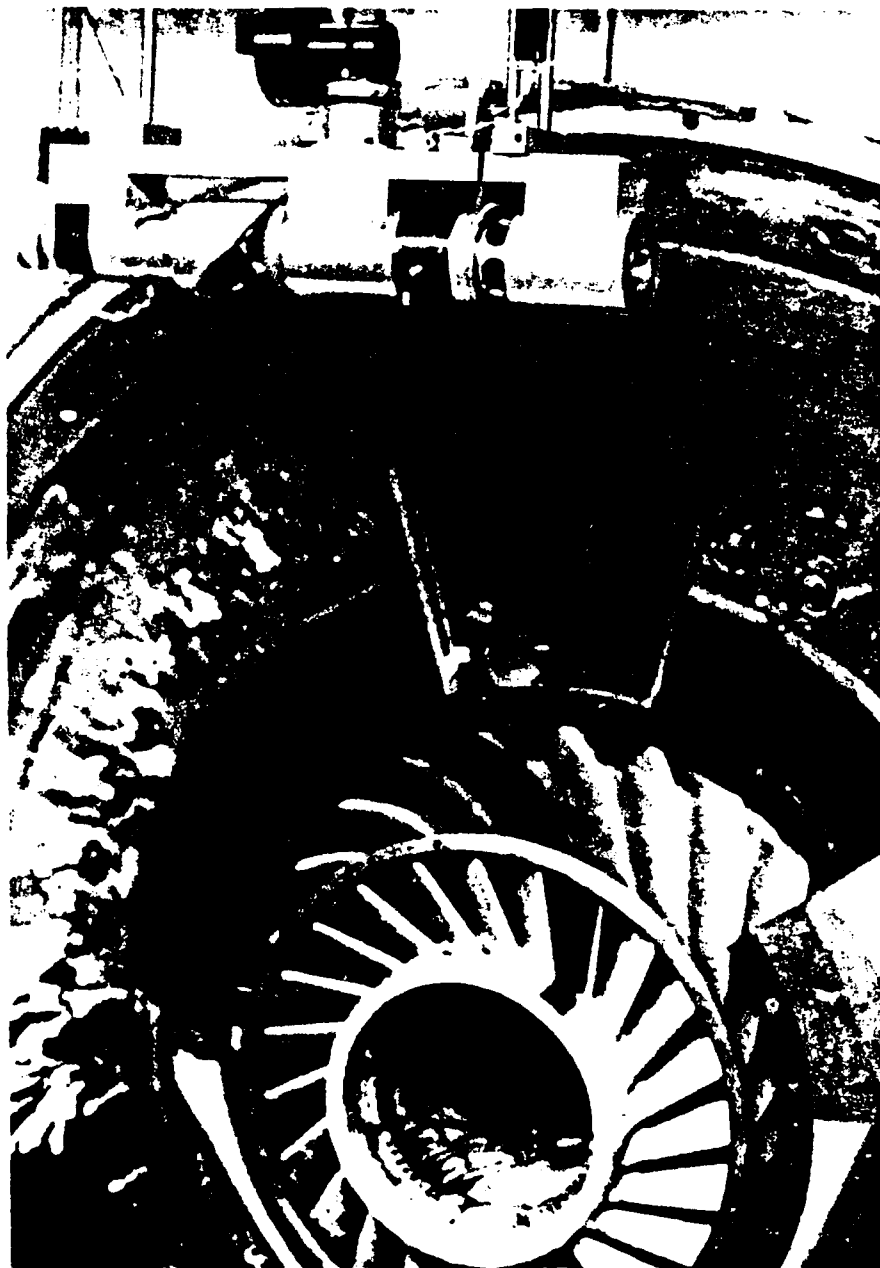


Figure 2.3 Optical Access to Compressor Flow Path

CHAPTER 3 - DATA ACQUISITION AND ANALYSIS

Bryan and Fleeter [17] measured the impeller inlet and exit flow velocity and direction and the static pressure on the impeller and in the diffuser to determine the overall aerodynamic performance of the compressor. The present investigation requires LDV and unsteady pressure measurements to quantify and describe particular phenomena in the flow field.

3.1 Laser Doppler Velocimeter

A dual-beam LDV system operated in backscatter mode is utilized, Figure 3.1. A beam splitter divides the incident beam into two parallel, equal strength beams which enter the focusing lens symmetrically about the system axis. The two beams cross at the focal plane of the lens, with the probe volume formed by the intersection of the two beams. The light scattered from small particles passing through the probe volume is collected with the same focussing lens. The lens collimates the scattered light which is reflected by a turning mirror located on the axis of the optical system. This light is imaged to a aperture at the photodetector surface with the receiving lens.

The frequency of the photodetector output signal is given by Equation 3.1. The first term on the right hand side of Equation 3.1 is the frequency difference of the two illuminating beams. The second term is proportional to the velocity of the particle and is independent of the orientation of the detector. Consequently, the photodetector can be placed in any convenient location without regard to calibration. Also the aperture size is not limited by variation of the Doppler frequency shift over the aperture.

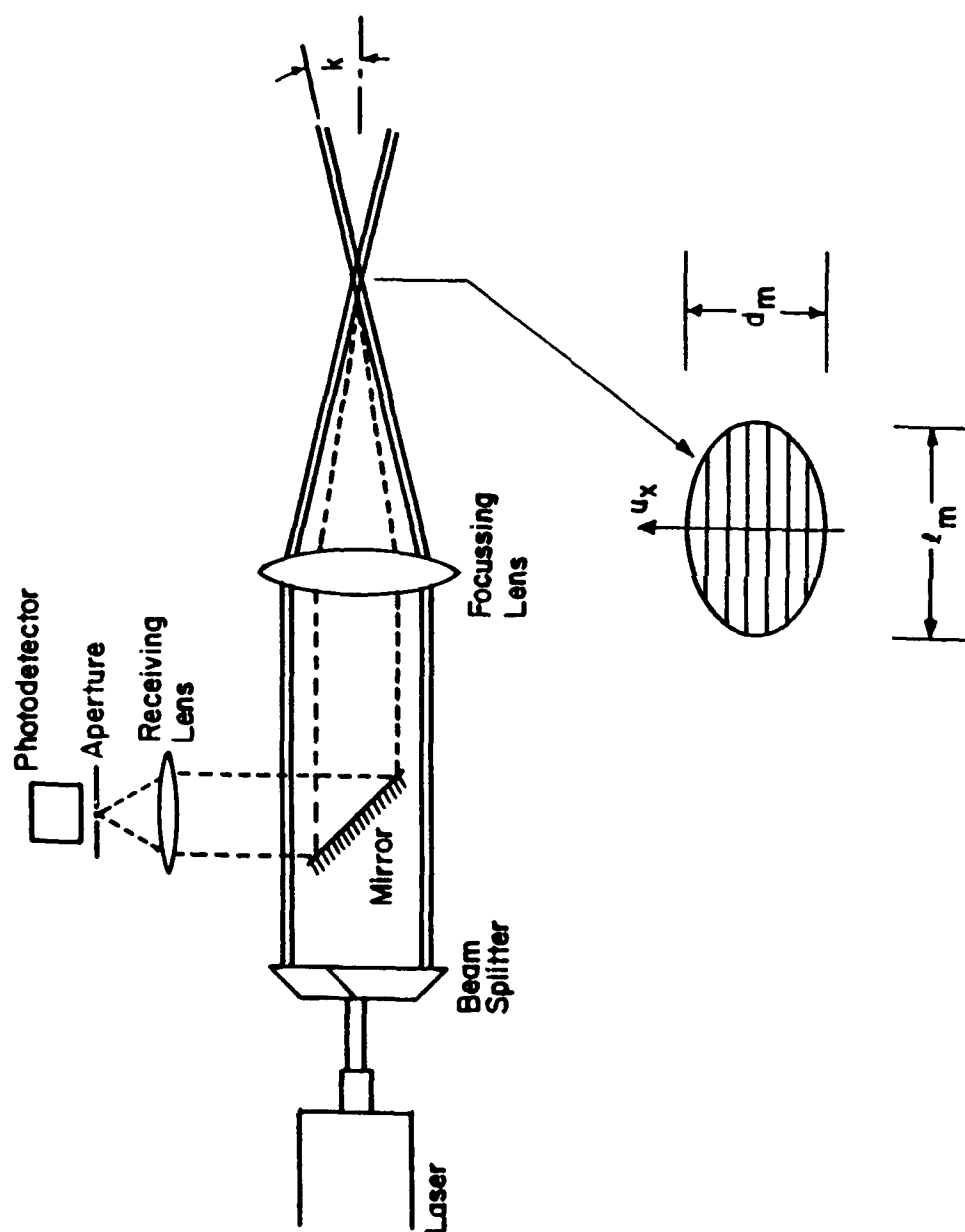


Figure 3.1 Dual Beam Laser Doppler Velocimeter

$$\nu_1 - \nu_2 = \nu_{01} - \nu_{02} + \frac{\bar{v} \cdot (\hat{s}_2 - \hat{s}_1)}{\lambda} = \nu_{01} - \nu_{02} + \frac{2 \sin k}{\lambda} u \quad (3.1)$$

ν_{01}, ν_{02} - illumination beam frequencies

s_1, s_2 - direction vectors of illumination beams

u - component of velocity which lies in the plane of
the illumination beams and is perpendicular to
their bisector

The probe volume is defined as the region in which the resulting Doppler signal from a scattering particle is greater than $1/e^2$ of the signal that the particle passing through the center would produce. Thus, the probe volume size is a function of the scattering particle, the photomultiplier gain, and the optical geometry. This definition results in an ellipsoidal probe volume. An estimate of the axis lengths of the ellipsoid d_m, l_m, h_m and enclosed volume V_D for typical receiving optics and seeding particles is given in Equations 3.2 and 3.3, respectively. The characteristic dimensions for the probe volume of the LDV system used in this research is given in Table 3.1.

$$d_m = \frac{de^{-2}}{\cos k} \quad (3.2a)$$

$$l_m = \frac{de^{-2}}{\sin k} \quad (3.2b)$$

$$h_m = de^{-2} \quad (3.2c)$$

Table 3.1 LDV Probe Volume Dimensions

d_m :	126.6 μm	(.005 in)
h_m :	126.6 μm	(.005 in)
l_m :	1266 μm	(.050 in)
V_D :	.0106 mm^3	(6.47 x 10 ⁻⁷ in ³)
d_f :	2.585 μm	(1.018 x 10 ⁻⁴ in)
N_{fr} :	49	

where

$$de^{-2} = \frac{4f\lambda}{\pi De^{-2}}$$

De^{-2} - diameter of illumination beams

λ - wavelength of illumination beams

k - half angle between illumination beams

f focal length of lens

$$V_D = \frac{\pi(de^{-2})^3}{6 \cos k \sin k} \quad (3.3)$$

The LDV system is utilized in backscatter mode. The advantages of operating in the backscatter mode include a reduced number of optical components and simplified optical access and alignment. Unfortunately, the light intensity in the backscatter configuration can be two to three orders of magnitude less than the intensity of the light collected in a forward scattered system operating under the same conditions. As a consequence, successful backscatter measurements require the optimization of the illumination beam coherence and intensity, particle size and refractive index, collection aperture size, and photodetector sensitivity.

3.1.1 Flow Seeding

Laser velocimeters do not actually measure the velocity of the fluid. Instead, they measure the velocity of small particles convected by the fluid. For these measurements, it is necessary to artificially seed the flow. There are two issues that need to be considered when choosing the seeding medium. First, the seed particle must provide an adequate scattering surface for the incident laser light. This is particularly important as the scattered light is being collected in backscatter mode and surface reflections can be bothersome. For example, an order of magnitude increase in the diameter of the scattering particle can result in an increase of signal strength by a factor of 10^2 . Significant gains may also be realized by increasing the refractive index of the particle.

The second issue is the ability of the particle to follow the fluctuations in the flow. The limiting case is the requirement for the particle to respond to the steep velocity gradient that characterizes a shock wave. The Purdue Research Centrifugal Compressor operates exclusively in the subsonic flow regime. Consequently, the size restriction on the seed particle is due solely to the ability of the particle to follow frequency fluctuations characteristic of the turbulence.

3.1.2 Signal Analysis

The laser Doppler velocimeter employed for this study uses a 250 MHz frequency counter interfaced to a HP1000 computer for analyzing the photodetector signal. Several features are included in the counter to validate the frequency measurement. Positive and negative threshold detectors are included in the Schmidt trigger circuit to discriminate between a valid signal and oscillations due to noise. The device also includes a comparison circuit that times for $N/2$ cycles. The circuit compares the Doppler frequencies calculated for both N and $N/2$ cycles and invalidates the count if the difference exceeds a prescribed error.

The one-dimensional laser Doppler velocimeter measures the velocity component: (1) spatially-averaged over the probe volume and (2) temporally-averaged over the period of the burst. Assuming that the probe volume and the burst period are small as compared to the relevant length and time scales of the flow, the measurement is assumed to be instantaneous at a point. For turbulent flows, the statistical mean and standard deviation quantities are more enlightening than the instantaneous velocity in describing the flow. As a consequence, large quantities of data must be acquired and analyzed with a computer.

3.1.3 Frequency Shifting

As will be described in the next section several potential measurement errors in laser Doppler velocimetry systems can be minimized or eliminated by proper use of frequency shifting. Frequency shifting is accomplished with an acousto-optic device called a Bragg cell. The Bragg cell is a crystal through which the laser light passes. The

crystal is driven with an acoustic wave which results in a series of beams exiting at different angles. Figure 3.2 demonstrates the operation of a Bragg cell. Of interest are the zero order (undeflected) and first order beam (deflected by a slight angle from the zero order beam). The zero order beam has no frequency shift and the first order beam is up or down shifted by the acoustic frequency of the crystal depending upon the direction the laser light passes. The operating frequency of the Bragg cells is between 30 and 50 MHz, with these flow measurements requiring a frequency shift of 10 MHz. Consequently the separate beams are individually shifted at frequencies with the required difference.

For use in this LDV system the input power to each Bragg cell is set and the cell aligned for maximum intensity of the first order beam, with the other beams eliminated by a beam block. The first order beam with the desired frequency shift is used for the flow field measurements. Additionally, the beam intensity is modulated by controlling the input power to the Bragg cells for the strobing of the incident beams as the blades pass.

3.1.4 Measurement Errors

Measurement errors are divided into two categories. Typical of most measurement techniques, sources of errors such as spatial averaging due to finite probe size, positioning accuracy, and instrument resolution need to be considered. There are also sources of error that are particular to laser Doppler velocimetry systems. Examples include fringe bias and velocity bias. More emphasis will be placed on the sources particular to the laser Doppler velocimeter because the concepts are generally less familiar and more difficult. Examples are presented with typical parameters for measurements in the Purdue Research Centrifugal Compressor.

Particle Lag

For application in the Purdue Research Centrifugal Compressor, the particles must adequately follow the velocity fluctuations due to turbulence in the flow field. An estimate of the relevant frequency range can be found from the study of turbulent boundary layers on a flat plate. The amplitude of the fluctuations decrease with

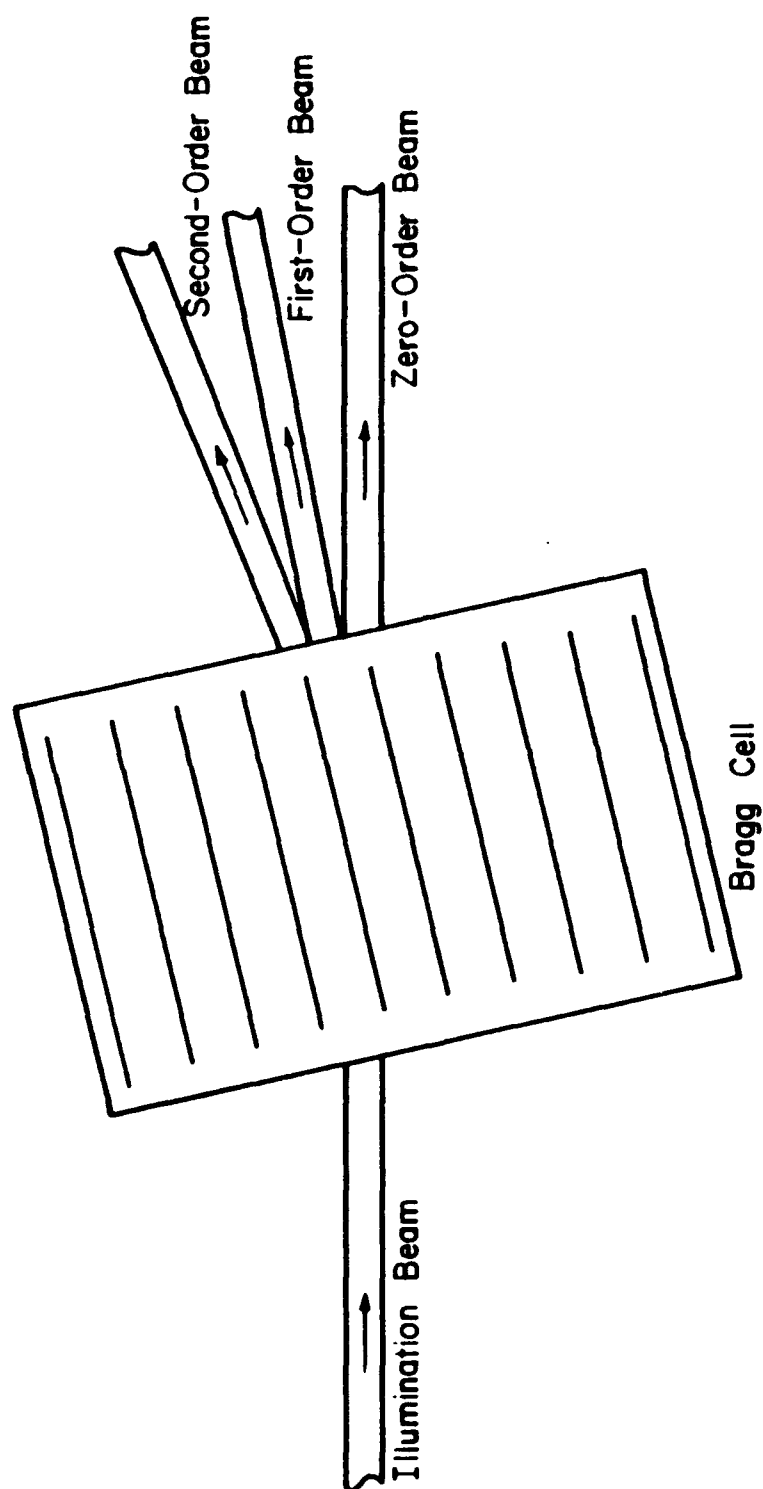


Figure 3.2 Bragg Cell Operation

increasing turbulence, Schlichting [18]. The upper frequency limit (above which the amplitude of fluctuation is less than three percent of the maximum amplitude) is given by Equation 3.4.

$$\nu_{\max} = (200 m^{-1}) \frac{|\bar{v}|}{2\pi} \quad (3.4)$$

Typically, the absolute velocity in the Purdue Research Centrifugal Compressor impeller passage is less than 80 m/s, resulting in a ν_{\max} of 2.55 kHz. A mixture of propylene glycol and ethanol is used as seed material for this research, with a density ratio of 900:1 and a particle diameter between .5 μm and 1.5 μm . Results from Maxwell and Seasholtz [19] predict that the amplitude ratio of the particle to fluid velocities is above 98% for particles with these properties in a gas flow with velocity fluctuations at the above frequency. This particle size range is adequate to determine the mean flow field and estimate the turbulence intensity in the compressor.

Fringe Bias

Fringe bias is unique to laser Doppler velocimeters. It results from the LDV system only being sensitive to the component of velocity in the plane of the incident beams and perpendicular to their bisector. As seen from Equation 3.1, the beat frequency consists of two terms: the first is equal to the frequency difference between the two incident beams, the second is proportional to the velocity component in the measurement direction. If the path of the particle through the probe volume deviates sufficiently from the measurement direction, an insufficient number of Doppler beats may occur to validate the measurement during the period in which the particle is resident in the probe volume. As a consequence, the velocity statistics are biased towards the velocity of particles with paths at the smallest angle to the measurement direction. The directions where the velocity field can be observed can be described as the cone with an axis in the measurement direction and the semi-angle ϕ , Equations 3.5 and 3.6. For N_{cr} equal to 16 and N_{fr} equal to 49 the cone angle is 71.0 degrees.

$$\cos \phi = \frac{N_{cr}}{N_{fr}} \quad (3.5)$$

$$N_{fr} = \frac{2de^{-2}}{\lambda} \tan k \quad (3.6)$$

N_{cr} - number of cycles required for a validated measurement

N_{fr} - number of fringes in the probe volume

Frequency shifting can be used to eliminate fringe bias. For the system used in this research, each incident beam is shifted with Bragg cells by a different frequency. As a result, the first term in Equation 3.1 does not equal zero. With the proper choice of the shift frequencies, measurements from particles passing perpendicular to the measurement direction will be validated. After adding the effect of frequency shifting, the relation for ϕ is given by Equation 3.7. For ν_s equal to 10 MHz and ν_D equal to 20 MHz the cone angle becomes 100.0 degrees and any particle with a velocity vector within 100.0 degrees of the measurement direction is observed.

$$\cos \phi = \frac{N_{cr}}{N_{fr}} - \frac{\nu_s}{\nu_D} \quad (3.7)$$

ν_s - shift frequency

ν_D - Doppler frequency

Directional Ambiguity

If the frequency of the two incident beams is the same, Equation 3.3 shows that the laser Doppler velocimeter can not distinguish between positive and negative velocities of the same magnitude. This problem is also resolved by frequency shifting. Namely, frequency shifting is used to make the frequency difference between the two illumination beams large enough that the histogram of the measured frequencies is on one side of the axis. Figure 3.3 demonstrates this concept. For example, if a measurement is made in a location in the flow with an average velocity of 0.0 m/s and a standard deviation of 2.0 m/s, a histogram with a spread of \pm four standard deviations requires a frequency shift greater than 3.1 MHz to move the histogram to one side of the axis.

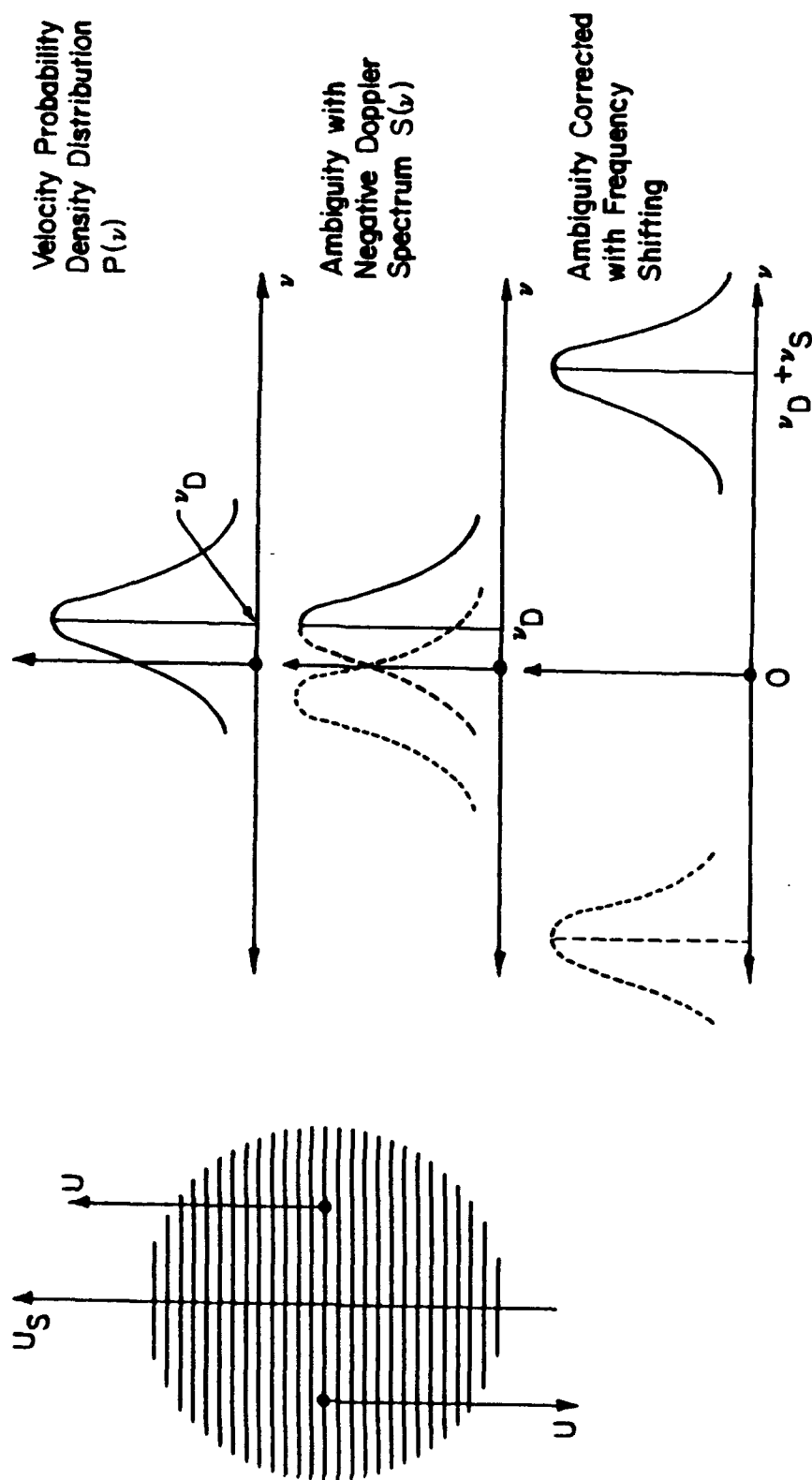


Figure 3.3 Correction of Directional Ambiguity by Frequency Shifting

Instrument Precision

The error in measuring the time of N cycles is \pm one bit of the clock circuit in the counter. The accuracy is maximized when the mantissa of the clock word is largest. For normal operation, this is accomplished by minimizing both the frequency shift required to eliminate other sources of error and the exponent without overflowing the mantissa. A measurement for 16 cycles at 80 m/s with a 10 MHz frequency shift gives a total time of 391 ns. With an exponent of one, the precision error is less than 0.26%.

Optics Alignment

Precise alignment of the optical train is required. However, two conditions can exist which would allow data to be acquired, but might introduce error into the measurements. If one or both incident beams are skewed so that there is only a partial beam intersection, both the size of the probe volume and the signal-to-noise ratio are reduced. Yet, the actual measurements are not biased. Additionally, if the beam waists do not coincide with the intersection point, the wavefronts are not planar but curved, and the beat frequency varies as a function of position in the probe volume. Both of these problems can be eliminated with proper optical alignment.

Velocity Bias

Velocity bias is unique to laser velocimetry systems and is due to the fact that measurements are made when a particle enters the probe volume. If the measurement rate is insufficient to reconstruct the time dependent velocity, the flow statistics must be calculated by ensemble averaging. Since the occurrence of a measurement is correlated to the instantaneous velocity, the velocity statistics are biased towards the higher velocities. Roesler, Stevenson, and Thompson [20] proposed an experimental technique to eliminate velocity bias. This method uses a constant frequency (equal time) sampling rate which is much slower than the average data realization rate. As a consequence, the correlation between the sampling rate and the instantaneous velocity is eliminated. Since the data from measurements in the rotating blade passages are put in bins according to circumferential position, the data in each bin is effectively equal time sampled and the results are not biased.

3.1.5 Optical Design

As a result of the limited optical access to the impeller of the Purdue Research Centrifugal Compressor, a custom optics assembly has been designed and built. The major innovation of the optics system is the use of a fiber-optic link to connect the laser and the preliminary optics to the final optics assembly. Consequently, the laser and the preliminary optics are mounted on a fixed optics bench, with the positioning and orientation of the probe volume accomplished by traversing the final optics assembly.

Preliminary Optics

A layout of the preliminary optics is shown in Figure 3.4. The system uses a 4 watt Argon-Ion laser operating at 514.5 nm. The beam is turned 180 degrees by two first surface mirrors and directed into the beam splitter. After the beam is split into beams with equal power, each of the separate beams is individually frequency shifted. One of the beams is frequency shifted by 40 MHz and the other by 30 MHz for an effective frequency shift of 10 MHz. Finally, the beams are directed into a translator module which provides the proper beam positioning for the input fiber-optic coupler. The beams are then transmitted to the final optics assembly through two polarization preserving fibers.

Final Optics Assembly

The final optics assembly is shown in Figure 3.5. The assembly includes the focussing lens, the probe volume positioning mirror, and the receiving optics system. The fibers are connected to the fiber-optic output coupler which is mounted on a bearing assembly. The output coupler can be rotated through 360 degrees around the transmission beam axis and is remotely driven by a stepping motor. The beams then pass through a thin optical window which supports the turning mirror for the backscattered signal. Finally, the beams are focussed by the focussing lens. The probe volume can be positioned in space by the mirror assembly which rotates in two planes about the transmission beam axis and is driven by independent stepping motors for each of the two planes. Since the system operates in the backscatter mode, the mirror and the lens are also used to collect the scattered light and image it on the photodetector surface.

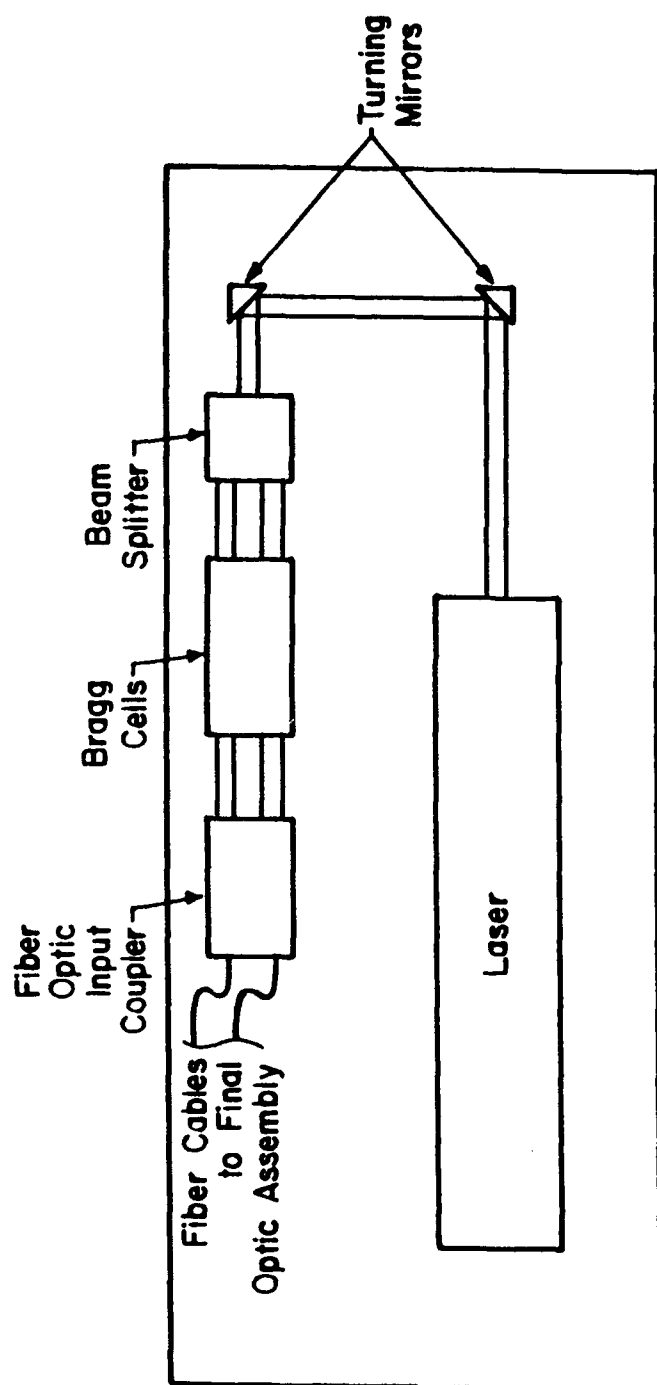


Figure 3.4 LDV Preliminary Optics

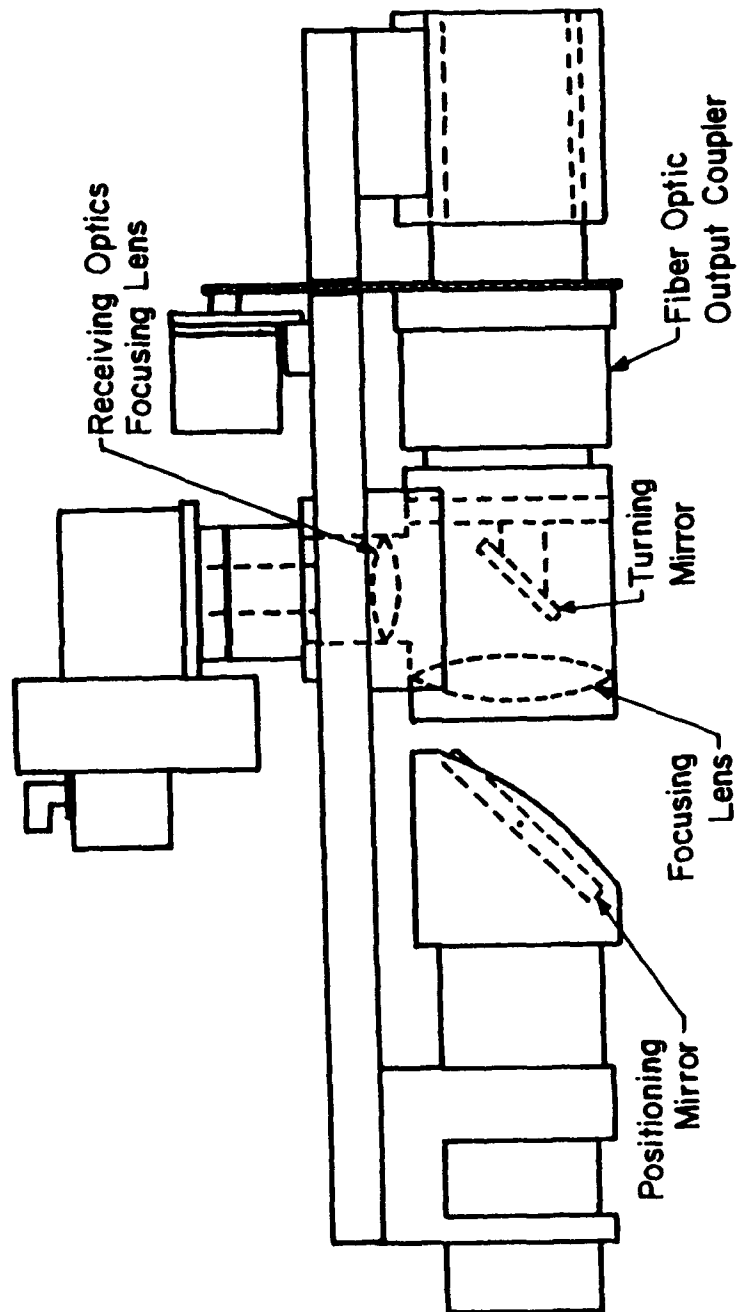


Figure 3.5 LDV Final Optics Assembly

After the scattered light is collected by the lens, it is turned by a mirror and oriented towards the receiving optics focussing lens. This lens images the scattered light on the photodetector surface.

3.1.6 Instrumentation

The three-dimensional flow field data is obtained by making measurements synchronized to the impeller rotation in a stationary meridional plane. An extensive instrumentation system, controlled with a HP1000 Data Acquisition Computer, is used for making these measurements. The functions controlled by the data acquisition instrumentation include: (1) the setting of the compressor operating point; (2) the positioning and orientation of the probe volume; (3) the strobing of the LDV illumination beams; (4) the encoding of the rotational position; and (5) the collection and recording of the LDV data. A block diagram showing the integration of the instrumentation is given in Figure 3.6.

Compressor Operating Point

The HP1000 Computer uses a feedback loop to set the required mass flow rate through the compressor. The volume flow rate is measured with a sharp edge orifice plate in the discharge piping, with the pressure across the orifice plate automatically sampled. A butterfly valve at the exit of the discharge piping is automatically adjusted to vary the compressor mass flow rate. A detailed description of the compressor flow system is given in reference 17.

LDV Traversing System

Positioning and orientation of the laser Doppler velocimeter probe volume is achieved with a six axis traversing system. The final optics assembly can be linearly traversed as a unit along three mutually orthogonal axes. The other three axes are incorporated in the final optics assembly as previously described. The three linear axes have a position encoder for feedback control during translation. The positions of the rotational axes are tracked by logging the number of motor steps. Table 3.2 gives the limits and precision of motion of each axis.

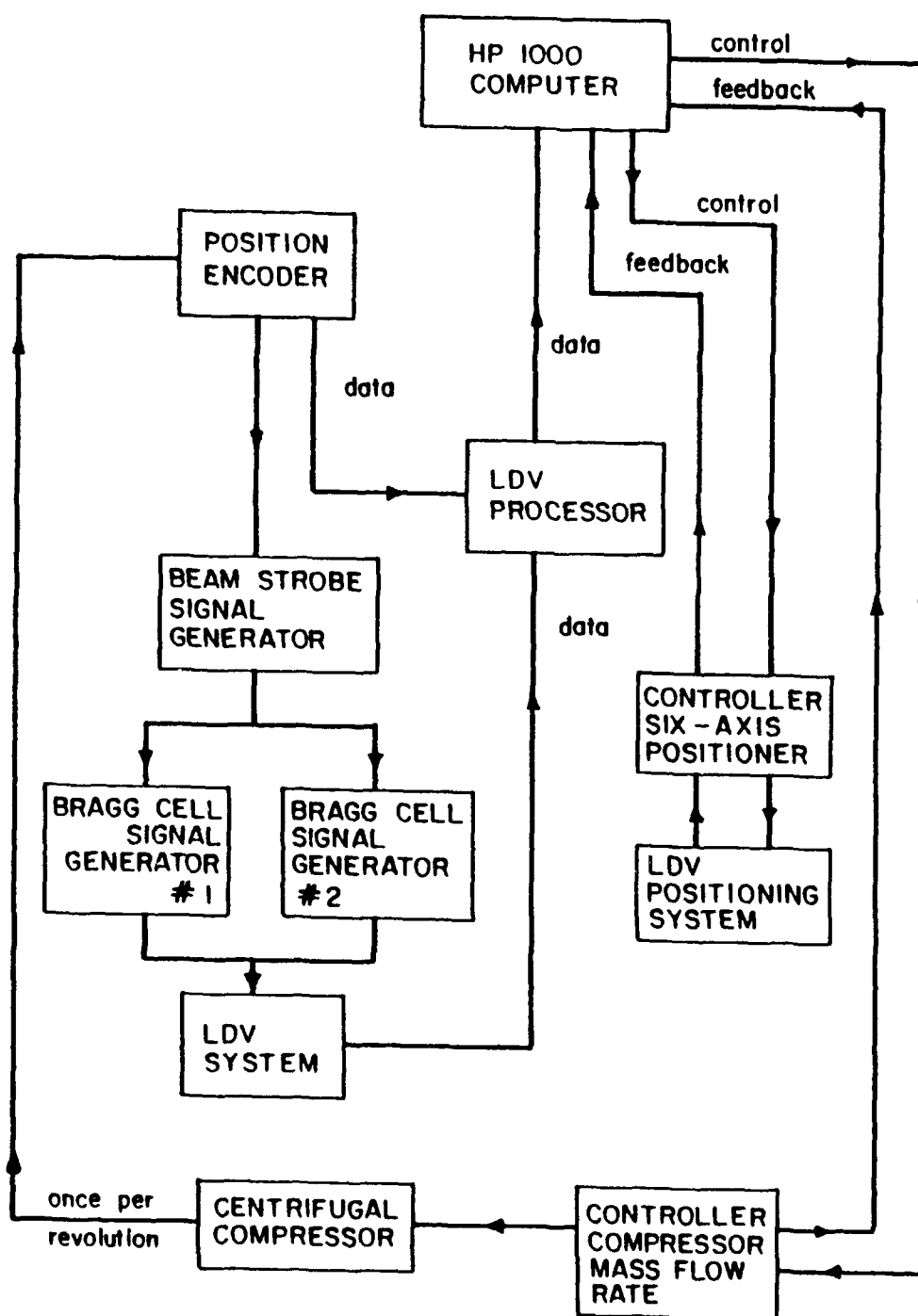


Figure 3.6 Instrumentation for LDV Measurements in the Centrifugal Compressor

Table 3.2 Traversing System Positioning Limits and Precision

Axial	Travel	Precision
x (vertical)	66.04 cm (26 in)	.025 mm (.001 in)
y (horizontal)	45.72 cm (18 in)	.025 mm (.001 in)
z (axial)	45.72 cm (18 in)	.025 mm (.001 in)
θ (mirror axis)	360°	.018°
ϕ (mirror axis)	30°	.450°
γ (beam rotation)	360°	.360°

Beam Strobing

Reflections of the illumination beams from the passing blades can provide sufficient light intensity to saturate the photodetectors. Consequently, the illumination beams must be strobed when making measurements in the blade passage. The Bragg cells used to frequency shift the laser light are also used to strobe the beams. A Hewlett-Packard square wave generator is used to modulate the power to the Bragg cells. The wave generator has an adjustable delay and adjustable pulse length and is triggered by a pulse for each blade pass. The trigger signal is generated by frequency multiplying the once per revolution pulse by the number of blades on the impeller. The signal is validated by checking that the rotational period does not vary by more than a prescribed error.

Position Encoding

The angular position of the impeller is determined with a timing circuit reset at each revolution of the impeller. The large mass of the Purdue Research Centrifugal Compressor impeller limits the fluctuations in the impeller rotational speed to a negligible level. Timing circuitry has been designed and built that includes a one MHz clock circuit which latches a timing word at the data ready pulse from the LDV system. The timing circuit is interfaced to the computer as a second counter, with the timing word passed with the LDV word to the computer and processed with the data analysis software.

LDV Data Acquisition

The LDV system is controlled by the LDV processor which is interfaced for data transmission to the HP1000 Computer. The LDV processor also passes position information from the position encoder to the computer. The data is binned according to circumferential position in the passage with data ensembled over all the blade passages. The computer continues to collect data until a sufficient number of samples are collected in each position bin. The LDV operating parameters used for these measurements are given in Table 3.3.

Table 3.3 LDV Measurement Parameters

Number of Samples:	3000
Number of Cycles:	16
Number of Position Bins:	20
Number of Histogram Bins:	20
Comparison:	3%
Lens Focal Length:	250 mm
Lens Half Angle:	5.711 deg

3.1.7 Measurement Procedure

Prior to making a measurement, the axis settings for the required measurement direction and the probe volume half angle must be determined. The complicated geometry of the impeller shroud prevents solution of a simple algebraic relation to find this information. An inverse ray trace algorithm which performs an exact ray trace from the probe volume to the focusing lens is used. A description of the algorithm is given in Appendix A. Additionally, the mass flow rate for the compressor must be set.

After the mass flow rate and the LDV position have been set, the illumination beam strobe is adjusted. The strobe is turned off (the probe volume is constantly illuminated), and the photodetector gain is slowly raised while viewing the photodetector output on an oscilloscope. When the gain is high enough to resolve the noise from the blade passing through the probe volume, the pulse delay and pulse length are adjusted to strobe the beam when the blade passes. After the strobe is set the system is ready to take data.

The next step is to set up the seed system. The seed is generated by two TSI six jet atomizers connected to a common manifold and delivered with a 1.2 m (48 in) wand at the bellmouth of the axial inlet. The length of the wand permits the support stand to be located away from the inlet to minimize any disturbance to the flow. The two atomizers provide a large range of control over the amount of seed added to the flow. After the seed is introduced, the receiving optics can be adjusted to optimize the count rate.

The final step before making a measurement is to check the LDV measurements. This is accomplished by making a scatter plot of the data across the blade passage. Two scatter plots from the measurements are included in Figures 3.7 and 3.8. In these plots the total time along the axis corresponds to $1/23$ of a revolution (23 blades), with the region with no data being the location of the blade. Examination of these plots are used to verify: (1) the band pass filter settings on the LDV processor are correct; (2) extraneous noise does not significantly affect the measurements; (3) there is adequate

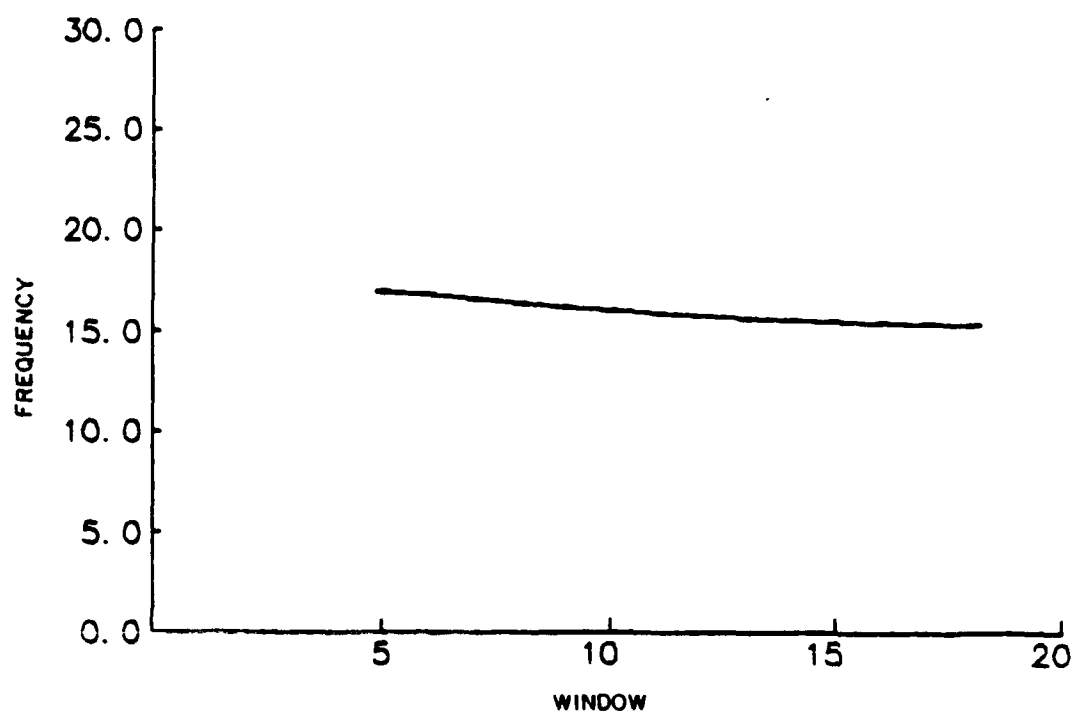
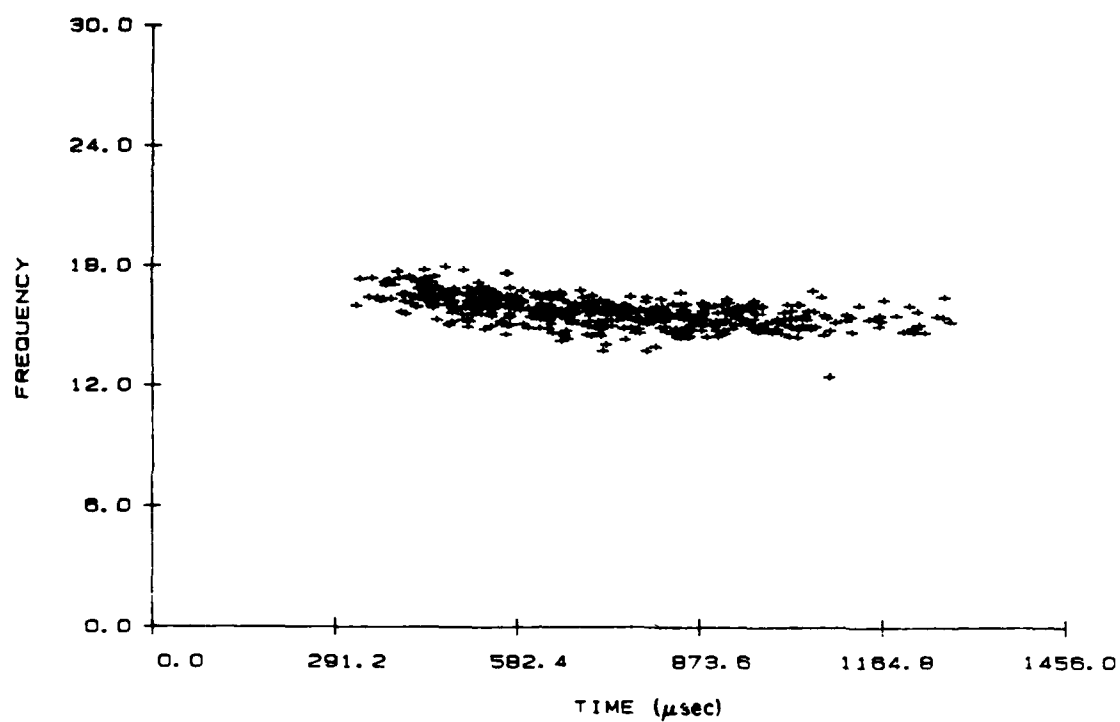


Figure 3.7 Scatter and Mean Frequency Plots (Low Turbulence)

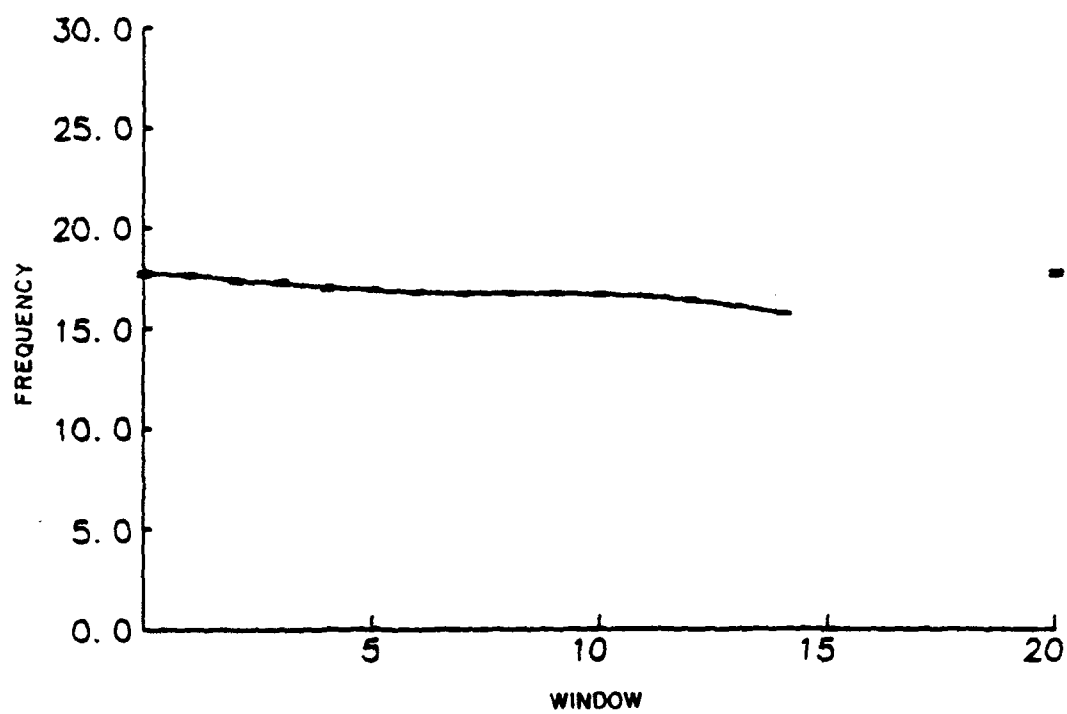
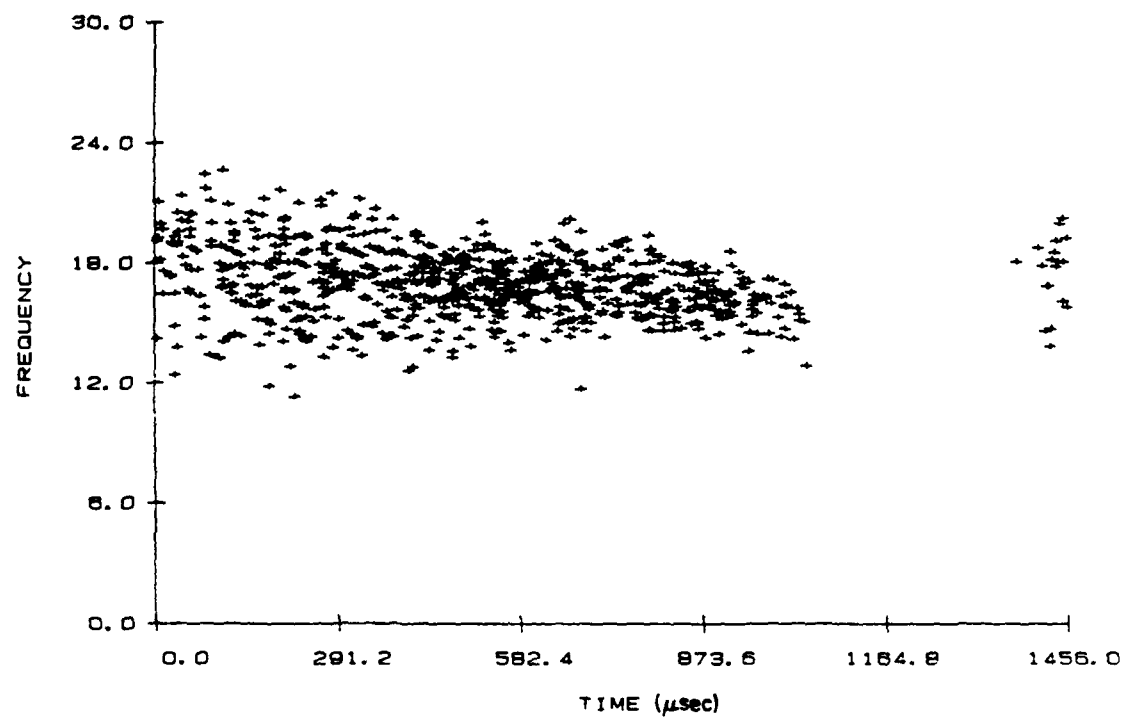


Figure 3.8 Scatter and Mean Frequency Plots (Moderate Turbulence)

seeding across the passage; (4) the position timing circuit is functioning properly; and (5) the beam strobe settings are correct. At this point there is a high degree of confidence that the LDV data accurately represents the flow field.

3.1.8 LDV Data Analysis

The laser Doppler velocimeter gives an instantaneous measure of the velocity at a point in the flow field. However, the value of the mean velocity and the turbulence intensity is of more interest than the instantaneous velocity. Statistical analysis is required to derive these quantities. Additionally, three independent measurements in different directions are required to resolve the three components of the mean velocity vector.

Statistical Analysis

The evaluation of the statistical mean and standard deviation of the velocity is defined by Equations 3.8 and 3.9. The velocity and the probability of measurement are correlated for laser Doppler velocimetry measurements. If this correlation can not be eliminated through experimental technique, w_i is a weighting function to correct for velocity bias. Since the data are effectively equal time sampled for measurements in rotating blade passages, the weighting function is unity.

$$\bar{U} = \frac{\sum_n U_i w_i}{\sum_n w_i} \quad (3.8)$$

$$[\overline{u'^2}]^{\frac{1}{2}} = \left[\frac{\sum_n (U_i - \bar{U}) w_i}{\sum_n w_i} \right]^{\frac{1}{2}} \quad (3.9)$$

The minimum sample size for each measurement is determined by choosing an acceptable uncertainty ϵ_u for a given confidence level and using Student's t distribution. The uncertainty is given by Equations 3.10 and 3.11.

$$\bar{U}_m - \epsilon_u < \bar{U} < \bar{U}_m + \epsilon_u \quad (3.10)$$

$$\epsilon_u = \frac{t s_d}{\sqrt{n}} \quad (3.11)$$

t - Student's t -parameter

s_d - sample standard deviation

n - number of samples

It has been demonstrated that the histogram of velocity measurements taken with a laser Doppler velocimeter has approximately a Gaussian distribution. As a consequence, measurements deviating by more than four standard deviations from the mean are rejected as noise.

Three-dimensional Mean Flow Field

Determination of the three-dimensional mean flow field using a one-dimensional velocimeter requires independent measurements in three unique directions for each location with constant flow conditions during each of the measurements. The three required measurements can not be made in mutually orthogonal directions due to limited optical access in the impeller blade passage. The direction of each measurement is described by a normalized vector referenced to a fixed coordinate system. The axes orientation of the orthogonal coordinate system is given in Figure 3.9. The mean velocity components along the three axes are then found by solving the three algebraic equations given in Equations 3.12 and 3.13

$$\begin{bmatrix} \bar{U}_1 \\ \bar{U}_2 \\ \bar{U}_3 \end{bmatrix} = [M]^{-1} \begin{bmatrix} \bar{U}_a \\ \bar{U}_b \\ \bar{U}_c \end{bmatrix} \quad (3.12a)$$

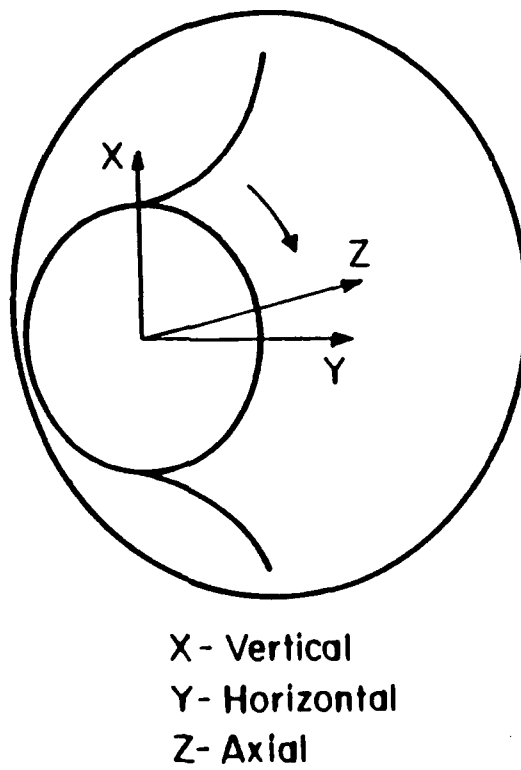


Figure 3.9 Orthogonal Coordinate System Orientation

$$[M] = \begin{bmatrix} \cos \alpha_{a1} & \cos \alpha_{a2} & \cos \alpha_{a3} \\ \cos \alpha_{b1} & \cos \alpha_{b2} & \cos \alpha_{b3} \\ \cos \alpha_{c1} & \cos \alpha_{c2} & \cos \alpha_{c3} \end{bmatrix} \quad (3.12b)$$

$$\bar{U}_a = \frac{\lambda}{2 \sin k_a} \bar{V}_{Da} \quad (3.13)$$

ν_{Da} - measured Doppler frequency

α_{ai} - the angle between the measurement direction
and the i th axis

U_a - velocity component in the measurement direction

U_i - velocity component along coordinate axis

Data Reduction

Scatter plots can again be used to check the data which quantify the flow field velocity vectors. Also shown in Figures 3.7 and 3.8 are plots of the mean frequency for each circumferential position. Error bars based upon a 95% confidence interval are included, but are barely distinguishable due to the thickness of the lines. These results are obtained by assuming a normal distribution and analyzing the data in each position bin. Figures 3.10 and 3.11 show typical histogram plots for the distribution of data in one position bin. The curve superimposed on the plots is the normal distribution curve with a mean and standard deviation corresponding to the sample mean and sample standard deviation of the data.

After the data for each of the three measurements at a single location in the meridional plane is analyzed, the mean velocity vector described by three mutually orthogonal components is determined from Equations 3.12 and 3.13. Since these results include information about the velocity field across the circumferential extent of the passage, a small number of measurements distributed along the measurement plane from hub to shroud are sufficient to describe the three-dimensional flow field. The

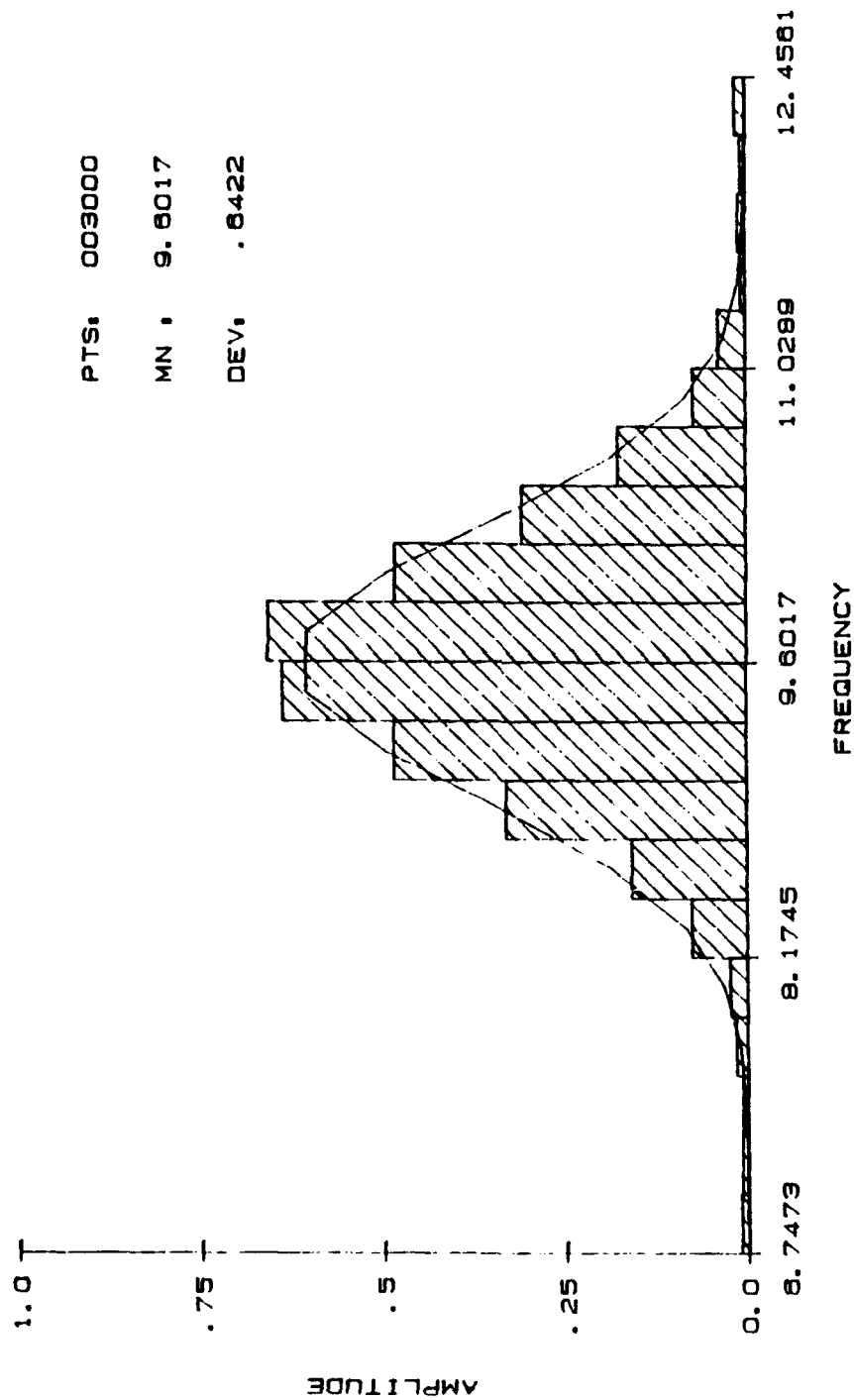


Figure 3.10 Frequency Histogram Plot (Low Turbulence)

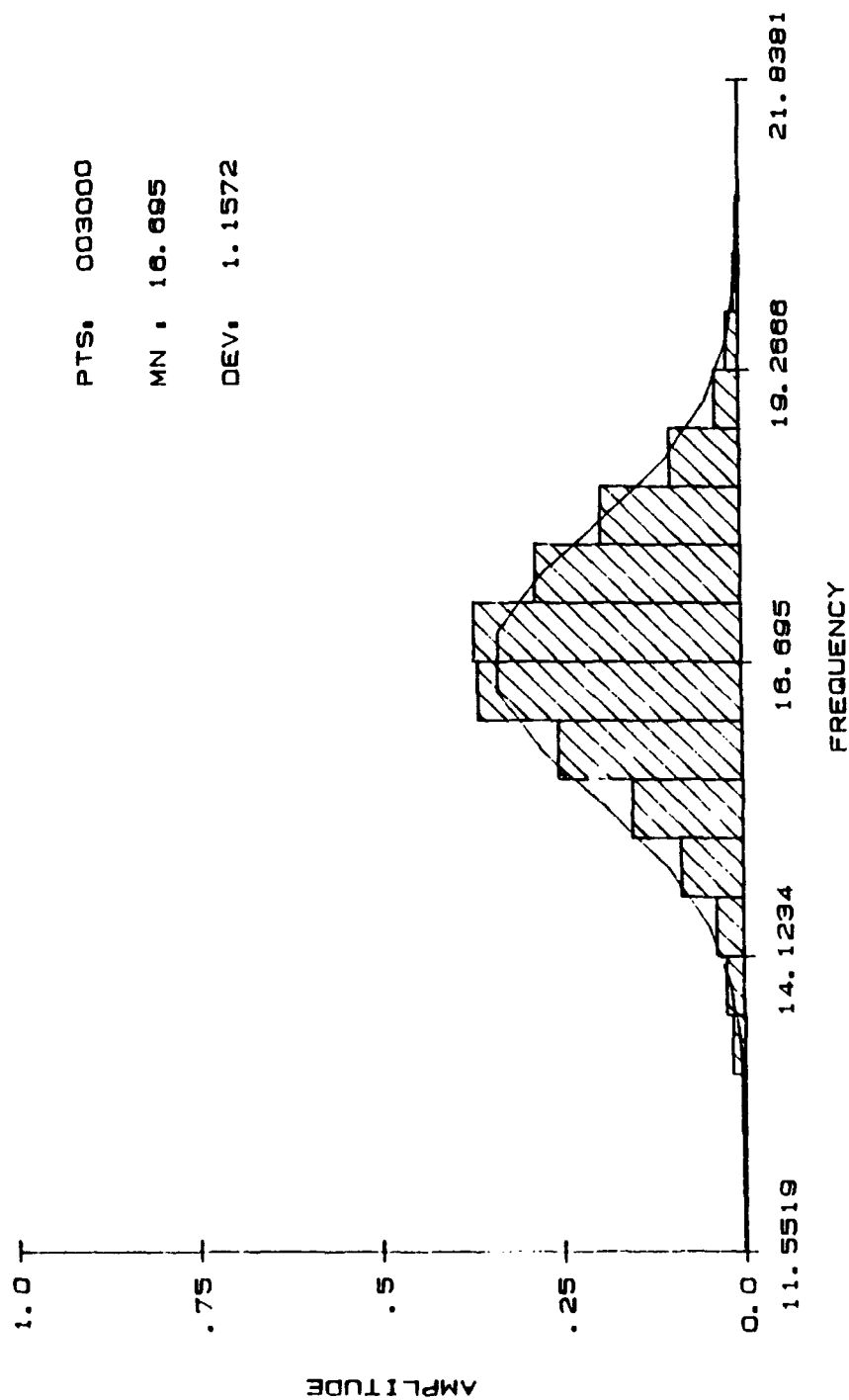


Figure 3.11 Frequency Histogram Plot (Moderate Turbulence)

distribution of measurement locations used to describe the flow in Plane 4 is given in Figure 3.12. An analysis of the uncertainty in determining the orthogonal velocity components is given in Appendix B.

3.1.9 L2F Evaluation

A limited number of measurements were made with a laser two-focus velocimeter in the rotating blade passage and diffuser of the Purdue Research Centrifugal Compressor. These results and a comparison of laser Doppler velocimetry and laser two-focus velocimetry are presented in Appendix C.

3.2 Unsteady Pressure Measurements

The measurements are made with PCB Piezotronics Model 103A high sensitivity miniature microphones. The microphones have a sensitivity of 0.22 mV/Pa (1500 mV/psi) and a resonant frequency of 13 kHz. The locations of the microphone installations are given in Figure 3.13. The signal from the microphones are amplified and passed to a Biomations A/D converter system, with all of the signals simultaneously sampled 2048 times at a user selected sampling frequency. The A/D converter system is interfaced to a HP1000 computer.

The data from the microphone signals are studied in both the time and the frequency domain. The raw data are unfiltered, and a 20 term non-recursive digital filter (100 Hz low-pass) is employed for time-domain signal analysis. The design of the digital filter is given by Walraven [21]. The harmonic composition of the signals are studied by employing a digital Fourier Transform. The data are sampled at both 200 Hz and 2000 Hz for each operating point of interest. Sampling at 2000 Hz results in a cutoff frequency of 1000 Hz, allowing the analysis of frequency components the order of the blade pass frequency (690 Hz). Sampling at 200 Hz provides sufficient resolution for studying the frequency components less than the rotational frequency (30 Hz) where rotating stall is expected to occur. The number of stall cells is determined by comparing the phase of the harmonic components to the angular separation of the transducers circumferentially distributed at the exit of the compressor.

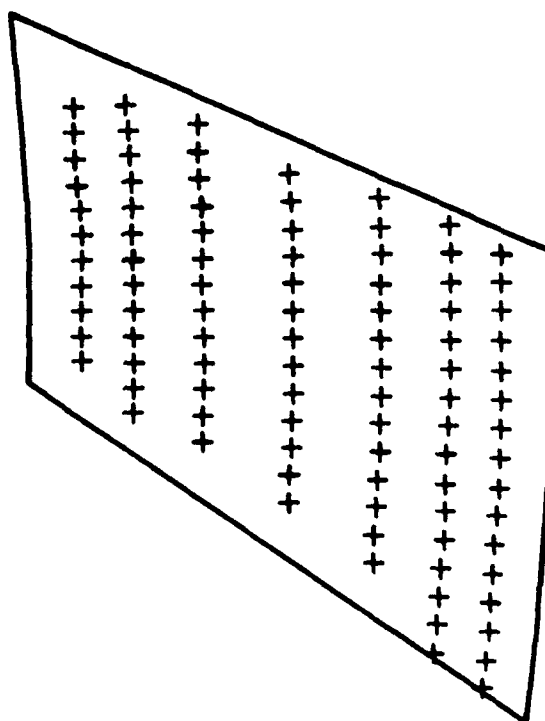


Figure 3.12 Impeller Measurement Locations - Plane 4

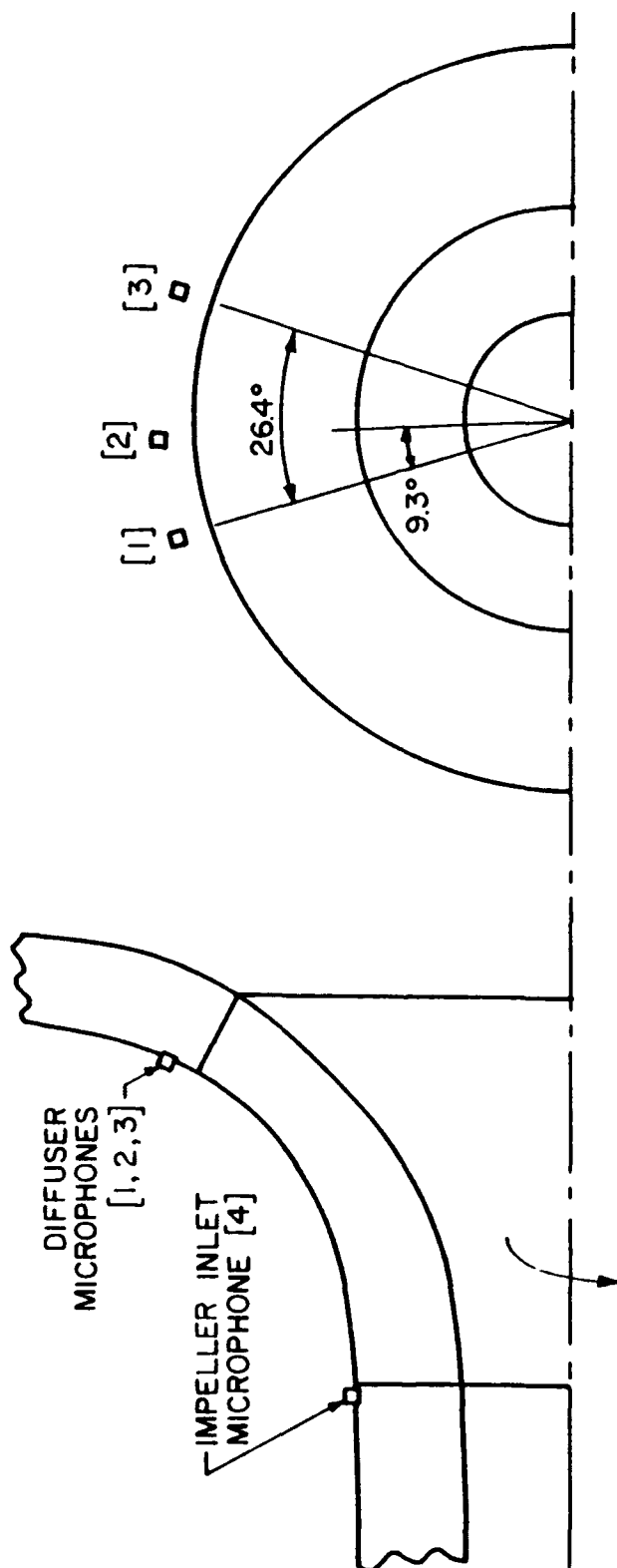


Figure 3.13 Microphone Locations in Centrifugal Compressor

CHAPTER 4 - IMPELLER FLOW FIELD MODELING

The flow through the passages of a centrifugal compressor is highly complex and three-dimensional. There are rapidly growing endwall and blade surface boundary layers, secondary flows driven by large blade-to-blade pressure gradients, and possible separated flow regions. As a consequence, adequate prediction of the flow field requires three-dimensional modeling techniques, broadly divided into viscous and inviscid flow models.

To completely describe the physics of the internal flow in turbomachinery, solutions of the compressible N-S equations are required. These equations in a three-dimensional, Cartesian, conservation law form are given by Equations 4.1 and 4.2.

$$\frac{\partial U}{\partial t} + \frac{\partial F}{\partial x} + \frac{\partial G}{\partial y} + \frac{\partial H}{\partial z} = \frac{\partial R}{\partial x} + \frac{\partial S}{\partial y} + \frac{\partial T}{\partial z} \quad (4.1)$$

$$U = \begin{bmatrix} \rho \\ \rho u \\ \rho v \\ \rho w \\ e \end{bmatrix}, \quad F = \begin{bmatrix} \rho u \\ \rho u^2 + p \\ \rho uv \\ \rho uw \\ (e + p)u \end{bmatrix}, \quad G = \begin{bmatrix} \rho v \\ \rho uv \\ \rho v^2 + p \\ \rho vw \\ (e + p)v \end{bmatrix}, \quad H = \begin{bmatrix} \rho w \\ \rho uw \\ \rho vw \\ \rho w^2 + p \\ (e + p)w \end{bmatrix} \quad (4.2a)$$

$$R = \begin{bmatrix} 0 \\ \tau_{xx} \\ \tau_{yx} \\ \tau_{zx} \\ R_4 \end{bmatrix}, \quad S = \begin{bmatrix} 0 \\ \tau_{yx} \\ \tau_{yy} \\ \tau_{yz} \\ S_4 \end{bmatrix}, \quad T = \begin{bmatrix} 0 \\ \tau_{zx} \\ \tau_{zy} \\ \tau_{zz} \\ T_4 \end{bmatrix} \quad (4.2b)$$

While these equations are valid for turbulent flows, the computational requirements far exceed practical computing capabilities for the complex internal geometries of

interest. As a consequence, current modeling has taken the approach of single point closure of the Reynold's averaged N-S equations. In this approach the Reynold's stress terms are modeled through the addition of auxiliary algebraic or differential relations. Computational limitations again influence simulations of the Reynold's averaged Navier-Stokes calculations. Generally, a fine grid can only be introduced in the direction normal to solid surfaces, allowing simulation of the viscous effects at high Reynold's numbers solely in that direction. The effect on the accuracy of simulated flows with separation and flows with large scale unsteady behavior is still unresolved.

The Reynold's averaged N-S equations are elliptic in nature. To reduce computational time and required storage, simplifying assumptions are often made which change the nature of the equations. For steady flows these can be grouped into three categories: partially parabolic, fully parabolic, and partially elliptic approximations.

The parabolic approximations assume an a priori knowledge of the main flow direction and neglect diffusion in this direction. Thus flows with separation and recirculation zones can not be simulated unless some correction is added. Generally, in these methods the pressure is treated as elliptic and stored at each grid point, with the remaining variables assumed parabolic and only stored in two or three cross-sections at one time. Given the approximate pressure field, the momentum and energy equations are space-marched through the computational domain in the flow direction and the variables are corrected locally to satisfy continuity. For the fully parabolic approximation, the initial pressure field is assumed to contain the full effects of boundary curvature, and the solutions are marched one iteration in the flow direction. The partially parabolic approximation assumes that the downstream conditions influence the upstream solution, and employs a multi-pass algorithm to march the momentum and energy equations to convergence while updating the pressure field after each step. Finally, the partially elliptic approximation is an enhancement to the above solutions for flows with small, but significant, reverse flows. This approximation determines a locally elliptic solution of the flow equations for the region of reverse flow.

As a simplification to solving the full N-S equations, the viscous terms are neglected, resulting in the Euler equations. The three-dimensional, Cartesian, conservation law form of these equations is given by Equations 4.3, with U , F , G , and H given by Equation 4.2a. The system is completed by an equation of state relating pressure, density, and energy, McNally and Sockol [22].

$$\frac{\partial U}{\partial t} + \frac{\partial F}{\partial x} + \frac{\partial G}{\partial y} + \frac{\partial H}{\partial z} = 0 \quad (4.3)$$

The system of equations changes character depending on the local Mach number. Probably the most developed technique for solving the Euler equations in the subsonic Mach number regime is to march in time until an asymptotic steady-state solution is attained. However, there are several difficulties. Any marching solution generates perturbation waves which move through the computational domain. Since the viscous terms have been eliminated, these perturbations must be radiated from open boundaries or damped by the addition of artificial viscosity terms. In either case, convergence tends to be slow, requiring large computational times. Additionally, a large number of primitive variables must be stored at each grid point and satisfactory boundary conditions must be derived for each variable. Unfortunately, both of these latter problems also apply for viscous numerical methods. One solution is to make further simplifications to the flow model equations. For example, the problem can be reduced to two dimensions and a stream function analysis employed, or the flow can be assumed to be irrotational and isentropic and a potential analysis used.

4.1 Inviscid Model

The inviscid predictions of the flow field in the impeller of the Purdue Research Centrifugal Compressor are obtained from a code based upon the time marching method for solving the Euler equations developed by J. D. Denton [23]. This code was chosen because it is widely used for turbomachinery analysis, with descriptions published in the turbomachinery and computational fluid dynamics literature. This model is based upon a finite volume, time marching solution of the Euler equations until convergence to a steady-state solution is reached. To employ a finite volume solution, the Euler equations

are integrated over a control volume. The system is modeled by Equations 4.4 and 4.5, with a brief summary of the important features of Denton's model presented in the following.

$$VOL \Delta(A) = \Delta t \sum (B) + \Omega \frac{\partial(A)}{\partial \theta} \Delta t VOL \quad (4.4)$$

$$A = \begin{bmatrix} \rho \\ \rho V_x \\ \rho r V_\theta \\ \rho V_r \\ \rho E \end{bmatrix}, \quad B = \begin{bmatrix} \rho \bar{V} \cdot \bar{A} \\ \rho \bar{i}_x \cdot \bar{A} + \rho V_x \bar{V} \cdot \bar{A} \\ \rho r \bar{i}_\theta \cdot \bar{A} + \rho r V_\theta \bar{V} \cdot \bar{A} \\ \rho \bar{i}_r \cdot \bar{A} + \rho V_r \bar{V} \cdot \bar{A} \\ \rho H \bar{V} \cdot \bar{A} \end{bmatrix} \quad (4.5)$$

Ω - rotational speed of the impeller

In the rotating frame, the solution is found using absolute flow quantities and applying the conservation equations to a fixed grid which instantaneously coincides with the rotating grid. The rate of change of property P at a point in the rotating grid is then related to the rate of change of the same property at the corresponding point in the fixed grid by Equation 4.6.

$$\left(\frac{\partial P}{\partial t} \right)_R = \left(\frac{\partial P}{\partial t} \right)_F + \Omega \frac{\partial P}{\partial \theta} \quad (4.6)$$

The distinctive feature of Denton's solution method is the "Opposed Difference Technique". The algorithm uses upwind differencing in the streamwise direction to insure stability, while downwind differencing is used for the pressure. Central differencing is used for all properties in the cross-stream direction. The steady-state errors due to the upwind and downwind differencing are completely removed through use of flux correction factors for errors in the original upwind and downwind flux estimates. An additional benefit of the "Opposed Difference Technique" is that its stability depends on the axial Mach number rather than the more strict requirement on the absolute Mach number.

The Denton code requires boundary and initial conditions. The blade geometry is input as a user specified number of blade sections. If the number of input sections does not match with the number of grid points in the hub to shroud direction, the grid locations are found by linear interpolation. At the inlet, the absolute stagnation temperature and pressure, the flow angle in the meridional plane, and the flow direction on the blade-to-blade stream surfaces must be specified. At the exit, the static pressure distribution from hub to shroud must be specified. Additionally, to correct for boundary layers an aerodynamic blockage distribution in the passage can be specified. The mass flow through the compressor varies with the exit pressure and blockage. Typically, a representative blockage distribution is entered and the exit pressure is iterated until the desired mass flow is obtained.

For application of this code to predict the flow field in the impeller of the Purdue Research Centrifugal Compressor, a $7 \times 7 \times 49$ grid was used with 9 grid points upstream of the blade leading edge and 9 grid points downstream of the trailing edge. The impeller geometry was entered through blade profiles at the hub and shroud. The grid was packed at the blade leading and trailing edges. Since static pressure data are available for the compressor, the initial intention was to input the measured pressure and then iterate to a blockage distribution which yielded a reasonable match for the mean flow rate at different operating points. Unfortunately, converged solutions have not been achieved when aerodynamic blockage is added. Thus, the results reported herein match the flow rate, but are not representative of the actual pressures in the impeller of the Purdue Research Centrifugal Compressor.

4.2 Viscous Model

The viscous results are from a modified version of the Impact (Implicit Parabolic Computational Technique) code developed by C. M. Rhie [24]. This method uses the parabolic approximation for solving the finite volume form of the Reynold's averaged Navier-Stoke's equations. After applying the isotropic turbulent viscosity hypothesis, the system is modeled by Equations 4.7 and 4.8. The system of equations is thus completed by assuming constant rothalpy and applying the perfect gas relationship.

$$\frac{\partial}{\partial x_i}(\rho u_i) = 0 \quad (4.7)$$

$$\frac{\partial}{\partial x_i}(\rho u_i u_j) = -\frac{\partial P}{\partial x_j} + \frac{\partial}{\partial x_i} \left[(\mu + \mu_t) \left(\frac{\partial u_i}{\partial x_j} + \frac{\partial u_j}{\partial x_i} \right) \right] - \frac{2}{3} \rho k \delta_{ij} \quad (4.8)$$

A two equation k - ϵ eddy viscosity turbulence model modified to account for streamline curvature and coriolis acceleration is used to close the system. The eddy viscosity μ_t is given by Equation 4.9, with the scalar transport mechanisms for k and ϵ given by Equations 4.10a and 4.10b, respectively.

$$\mu_t = C_u \rho \frac{k^2}{\epsilon} \quad (4.9)$$

C_u - empirical constant

k - turbulent kinetic energy

ϵ - turbulence energy dissipation

$$\frac{\partial}{\partial x_i}(\rho u_i k) = \frac{\partial}{\partial x_i} \left[\left(\frac{\mu_t}{\sigma_k} \right) \left(\frac{\partial k}{\partial x_i} \right) \right] + P - \rho \epsilon + G_c \quad (4.10a)$$

$$\frac{\partial}{\partial x_i}(\rho u_i \epsilon) = \frac{\partial}{\partial x_i} \left[\left(\frac{\mu_t}{\sigma_\epsilon} \right) \left(\frac{\partial \epsilon}{\partial x_i} \right) \right] + \left(\frac{\epsilon}{k} \right) (C_1 P - C_2 \rho \epsilon) + G_c \frac{\epsilon}{k} \quad (4.10b)$$

C_1 , C_2 , σ_k , and σ_ϵ - empirical constants

G_c - streamline curvature correction proposed

by Wilcox and Chamber [25]

The governing equations are written in the form of a single general relation for an arbitrary scalar dependent variable ϕ , Equation 4.11.

$$\frac{\partial}{\partial x_j}(\rho u_j \phi) = \frac{\partial}{\partial x_j} \left(\Gamma \frac{\partial \phi}{\partial x_j} \right) + S \quad (4.11)$$

Γ - effective diffusion

S - source term

To compute the solution, the conservative form of the general transport equation expressed in arbitrary curvilinear coordinates is integrated over a control volume, with subsequent approximations made to yield a finite-difference expression. The diffusion term in the streamwise direction is neglected to parabolize the governing equation. Linear interpolation of quantities between adjacent grid nodes results in a fully implicit expression with second-order accurate, centered differencing in the cross-stream direction and first-order accurate, upstream differencing in the streamwise direction. The difference relation is solved simultaneously at each point in the cross stream plane and, after obtaining satisfactory convergence, the procedure is repeated at the next cross stream plane. To treat reverse flow regions, the flare approximation is employed which neglects convection in the through-flow direction for the region.

After the momentum equations are marched through the computational domain, the pressure is corrected in a three-step process to satisfy local and global continuity. As part of the solution process at each cross stream plane, a one-dimensional global pressure correction is applied. Subsequently, a two-dimensional elliptic pressure correction is performed to satisfy local continuity. Finally, a three-dimensional elliptic pressure correction is executed after each complete forward marching pass. The entire solution procedure is iterated until adequate convergence of the flow field is obtained.

To apply this code to the impeller of the Purdue Research Centrifugal Compressor, several modifications were required. The grid generation program associated with the Impact code was designed for radial exit impellers. The Purdue facility has a mixed flow impeller with an exit turning angle of approximately 85 degrees from axial. Consequently, the code was modified to handle the mixed flow geometry.

A second modification was made to the boundary conditions on the shroud surface of the blade passage. The Purdue compressor is shrouded. Thus the no slip condition gives zero relative tangential velocity at the shroud wall. However, the code was written for unshrouded impellers where there is a relative tangential velocity at the shroud wall due to the relative motion between the passage and the wall.

The final modification was on the hub and shroud boundary conditions in the upstream and downstream sections of the computational domain. The code was modified to take into account the solid walls at the inlet and exit of the compressor.

Initial and boundary conditions must be specified to apply this code to centrifugal geometries. The computational grid is generated in an independent program, with the input having the same format as the input for the Denton Code. The information required to start the flow code includes the three velocity components, the static pressure, the enthalpy, the turbulent kinetic energy, and the turbulence dissipation at all locations in the inlet plane. The code does not require any information at the exit of the impeller and, since the input velocity specifies the mass flow, iteration of the input parameters is not required to match the mass flow.

The grid used to model the flow in the impeller of the Purdue Research Centrifugal Compressor is 15x19x50, with the blade leading edge at the 8th streamwise grid and the trailing edge at the 42nd grid. The major difficulty in running the Impact code is the determination of a suitable value of the inlet turbulent dissipation which affects the turbulent viscosity as determined by the $k-\epsilon$ model.

CHAPTER 5 - RESULTS

LDV flow field and unsteady pressure measurements were made to study the three-dimensional flow field in the compressor at the design operating point and at the incipient stall operating point. Predictions from three-dimensional inviscid and viscous flow models are also presented for correlation with the flow field data at the compressor design operating point.

The design operating point for the constant speed operating line (1,790 rpm) has a mass flow rate of 3.33 kg/s (7.35 lbm/s). The design operating point data are compared with the data taken at the incipient stall operating point and with predictions from the three-dimensional flow field models. The second operating point has a mass flow rate of 2.18 kg/s (4.80 lbm/s). This mass flow rate is slightly above the point at which rotating stall begins and is referred as the incipient stall operating point. The variation of the inlet stagnation temperature and pressure for the experiment from the nominal values of 298 K (537 R) and 101.3 kPa (14.69 psia) are less than the uncertainty in determining the compressor mass flow rate. Consequently, the corrected mass flow rate at each operating point is also constant. The incipient stall data are studied to quantify and describe the characteristic flow phenomena of incipient rotating stall.

5.1 LDV Measurements

LDV data were taken at five Planes in the impeller passage of the Purdue Research Centrifugal Compressor for two operating points. The planes are located at 16%, 42%, 62%, 76%, and 88% passage, Figure 5.1. The three-dimensional flow field data are interpolated onto a 11 x 15 regularly spaced grid, with the results presented in terms of the throughflow velocity (velocity component normal to the measurement plane) and the secondary velocity vector (velocity components in the measurement plane) for each plane.

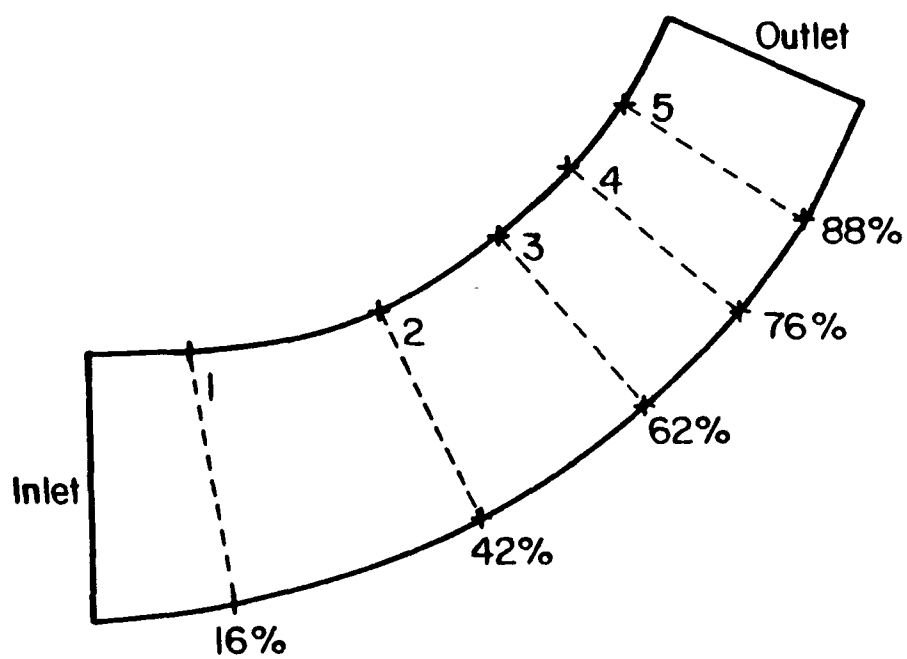


Figure 5.1 Measurement Plane Locations

5.1.1 Data Validation

The LDV data were also used to verify the mass flow rate through each measurement plane, with continuity being satisfied to the uncertainty in mass flow rate at all planes for both operating points. Additionally, the power input to the fluid as a function of passage position is calculated using the Euler turbine equation at each data plane, Equation 5.1. The data taken at both mass flow rates are presented in Figure 5.2, with the data points at 100% passage from the investigation by Bryan and Fleeter [17]. The good agreement between the results from the previous investigation and this work is evident.

$$P = \sum (h_{ij}) \dot{m}_{ij} \quad (5.1a)$$

$$h_{ij} = (U_{rot} U_t)_{ij} \quad (5.1b)$$

P - power

h - enthalpy

U_{rot} - rotational speed of the impeller

U_t - tangential velocity component

5.1.2 Mean Flow - Design Operating Point

The throughflow velocity data obtained at the design operating point are presented in Figures 5.3 through 5.10. The throughflow velocity plots for Planes 1-5 are presented in Figures 5.3 through 5.7. Rotated views of these data for Planes 3-5 are shown in Figures 5.8, 5.9, and 5.10.

The Plane 1 throughflow velocity data show a nearly linear velocity gradient from the suction to pressure surface along the passage. The throughflow velocity also increases from hub to shroud. At Plane 2, the throughflow velocity data indicate a thickening of the boundary layer on the hub surface. Additionally, the velocity gradient from the suction to pressure surface is reduced. At Plane 3, a low velocity region forms on the

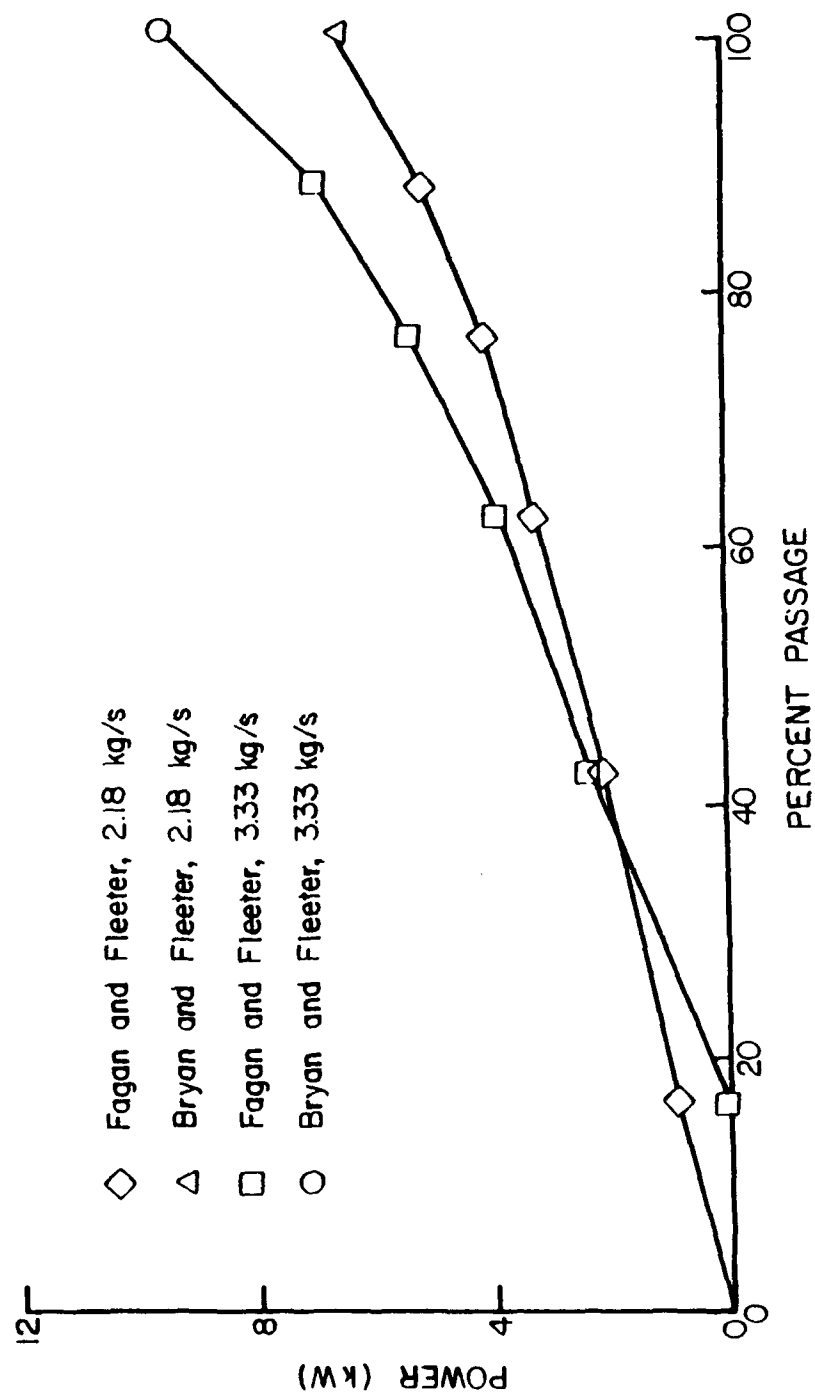


Figure 5.2 Impeller Passage Flow Work

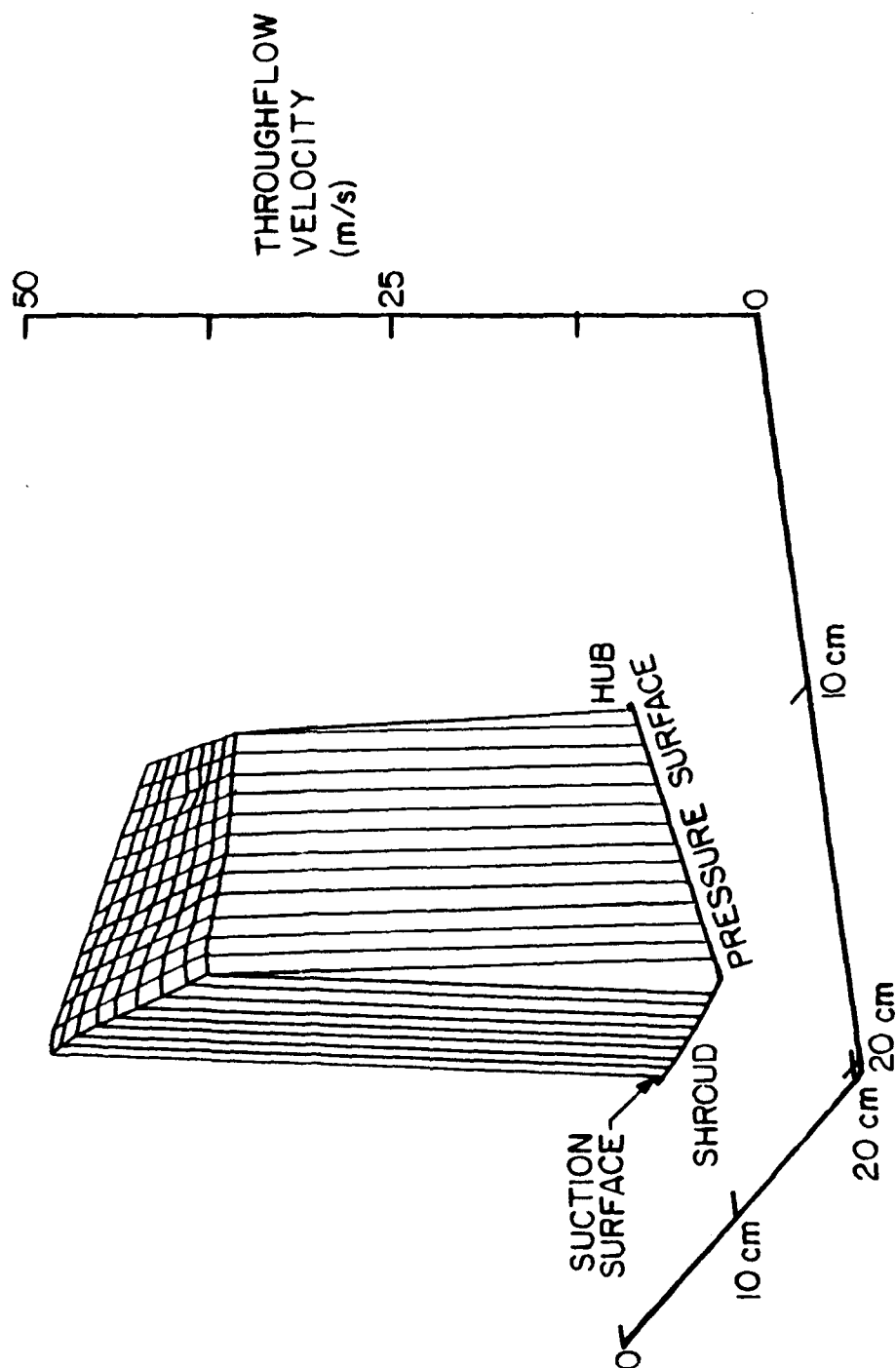


Figure 5.3 Throughflow Velocity Plot - LDV Data
Design Point - Plane 1

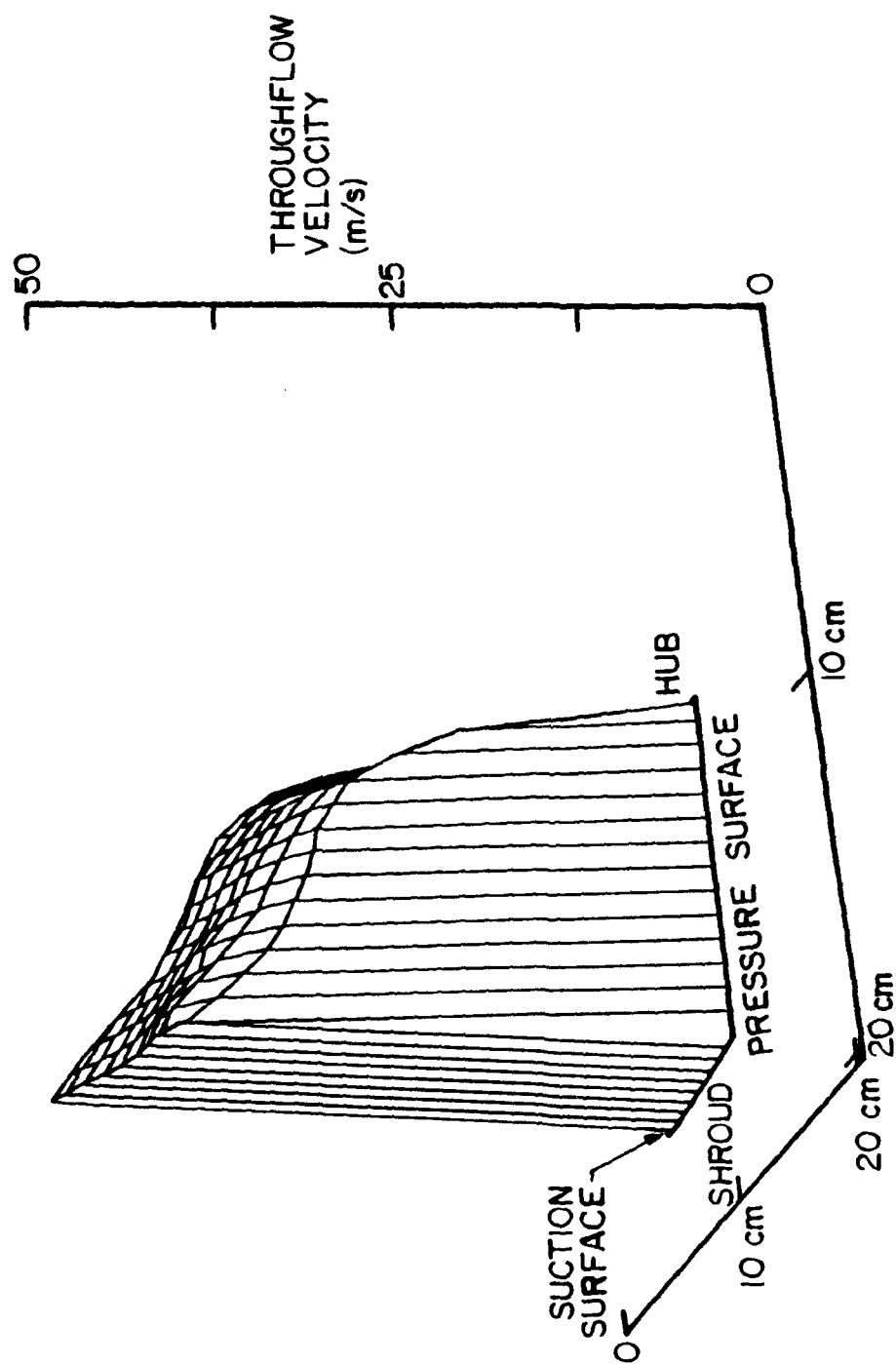


Figure 5.4 Throughflow Velocity Plot - LDV Data
Design Point - Plane 2

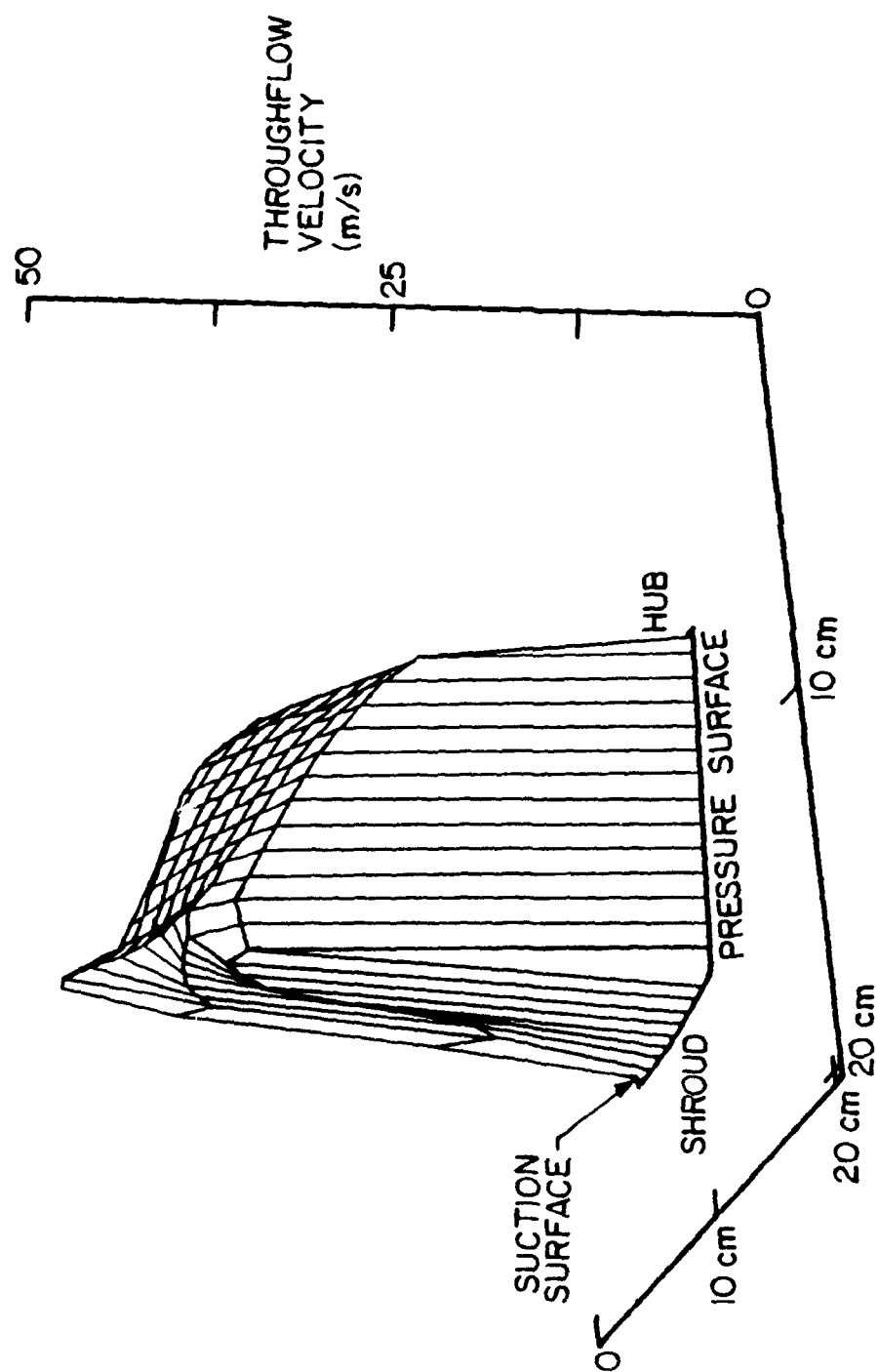


Figure 5.5 Throughflow Velocity Plot - LDV Data
Design Point - Plane 3

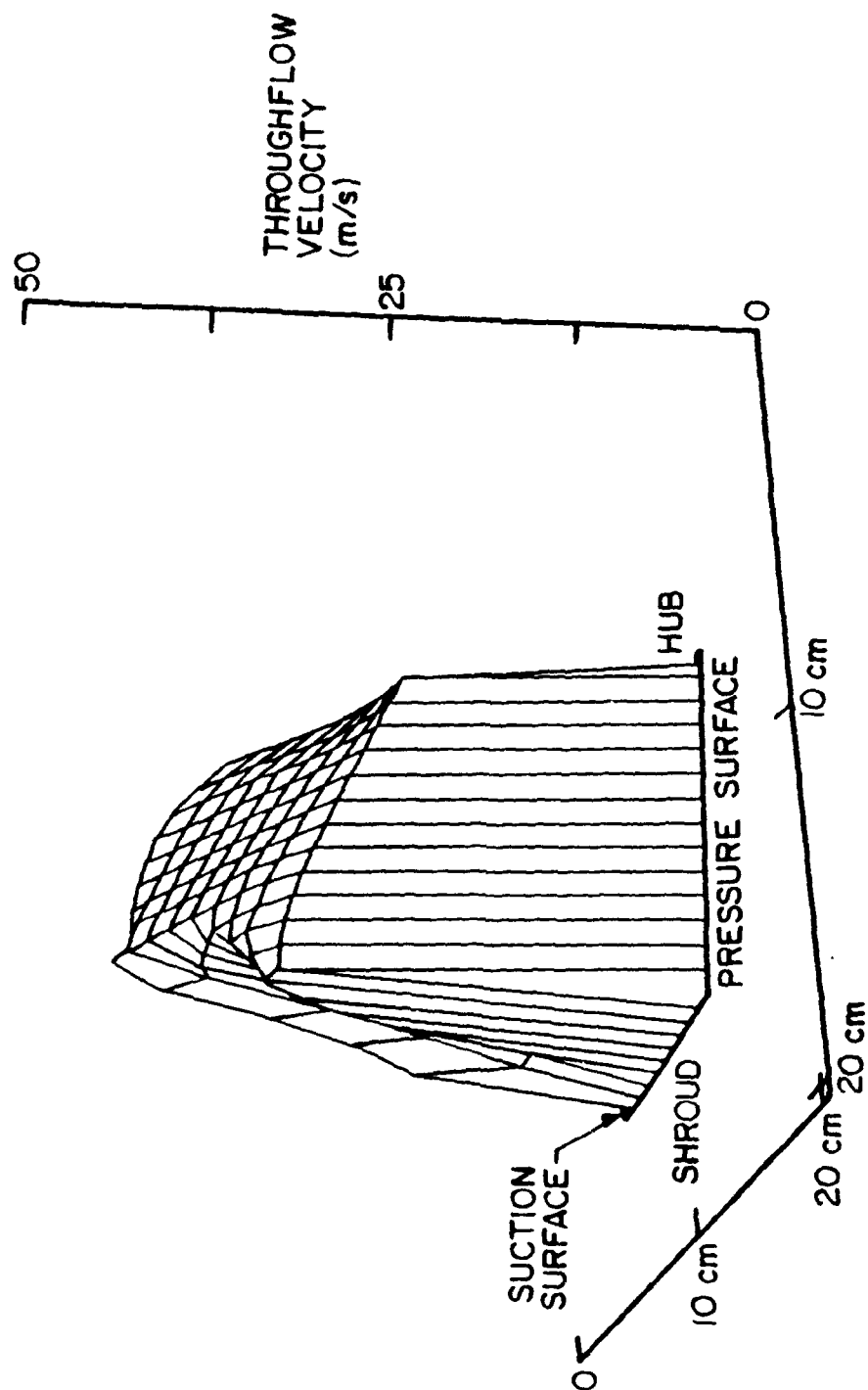


Figure 5.6 Throughflow Velocity Plot - LDV Data
Design Point - Plane 4

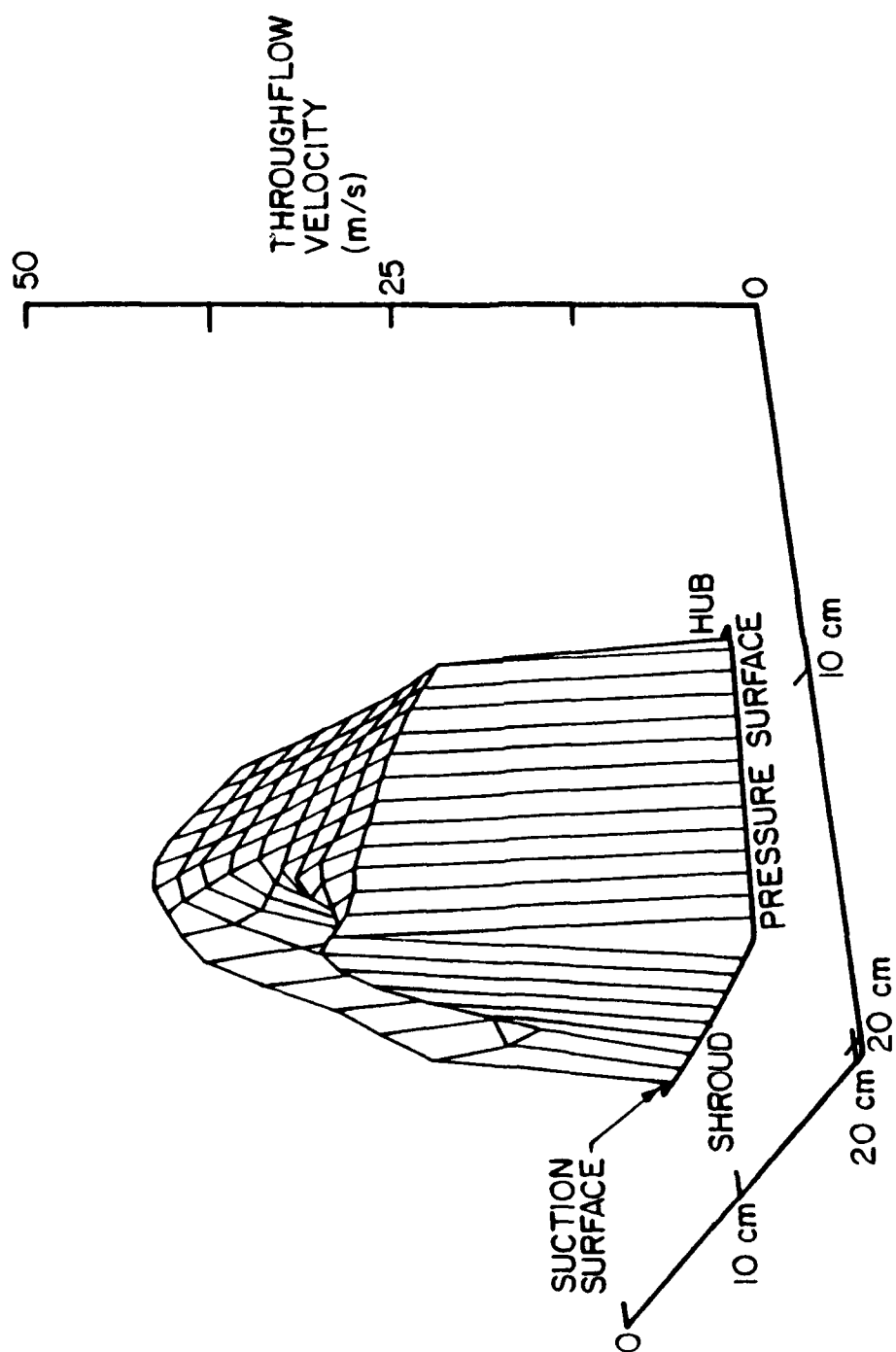


Figure 5.7 Throughflow Velocity Plot - LDV Data
Design Point - Plane 5

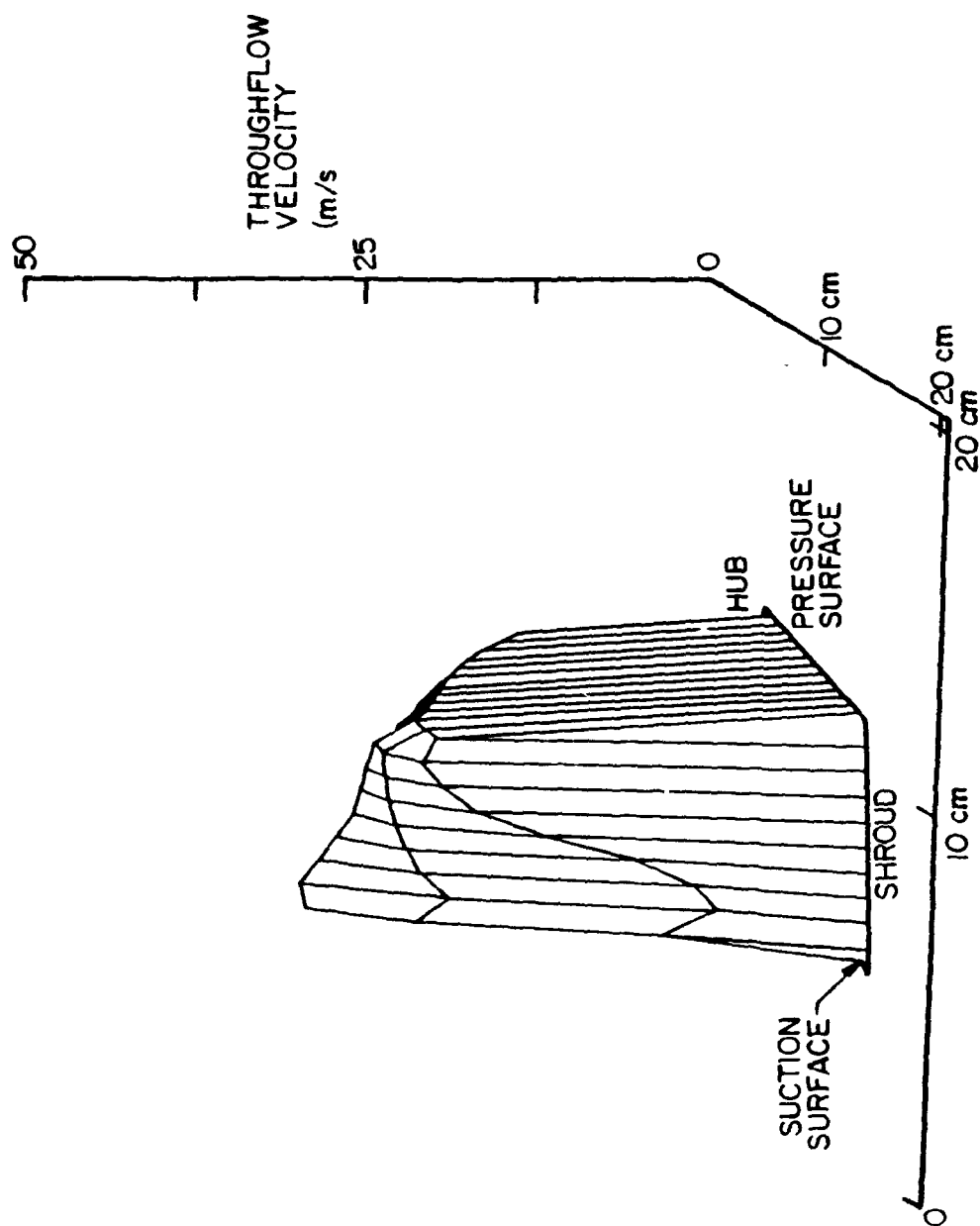


Figure 5.8 Throughflow Velocity Plot (Rotated View) - LDV Data
Design Point - Plane 3

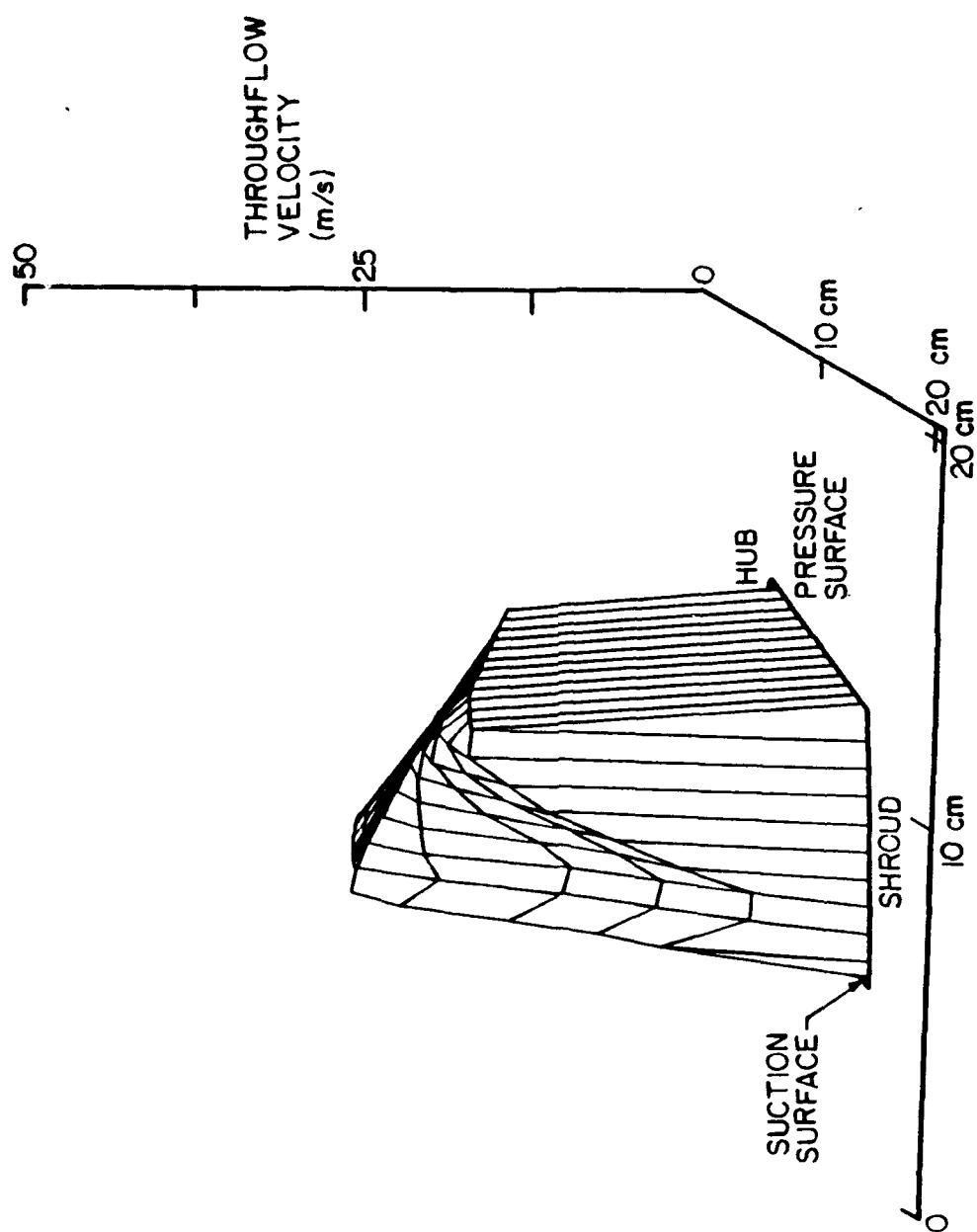


Figure 5.9 Throughflow Velocity Plot (Rotated View) - LDV Data
Design Point - Plane 4

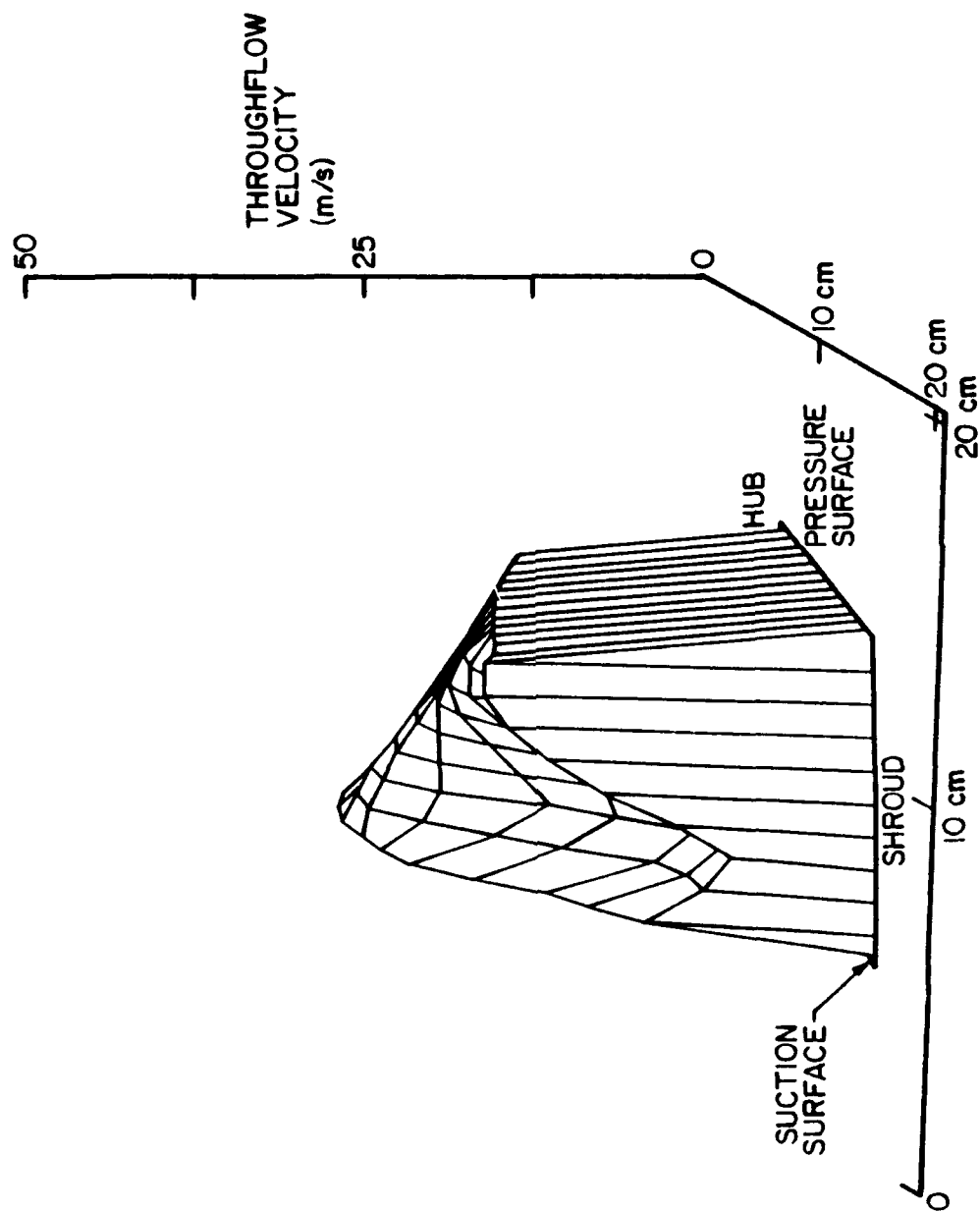


Figure 5.10 Throughflow Velocity Plot (Rotated View) - LDV Data
Design Point - Plane 5

shroud near the suction surface similar to the jet-wake pattern observed by Eckardt [2]. In Planes 4 and 5, similar profiles are observed, with the extent of the deficit region from the shroud surface growing along the passage. Note that the apparent spike in the Plane 3 velocity near the low velocity region, Figures 5.5 and 5.8, is an interpolation error due to the extremely steep gradient in velocity.

The design operating point secondary velocity vector and streamwise vorticity (the component of vorticity normal to the measurement plane) contour data for Planes 1-5 are presented in Figures 5.11 through 5.15, respectively. The secondary velocity vector data are somewhat difficult to interpret due to the large backsweep angle of the impeller blades. Since the data are taken at planes normal to the meridional plane, flow at the blade angle has a tangential component of velocity which is much larger than the imposed secondary flow. Consequently, the contour plots of the streamwise vorticity are also presented to define the secondary flow field. The contour values for the normalized vorticity and the normalizing dimensions are given in Table 5.1. Since the positive streamwise direction is oriented into the figure, a positive vorticity corresponds to a clockwise rotation.

At Plane 1, the vorticity data indicate regions of negative vorticity in several locations. However, the secondary velocity data show no discernable rotation of the flow in these regions. The Plane 3 data show that rotation of the flow is discernable when the magnitude of the normalized vorticity exceeds 1.2. Consequently, this value will be used as a minimum when discussing the presence of vorticity in the flow.

The first significant secondary flow is observed at Plane 3. A region of positive vorticity exists along the shroud corresponding to the deficit region observed in the throughflow velocity results. The magnitude of the streamwise vorticity is highest at approximately 70% of the distance from the pressure to the suction surface near the shroud. A region of weak negative vorticity is found along the suction surface, with the highest magnitude occurring at approximately 50% of the distance from hub to shroud. The secondary velocity vector results show the turning of the flow in both these locations, with the turning on the suction surface limited to the first grid near the blade surface. At Plane 4, the extreme turning of the flow and high vorticity along the shroud

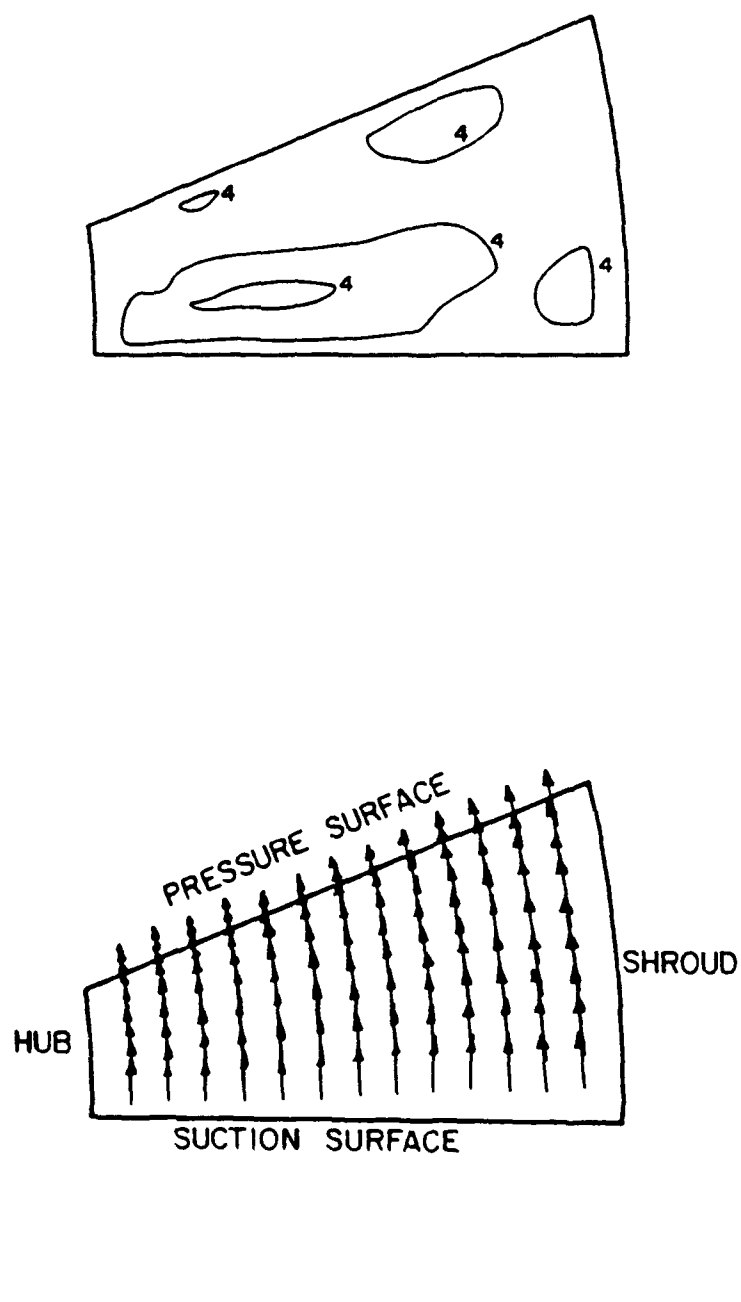


Figure 5.11 Secondary Velocity Vector and Vorticity Contour Plot - LDV Data
Design Point - Plane 1

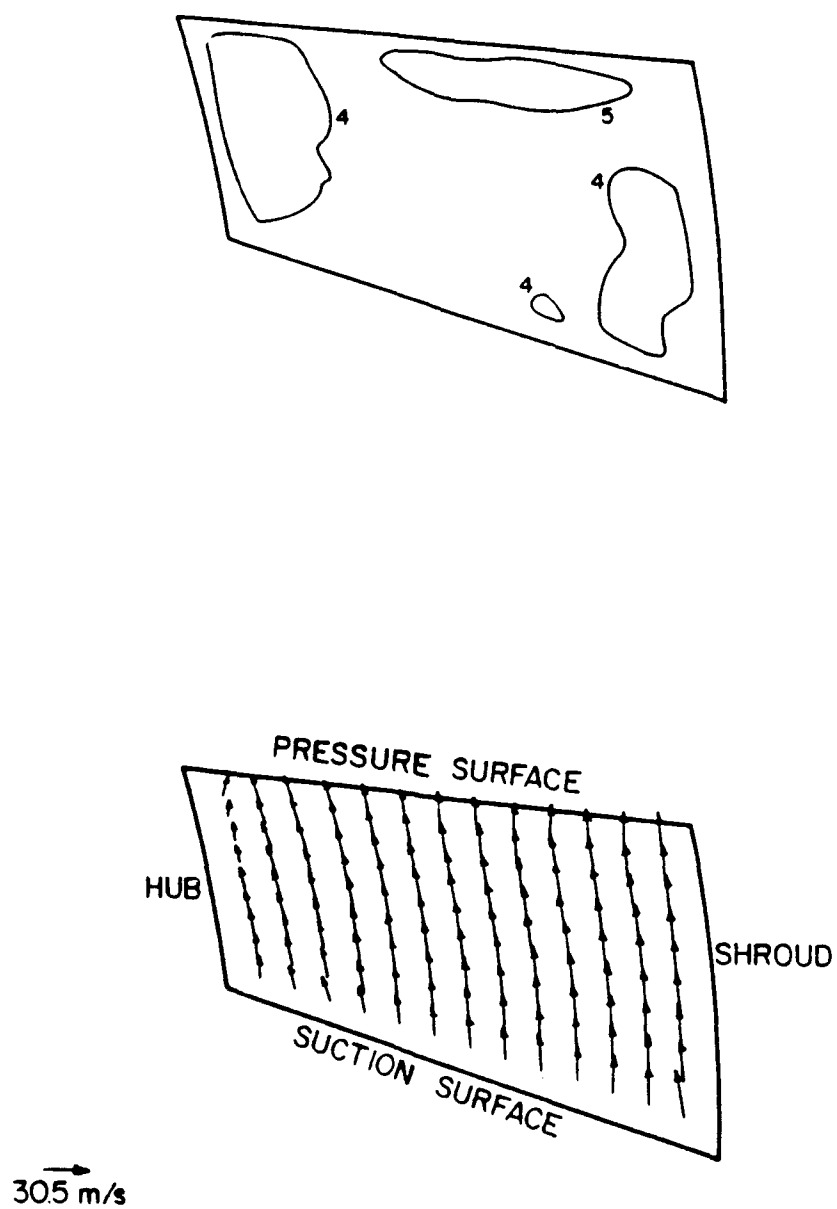


Figure 5.12 Secondary Velocity Vector and Vorticity Contour Plot - LDV Data
Design Point - Plane 2

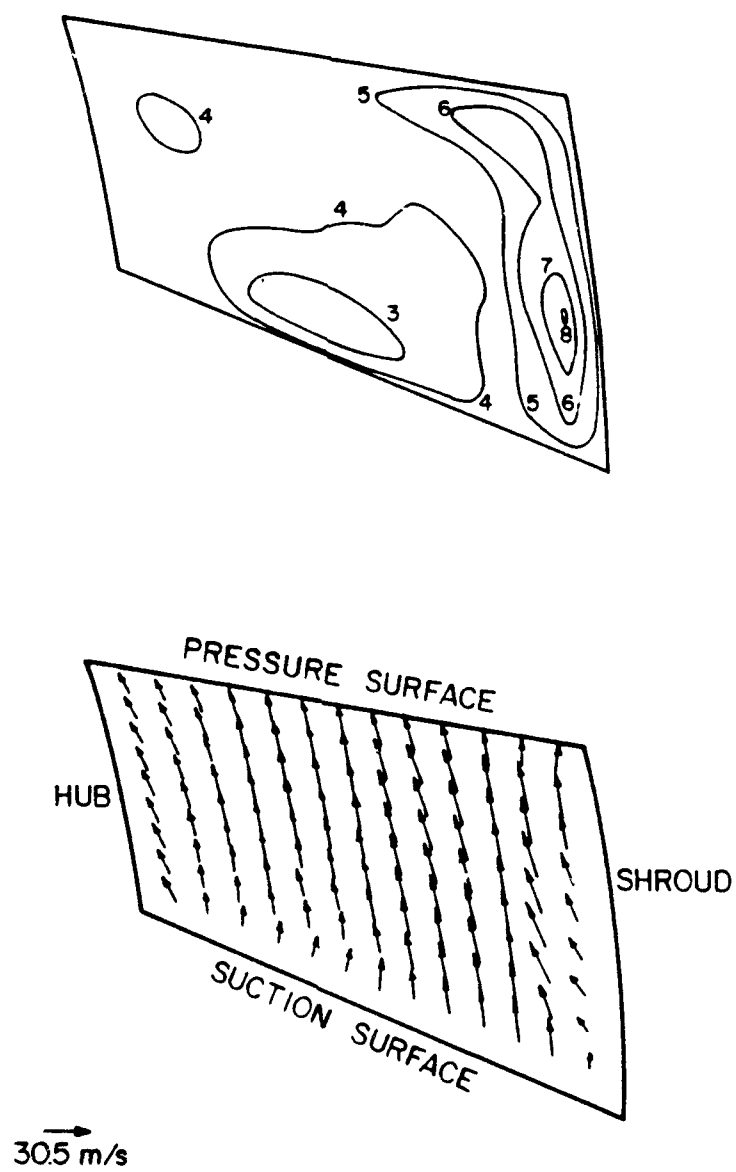


Figure 5.13 Secondary Velocity Vector and Vorticity Contour Plot - LDV Data Design Point - Plane 3

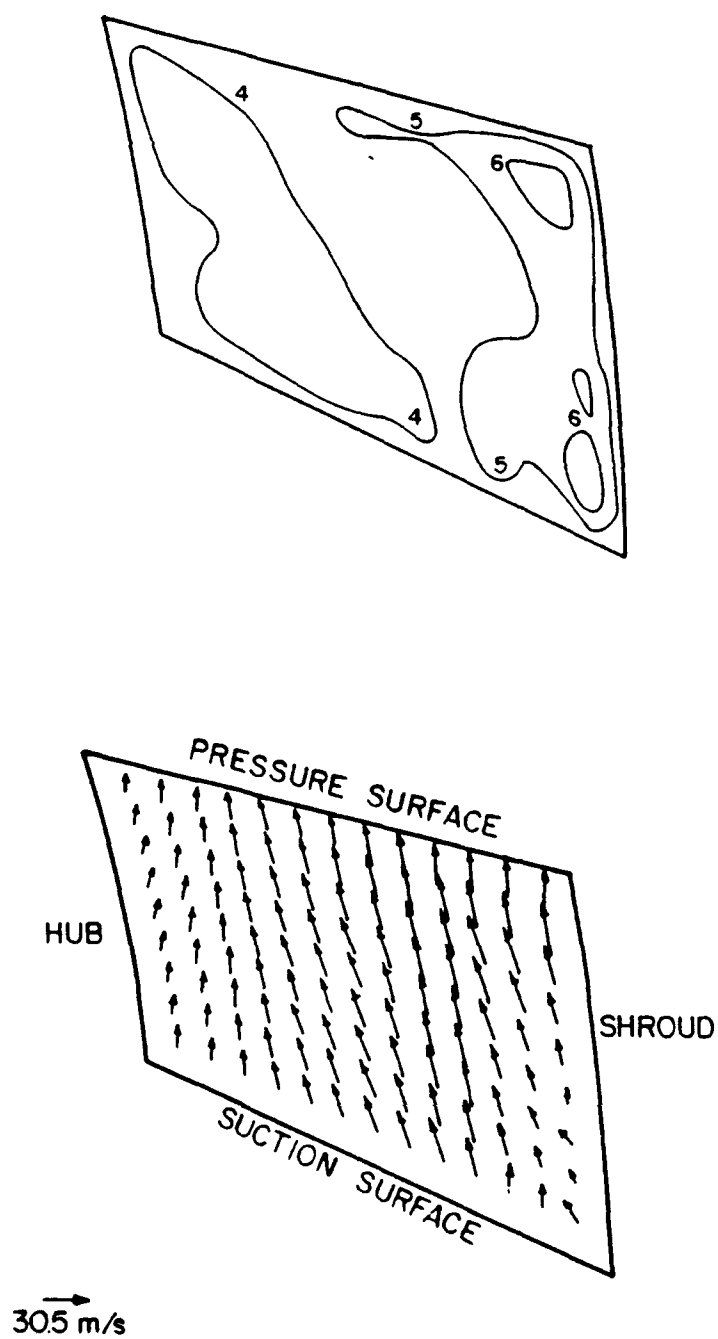


Figure 5.14 Secondary Velocity Vector and Vorticity Contour Plot - LDV Data
Design Point - Plane 4

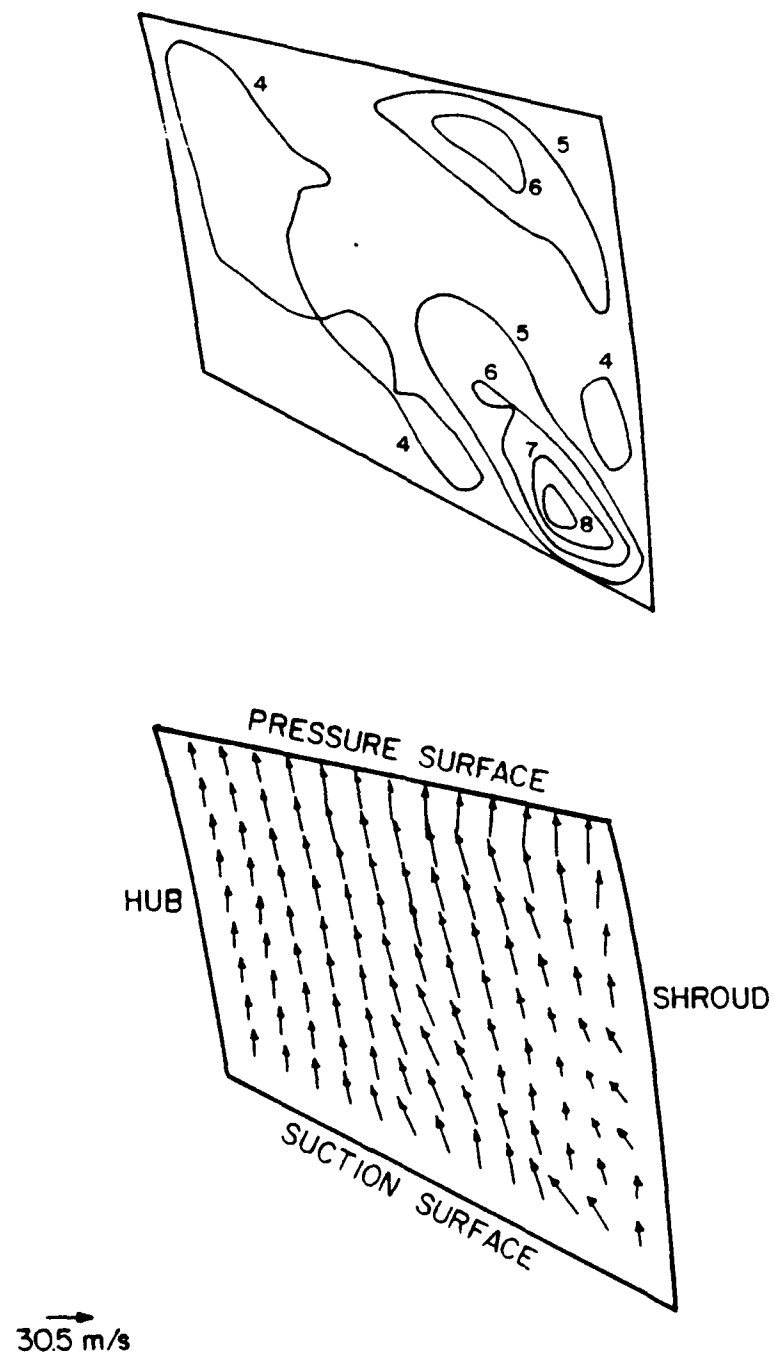


Figure 5.15 Secondary Velocity Vector and Vorticity Contour Plot - LDV Data
Design Point - Plane 5

Table 5.1 Vorticity Contour Levels

Normalizing Dimensions:

Velocity - Impeller Exit Rotational Speed (68.6 m/s)

Length - Nominal Passage Height (7.6 cm)

Contour	Normalized Vorticity
1	-2.80
2	-2.00
3	-1.20
4	-0.40
5	0.40
6	1.20
7	2.00
8	2.80

has dissipated. Regions of weak positive vorticity are observed in the shroud pressure and shroud suction corners. A similar pattern is observed at Plane 5, with a large magnitude increase of the vorticity in the region of the shroud suction corner.

5.1.3 Mean Flow - Incipient Rotating Stall

The incipient stall operating point throughflow velocity results are presented in Figures 5.16 through 5.23. The throughflow velocity data for Planes 1-5 are shown in Figures 5.16 through 5.20, respectively, with a rotated view of the same results for Planes 3, 4, and 5 given in Figures 5.21 through 5.23.

At Plane 1, a velocity deficit region along the shroud is already evident. Along the remainder of this plane, the suction to pressure surface velocity gradient is smaller than for the design operating point data. By Plane 3, 50% of the passage area is affected by the velocity deficit region. At Plane 4, a velocity gradient is observed from the suction to the pressure surface in the deficit region, with reverse flow observed at Plane 5. An important difference between the flow patterns at the design operating point and the incipient stall operating point is the location of the maximum throughflow velocity deficit. At the design operating point, the region of lowest throughflow velocity is located on the shroud at 70% of the distance from the pressure to the suction surface. The region of reverse flow at the incipient stall operating point is located in the shroud suction corner.

The incipient stall operating point secondary velocity vector results are presented in Figures 5.24 through 5.28. At Plane 1, a weak positive vorticity region is located in the shroud suction corner. By Plane 2, the magnitude of the vorticity in that region is negligible, but flow away from the surface is observed along the shroud. Strong positive vorticity, located in the hub pressure corner, is indicated for Planes 2 and 4 in both the vorticity and the secondary velocity vector results. Examination of the raw data shows a slight turning of the flow in these regions, with the large positive vorticity magnitude caused by interpolation errors due to locally sparse data. At Plane 3, a region of negative vorticity is observed on the blade suction surface. The location and the local secondary flow pattern are nearly identical to that observed at this plane at the design operating

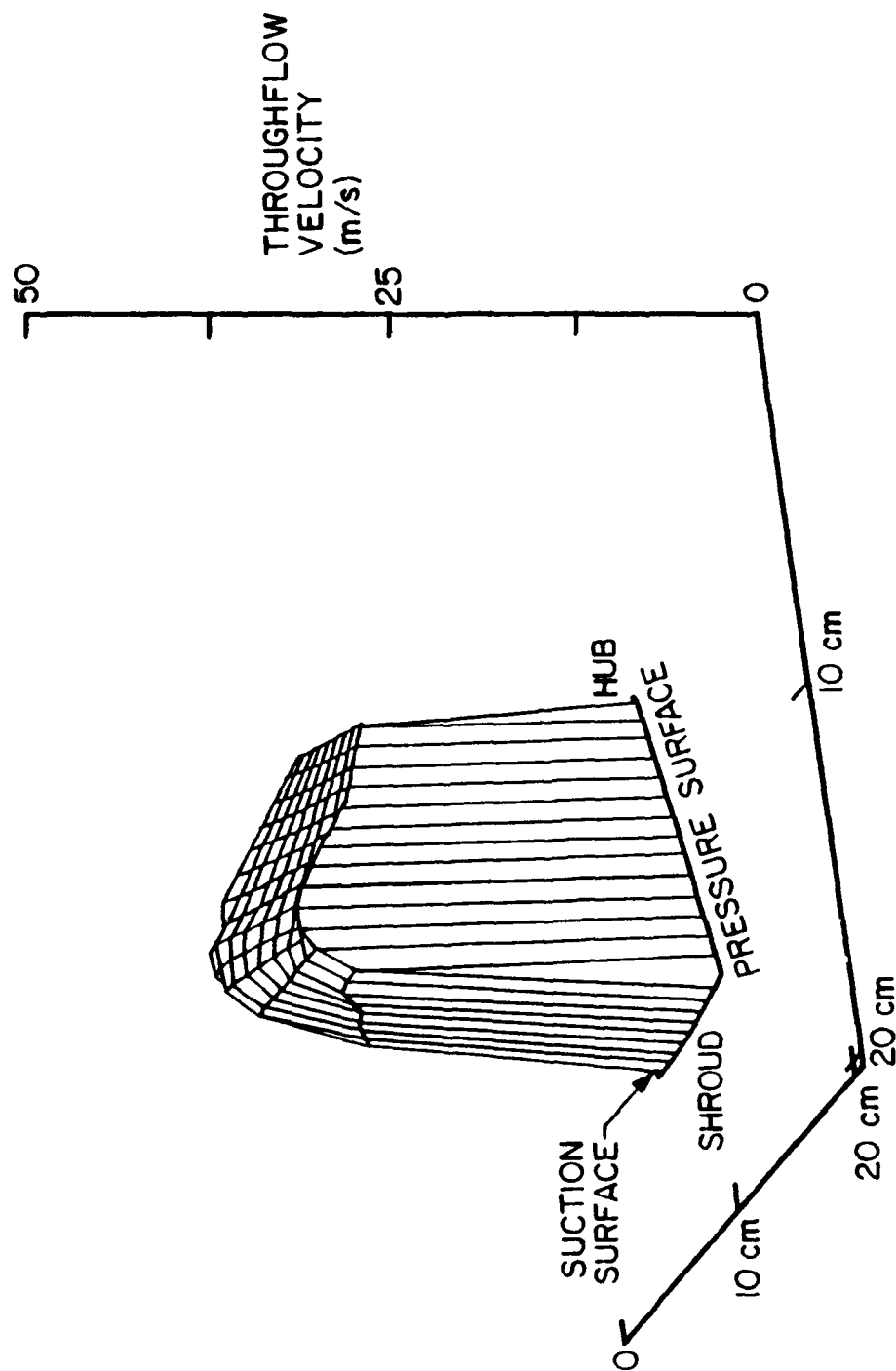


Figure 5.16 Throughflow Velocity Plot - LDV Data
Incipient Stall Point - Plane 1

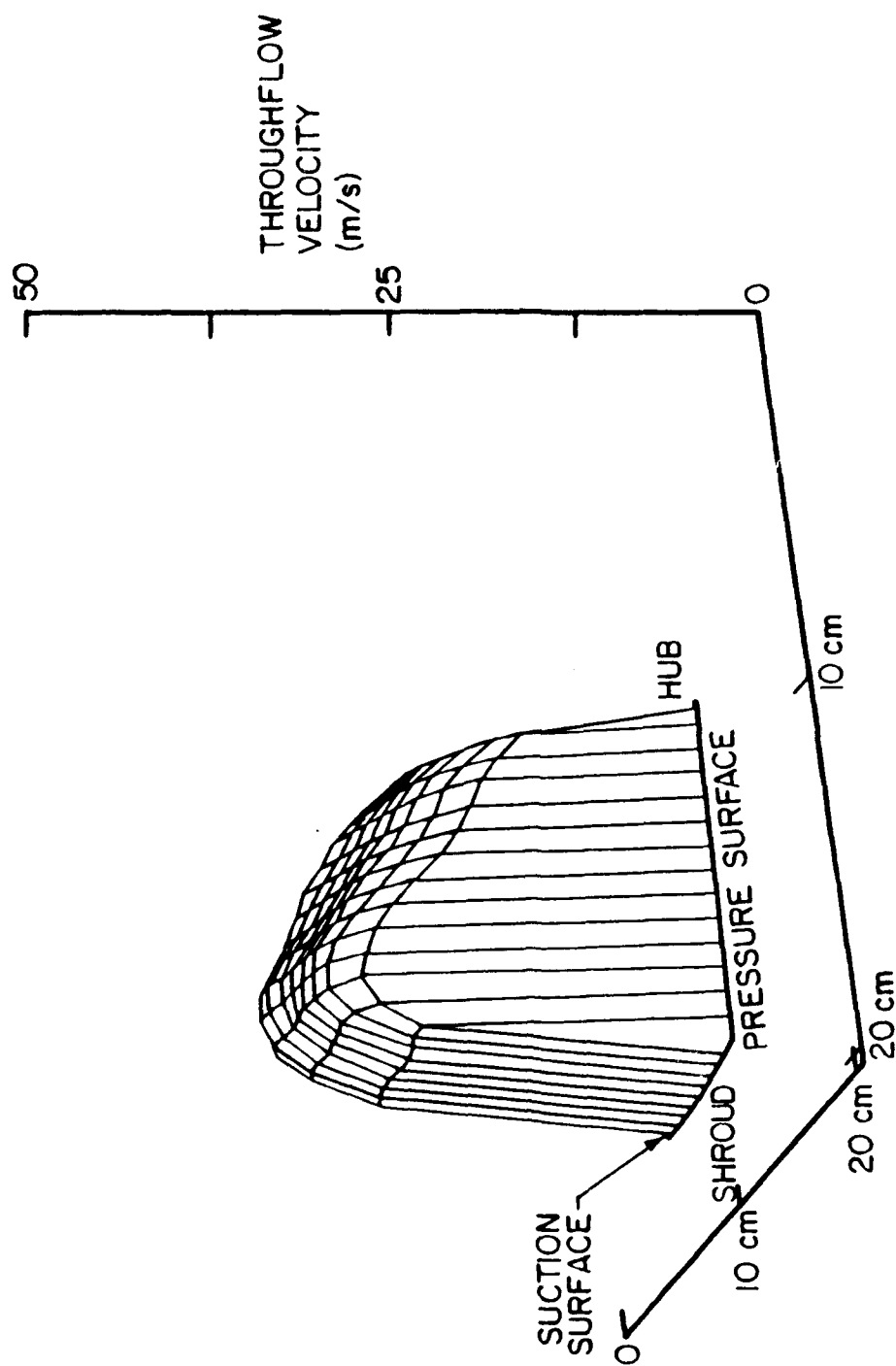


Figure 5.17 Throughflow Velocity Plot - LDV Data
Incipient Stall Point - Plane 2

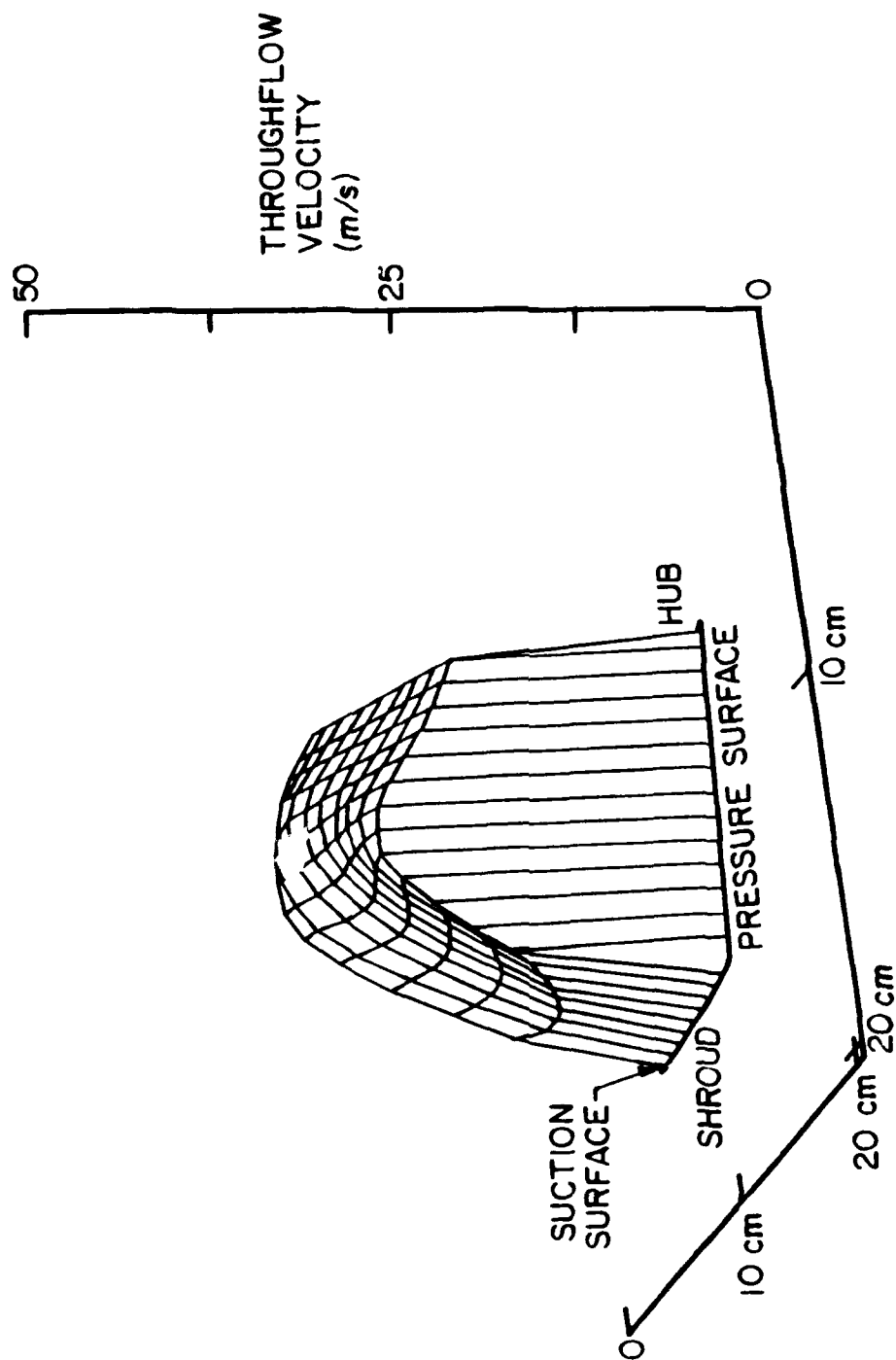


Figure 5.18 Throughflow Velocity Plot - LDV Data
Incipient Stall Point - Plane 3

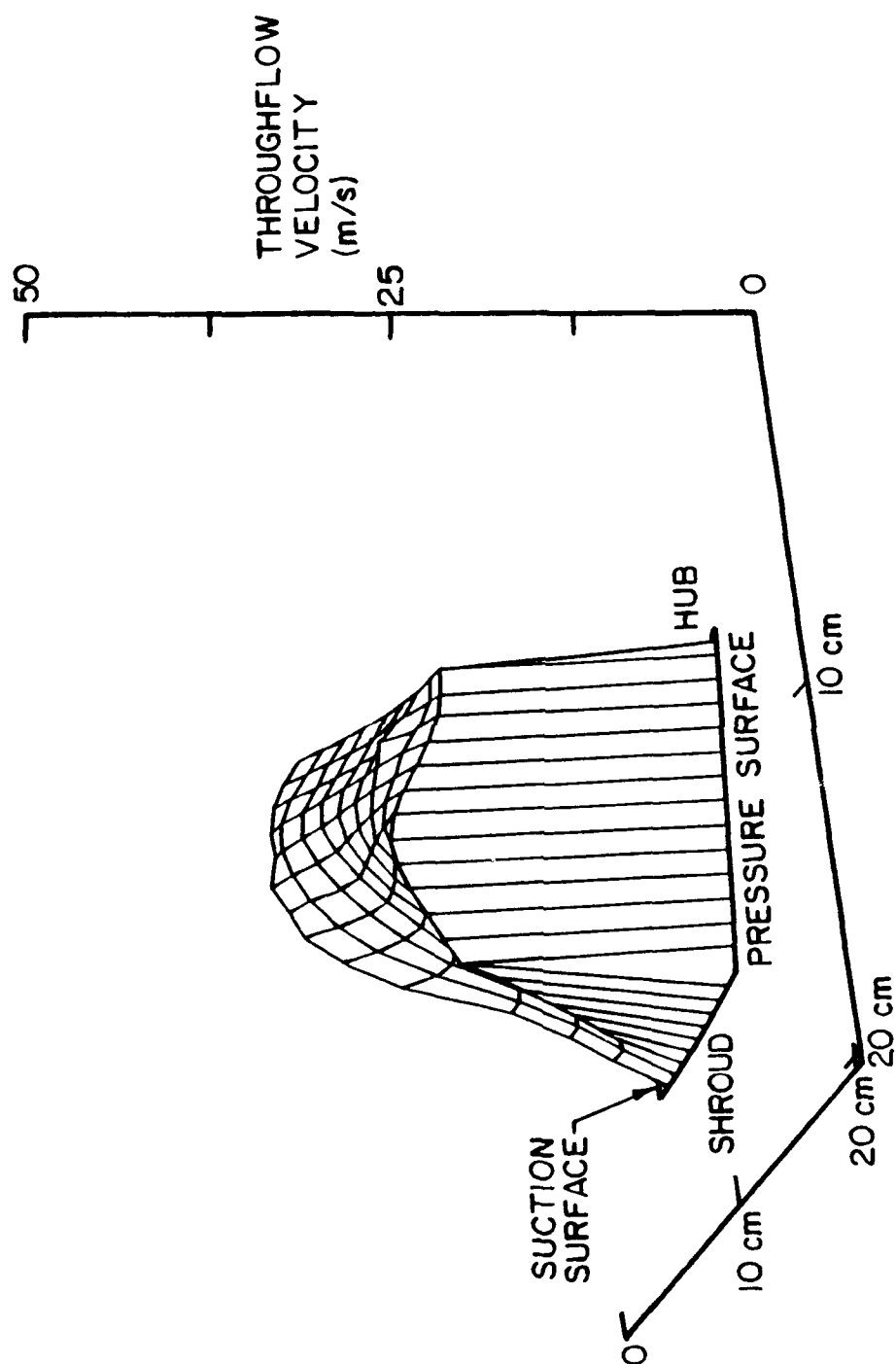


Figure 5.19 Throughflow Velocity Plot - LDV Data
Incipient Stall Point - Plane 4

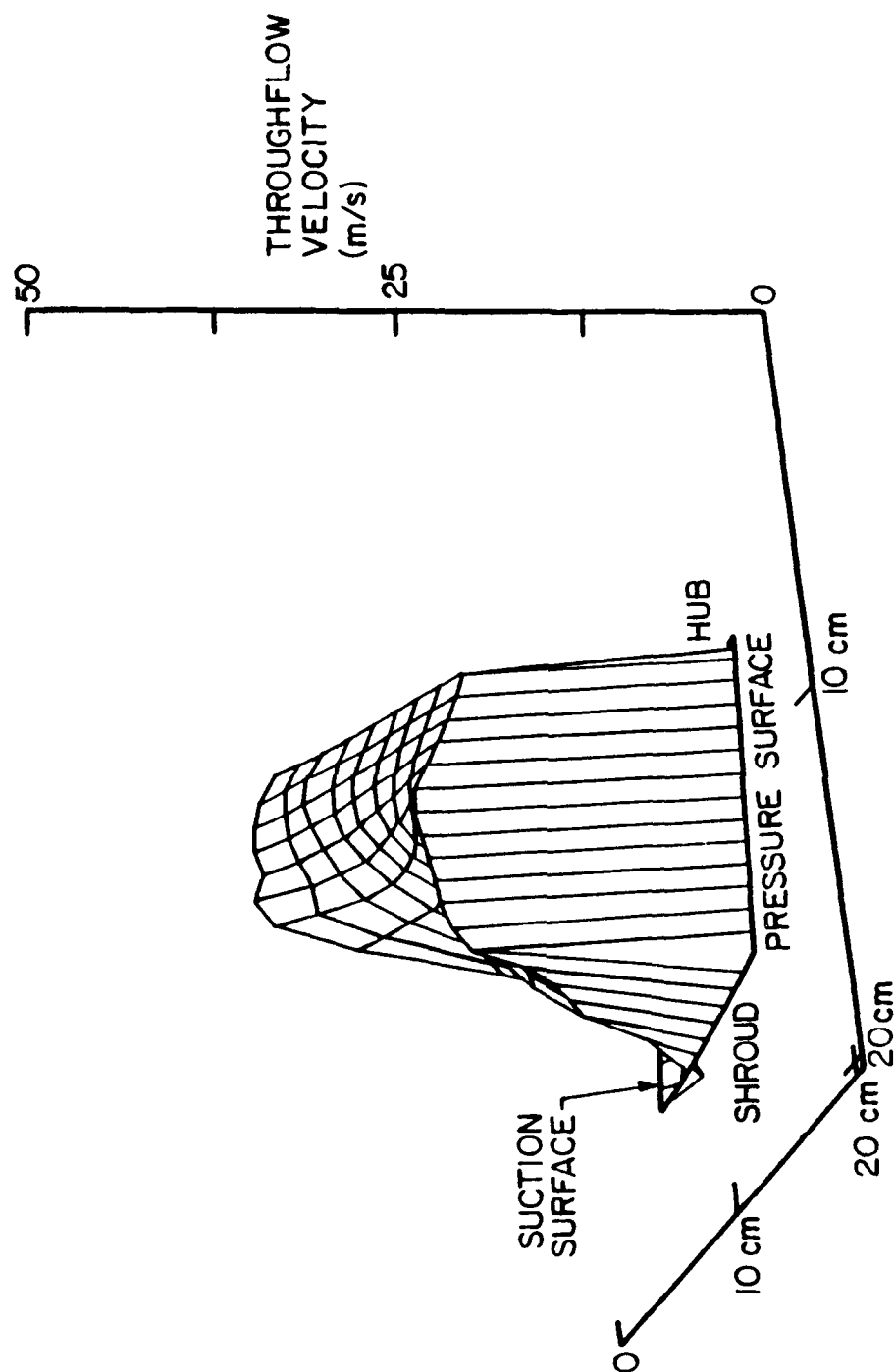


Figure 5.20 Throughflow Velocity Plot - LDV Data
Incipient Stall Point - Plane 5

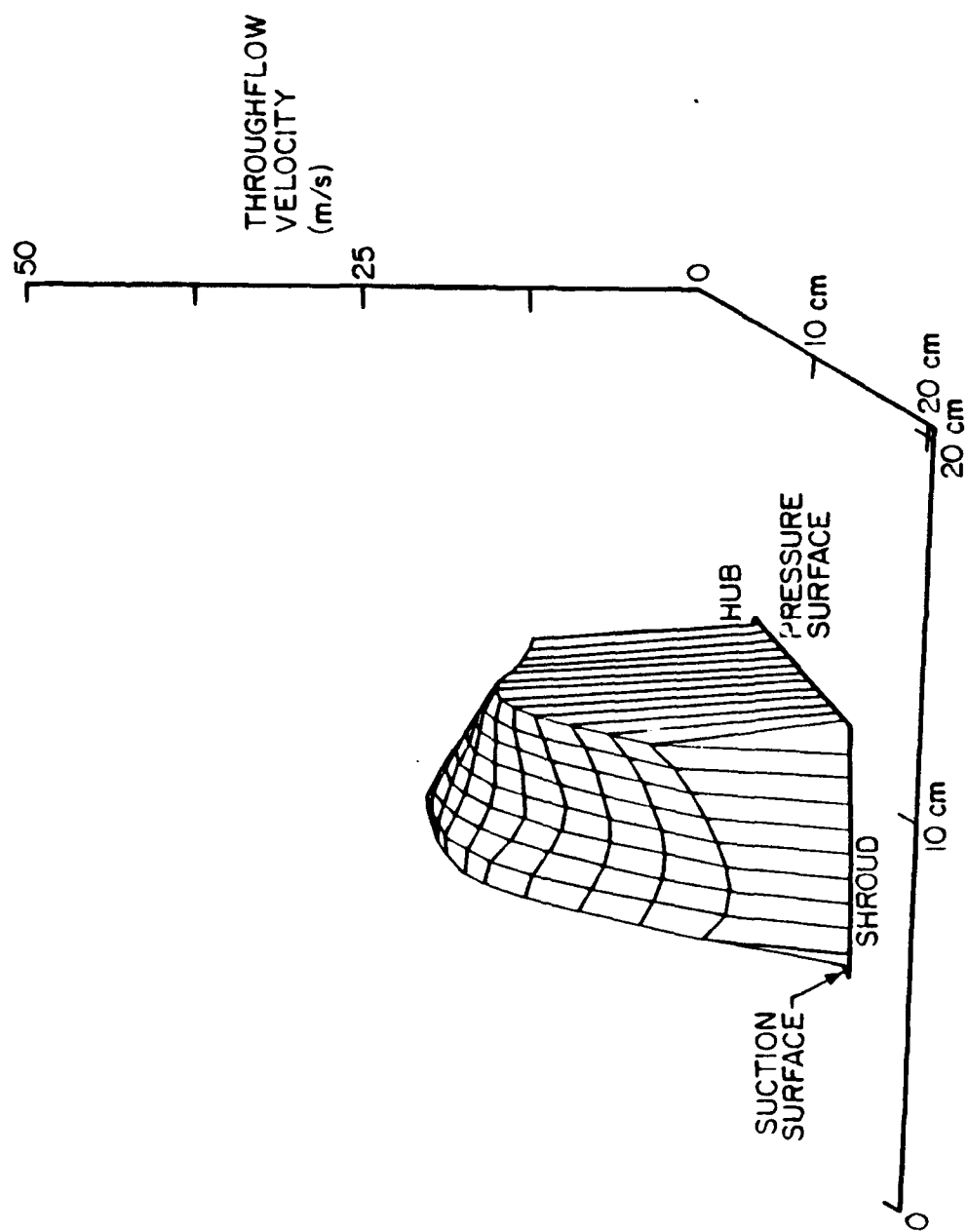


Figure 5.21 Throughflow Velocity Plot (Rotated View) - LDV Data
Incipient Stall Point - Plane 3

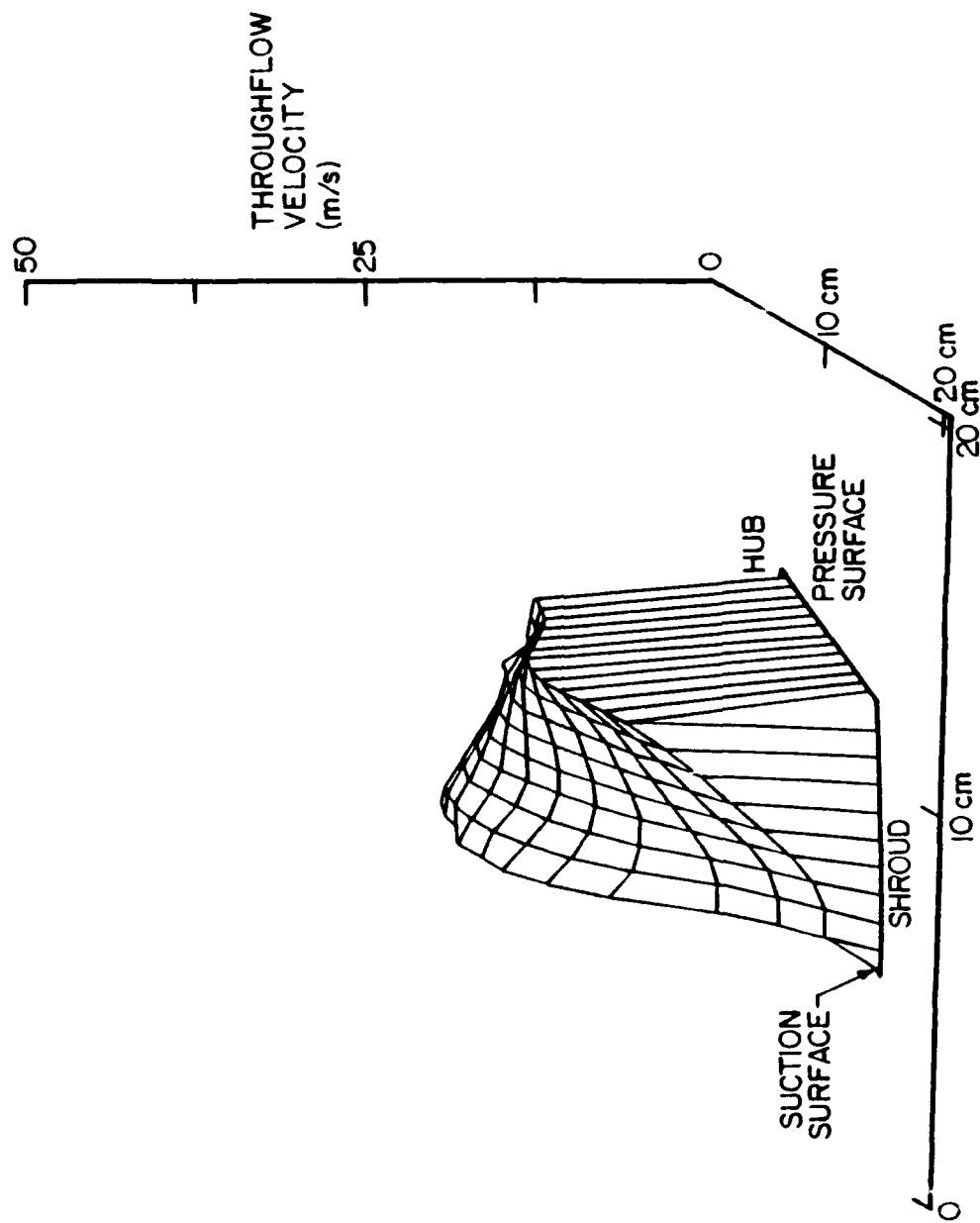


Figure 5.22 Throughflow Velocity Plot (Rotated View) - LDV Data
Incipient Stall Point - Plane 4

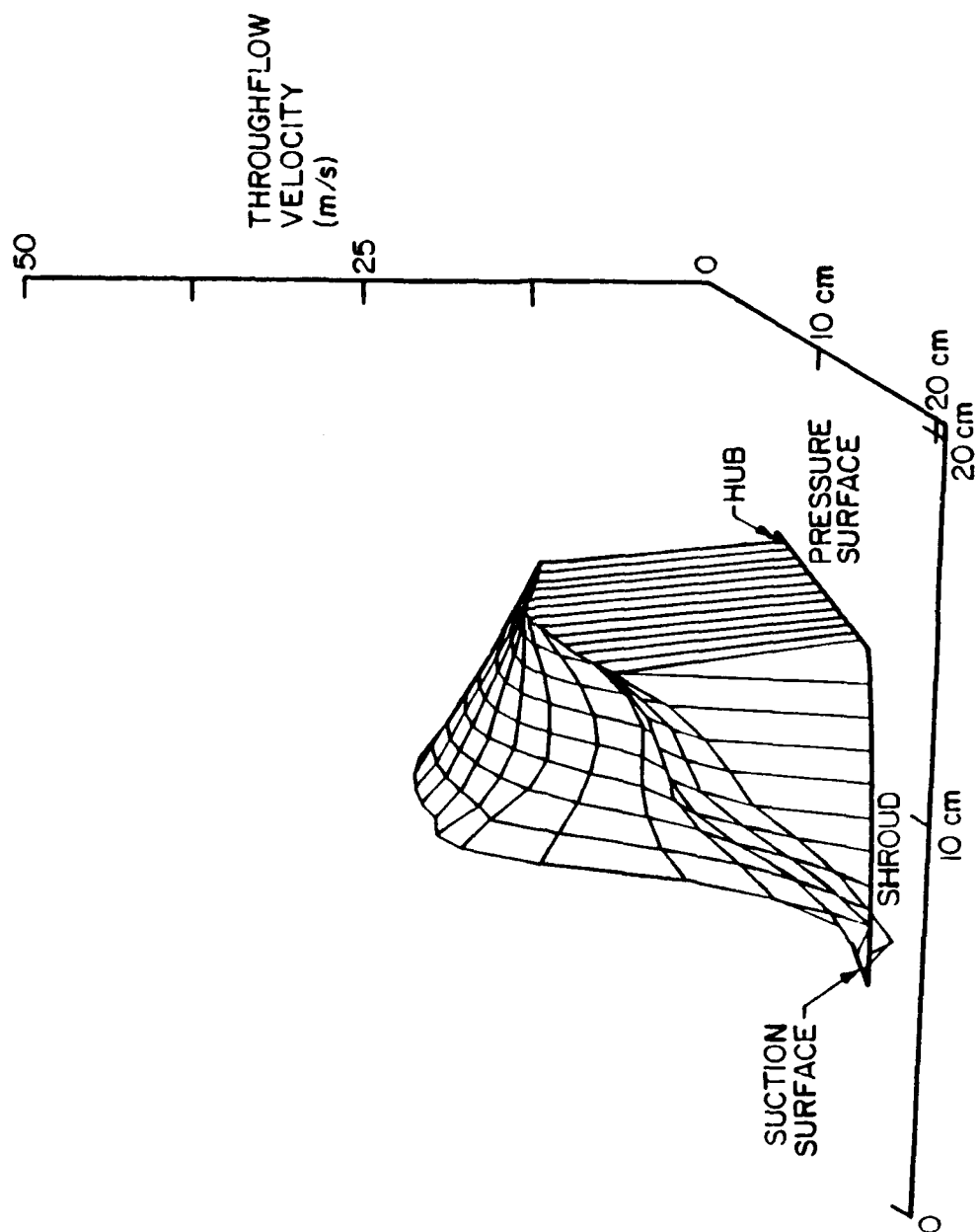


Figure 5.23 Throughflow Velocity Plot (Rotated View) - LDV Data
Incipient Stall Point - Plane 5

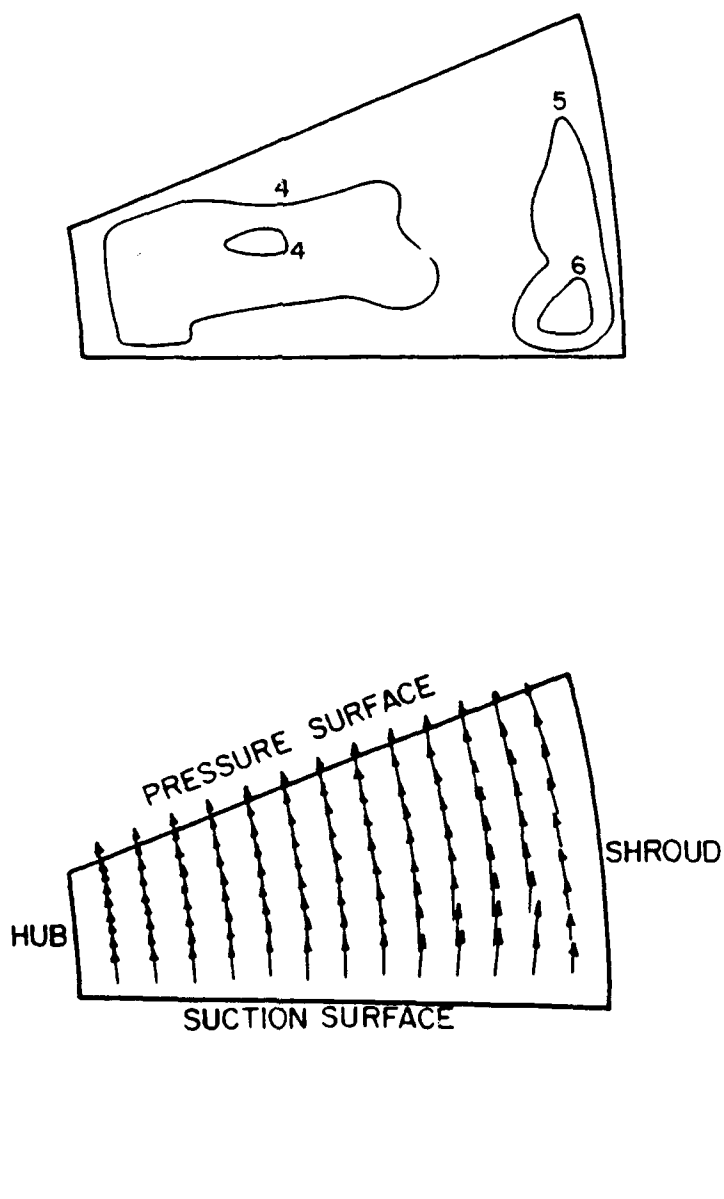


Figure 5.24 Secondary Velocity Vector and Vorticity Contour Plot - LDV Data
Incipient Stall Point - Plane I

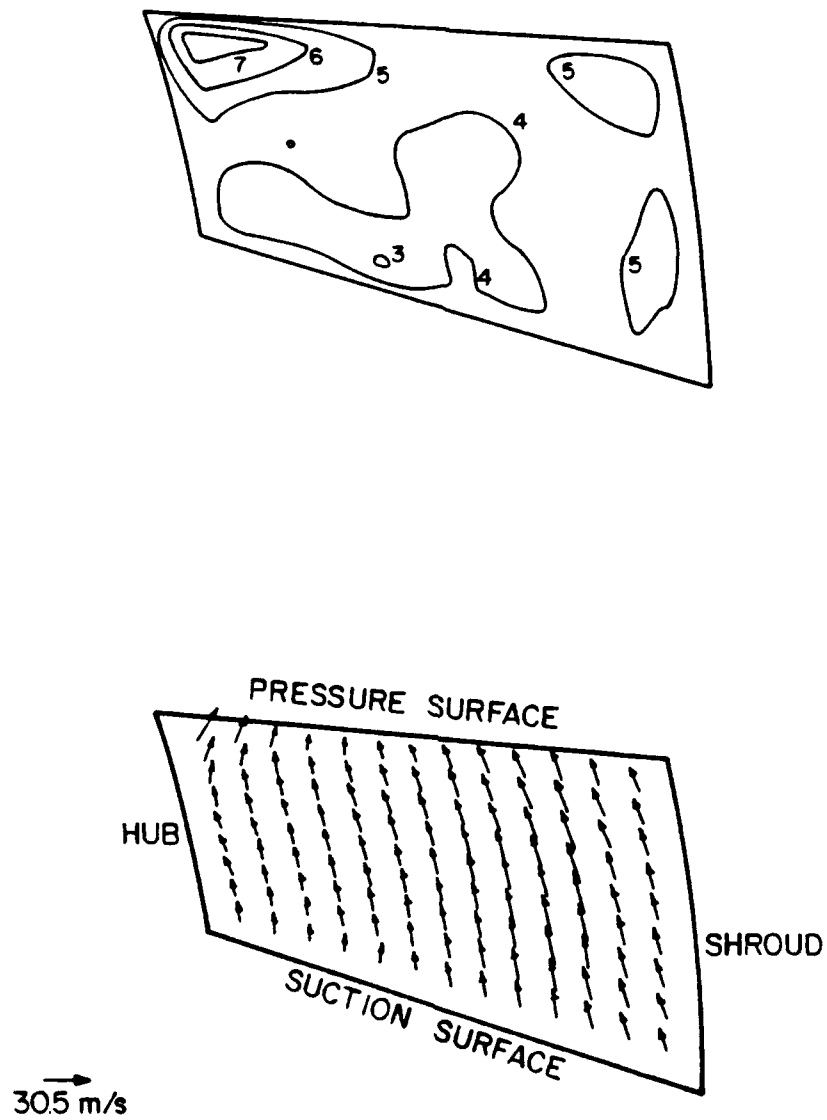


Figure 5.25 Secondary Velocity Vector and Vorticity Contour Plot - LDV Data
Incipient Stall Point - Plane 2

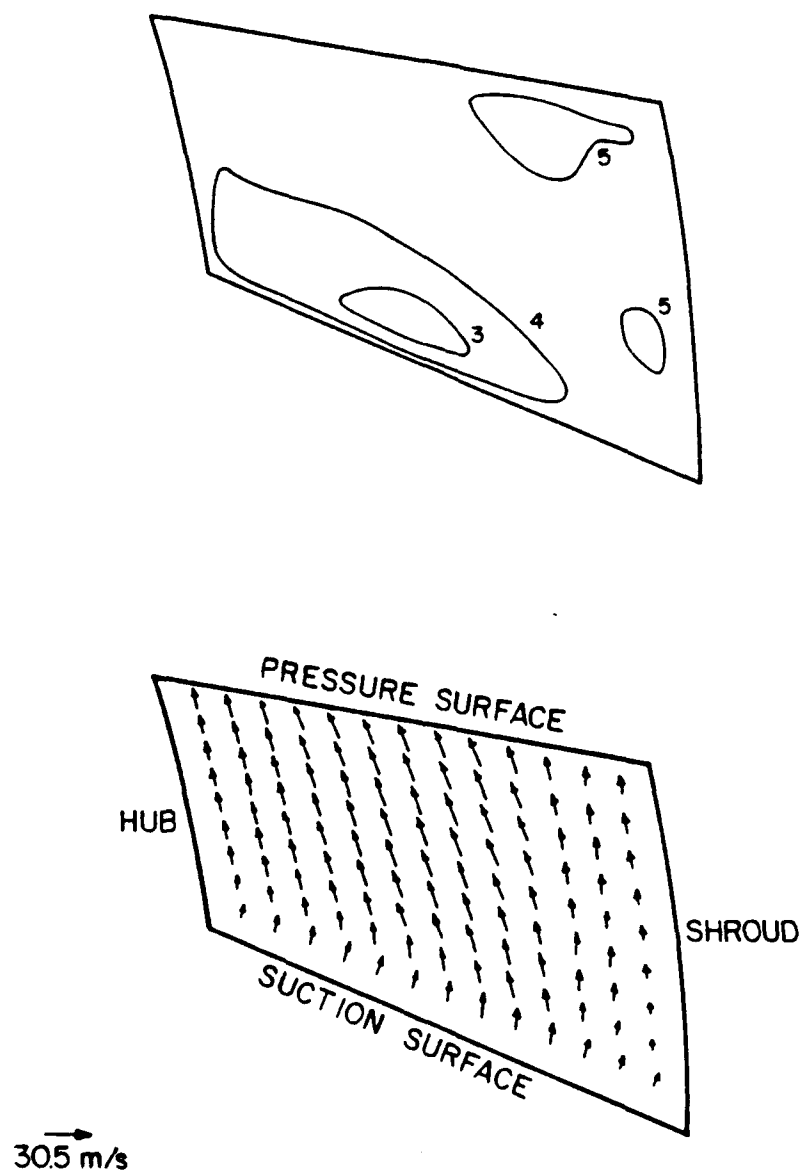


Figure 5.26 Secondary Velocity Vector and Vorticity Contour Plot - LDV Data
Incipient Stall Point - Plane 3

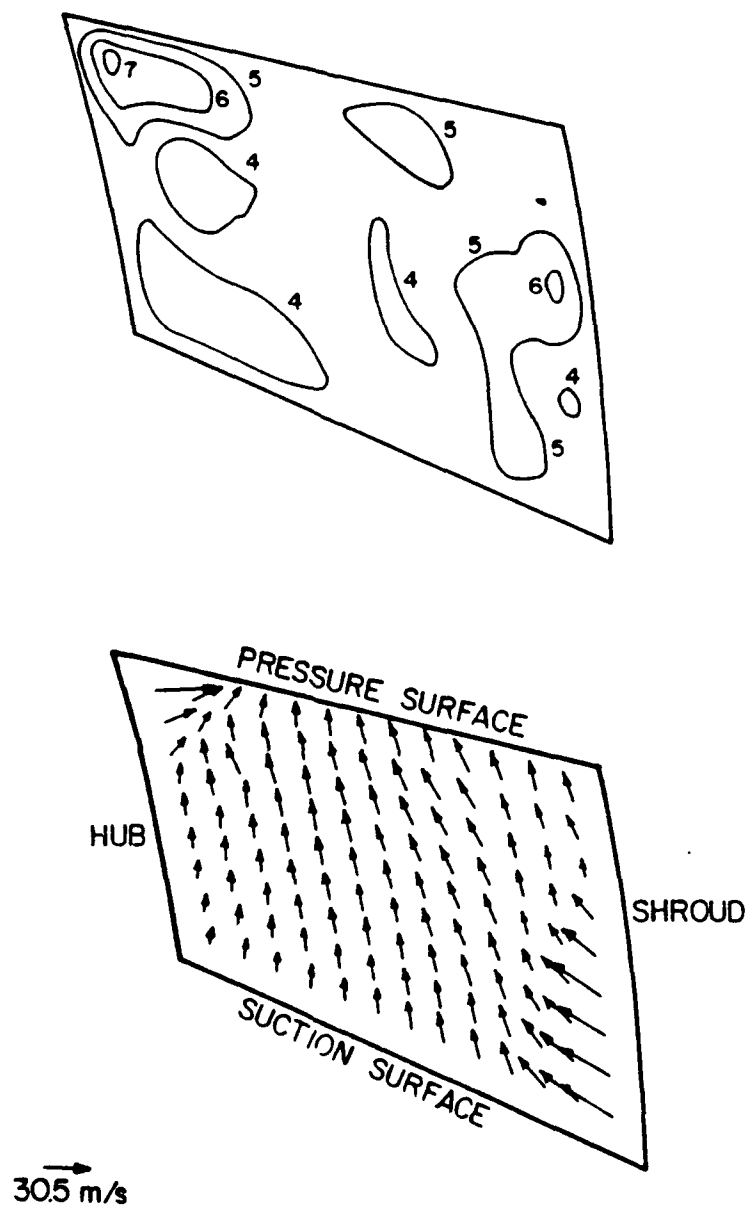


Figure 5.27 Secondary Velocity Vector and Vorticity Contour Plot - LDV Data
Incipient Stall Point - Plane 4

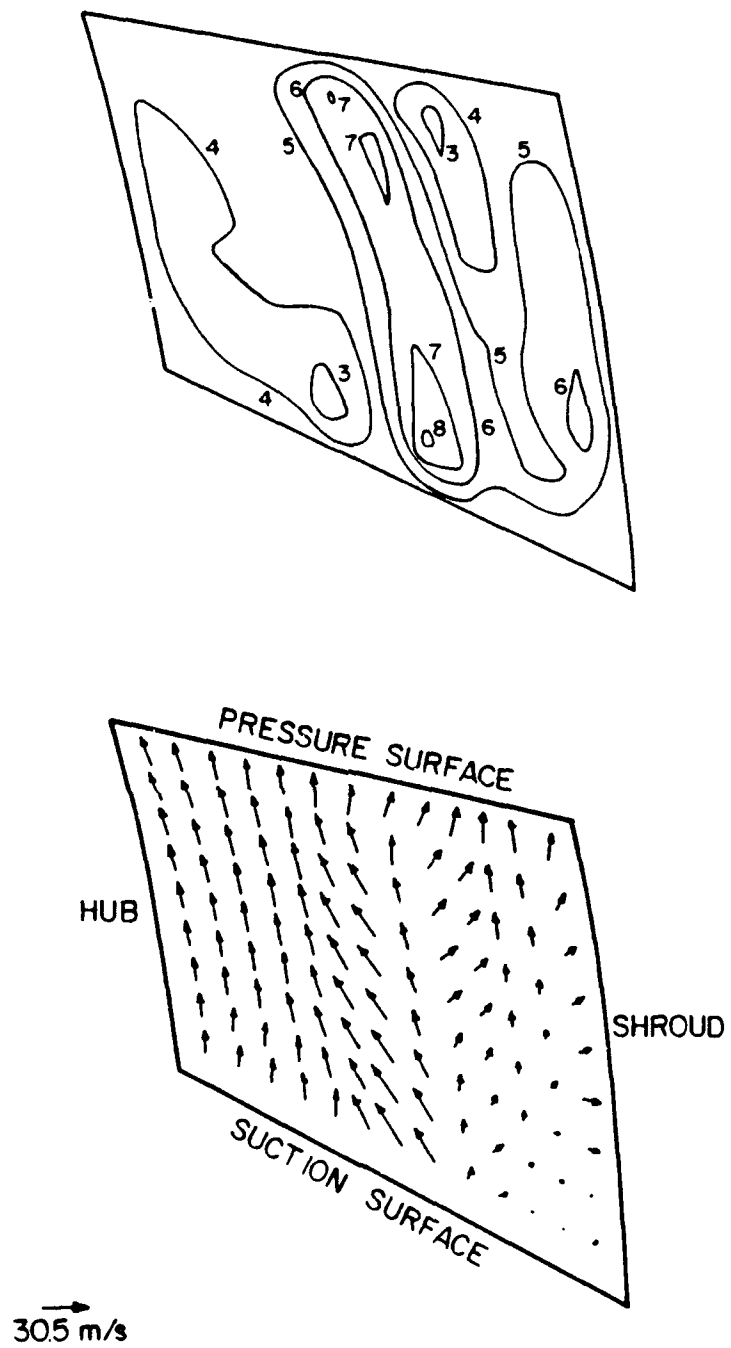


Figure 5.28 Secondary Velocity Vector and Vorticity Contour Plot - LDV Data
Incipient Stall Point - Plane 5

point. Additionally, the magnitude of the secondary velocity vector for the flow near the shroud is very small. By Plane 4, the flow field in this region has drastically changed. The secondary flow is dominated by a region with a large component of velocity away from the shroud where the throughflow velocity deficit is maximum. At Plane 5, the reverse flow region is evident in the secondary velocity vector results. Additionally, a line exists across the passage at a location 65% of the length from hub to shroud, with the secondary velocity vector oriented towards the shroud on the shroud side of the line and towards the hub on the hub side. This corresponds to the interface between the throughflow velocity deficit region and the core flow. The vorticity contour results show positive vorticity in this region, with local maxima on the suction and pressure surfaces.

5.1.4 Turbulence Intensity and Enthalpy

In addition to defining the mean velocity component in each measurement direction, the standard deviation of the velocity fluctuations and the enthalpy at each grid point is also determined. Unfortunately, it would require six independent measurements at each location to determine the standard deviation of the velocity fluctuations along each of the mutually orthogonal axes from which the turbulence intensity could be determined. Thus, for the results presented herein the turbulence intensity is estimated by the standard deviation of the velocity fluctuations in the measurement directions and normalized with the square of the impeller exit rotational speed, Equation 5.2. The enthalpy is calculated by finding the product of the blade rotational speed and the tangential component of the absolute velocity at each location assuming a reference enthalpy of zero at the inlet to the impeller. The enthalpy is also normalized with the square of the impeller exit rotational speed. Table 5.2 gives the contour values for both types of results.

Table 5.2 Turbulence Intensity and Enthalpy Contour Levels**Turbulence Intensity**

Contour	Normalized Turbulence Intensity
1	0.05
2	0.10
3	0.15
4	0.20
5	0.25
6	0.30
7	0.35
8	0.40

Enthalpy

Contour	Normalized Enthalpy
1	0.00
2	0.10
3	0.20
4	0.30
5	0.40
6	0.50
7	0.60
8	0.70
9	0.80
10	0.90

$$T = \sqrt{\frac{\frac{1}{3}(u_A^2 + u_B^2 + u_C^2)}{U_T^2}} \quad (5.2)$$

The design operating point turbulence intensity contour results for Planes 1-5 are given in Figures 5.29 through 5.33, respectively. At Plane 1, the turbulence intensity is low across the entire plane. Regions of higher turbulence are located in the hub pressure corner and along the suction surface at the second plane. At Plane 3, regions of high turbulence are still found in these locations and, additionally, the high turbulence intensity associated with the velocity deficit region is observed on the shroud near the suction surface. At Planes 4 and 5, the turbulence associated with the growing deficit region is observed, with the turbulence at the hub pressure corner and along the suction surface reduced.

The turbulence intensity contour results for the incipient rotating stall point for Planes 1-5 are given in Figures 5.34 through 5.38, respectively. Unlike the design operating point results at Plane 1, a region of high turbulence is located along the shroud surface across the plane. The growth of the turbulent region associated with the throughflow velocity deficit is observed throughout the passage. At Planes 4 and 5, the region of highest turbulence has moved off the shroud and is located near the suction surface at a position 75% of the length from hub to shroud.

The design operating point enthalpy contours for Planes 1-5 are given in Figures 5.39 through 5.43, respectively. The enthalpy is negative over 55% of Plane 1, with the net power input to the flow over the first 16% of the passage zero. The enthalpy rise over the plane is fairly constant between Planes 1 and 2. At Plane 3, an interesting feature of backswept blades is first observed. Namely, work is done on the air as the relative velocity is reduced because the tangential component of the absolute velocity and subsequently the enthalpy of the air is increased. However, the power input to the air in the low throughflow velocity regions is small because the mass flow is small. As a consequence, the regions of highest enthalpy are in the boundary layers. A similar trend is observed in Planes 4 and 5.

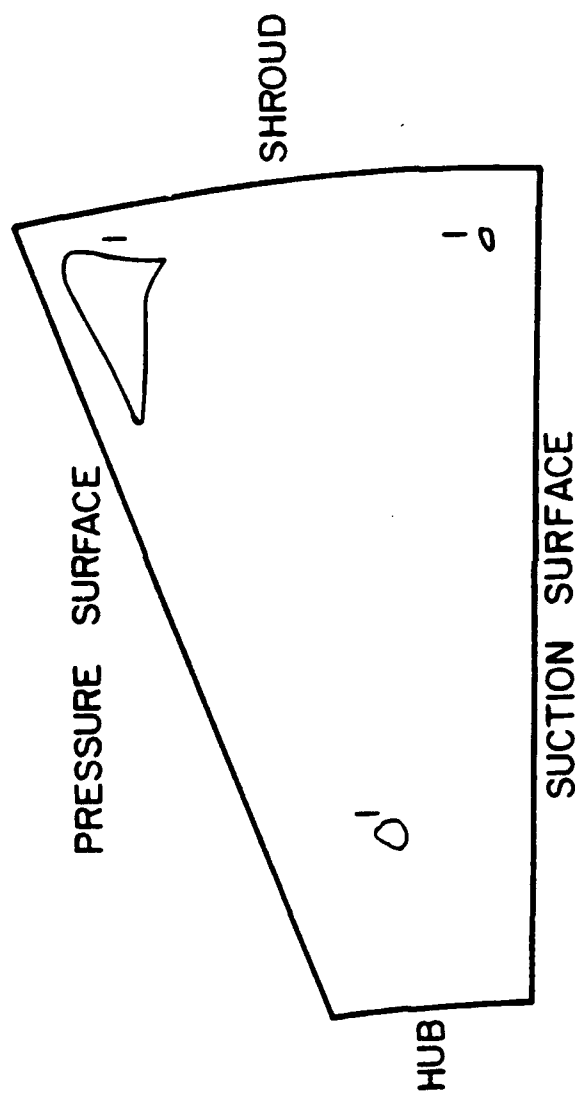


Figure 5.29 Turbulence Intensity Contour Plot - LDV Data
Design Point - Plane 1

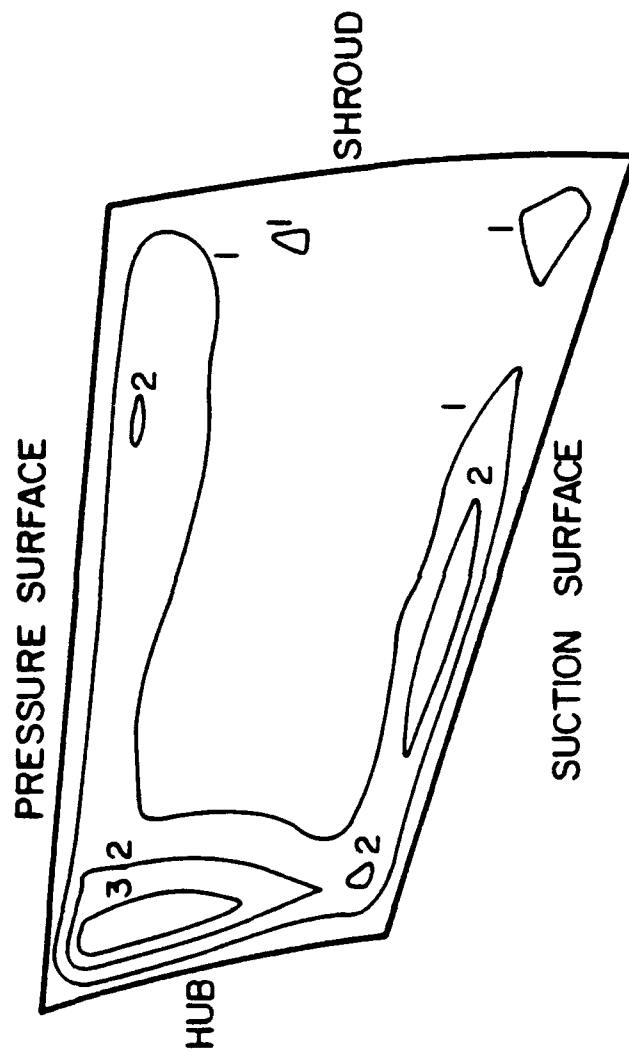


Figure 5.30 Turbulence Intensity Contour Plot - LDV Data
Design Point - Plane 2

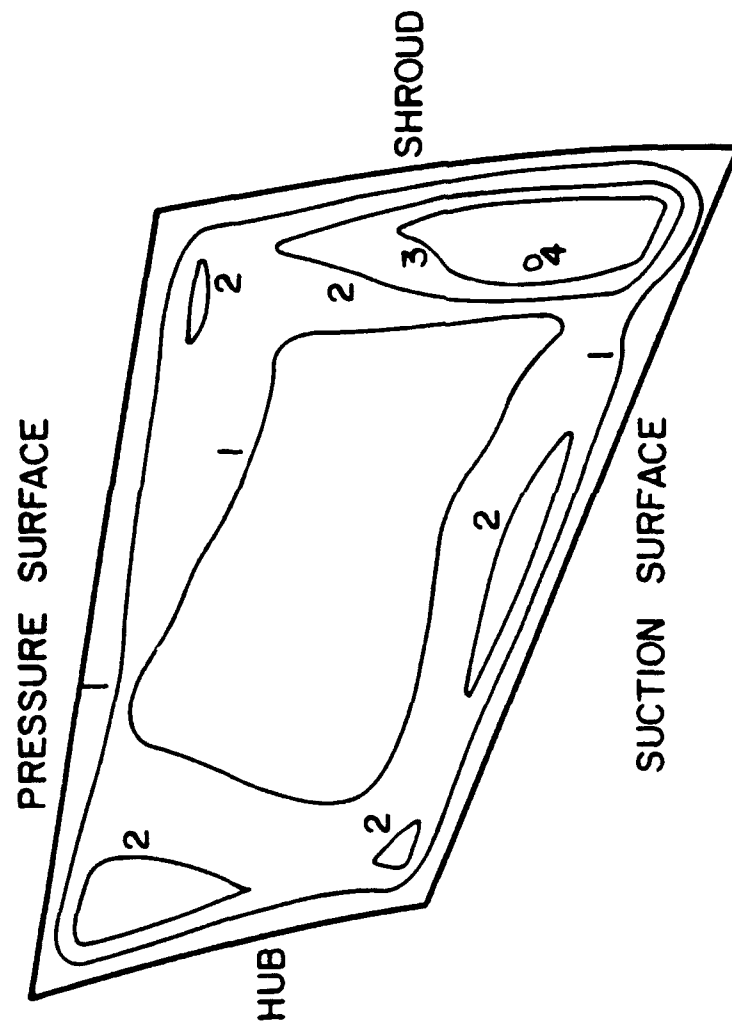


Figure 5.31 Turbulence Intensity Contour Plot - LDV Data
Design Point - Plane 3

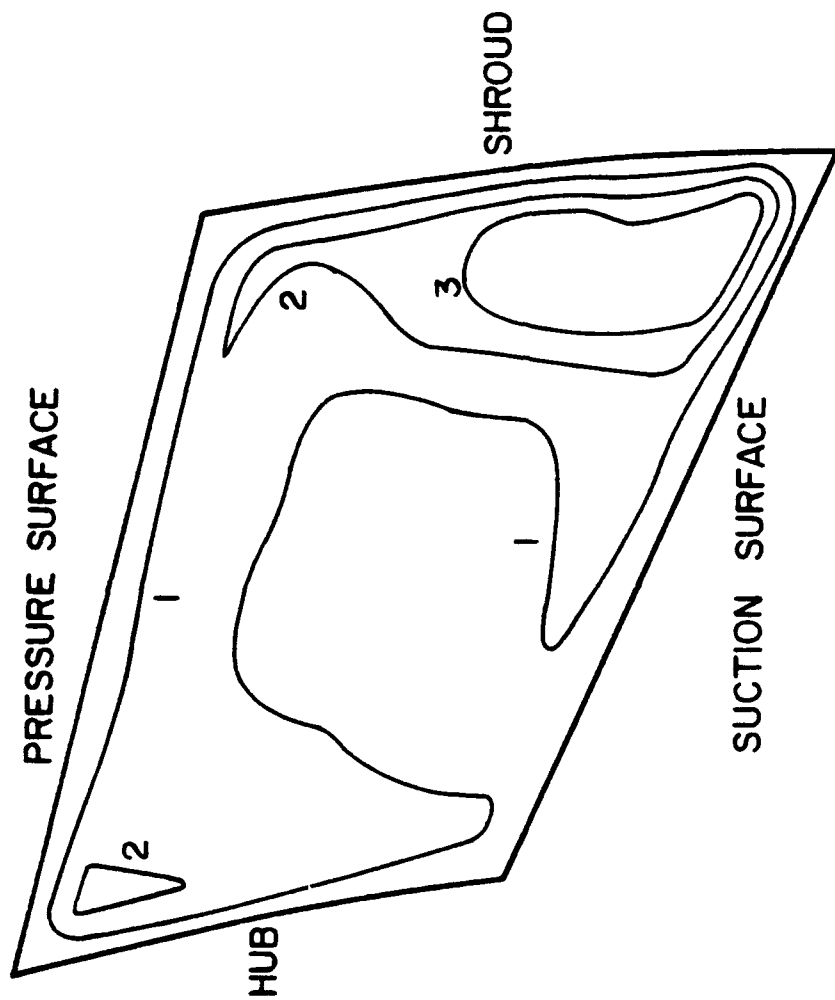


Figure 5.32 Turbulence Intensity Contour Plot - LDV Data
Design Point - Plane 4

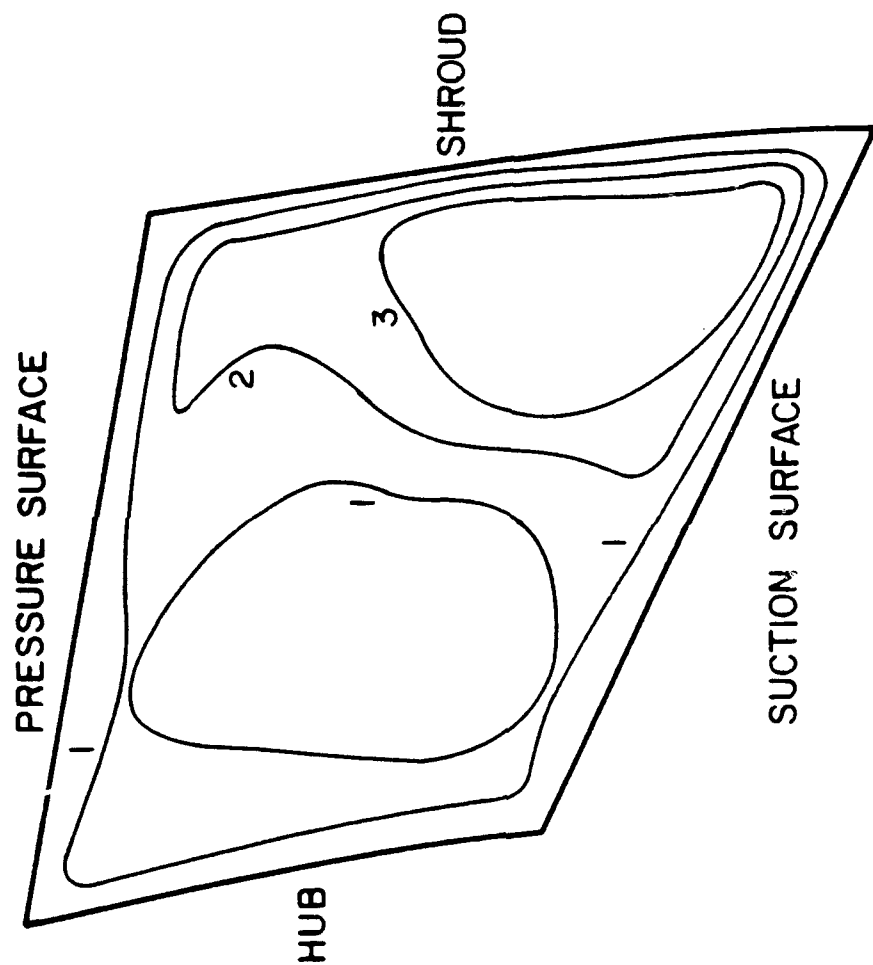


Figure 5.33 Turbulence Intensity Contour Plot - LDV Data
Design Point - Plane 5

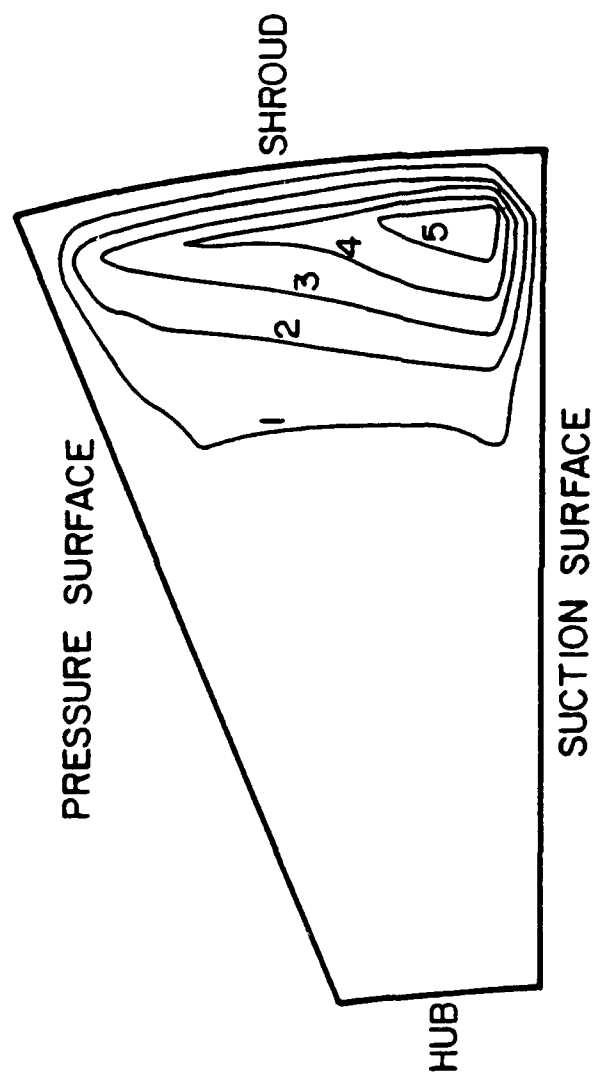


Figure 5.34 Turbulence Intensity Contour Plot - LDV Data
Incipient Stall Point - Plane 1

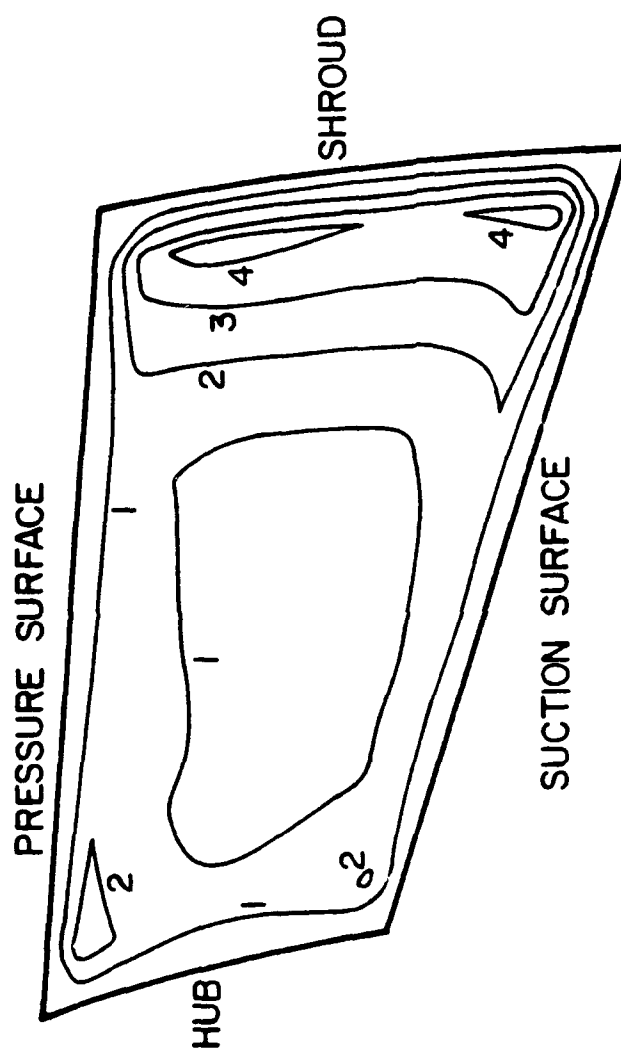


Figure 5.35 Turbulence Intensity Contour Plot - LDV Data
Incipient Stall Point - Plane 2

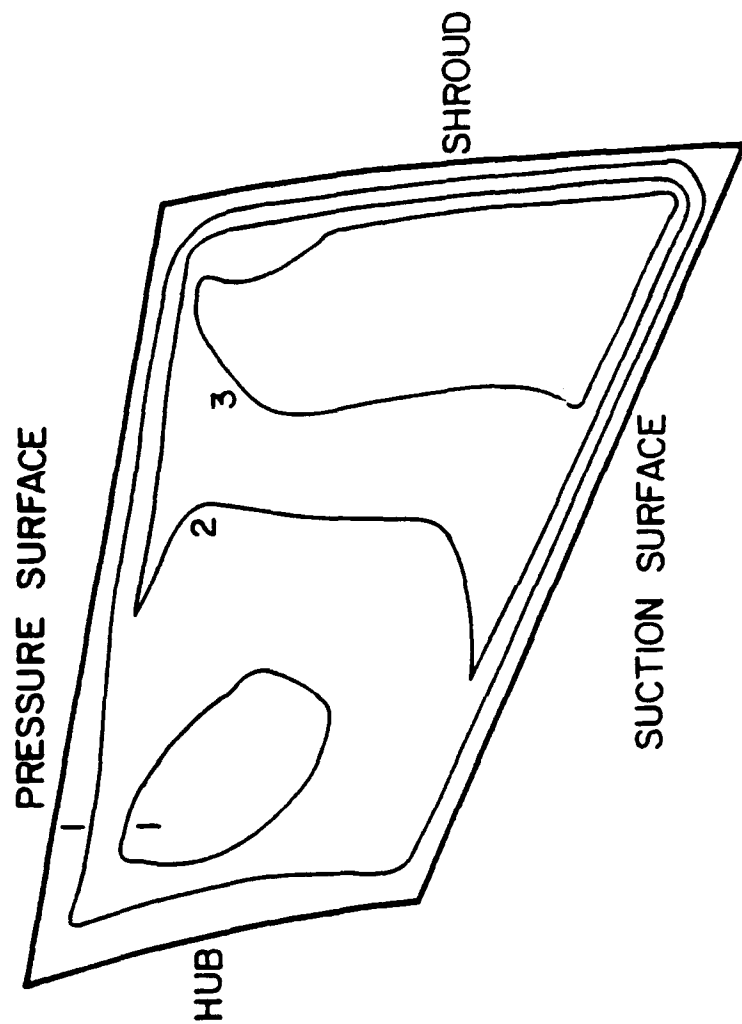


Figure 5.36 Turbulence Intensity Contour Plot - LDV Data
Incipient Stall Point - Plane 3

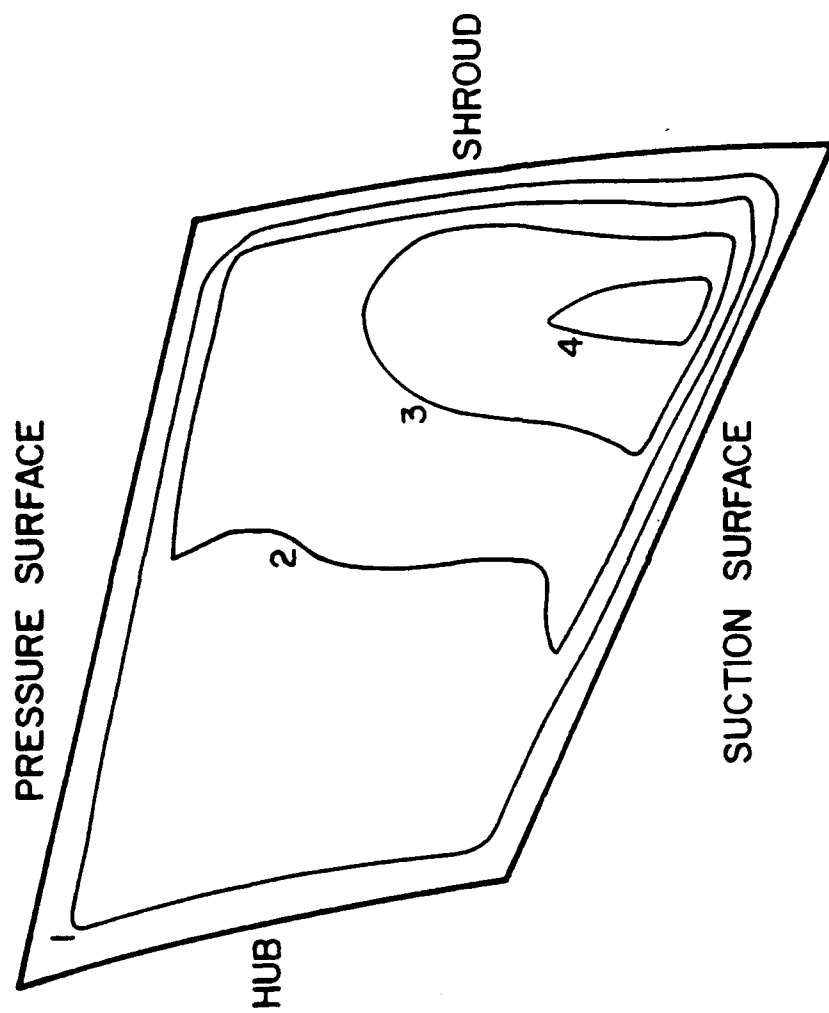


Figure 5.37 Turbulence Intensity Contour Plot - LDV Data
Incipient Stall Point - Plane 4

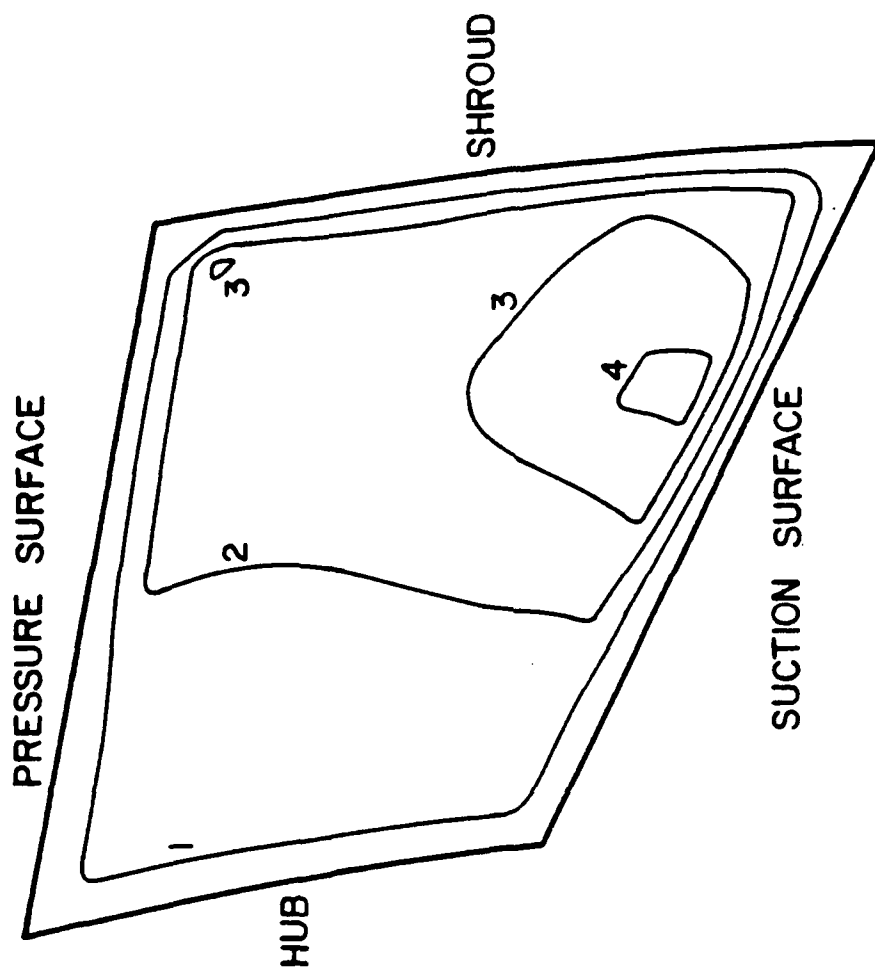


Figure 5.38 Turbulence Intensity Contour Plot - LDV Data
Incipient Stall Point - Plane 5

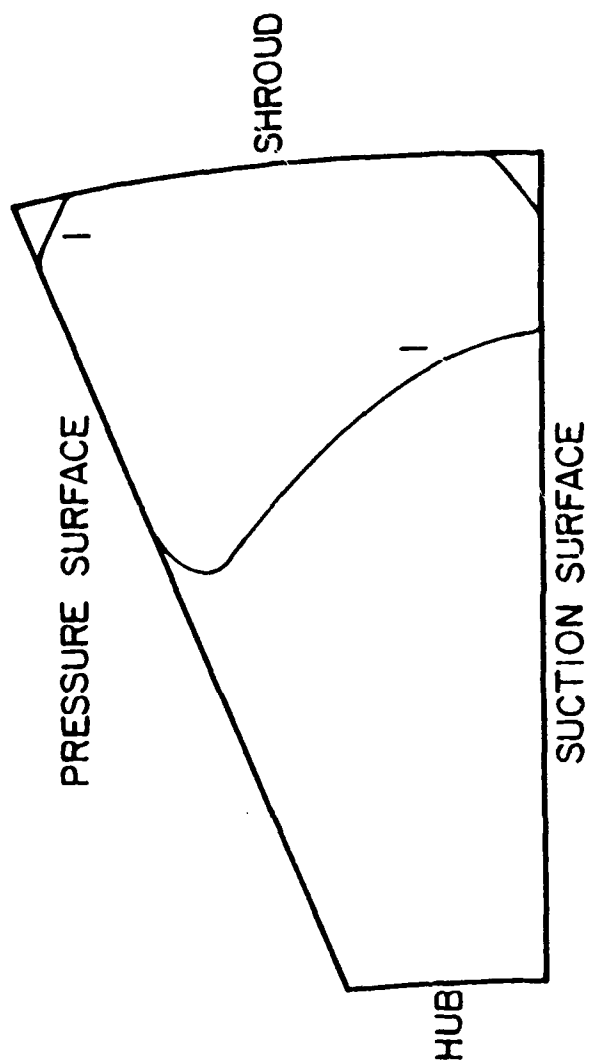


Figure 5.39 Enthalpy Contour Plot - LDV Data
Design Point - Plane 1

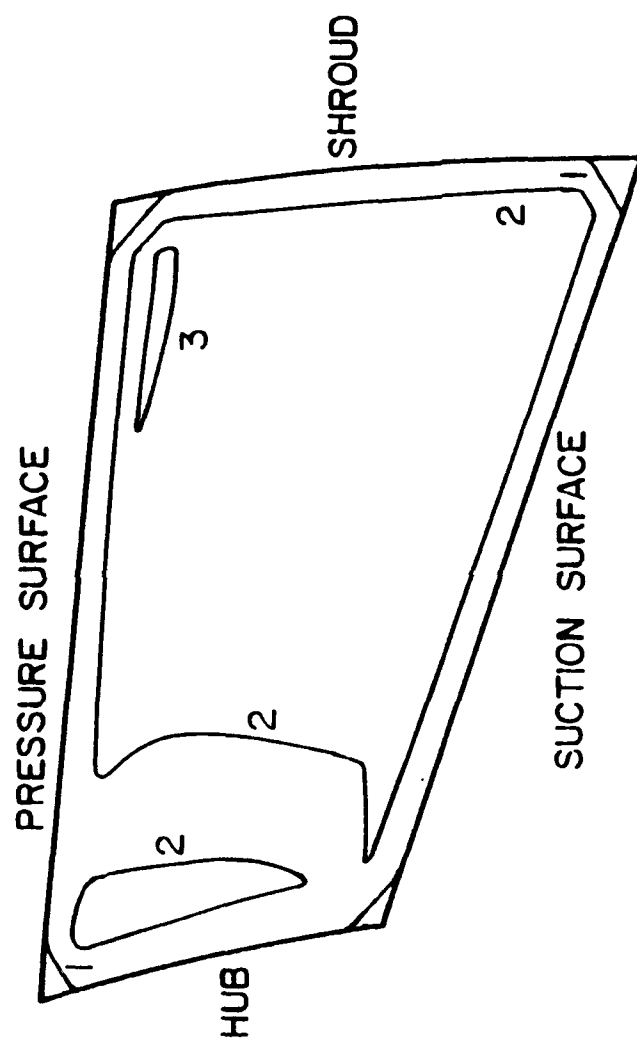


Figure 5.40 Enthalpy Contour Plot - LDV Data
Design Point - Plane 2

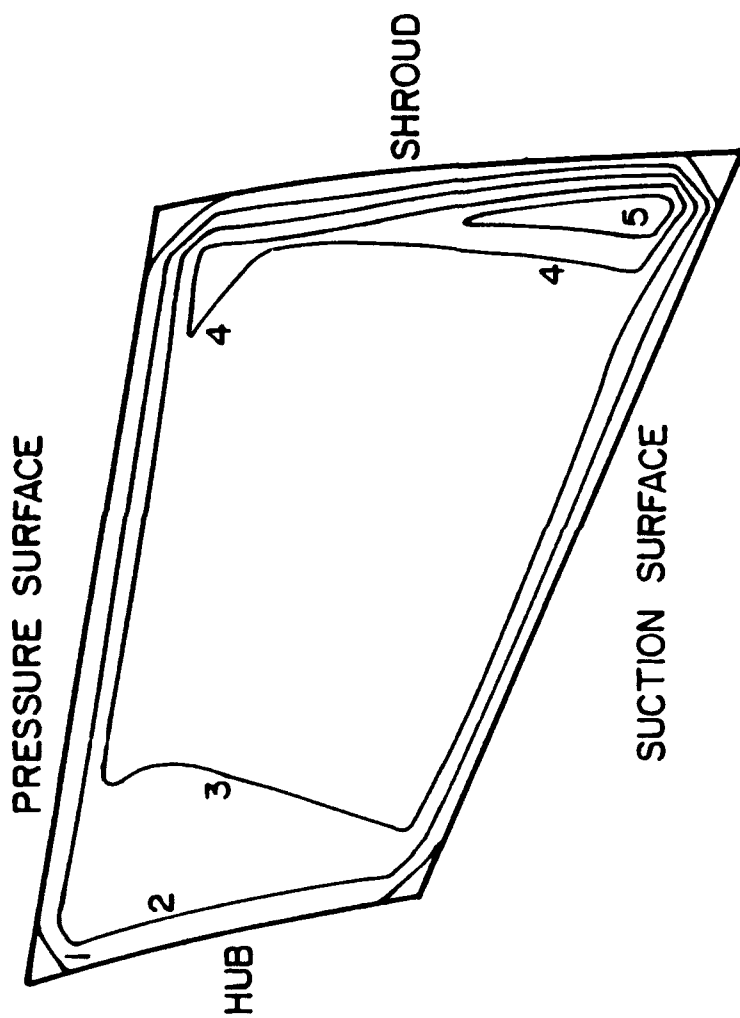


Figure 5.41 Enthalpy Contour Plot - LDV Data
Design Point - Plane 3

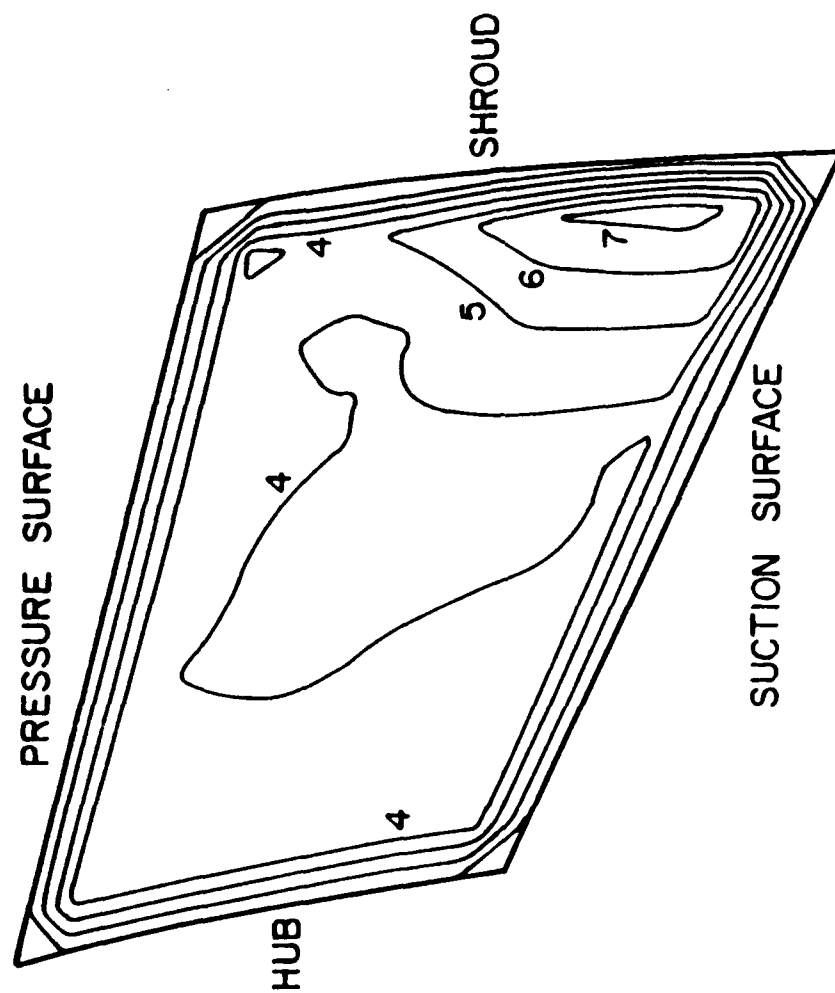


Figure 5.42 Enthalpy Contour Plot - LDV Data
Design Point - Plane 4

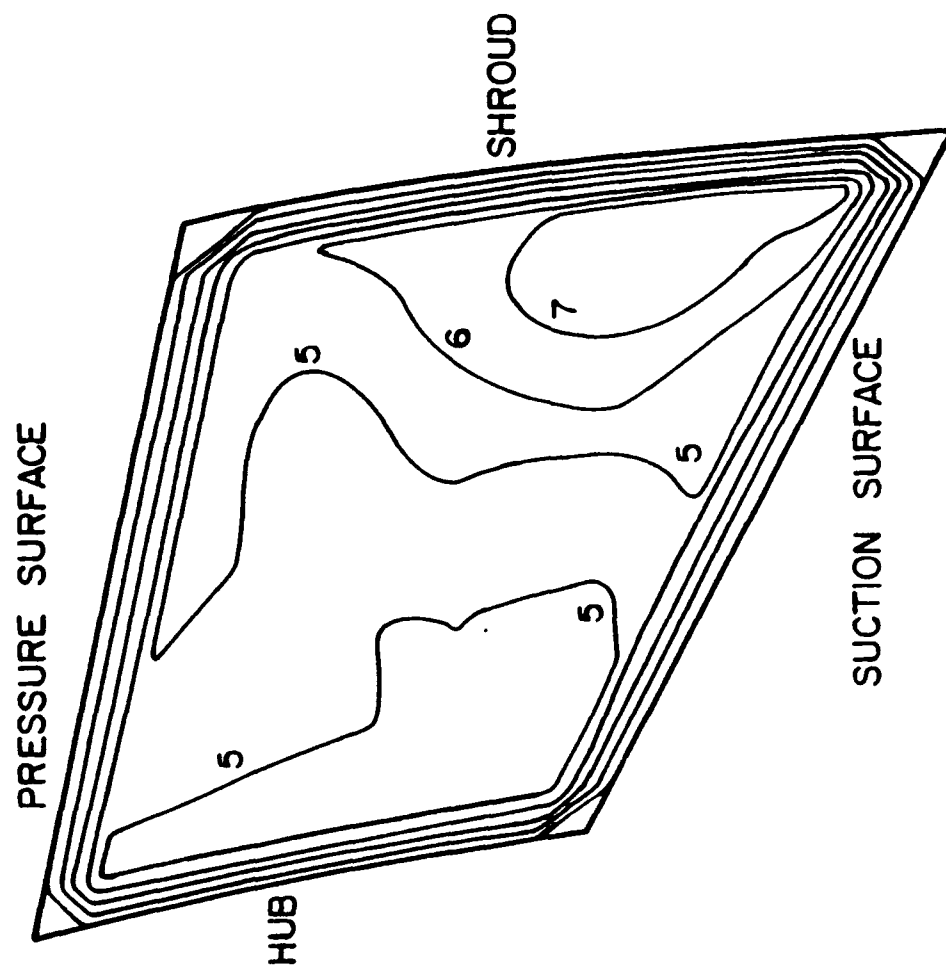


Figure 5.43 Enthalpy Contour Plot - LDV Data
Design Point - Plane 5

The incipient stall operating point enthalpy contours for Planes 1-5 are given in Figures 5.44 through 5.48, respectively. At Plane 1, high enthalpy air is found near the shroud in the velocity deficit region. Additionally, the enthalpy is positive over the entire plane. Through the rest of the passage the development of the flow is very similar to that at the design operating point, with the exception of the larger deficit region.

5.1.5 Discussion

The LDV results at the compressor design operating point indicate a slight disturbance to the flow near the hub in the first 40% of the passage. This is observed in the throughflow velocity and turbulence intensity results at Plane 2. These results indicate a boundary layer in the hub pressure corner, which becomes smaller at Plane 3. Another indication of a flow disturbance is the region with negative enthalpy observed near the hub in Plane 1. However, all indications of a disturbance disappear as the flow is turned radially. At Plane 3, a deficit region with large positive vorticity similar to the jet-wake flow found in most centrifugal compressors is observed. The deficit or wake region is located on the shroud but not in the suction corner. Through the remainder of the passage, the extent of the deficit region continues to grow. At the final data plane, regions of positive vorticity are located on either side of the wake.

The results at the incipient stall operating point indicate a severe disturbance to the flow near the shroud. At Plane 1, the various results indicate a boundary layer along the shroud. The boundary layer continues to grow through the passage. Again, the first indication of a deficit or wake region is observed at Plane 3. At this location, a circumferential variation of the throughflow velocity in the boundary layer is observed, similar to the jet-wake flow observed at the design operating point. At Plane 4, the wake is located in the shroud suction corner. Reverse flow with regions of positive vorticity located on the shroud and on the suction surface near the corner are observed at Plane 5.

The location of the wake is dependent upon a balance of the forces due to streamline curvature, which drives the wake toward the center of the channel, and rotation, which drives the wake toward the suction surface. The balance of these forces

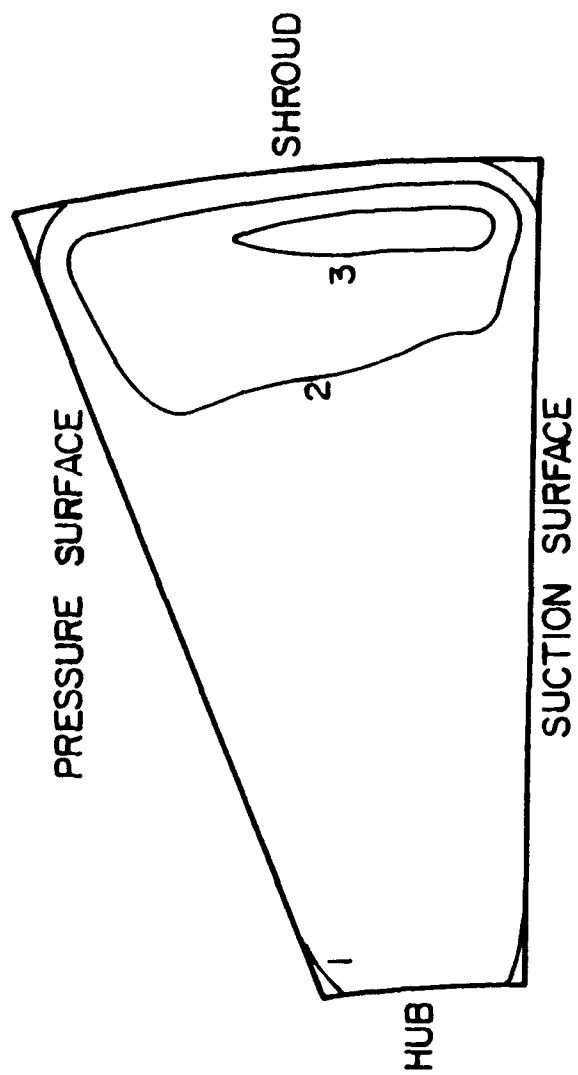


Figure 5.44 Enthalpy Contour Plot - LDV Data
Incipient Stall Point - Plane 1

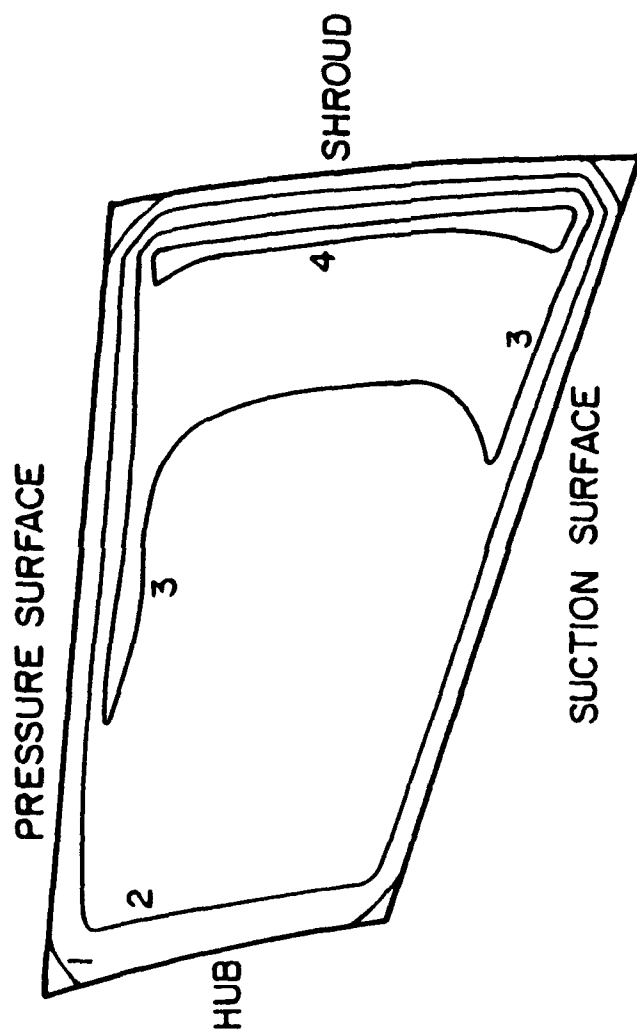


Figure 5.45 Enthalpy Contour Plot - LDV Data
Incipient Stall Point - Plane 2

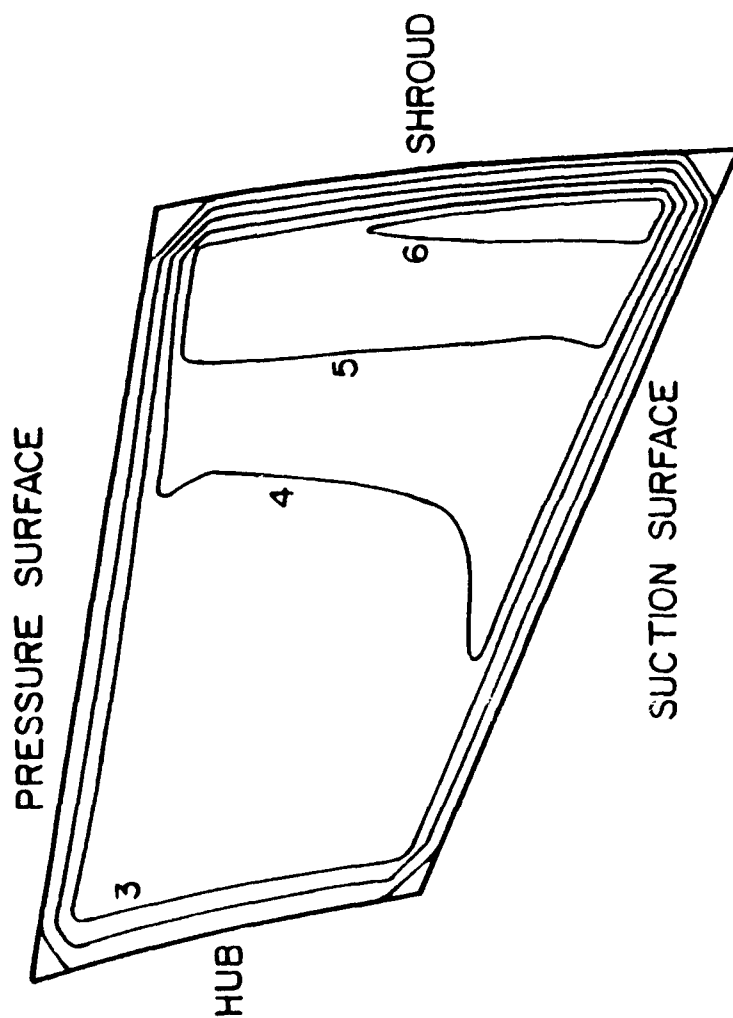


Figure 5.46 Enthalpy Contour Plot - LDV Data
Incipient Stall Point - Plane 3

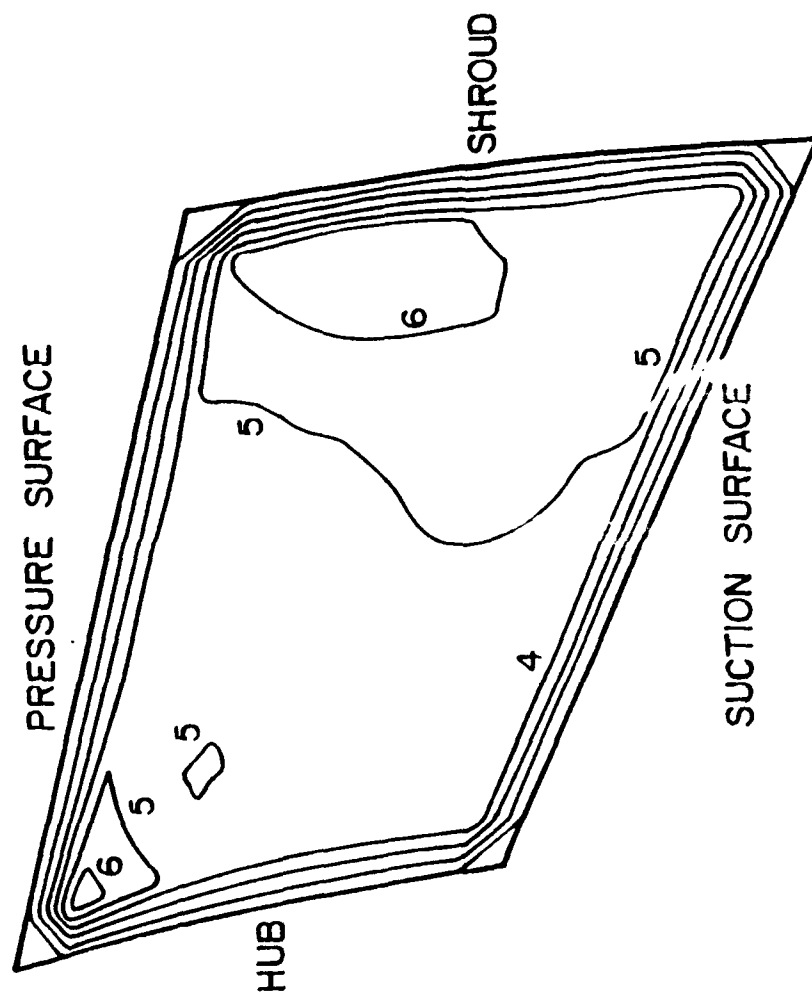


Figure 5.47 Enthalpy Contour Plot - LDV Data
Incipient Stall Point - Plane 4

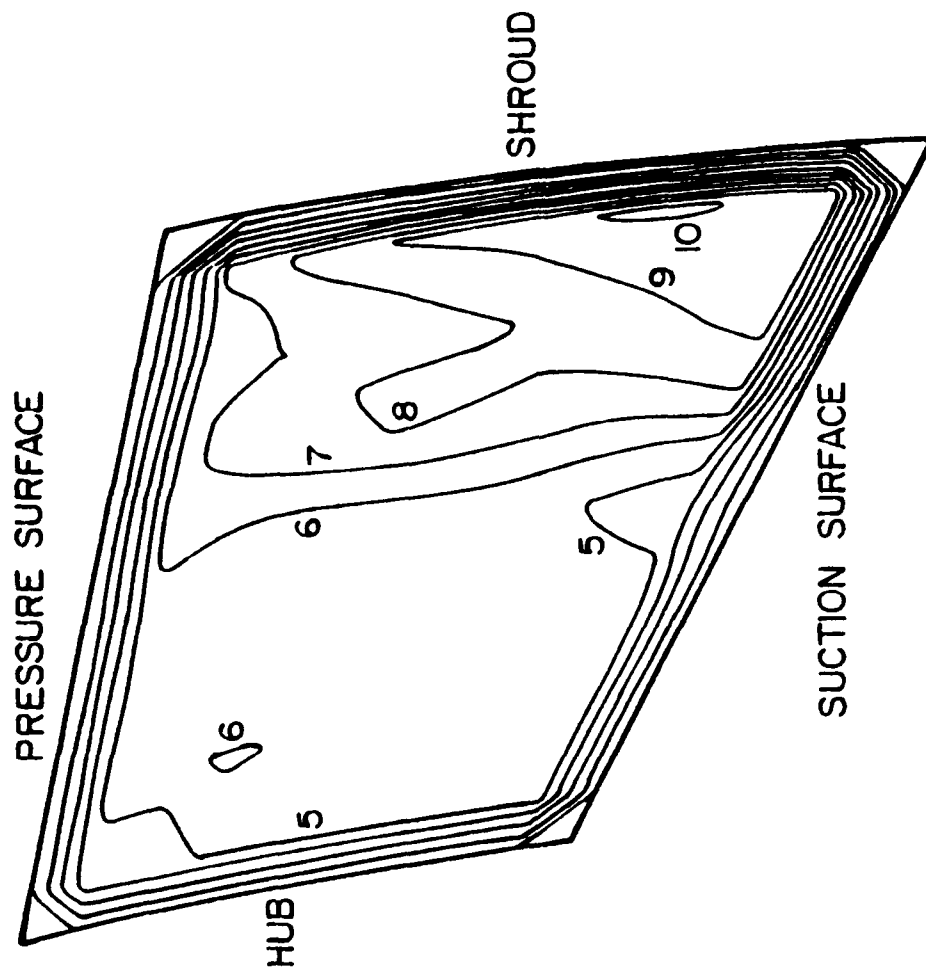


Figure 5.48 Enthalpy Contour Plot - LDV Data
Incipient Stall Point - Plane 5

is determined by the dimensionless Rosby number, Equation 5.3. For an unshrouded impeller, Moore, Moore and Johnston [27] suggest that a Rosby number less than 0.25 indicates that rotational effects dominate and the wake is in the suction shroud corner. The Rosby number for the design and the incipient stall operating points are 0.92 and 0.75, respectively. The discrepancy between the critical Rosby number indicated by this work and that suggested by Moore et al is probably due to the shroud on the Purdue Research Centrifugal impeller. As a result, the mass flow rate in an unshrouded impeller would have to be reduced further than in a shrouded impeller with similar geometry to move the wake to the shroud suction corner. Assuming that the wake must be on the suction surface for the onset of rotating stall, one effect of tip leakage in unshrouded impellers is stabilization of the flow.

$$R_o = \frac{W}{\omega R_N} \quad (5.3)$$

W - relative velocity

R_N - radius of curvature

The reduction of the mass flow rate at the incipient rotating stall point is partially realized by a thickening of the boundary layer on the shroud. However, the location in the passage where the wake is first observed is the same at both the design and incipient stall operating points. Consequently, the extent of the wake region, from the end of the passage to the front, does not increase as the mass flow rate is reduced, with rotating stall ultimately triggered by a small perturbation which extends the wake to the blade leading edge. The results obtained herein indicate that the onset of rotating stall is marked by a sudden and significant change to the impeller passage flow field.

5.2 Unsteady Pressure Measurements

Unsteady pressure measurements were made as the mass flow rate was slowly reduced in discrete steps from an operating point just above that of the onset of rotating stall through operating regions with three distinct modes of rotating stall. Additionally, a

baseline set of data was taken far above the critical mass flow rate where rotating stall begins. A constant speed operating line for the compressor, marked at the operating point where rotating stall begins, is given in Figure 5.49, with a summary of the characteristics of each of the three modes of rotating stall presented in Table 5.3. For each of the operating points the signal from microphones 1 and 2 are the similar to the signal from microphone 3, with the phase difference of the signals and the circumferential displacement of the microphones indicating the number of cells in the pattern.

5.2.1 Baseline

The baseline data were taken at a mass flow of 2.72 kg/s (6.0 lbm/s), far above the onset of rotating stall. An unfiltered and filtered time history of the baseline unsteady pressure signals from Microphones 3 and 4 are given in Figures 5.50 and 5.51, respectively (the microphone locations are shown in Figure 3.13). The sampling rate for these data sets is 2000 Hz, with the 2000 data points corresponding to a full scale time of one second. The harmonic content of the signal from the two microphones is presented in Figures 5.52 and 5.53. The same formats are used for all subsequent results. These data show significant harmonic content at 96 and 687 Hz. The 687 Hz signal corresponds to the blade pass frequency, but the content at 96 Hz is not easily explained. It likely corresponds to a passage resonance which is observed to decrease as the compressor enters rotating stall. The upstream microphone also measures a signal frequency component at 30 Hz which is the rotational frequency of the impeller.

5.2.2 Incipient Rotating Stall

The mass flow was slowly reduced and unsteady pressure data taken at a point immediately preceding the onset of rotating stall. This process was repeated several times to determine whether the onset of rotating stall occurs abruptly or a small disturbance precedes or progresses to rotating stall. Because rotating stall recovery displays hysteresis, the incipient point was always approached by reducing the mass flow rate. The data presented were taken at a mass flow rate of 2.16 kg/s (4.77 lbm/s). The time history for

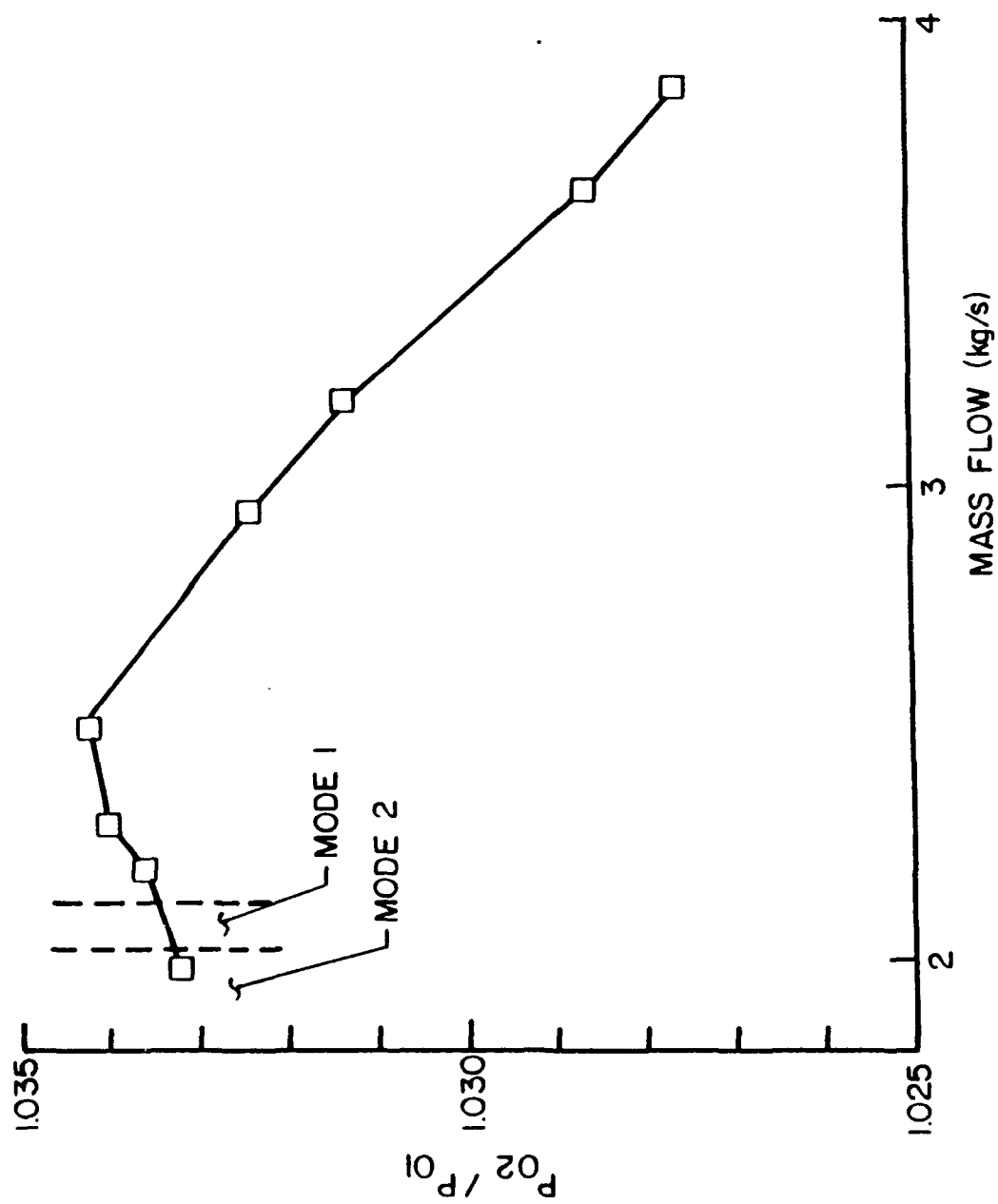


Figure 5.49 Constant Speed Operating Line for the Centrifugal Compressor

Table 5.3 Centrifugal Compressor Rotating Stall Modes

Mode	Mass Flow (kg/s)	Cell Number	Relative Rotational Speed (Frequency) (% Wheel Speed)		Harmonic Content (Frequency)			Notes
					Fundamental	Harmonic	Interaction	
1	< 2.09	Pattern 1-1	4.7	16	25.2		79	- Strongest at Impeller Inlet - Not Stable
							134	
	> 2.00	Pattern 2-2	2.0	7	55.8	110	158	
2	< 2.00	1	25.5	85	4.4	8.8 13.2 17.6 22.0 26.4		- Strongest at Diffuser - Stable
	> 1.72							
3	< 1.72	2	26.0	87	7.7	15.4 23.1		- Strongest at Diffuser - Only 2nd Harmonic measured at impeller inlet

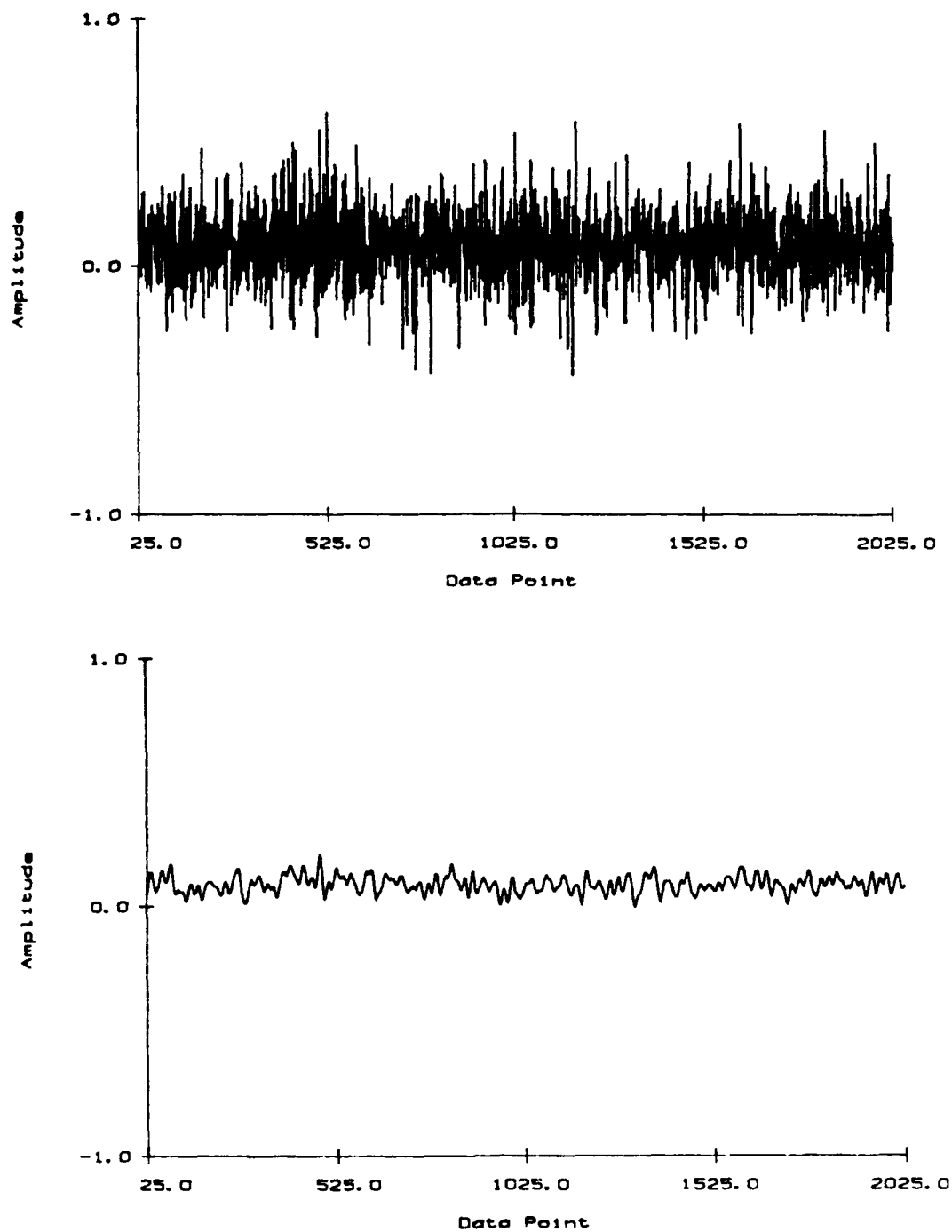


Figure 5.50 Unfiltered and Filtered Unsteady Pressure Signal - Baseline (Microphone 3)

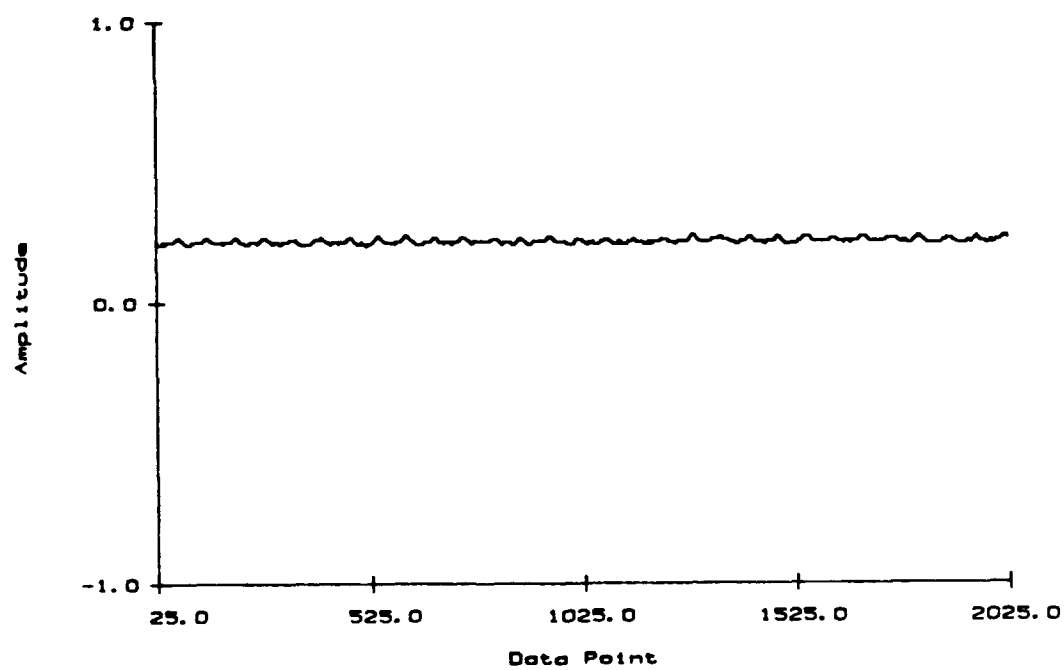
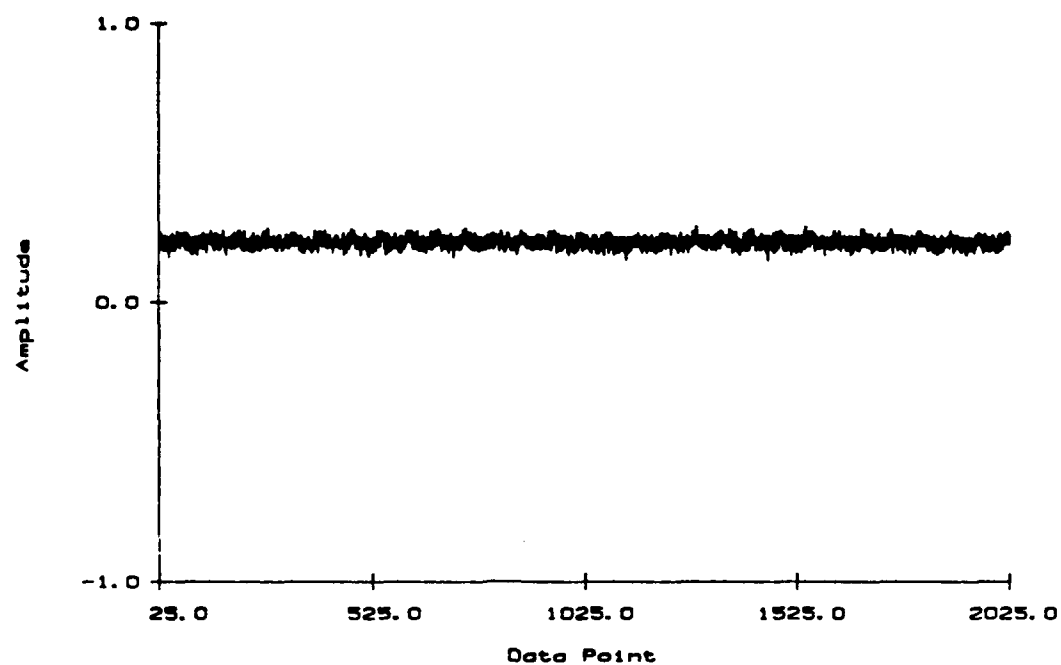


Figure 5.51 Unfiltered and Filtered Unsteady Pressure Signal - Baseline (Microphone 4)

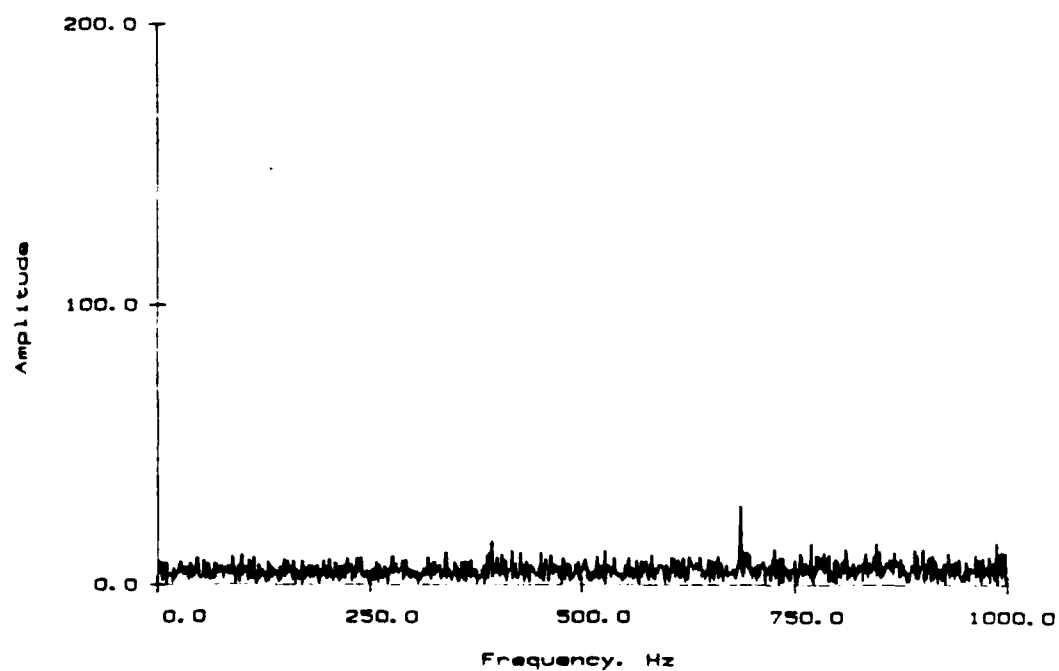
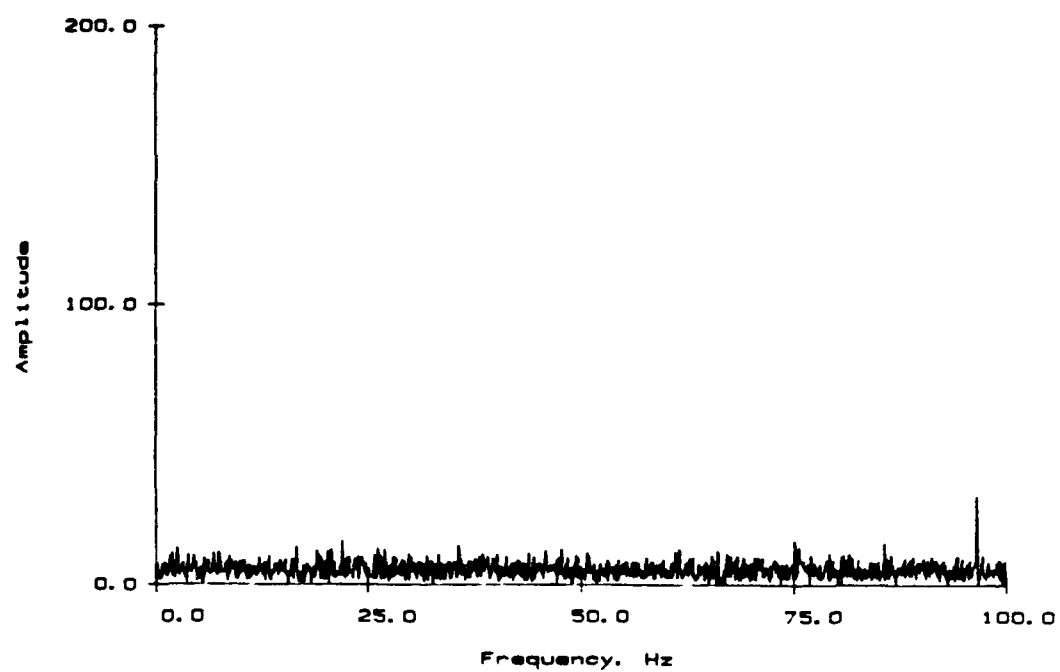


Figure 5.52 Fourier Analysis of Unsteady Pressure Signal - Baseline
(Microphone 3)

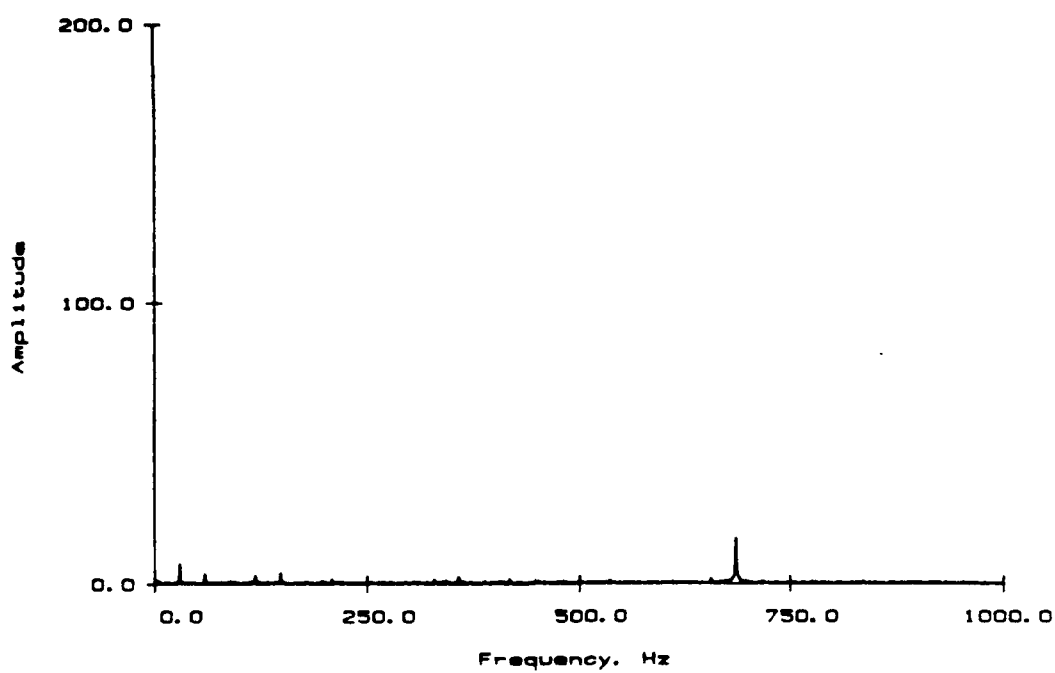
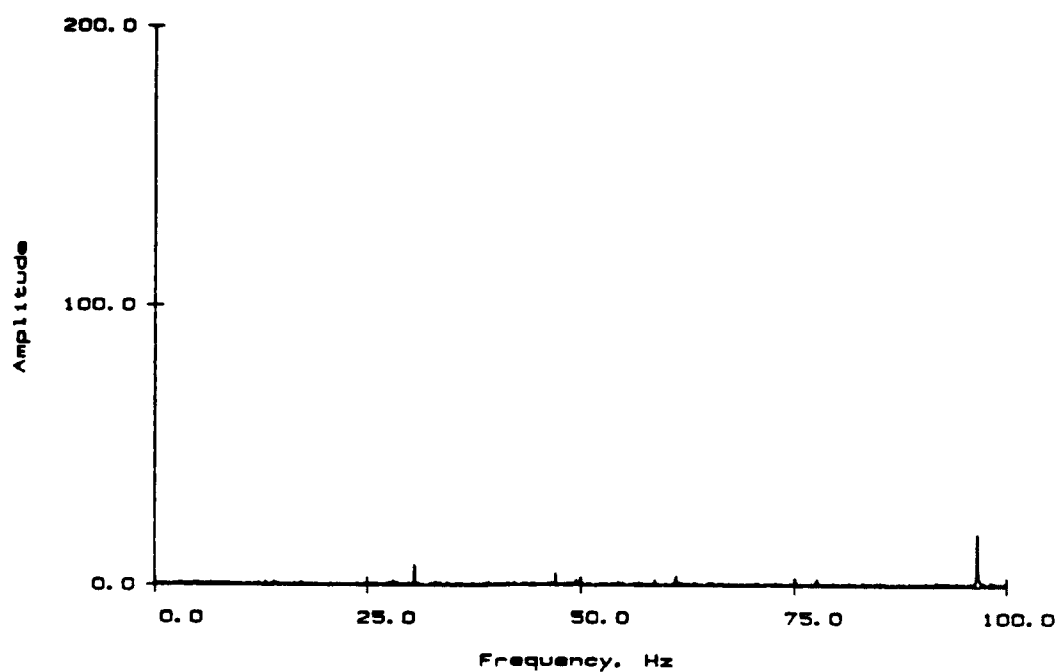


Figure 5.53 Fourier Analysis of Unsteady Pressure Signal - Baseline
(Microphone 4)

the signal from Microphones 3 and 4 are presented in Figures 5.54 and 5.55, respectively. The harmonic analysis of each is given in Figures 5.56 and 5.57. The harmonic content of the data taken at the incipient stall operating point is almost identical to that at the baseline, indicating that the transition to rotating stall is very abrupt.

5.2.3 Mode 1 Rotating Stall

As the mass flow rate is reduced, the compressor suddenly enters the first mode of rotating stall at a mass flow rate of 2.09 kg/s (4.60 lbm/s). This mode is the most violent and the least stable of the three modes. It exists over only a narrow range of flow rates (2.00 - 2.09 kg/s), with frequency analysis indicating two separate stall patterns rotating concurrently. The patterns can be described as circular waves with a fixed number of nodes or cells rotating at a constant frequency, Figure 5.58. Mode 1 proved to be the most difficult to analyze because the amplitude of the two patterns fluctuated with each sometimes disappearing.

The unfiltered and filtered time history for data taken at a mass flow rate of 2.05 kg/s (4.51 lbm/s) of the signals from Microphones 3 and 4 are given in Figures 5.59 and 5.60, respectively. The harmonic analysis of the signals from the microphones is presented in Figures 5.61 and 5.62. Harmonic content corresponding to stall patterns are clearly identifiable in the data from both microphones at 25.2 and 55.8 Hz. The amplitude of the frequency spikes corresponding to stall patterns, particularly the pattern at 55.8 Hz, and the frequency spikes corresponding to higher harmonics and interactions are stronger at Microphone 4. Also, the data from Microphone 4 indicate significant harmonic content at 81, 88, 109, and 134 Hz as well as at the stall pattern and the blade pass frequencies. Except for 88 Hz, which is presently unexplained, each can be attributed to a higher harmonic or interaction between the stall patterns. Harmonic analysis of the data from Microphone 3 does not show the higher harmonics and interactions of the stall pattern frequencies, confirming that the patterns are stronger at the impeller inlet. Similar to data taken at the baseline, harmonic content is observed in the data from both microphones.

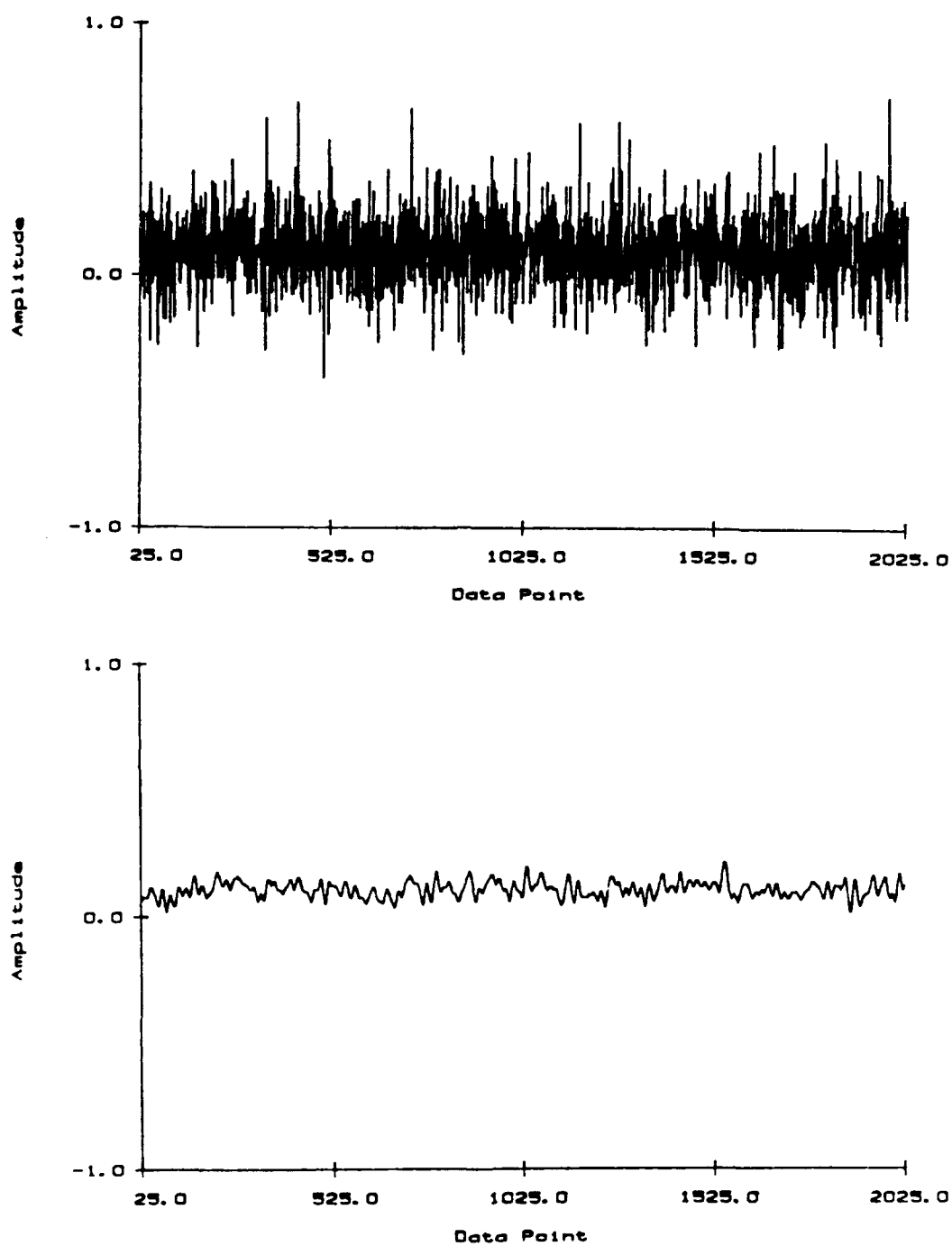


Figure 5.54 Unfiltered and Filtered Unsteady Pressure Signal - Stall Onset (Microphone 3)

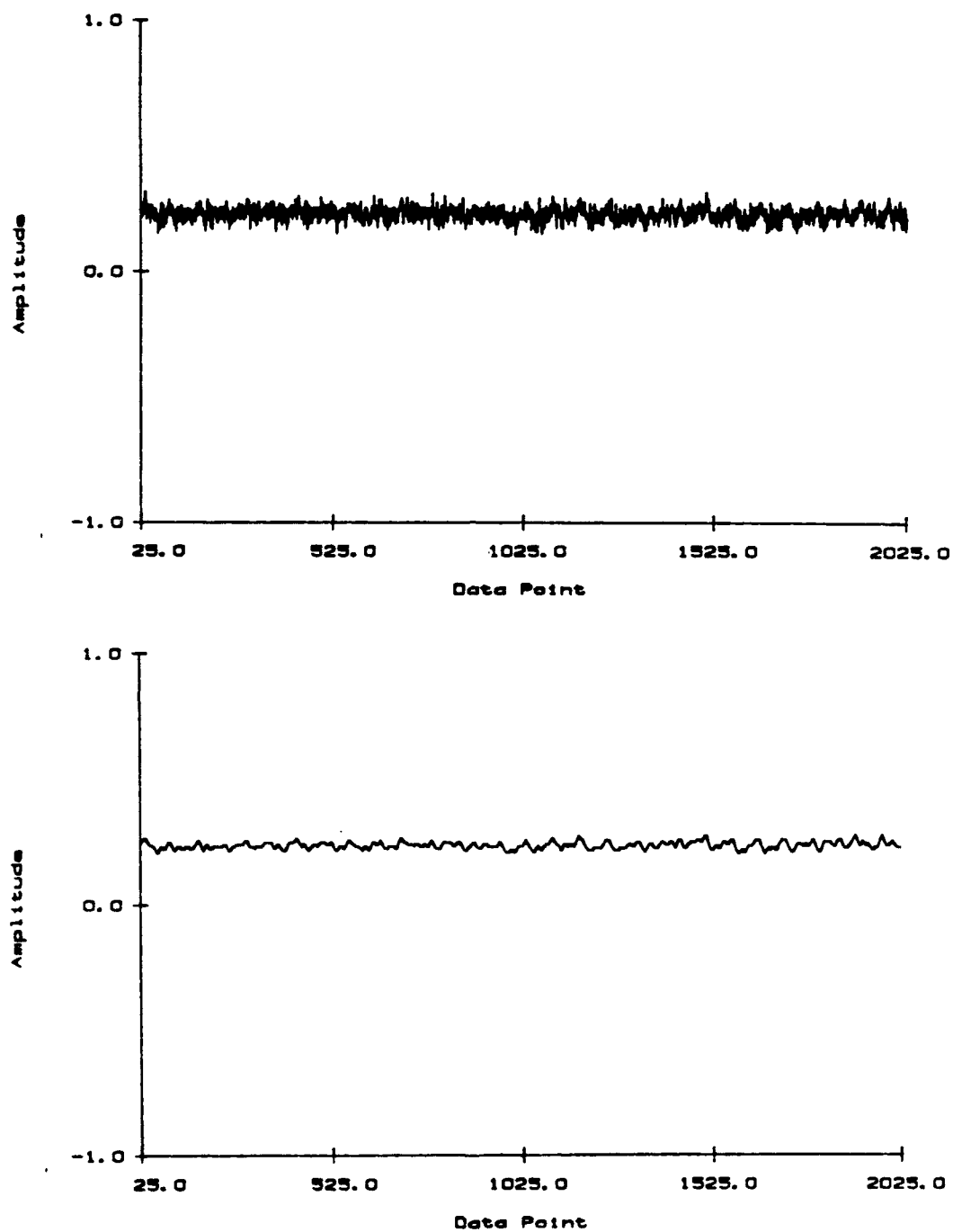


Figure 5.55 Unfiltered and Filtered Unsteady Pressure Signal - Stall Onset (Microphone 4)

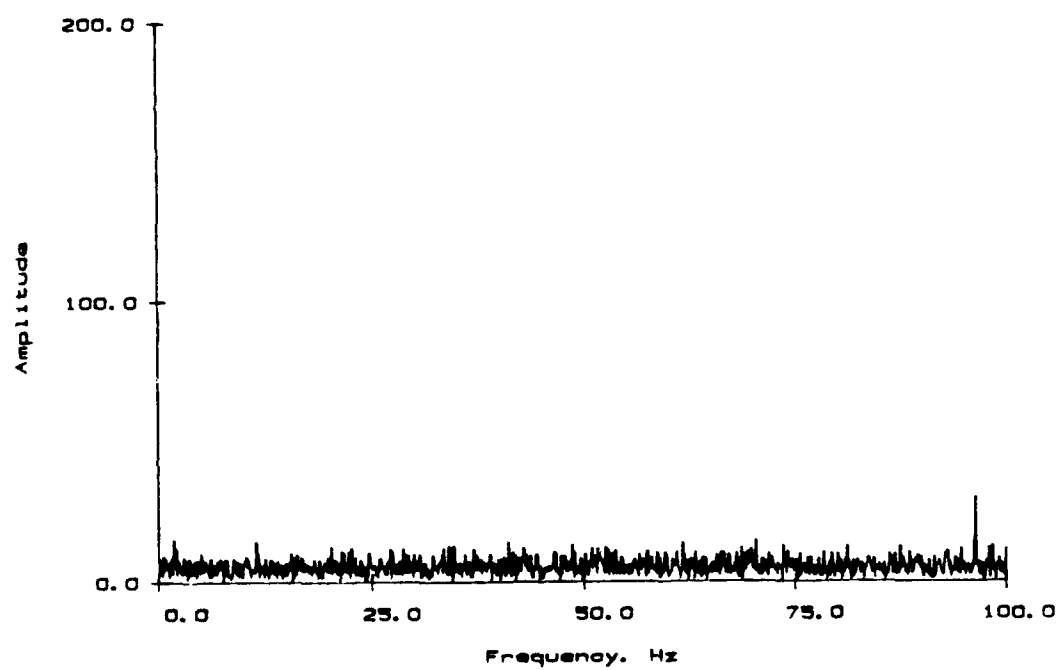
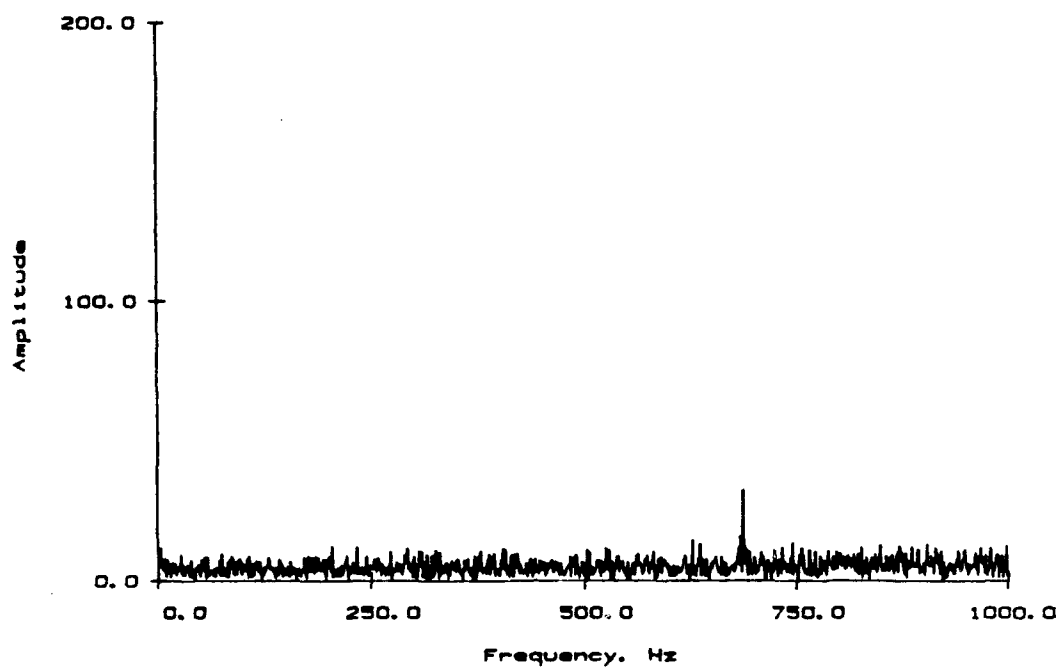


Figure 5.56 Fourier Analysis of Unsteady Pressure Signal - Stall Onset
(Microphone 3)

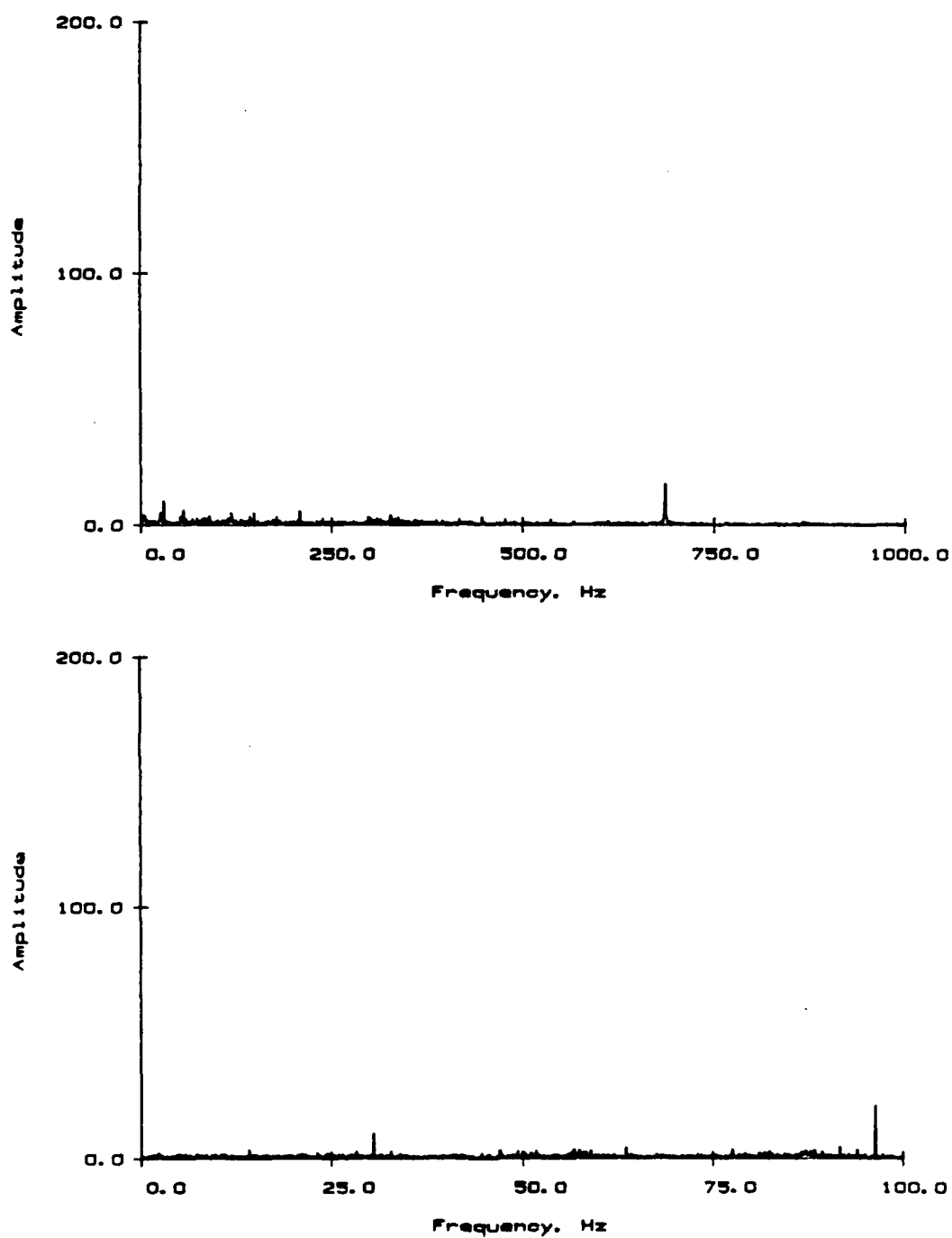


Figure 5.57 Fourier Analysis of Unsteady Pressure Signal - Stall Onset (Microphone 4)

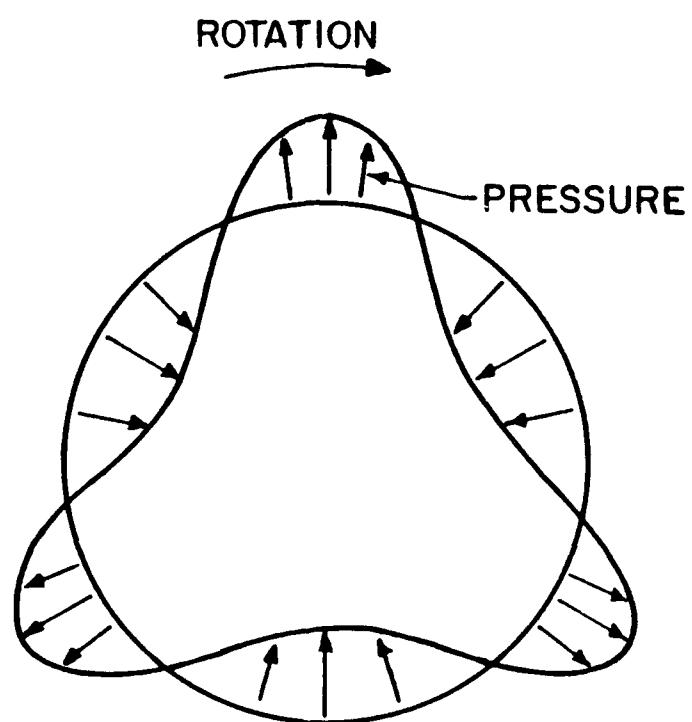


Figure 5.58 Rotating Stall Pattern - Three Cells

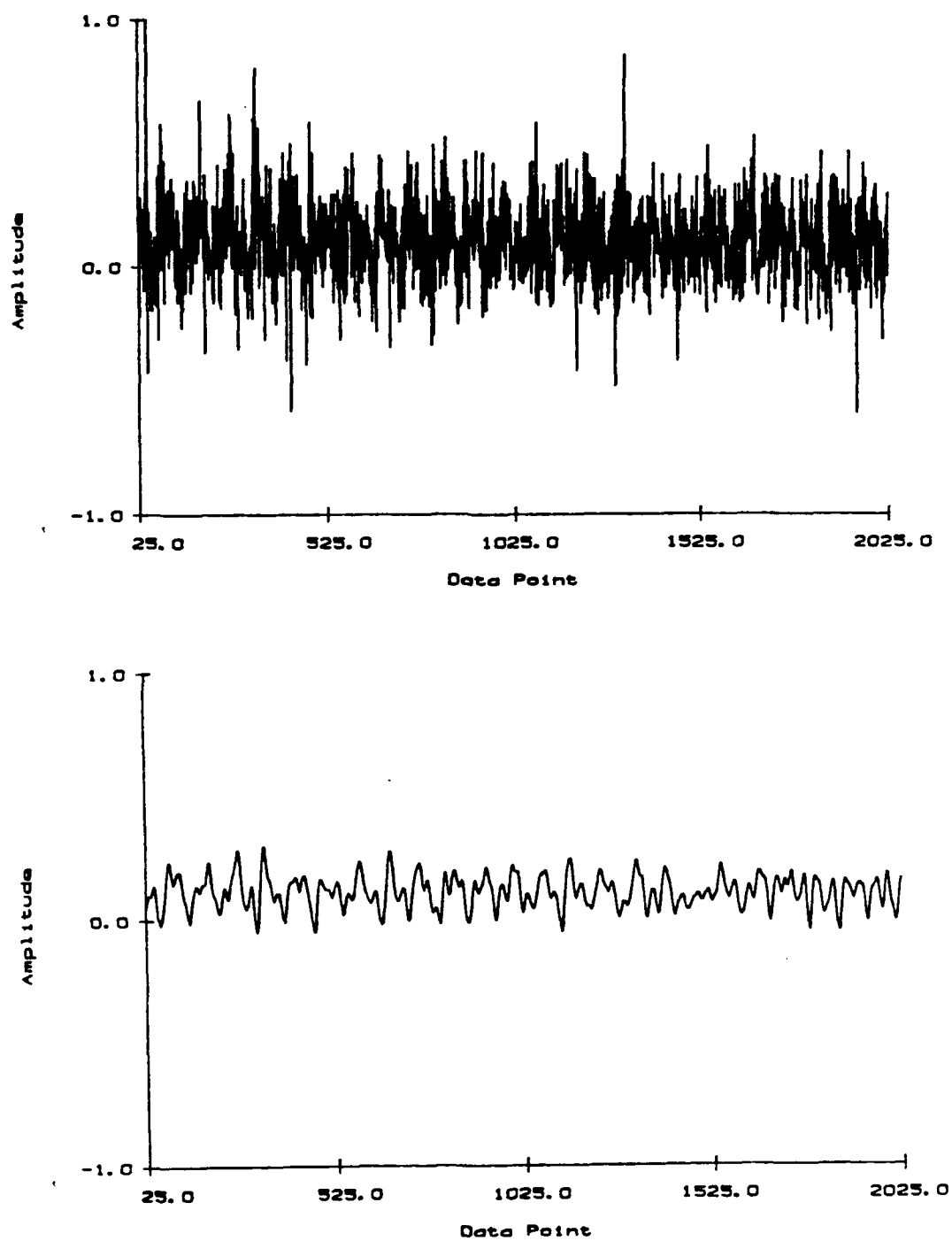


Figure 5.59 Unfiltered and Filtered Unsteady Pressure Signal - Mode 1 (Microphone 3)

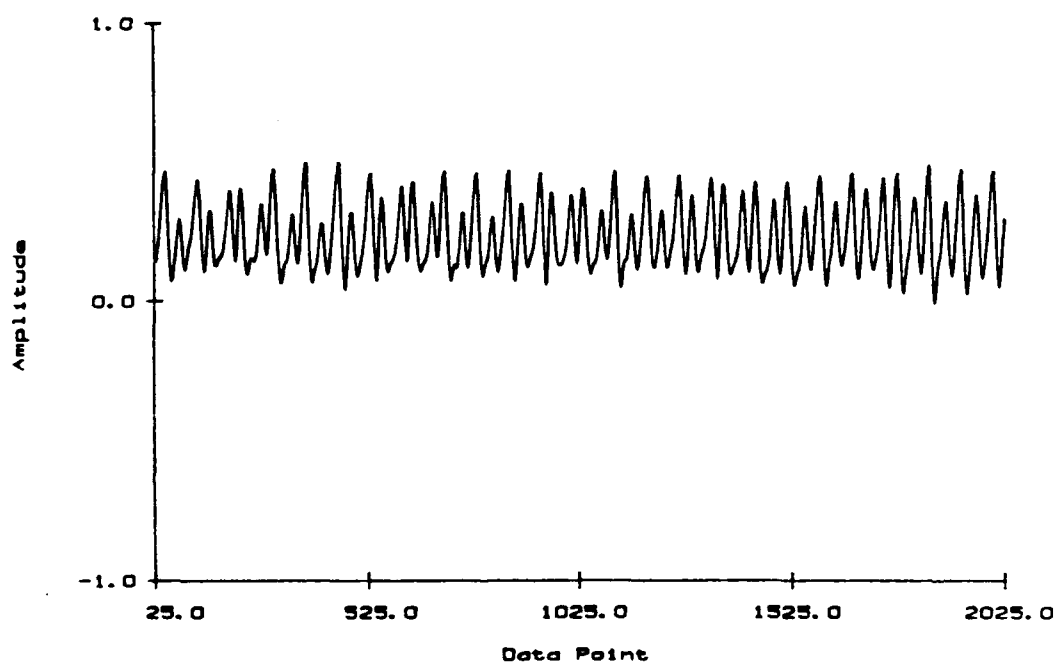
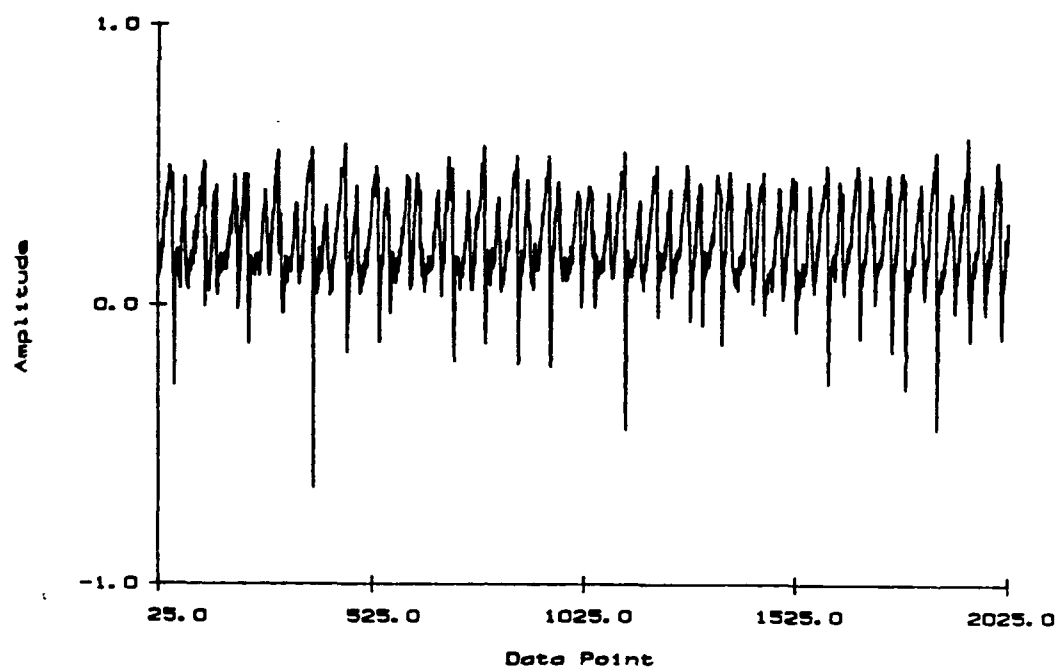


Figure 5.60 Unfiltered and Filtered Unsteady Pressure Signal - Mode 1 (Microphone 4)

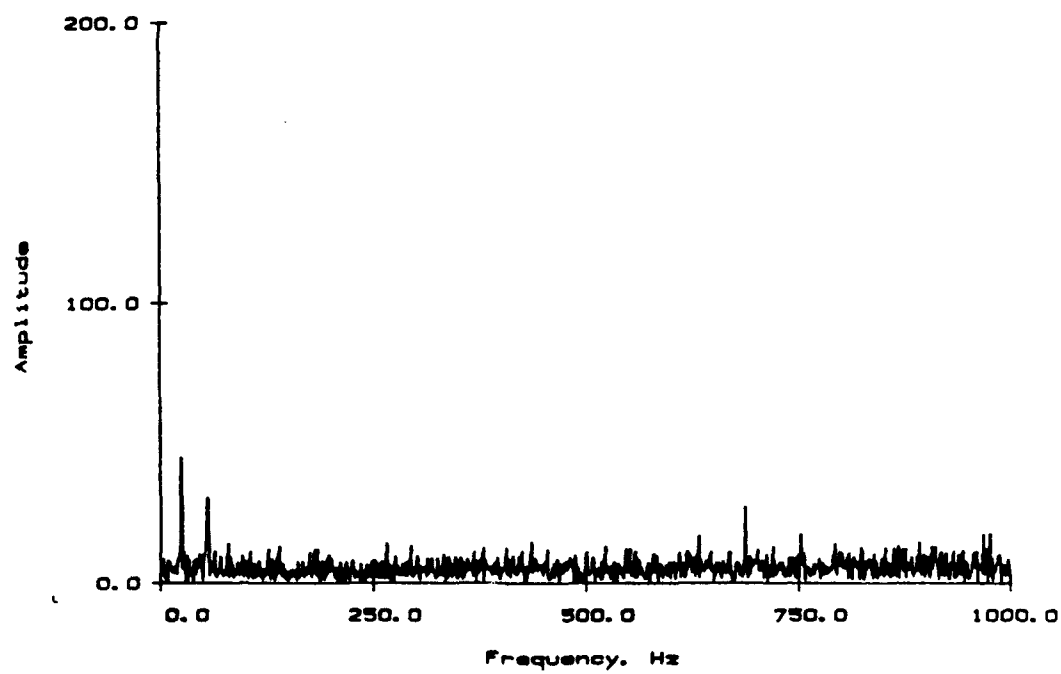
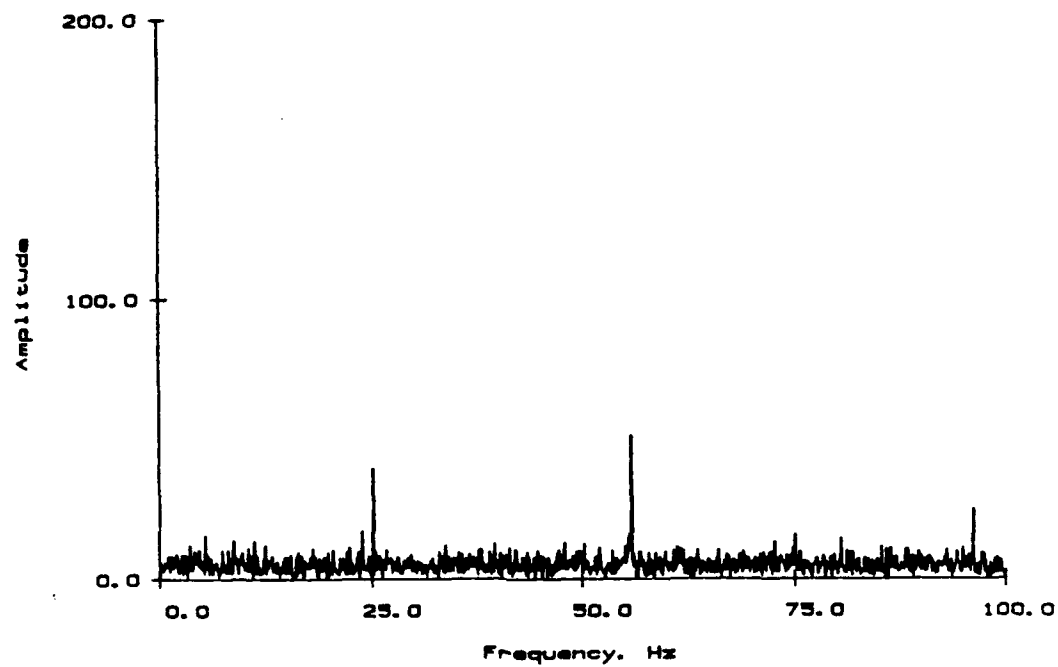


Figure 5.61 Fourier Analysis of Unsteady Pressure Signal - Mode 1
(Microphone 3)

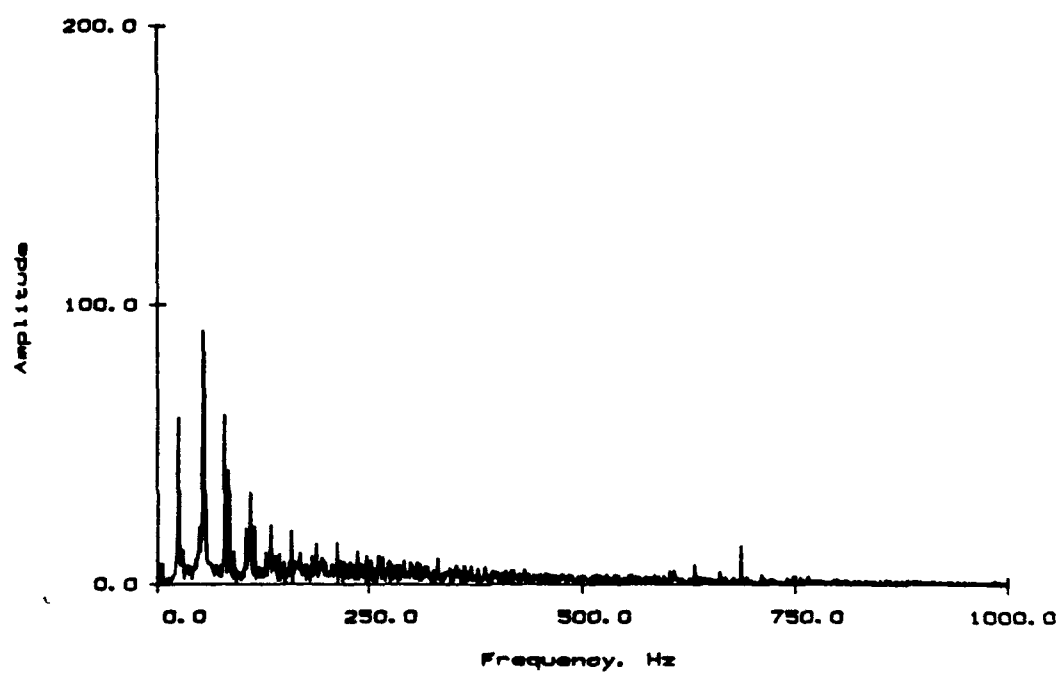
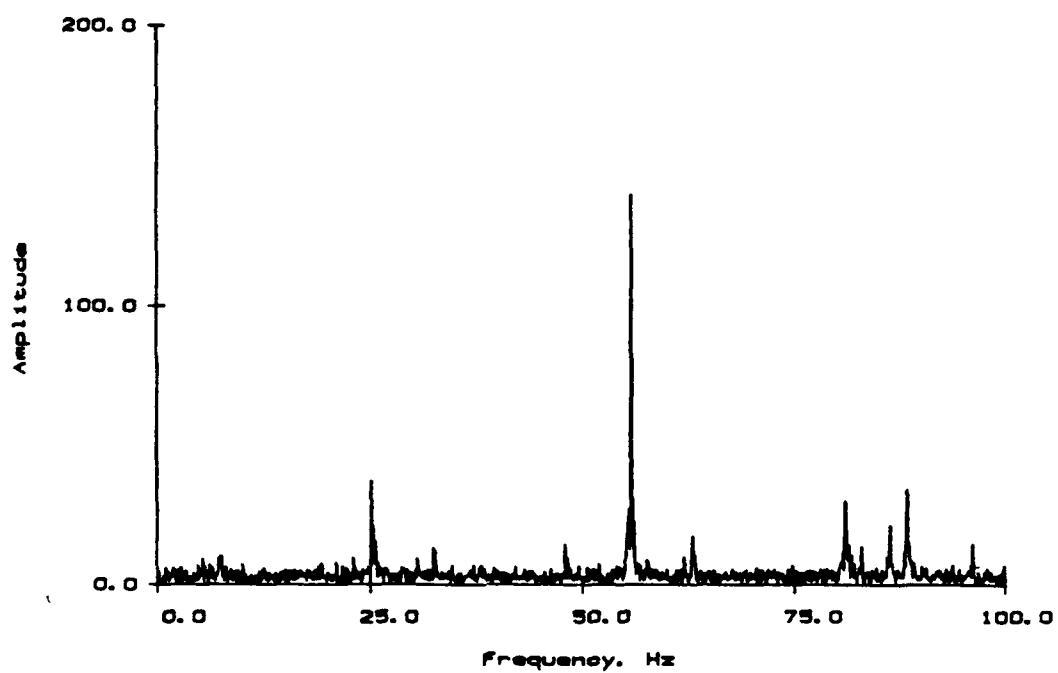


Figure 5.62 Fourier Analysis of Unsteady Pressure Signal - Mode 1
(Microphone 4)

Analysis of the phase information from the microphones indicates that the harmonic content at 55.8 Hz is attributable to a stall pattern with two symmetric cells rotating at 27.9 Hz. The content at 25.2 Hz is a single cell pattern with that rotational frequency. After transforming to a rotating frame of reference stationary on the impeller, the two cell pattern is found to rotate at 2 Hz and the single cell pattern at 4.7 Hz, both opposite to the direction of the impeller rotation.

5.2.4 Mode 2 Rotating Stall

Reducing the mass flow below 2.00 kg/s (4.40 lbm/s) results in the stall eventually shifting to a more stable mode, Mode 2, which exists from 2.00 to 1.72 kg/s (4.40 to 3.80 lbm/s). It is characterized by a single stable stall pattern with strong harmonic content. The data presented were taken at a mass flow rate of 1.90 kg/s (4.19 lbm/s).

The unfiltered and filtered time history for the signals from Microphones 3 and 4 are presented in Figures 5.63 and 5.64, respectively. The data from Microphone 3 indicate a distinct pattern, with a pressure peak lasting approximately 25% of the period of the pattern. The harmonic analysis of the data from the microphones is given in Figures 5.65 and 5.66. Data from the Microphone 3 have strong content at the fundamental frequency of 4.4 Hz and its first five harmonics. Data from Microphone 4 show content at 4.4 Hz, but none of the higher harmonics. Harmonic content at 96 Hz is very weak. The phase information indicates a single stall pattern rotating at 4.4 Hz. After transforming to the rotating frame of reference, the pattern is found to rotate at 25.5 Hz opposite to the impeller rotation direction.

5.2.5 Mode 3 Rotating Stall

Reducing the mass flow below 1.72 kg/s (3.80 lbm/s) results in the third mode of rotating stall. Although the transition is abrupt, there is a region near 1.72 kg/s (3.80 lbm/s) where the stall oscillates between Modes 2 and 3. The third mode is also characterized by a single stable pattern with strong harmonic content. The data presented were taken at a mass flow rate of 1.63 kg/s (3.59 lbm/s).

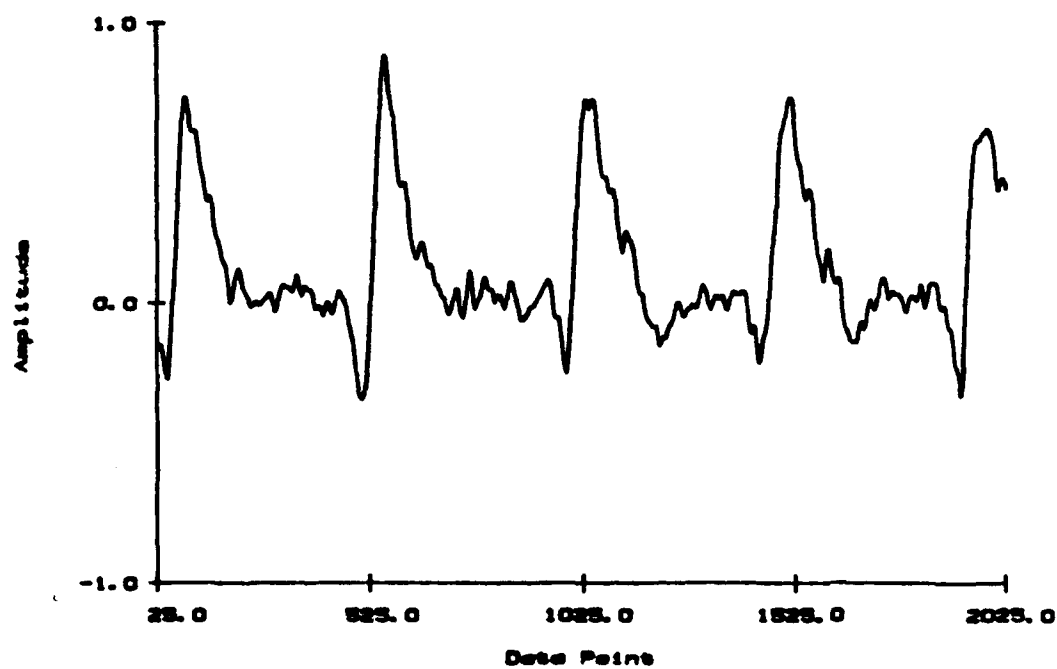
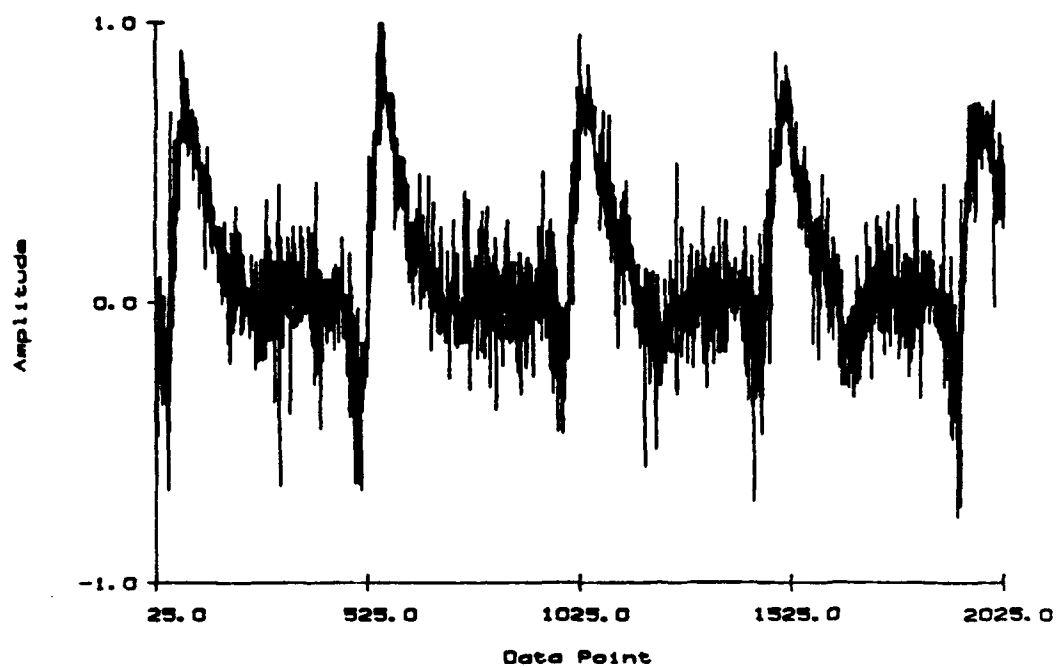


Figure 5.63 Unfiltered and Filtered Unsteady Pressure Signal - Mode 2 (Microphone 3)

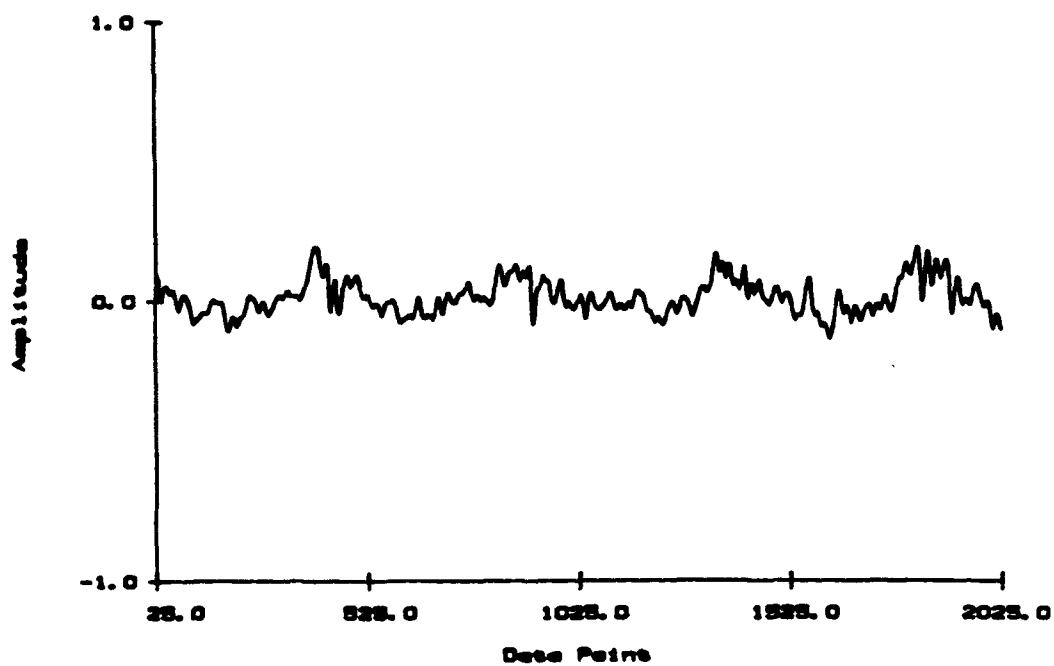
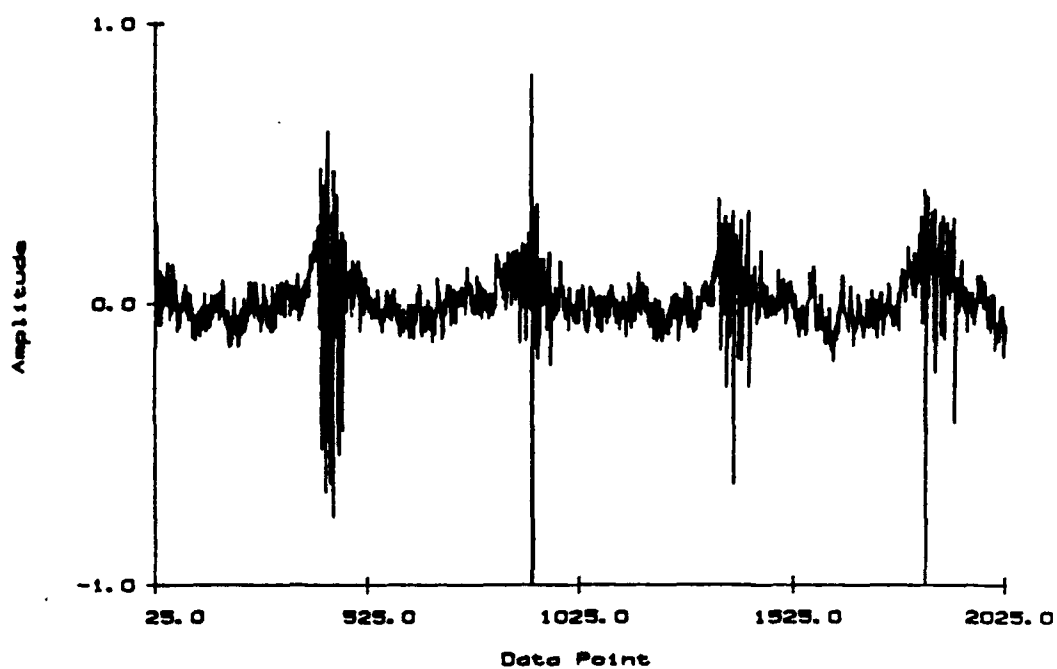


Figure 5.64 Unfiltered and Filtered Unsteady Pressure Signal - Mode 2
(Microphone 4)

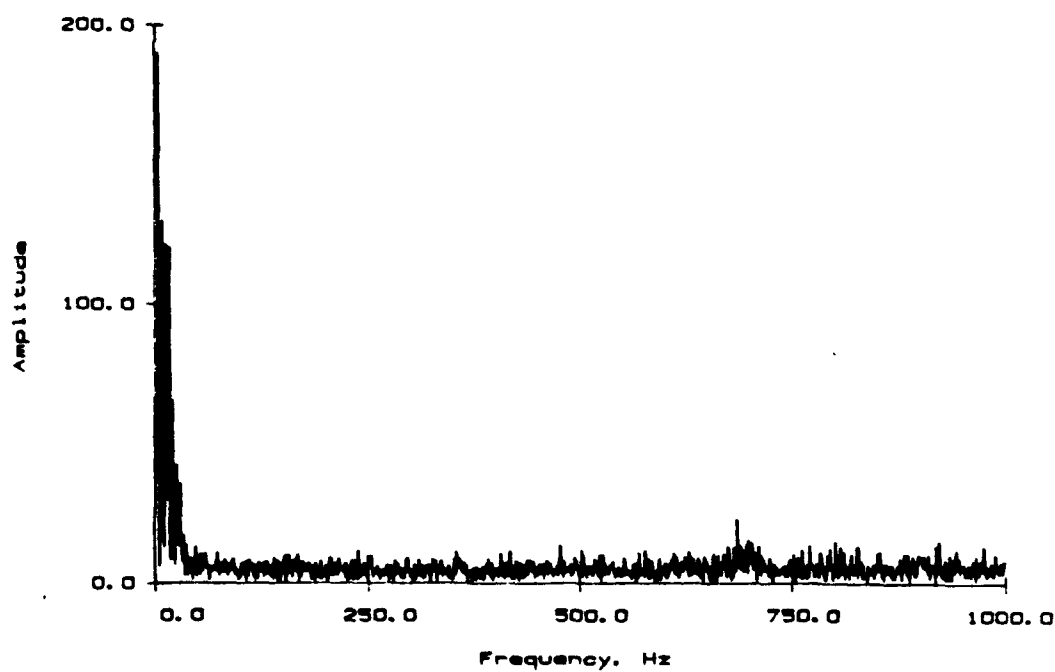
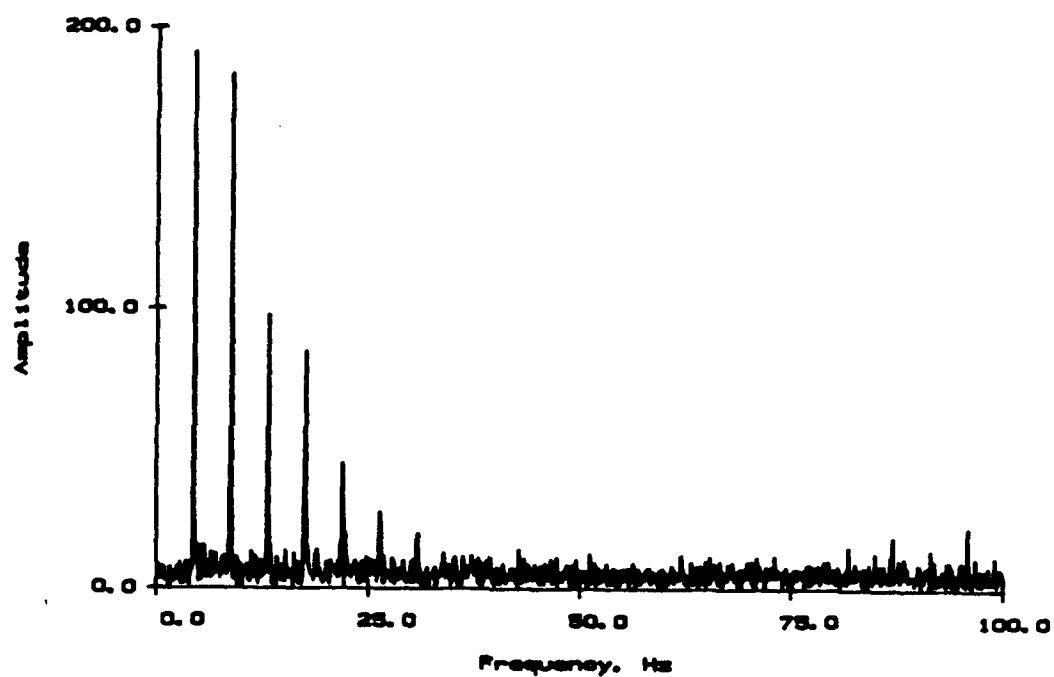


Figure 5.65 Fourier Analysis of Unsteady Pressure Signal - Mode 2
(Microphone 3)

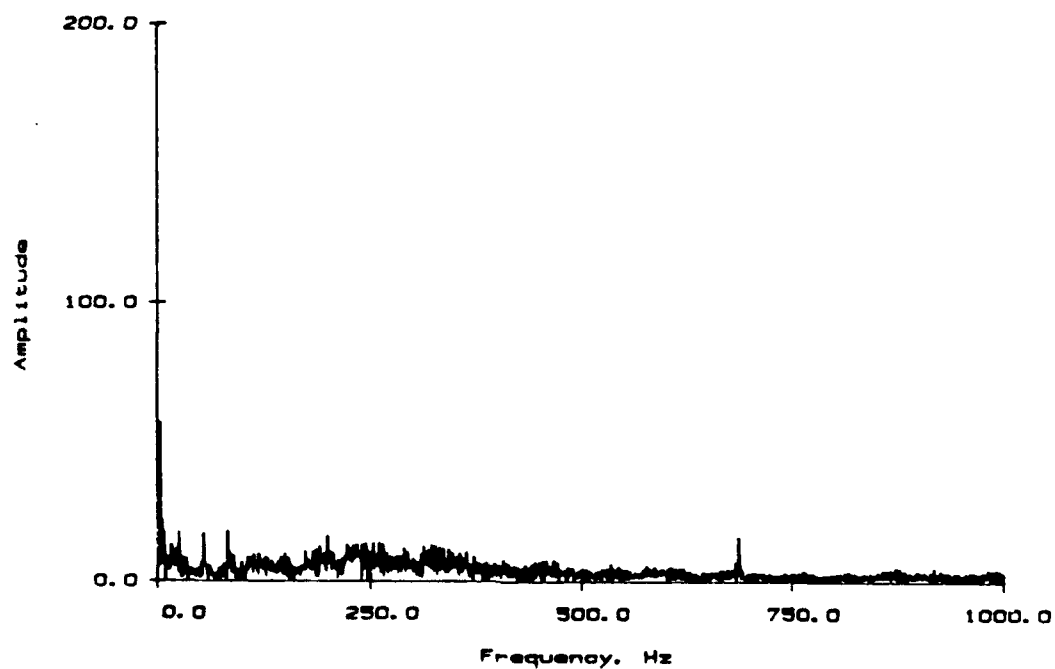
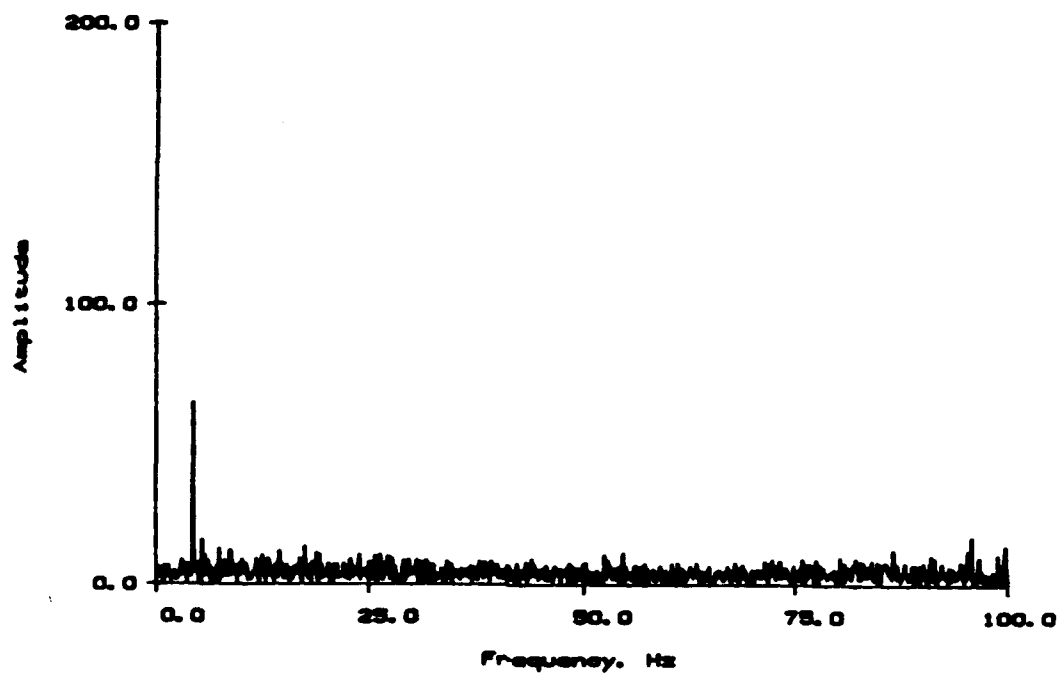


Figure 5.66 Fourier Analysis of Unsteady Pressure Signal - Mode 2
(Microphone 4)

The unfiltered and filtered time history for the signals from Microphones 3 and 4 are presented in Figures 5.67 and 5.68, respectively. The harmonic analysis of these data is given in Figures 5.69 and 5.70. Data from Microphone 3 show a strong content at the fundamental frequency of 7.7 Hz and the first two harmonics. Data from Microphone 4 show content at 23.2 Hz, the second harmonic. The harmonic content at 96 Hz is very weak. The phase information indicates a single pattern with two stall cells rotating at 3.9 Hz. This corresponds to a pattern rotating at 26.0 Hz in the rotating frame of reference opposite to the impeller rotation.

5.2.6 Discussion

Rotating stall in the Purdue Research Centrifugal Compressor is characterized by three distinct modes depending upon the mass flow rate. The first mode abruptly appears as the mass flow rate is reduced from the normal operating range of the compressor and is characterized by two concurrently rotating stall patterns both with relative rotational speeds below 15% of the impeller rotational speed. This mode is the least stable of the three, existing over only a narrow range of mass flow rate, with the amplitude of the two patterns fluctuating severely. Comparison of the unsteady pressure signals at the impeller inlet and the diffuser inlet indicates the stall patterns are strongest at the impeller inlet.

The other two rotating stall modes occur at reduced mass flow rates and are characterized by single rotating patterns. The structure of the patterns is observed both in the time history and the harmonic analysis of the unsteady pressure signals. Both modes appear to be quite stable, existing over a wide range of mass flow rate. The patterns in both modes rotate with relative speeds exceeding 90% of the impeller rotational speed, with the patterns strongest at the diffuser inlet.

Comparison of these results to other data found in the literature is difficult. This is a result of the large variation in geometry for machines defined as centrifugal compressors. Two features of the impeller in the Purdue Research Centrifugal Compressor make it unique compared to most other centrifugal compressors used for the study of rotating stall. The impeller is shrouded and it is a mixed-flow design.

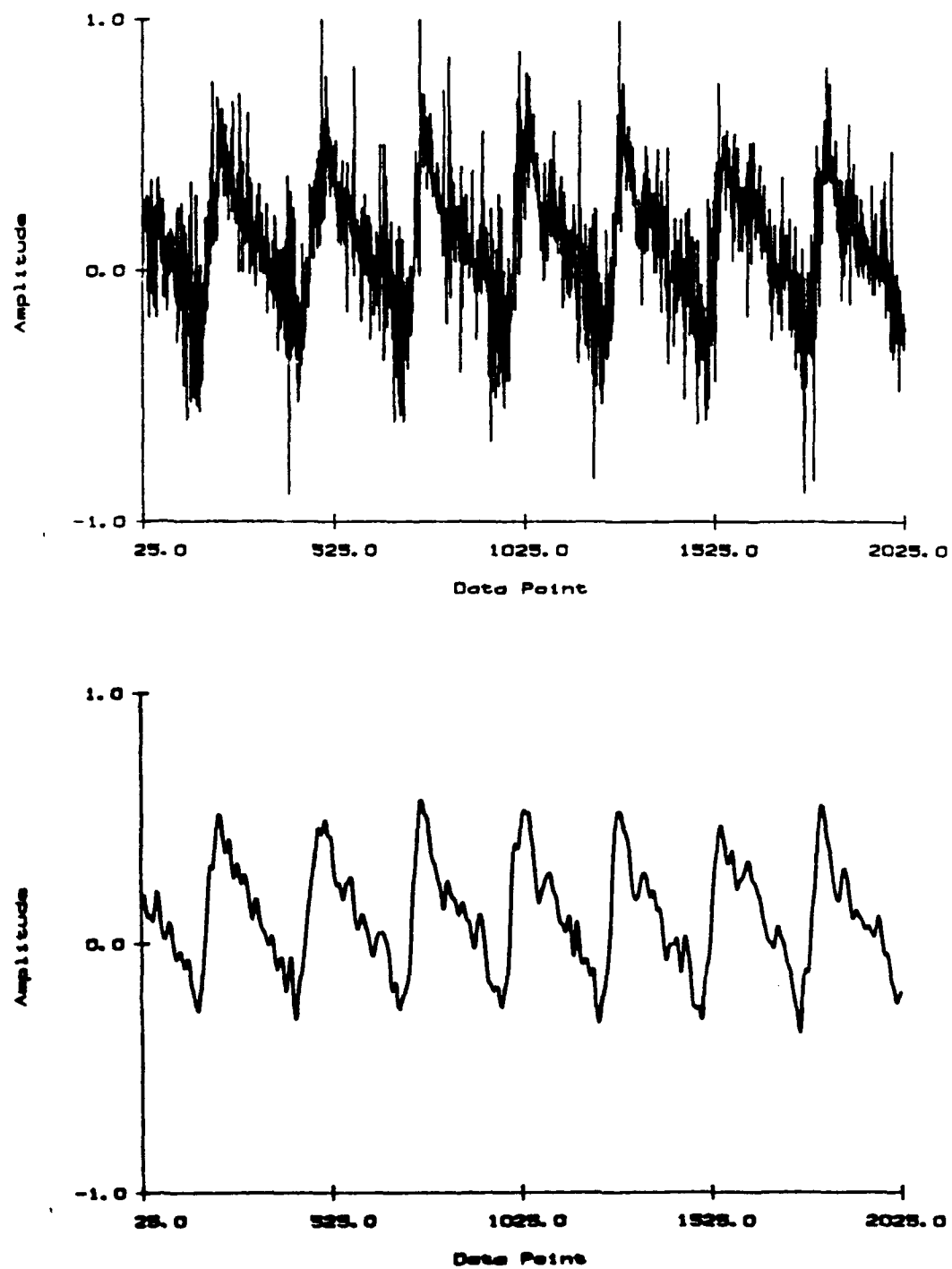


Figure 5.67 Unfiltered and Filtered Unsteady Pressure Signal - Mode 3 (Microphone 3)

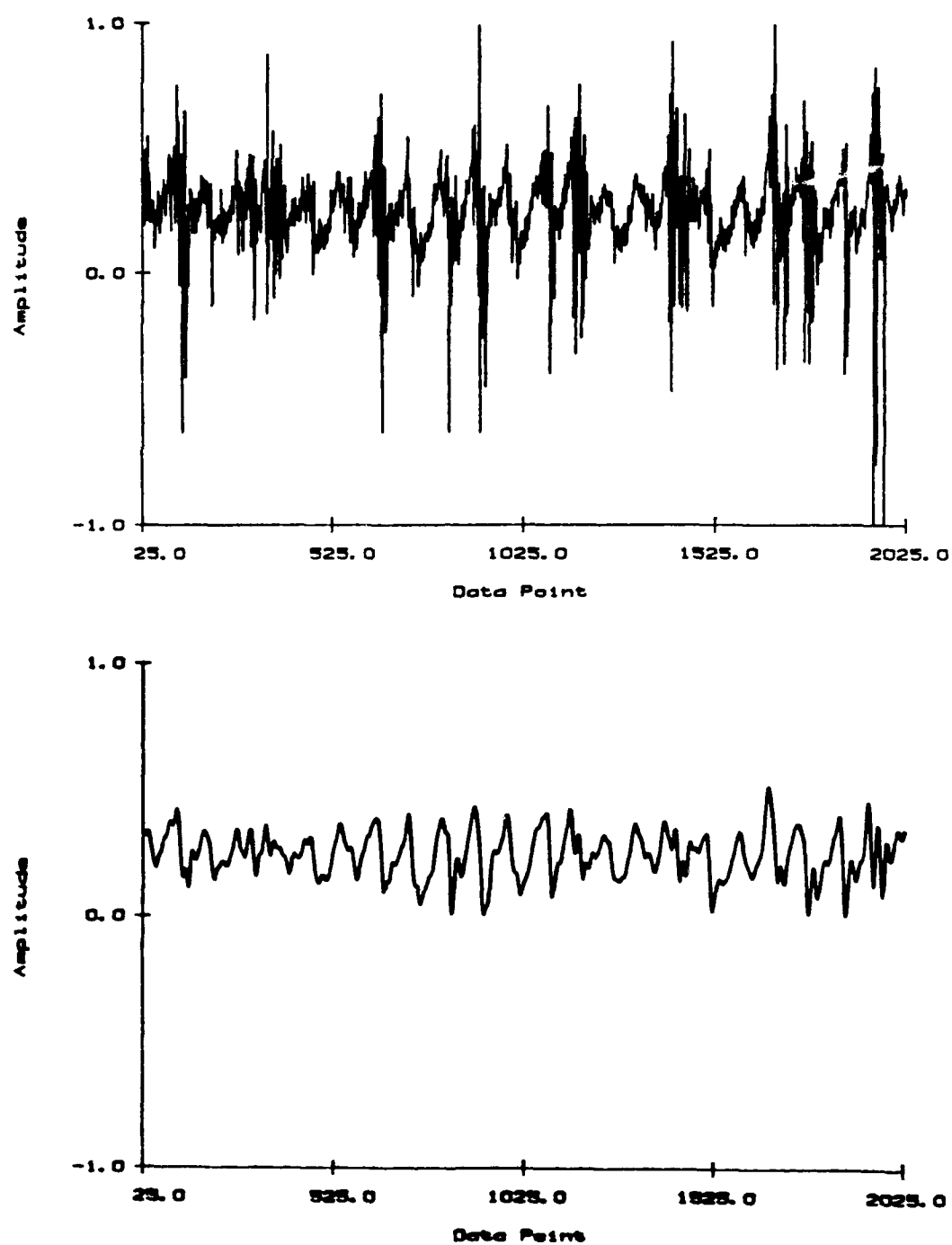


Figure 5.68 Unfiltered and Filtered Unsteady Pressure Signal - Mode 3 (Microphone 4)

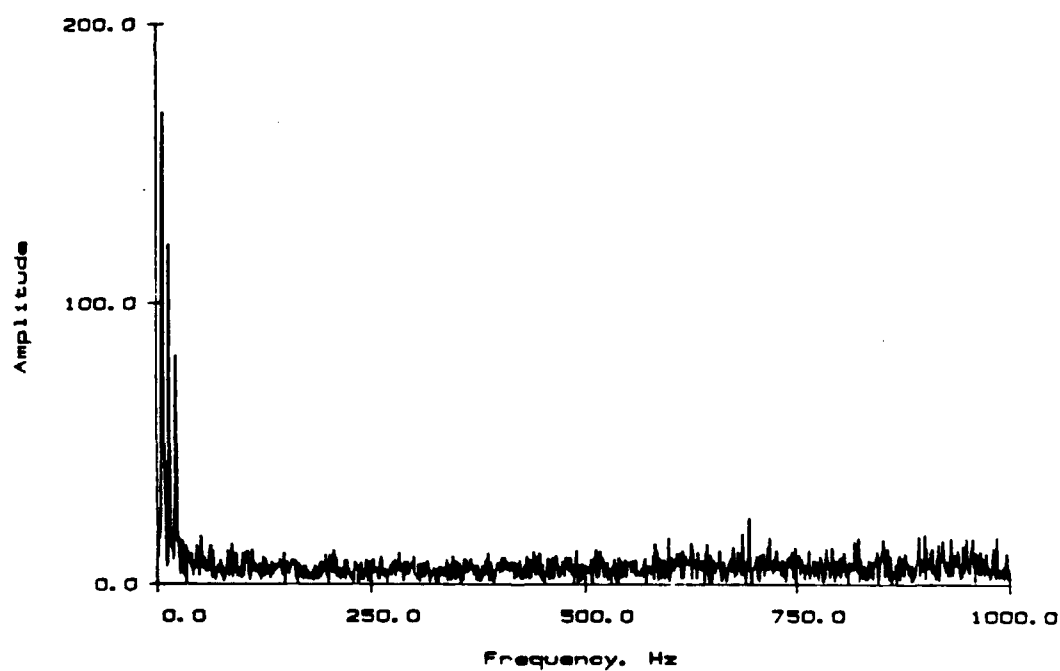
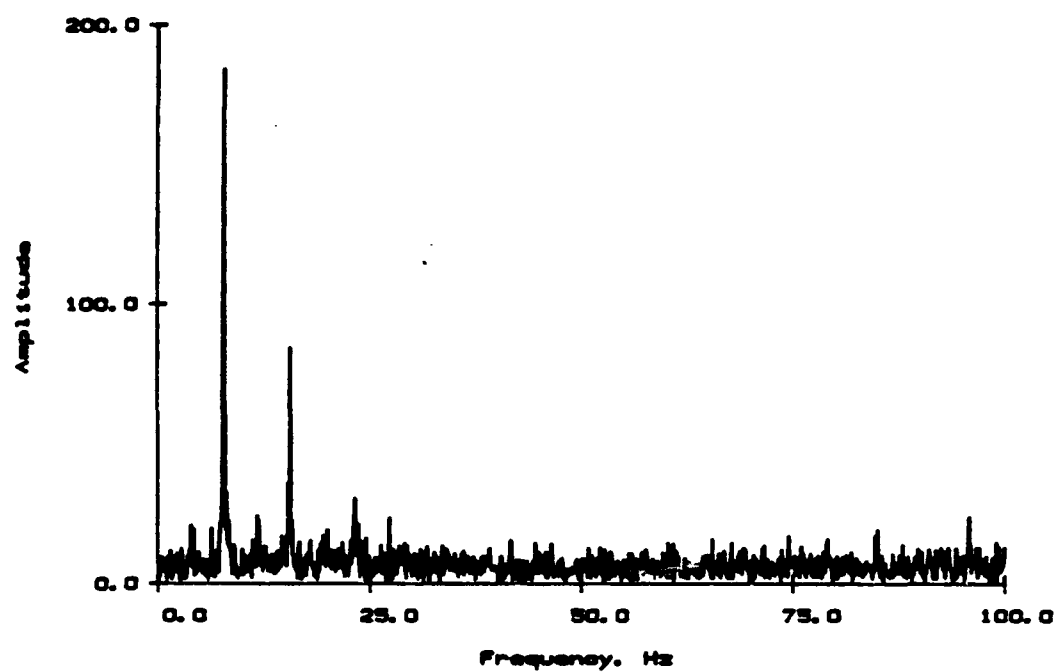


Figure 5.69 Fourier Analysis of Unsteady Pressure Signal - Mode 3
(Microphone 3)

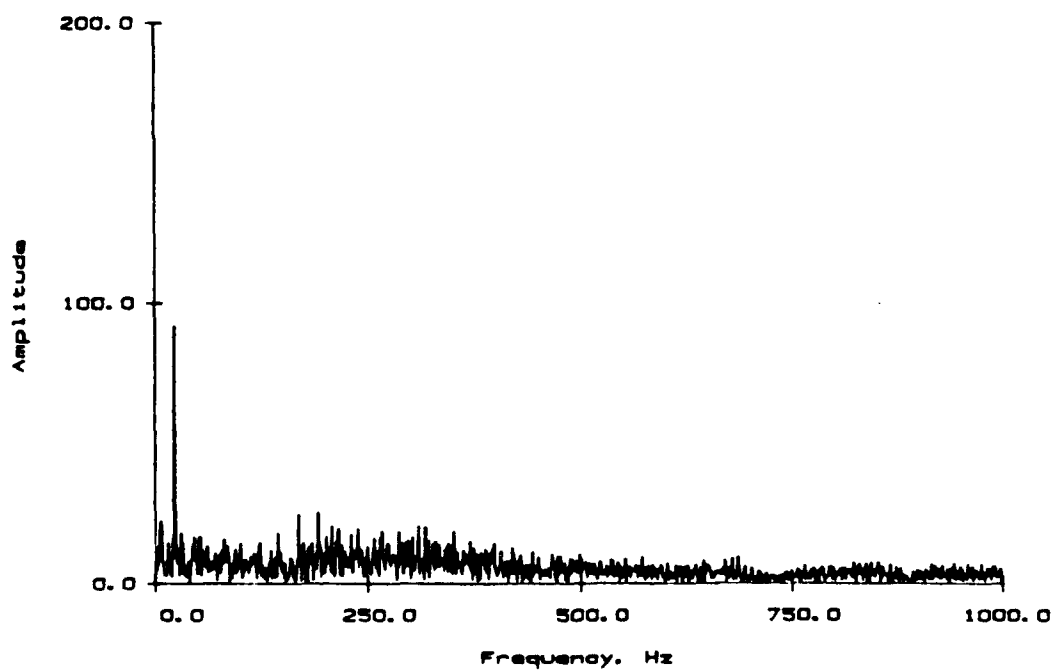
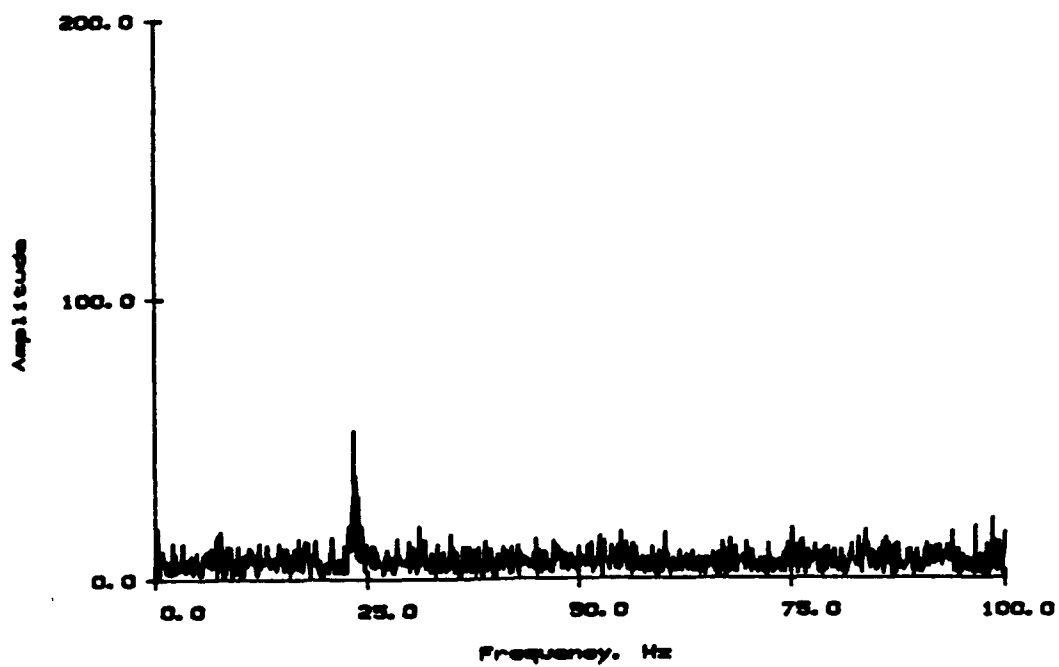


Figure 5.70 Fourier Analysis of Unsteady Pressure Signal - Mode 3
(Microphone 4)

The shroud prevents tip leakage which should have a strong influence on rotating stall. For example, the results of Haupt, Chen, and Rautenberg [11] indicated the stall cell in their compressor is strongest near the shroud on the blade suction surface. They also found the fluid originated from the pressure side of the same blade. If this is a general characteristic of rotating stall in an impeller passage, tip leakage should stabilize the flow. Additionally, the nature of the stall cell in a shrouded impeller could differ significantly from that in an unshrouded impeller.

The mixed-flow impeller design introduces significant difficulties in the modeling of rotating stall. The models developed to date primarily perform a stability analysis for a rotating wave in a vaneless diffuser. An essential feature of developing a tractable solution in these models is the assumption of two-dimensional flow in the diffuser. While this assumption is not accurate even in a radial outflow impeller, there are more serious limitations for a mixed-flow impeller.

Several analogies can still be drawn to the data acquired herein and that reported in the literature. One conclusion, drawn by several researchers, is that rotating stall observable at the inlet and the exit of the impeller is impeller, rather than diffuser, rotating stall. This would indicate that all three stall modes in the Purdue Research Centrifugal Compressor are impeller rotating stall.

Frigne and Van Den Braembussche [10] did extensive work in attempting to characterize various types of rotating stall. Assuming their conventions concerning the relative rotational speed of the stall pattern, Mode 1 would be "mild" impeller rotating stall and Modes 2 and 3 would be "progressive" impeller rotating stall. However, there are inconsistencies with both of these classifications. "Mild" rotating stall is characterized by a large number of stall cells (approximately four) with no harmonic content, which contradicts the results from this research. Additionally, there is no mention of multiple patterns rotating concurrently. "Progressive" impeller rotating stall is characterized by a single cell stall pattern with significant harmonic content. Both Modes 2 and 3 contain significant content at the harmonics of the stall rotational frequency. However, Mode 2 has a two cell pattern. Furthermore, the trend that the relative rotational frequency of the stall pattern for "progressive" rotating stall decreases as the mass flow rate is reduced,

observed by Frigne and Van Dem Braembussche, is contradicted by these data. Finally, although the periodic pressure fluctuations attributed to the rotating stall cells in the Purdue Research Centrifugal Compressor are observable at both the inlet and exit of the impeller, the relative strengths at the two locations differ significantly between Mode 1 and Modes 2 and 3. It is evident the character of the stall is significantly different for the two cases.

5.3 Flow Field Predictions

An inviscid and a viscous model are used to predict the design operating point flow field in the Purdue Research Centrifugal Compressor. These predictions are presented in terms of the throughflow and secondary velocities, corresponding to the presentation of the experimental results.

5.3.1 Inviscid Model

The Denton model [23] was used to provide inviscid flow field predictions in the impeller at the compressor design operating point. The mass flow rate for the prediction is 3.47 kg/s (7.65 lbm/s), which is 4.1% higher than the nominal flow rate at which the experimental flow field measurements were made. The predictions are presented at Planes 1-5 (15%, 40%, 62%, 78%, and 88% passage), near to the location of the LDV measurement planes. Throughflow velocity results are given in Figures 5.71 through 5.75, with the secondary velocity vector results from the inlet to the exit of the impeller given in Figures 5.76 through 5.80.

Despite repeated attempts to vary the grid spacing and the leading edge cusp, smooth flow at the leading edge of the impeller blades could not be achieved. Consequently, the predictions of the flow field near the inlet of the impeller are very distorted. At Plane 1, the predictions indicate a large velocity gradient across the passage with a high velocity at the suction surface in the hub region and an inverse velocity gradient near the shroud. At Plane 2, the predicted velocity gradient across the passage is nearly constant from hub to shroud. The gradient is extremely large with the high velocity at the suction surface. The predictions indicate the throughflow velocity is

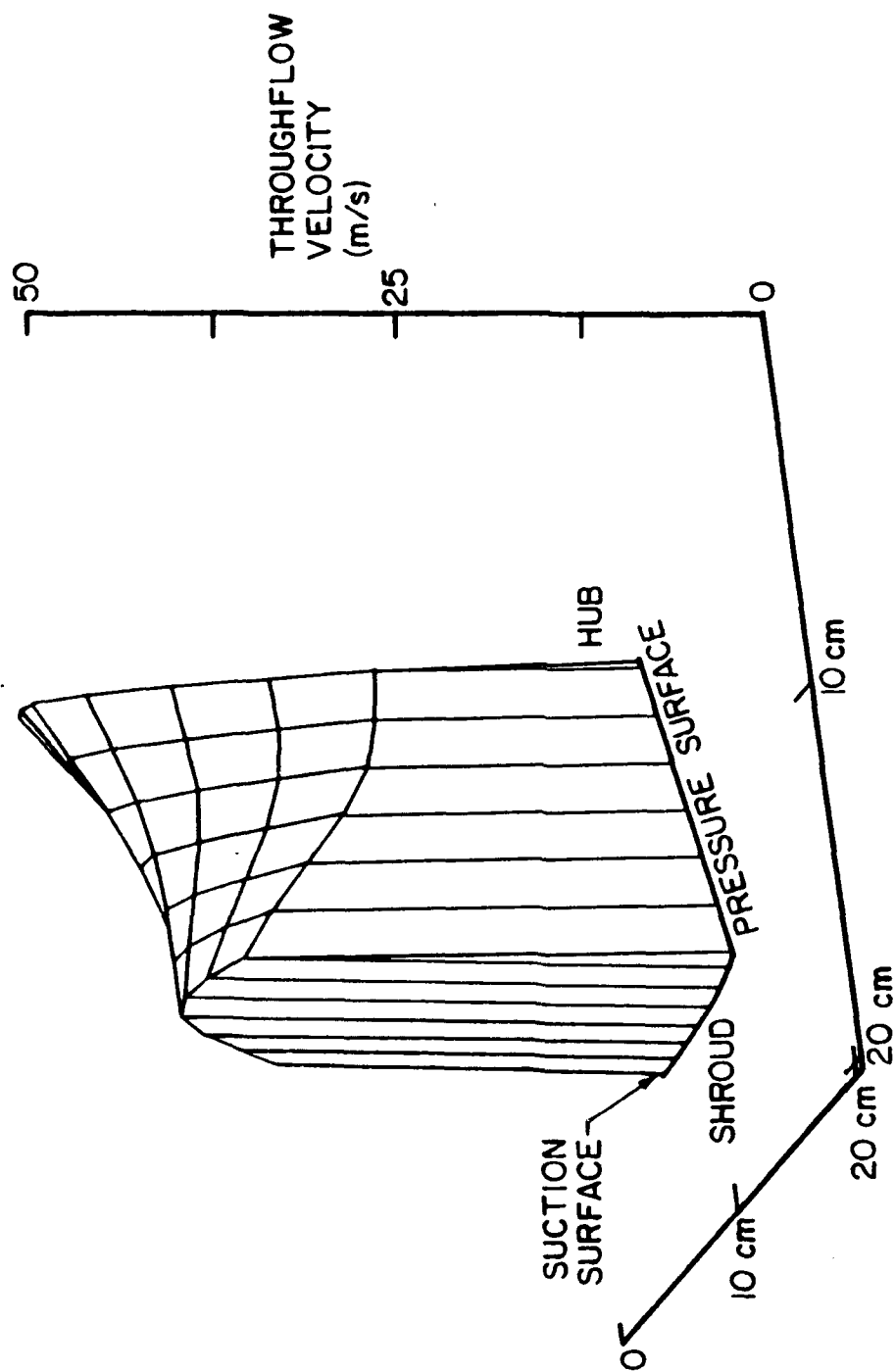


Figure 5.71 Throughflow Velocity Plot - Inviscid Prediction
Design Point - Plane 1

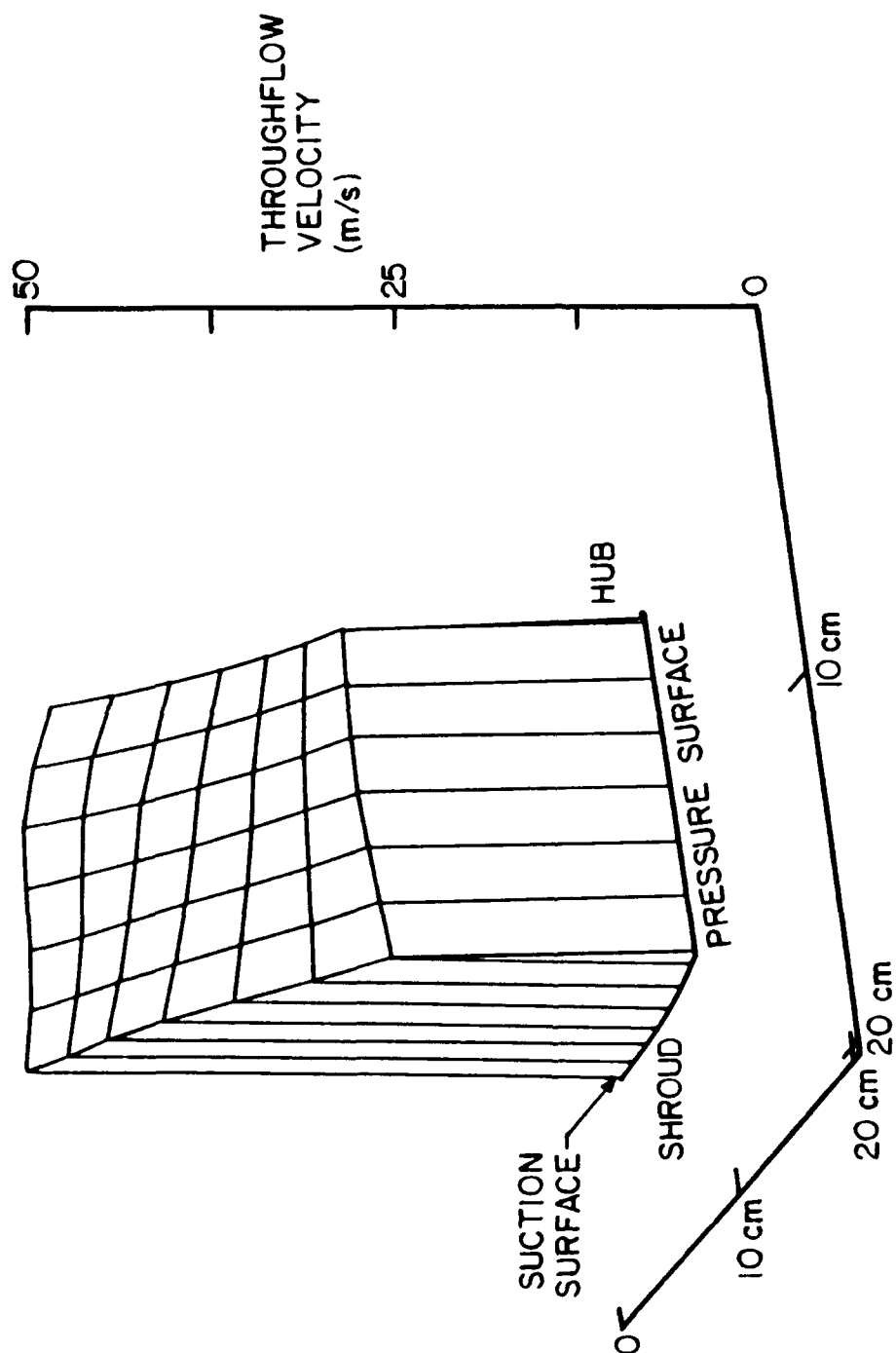


Figure 5.72 Throughflow Velocity Plot - Inviscid Prediction
Design Point - Plane 2

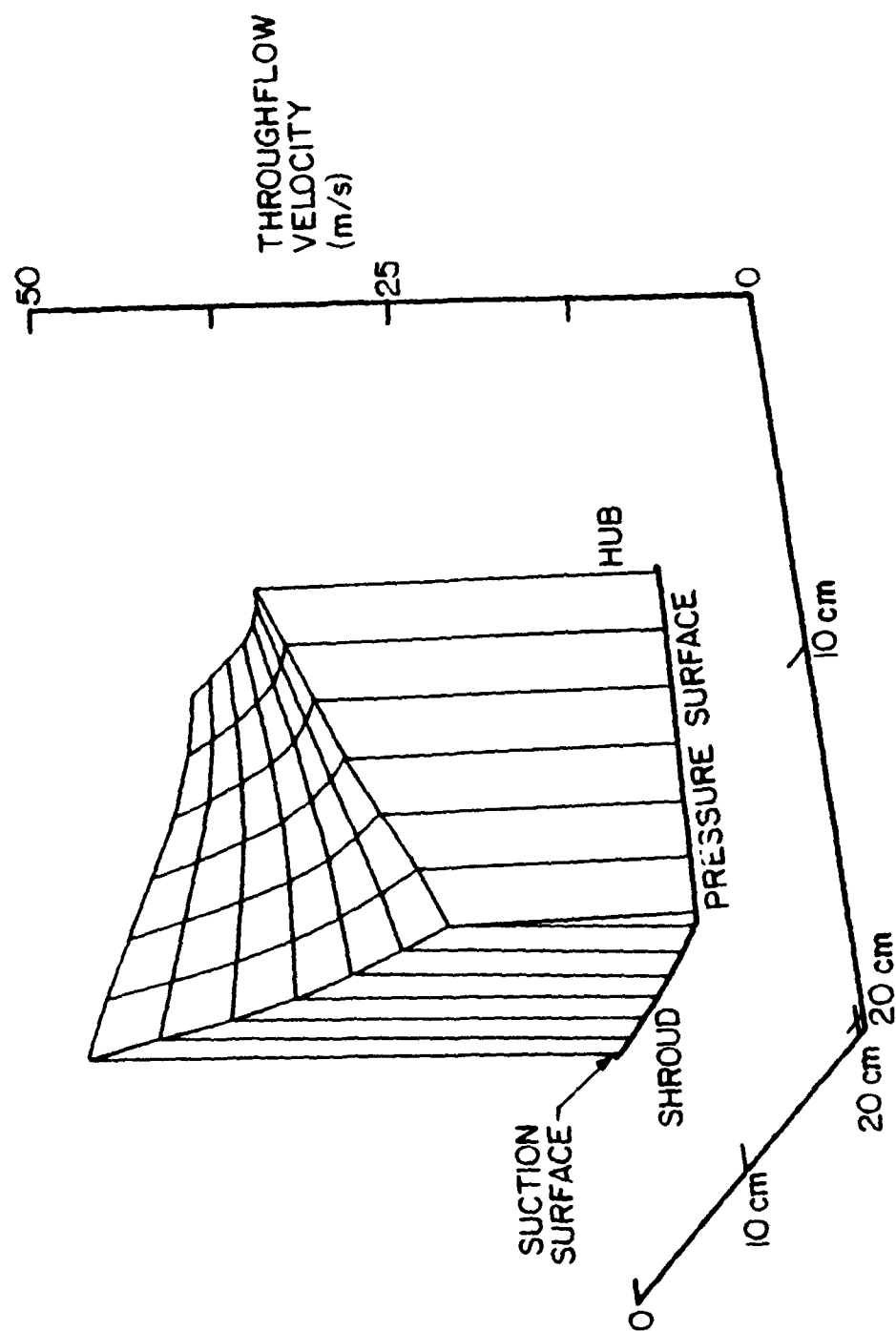


Figure 5.73 Throughflow Velocity Plot - Inviscid Prediction
Design Point - Plane 3

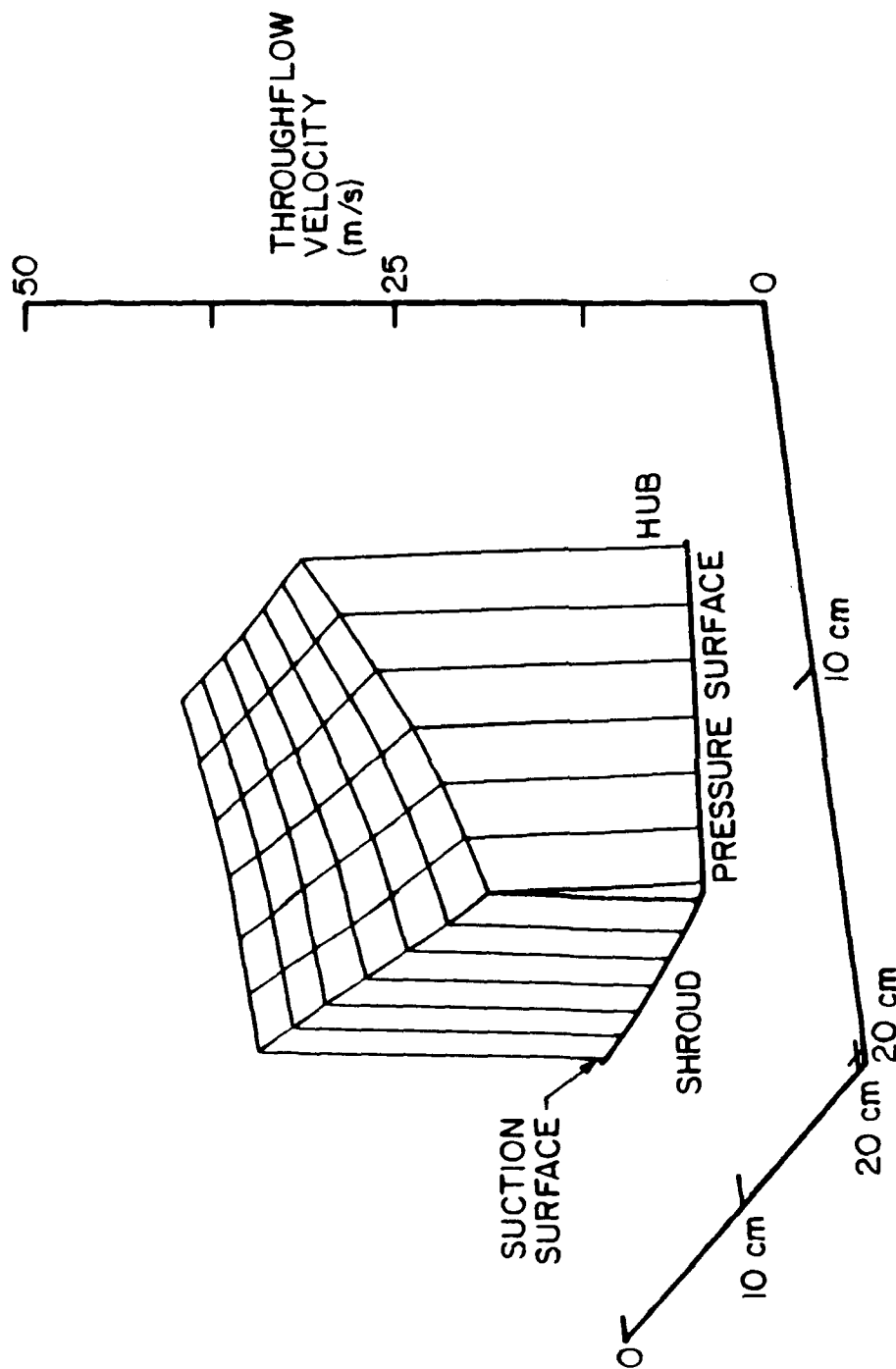


Figure 5.74 Throughflow Velocity Plot - Inviscid Prediction
Design Point - Plane 4

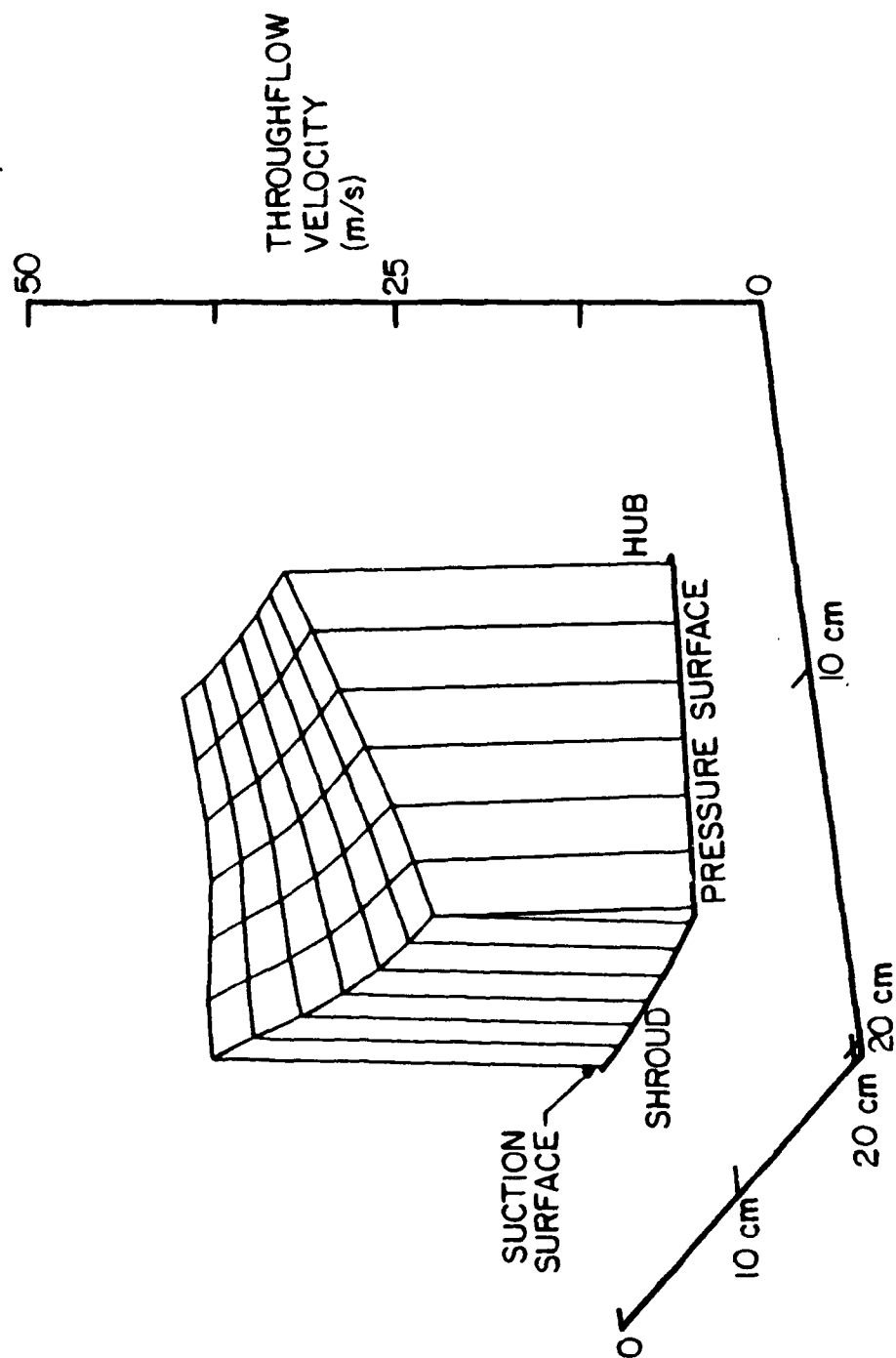


Figure 5.75 Throughflow Velocity Plot - Inviscid Prediction
Design Point - Plane 5

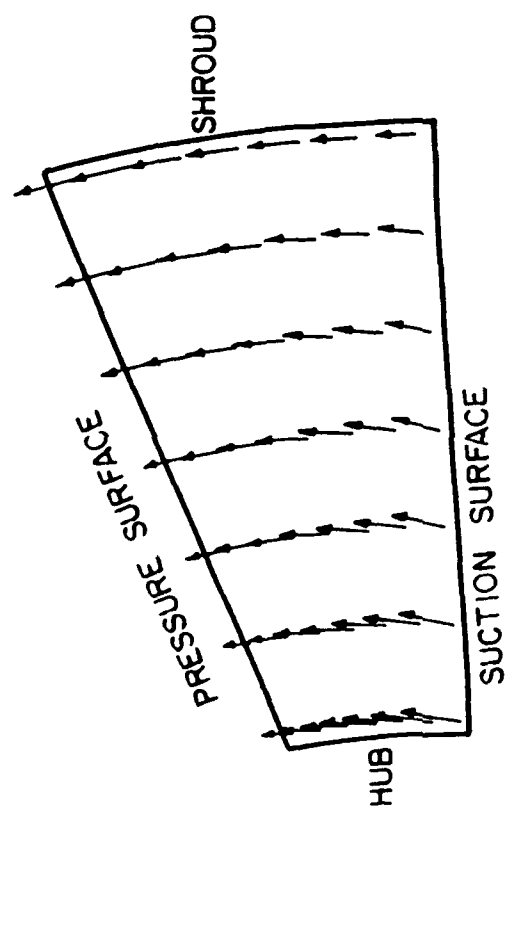


Figure 5.76 Secondary Velocity Vector Plot - Inviscid Prediction
Design Point - Plane 1

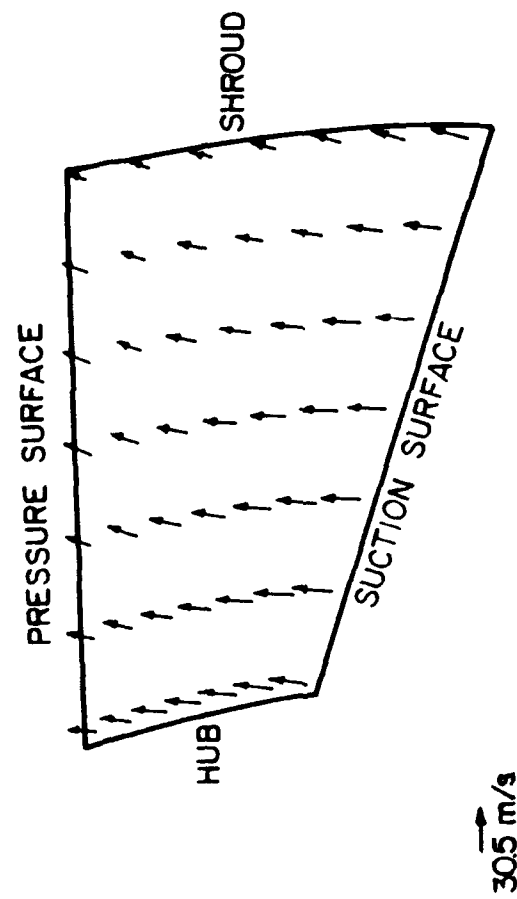


Figure 5.77 Secondary Velocity Vector Plot - Inviscid Prediction
Design Point - Plane 2

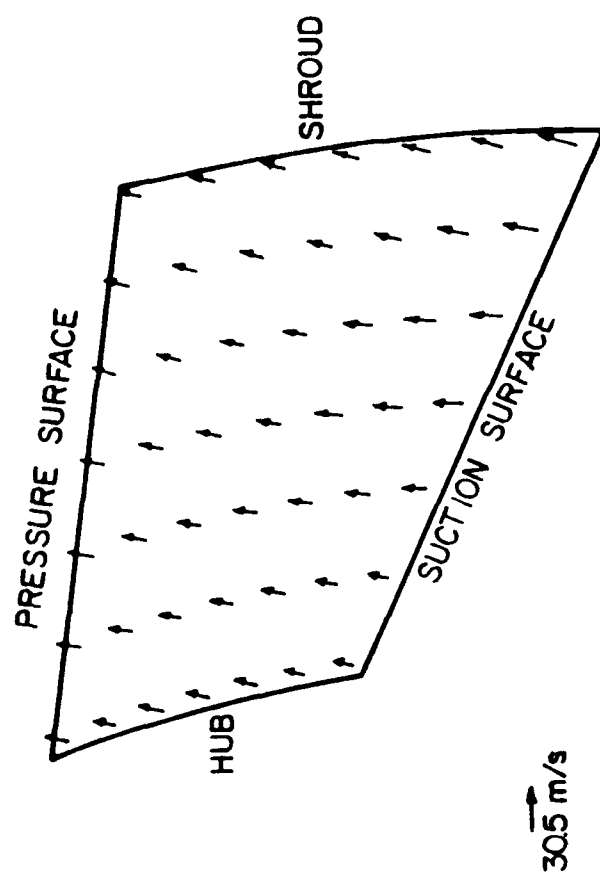


Figure 5.78 Secondary Velocity Vector Plot - Inviscid Prediction
Design Point - Plane 3

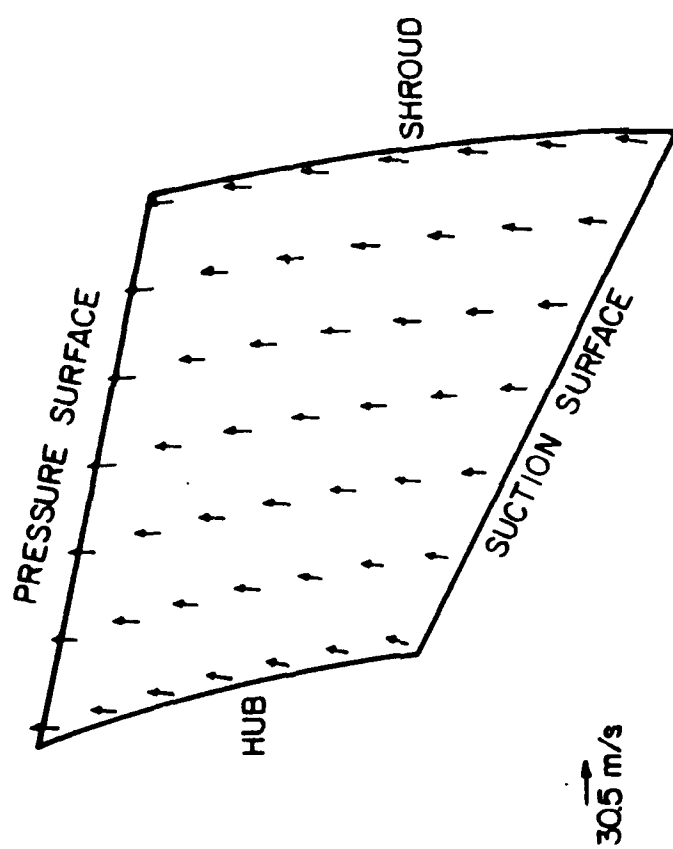


Figure 5.79 Secondary Velocity Vector Plot - Inviscid Prediction
Design Point - Plane 4

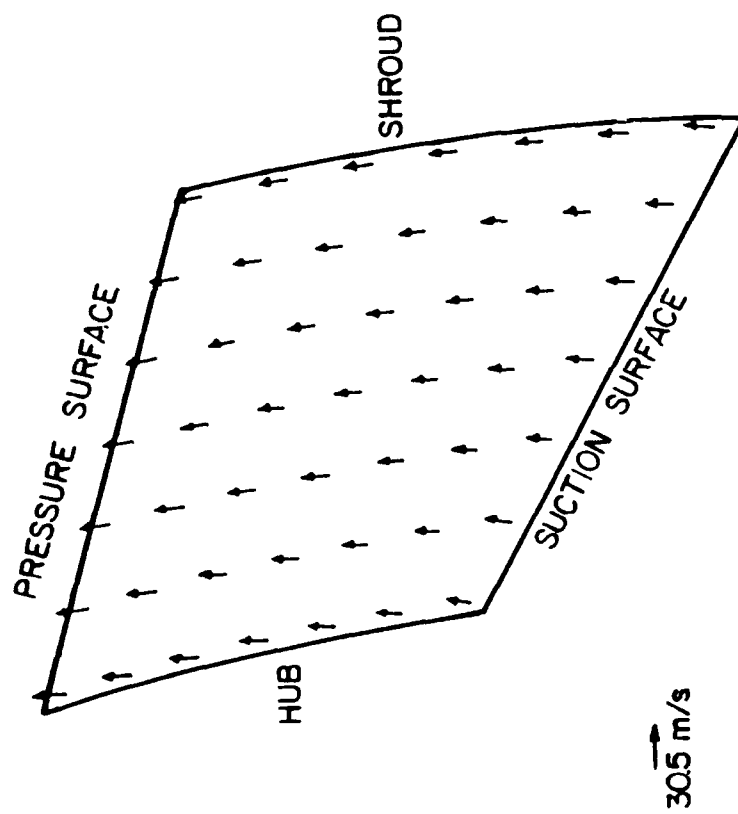


Figure 5.80 Secondary Velocity Vector Plot - Inviscid Prediction
Design Point - Plane 5

nearly constant across the passage at the hub, but still has a large slope near the shroud at Plane 3. At Plane 4, the velocity gradient is greatly reduced from hub to shroud. The predictions at Plane 5 indicate little change from the results at Plane 4.

The secondary velocity vector predictions indicate little of interest. At Planes 2 and 3, where the predicted throughflow velocity gradient is highest, the secondary velocity vector results indicate a velocity component in the hub to shroud direction oriented outwardly strongest near the shroud and pressure surfaces. There is no indication throughout the passage of separation or any strong vortical structure.

5.3.2 Viscous Model

Rhie's Impact code [24] was utilized to provide viscous flow field predictions in the impeller at the compressor design operating point. The mass flow rate is 3.40 kg/s (7.50 lbm/s), which is 2.0% higher than the nominal flow rate at which the experimental flow field measurements were made. The predictions are presented at Planes 1-5 (15%, 41%, 62%, 76%, and 88% passage), near the location of the LDV measurement planes. Throughflow velocity results are given in Figures 5.81 through 5.85 and secondary velocity vector results from the inlet to the exit of the impeller are given in Figures 5.86 through 5.90.

The throughflow velocity at Plane 1 passage indicates a smooth gradient from hub to shroud. The predicted velocity near the hub is slightly less than the velocity in the shroud region. At Plane 2, similar trends are indicated, with the addition of a predicted high velocity region near the shroud along the suction surface. The throughflow velocity prediction at Plane 3 indicates that the high velocity region extends over most of the passage height from hub to shroud. At Plane 4, a region of very low throughflow velocity is predicted at the shroud wall near the suction surface. The results at Plane 5 show reverse flow at the shroud suction corner.

Analysis of the secondary velocity results indicates some interesting characteristics. However, there appears to be no strong vortical structure. At Plane 1, the secondary flow is minimal. At Planes 2, 3, and 4, a significant velocity component in the hub to

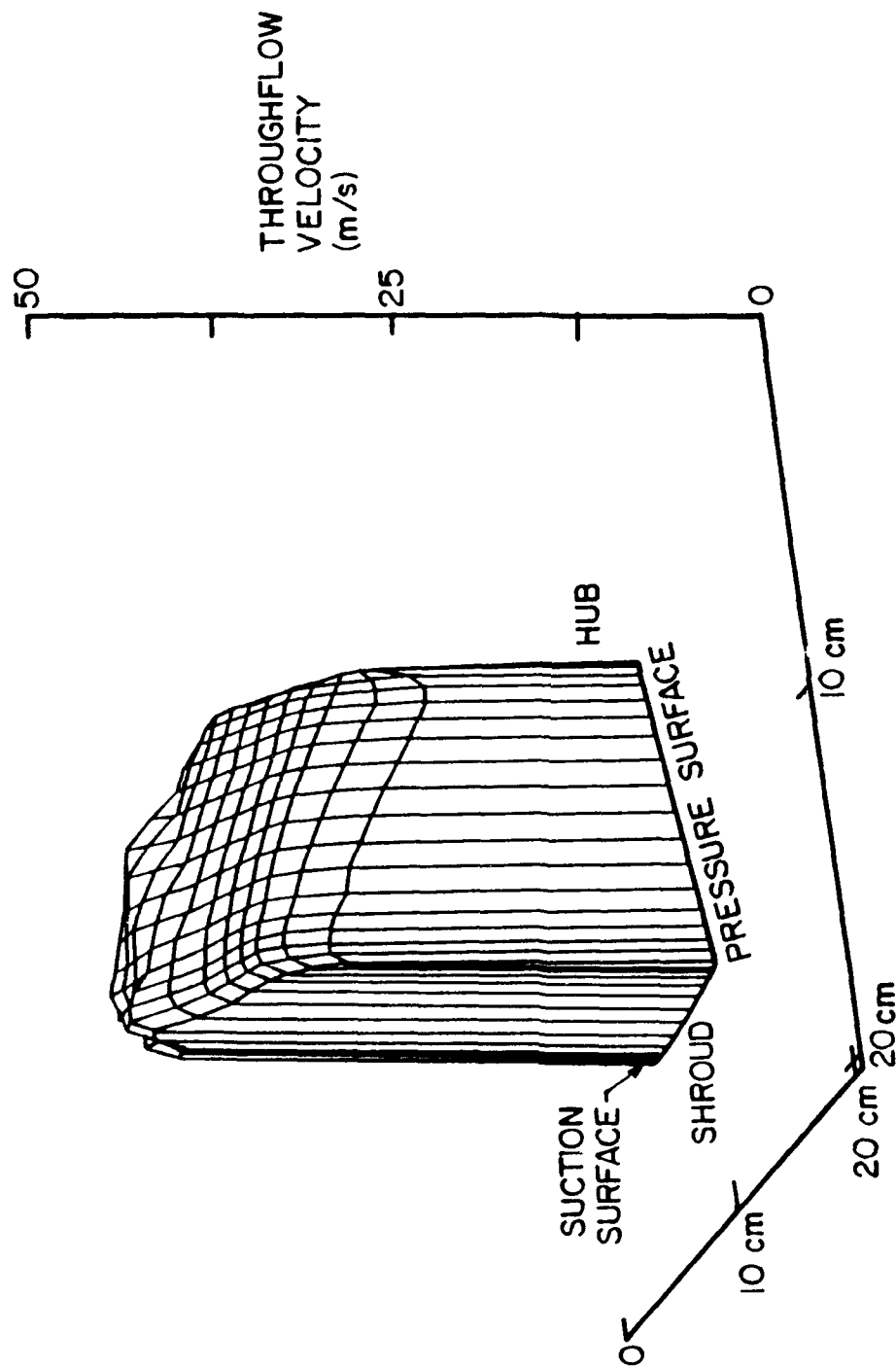


Figure 5.81 Throughflow Velocity Plot - Viscous Prediction
Design Point - Plane 1

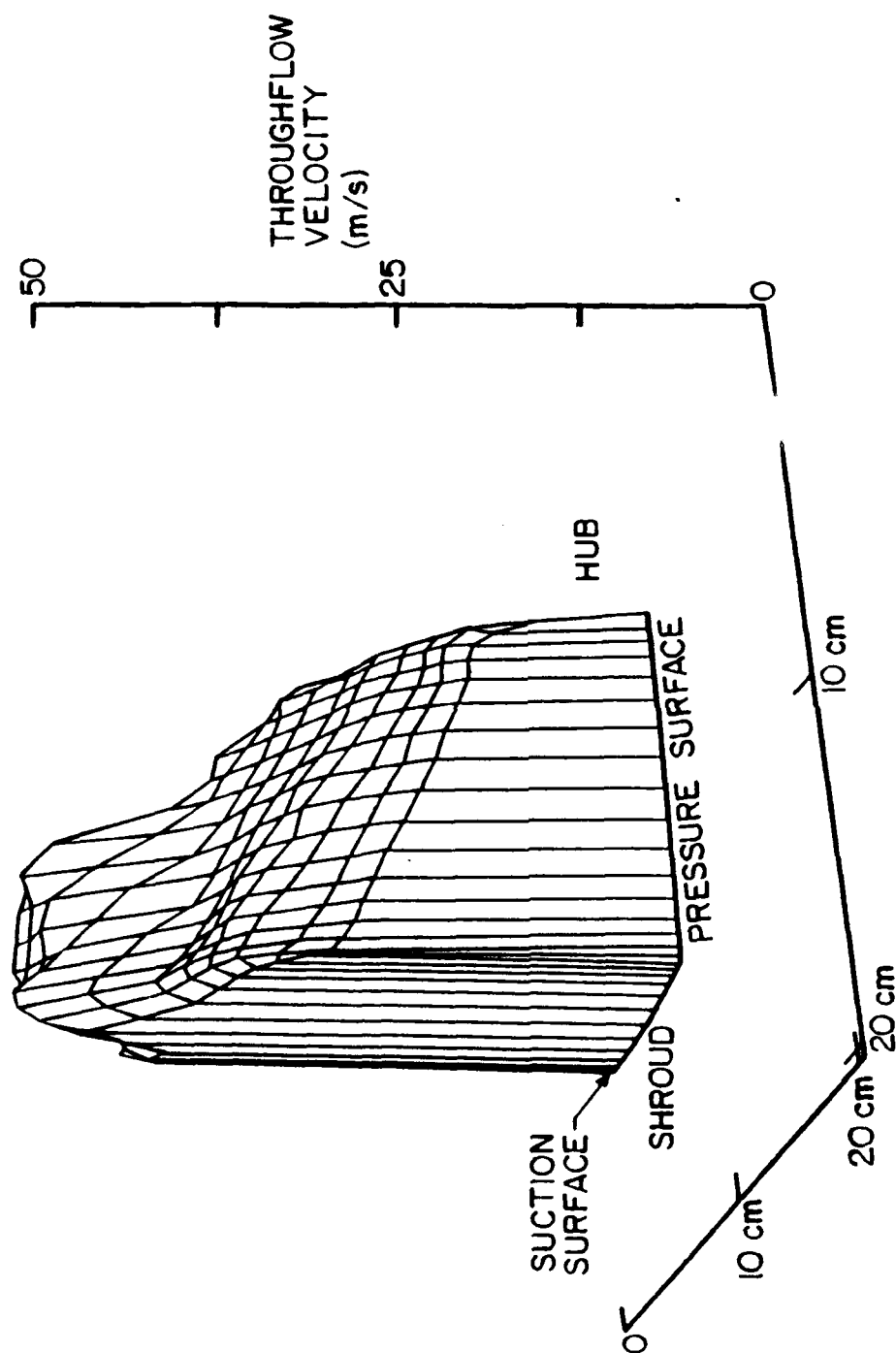


Figure 5.82 Throughflow Velocity Plot -- Viscous Prediction
Design Point - Plane 2

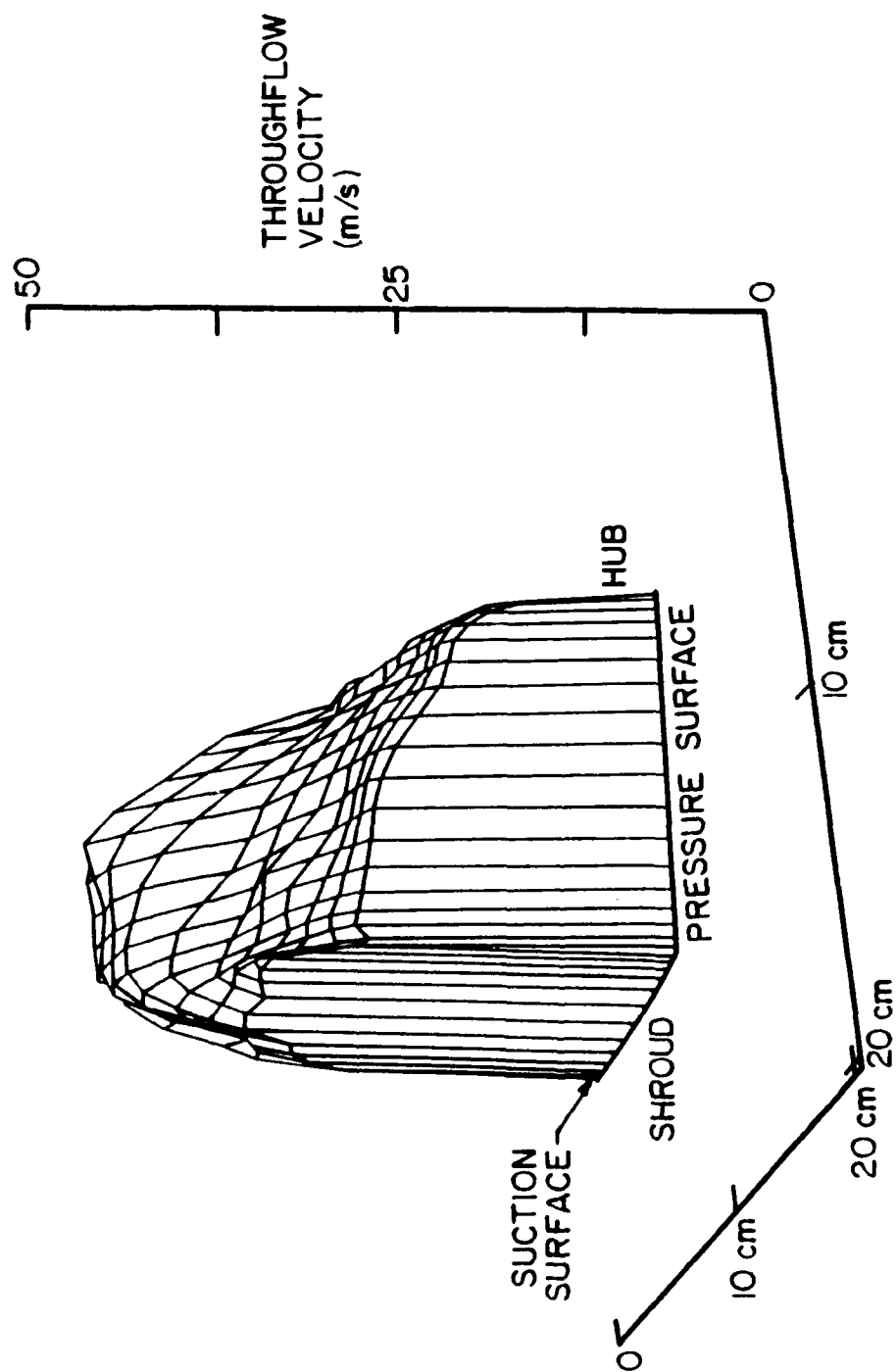


Figure 5.83 Throughflow Velocity Plot - Viscous Prediction
Design Point - Plane 3

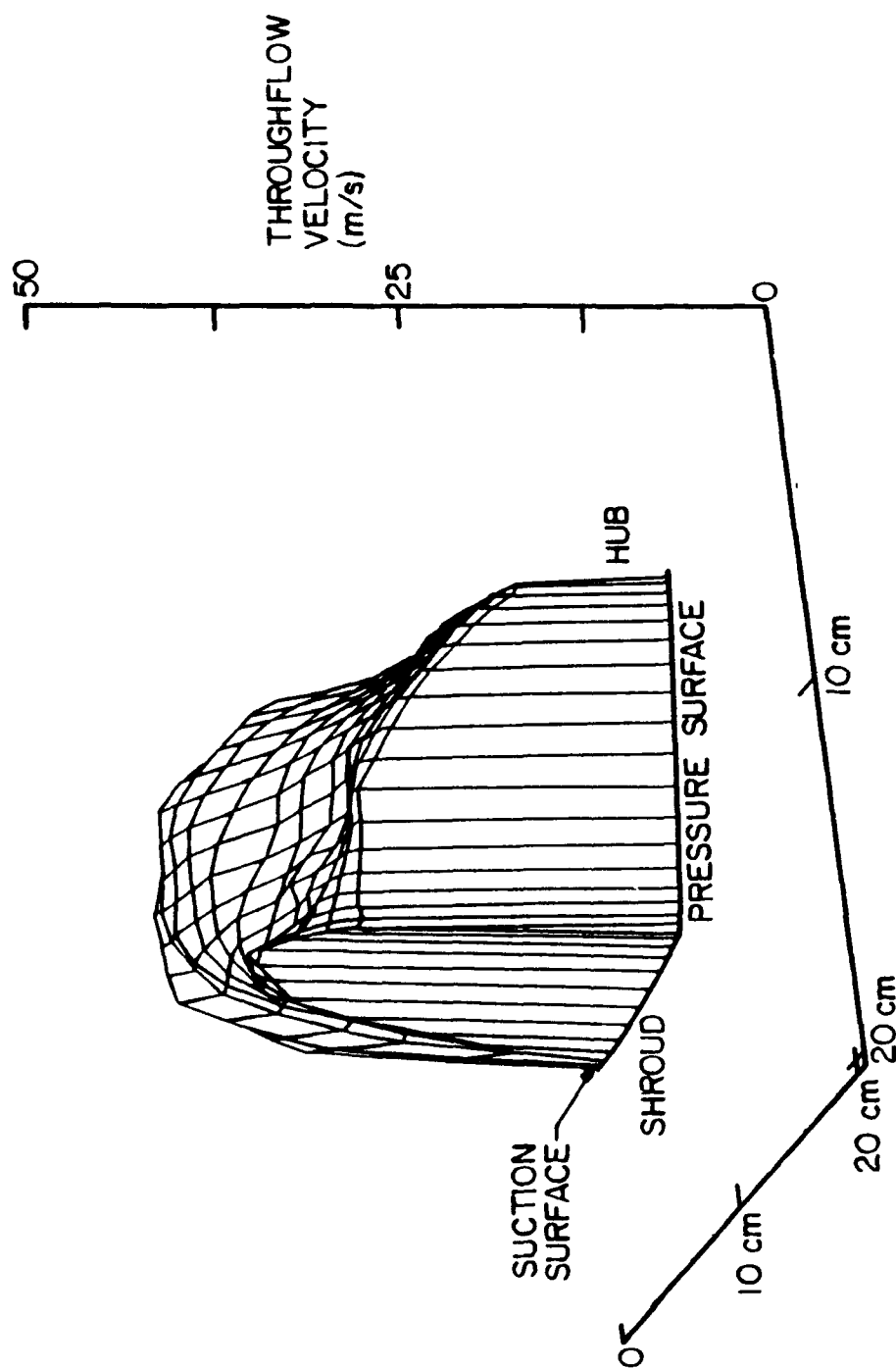


Figure 5.84 Throughflow Velocity Plot - Viscous Prediction
Design Point - Plane 4

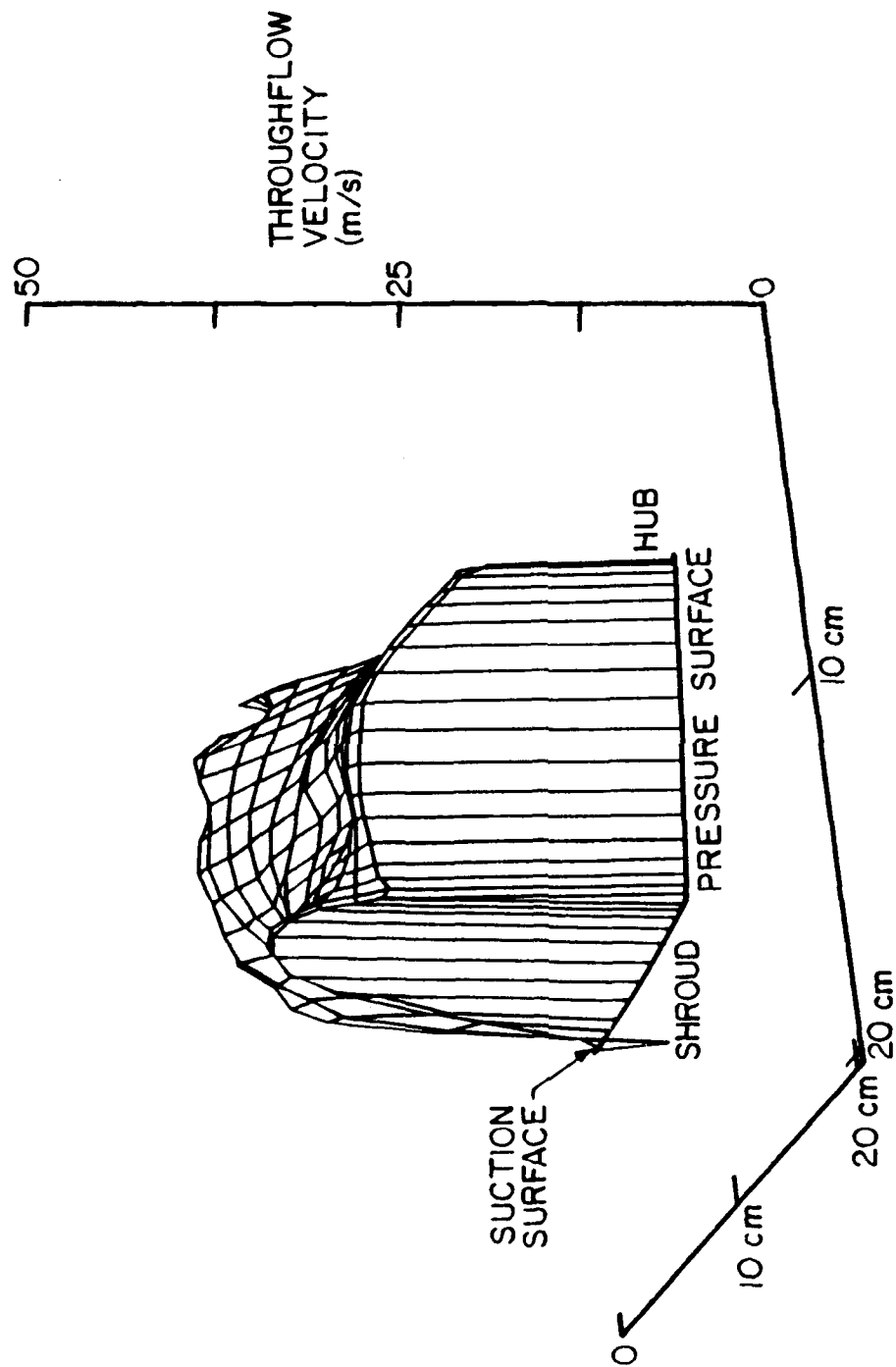
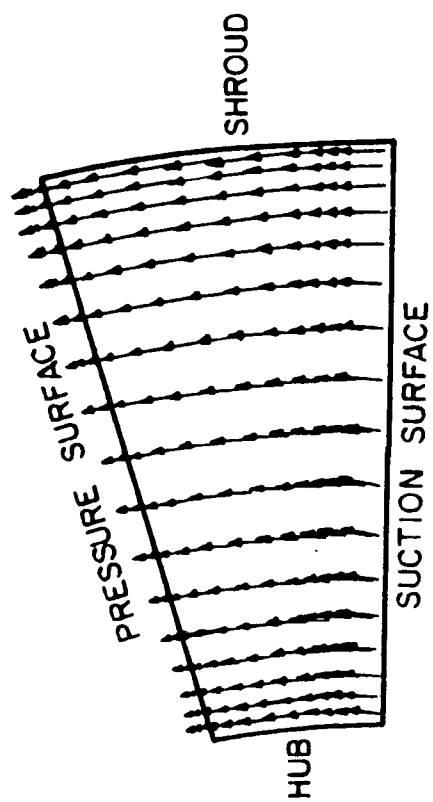


Figure 5.85 Throughflow Velocity Plot - Viscous Prediction
Design Point - Plane 5



→ 30.5 m/s

Figure 5.86 Secondary Velocity Vector Plot - Viscous Prediction
Design Point - Plane 1

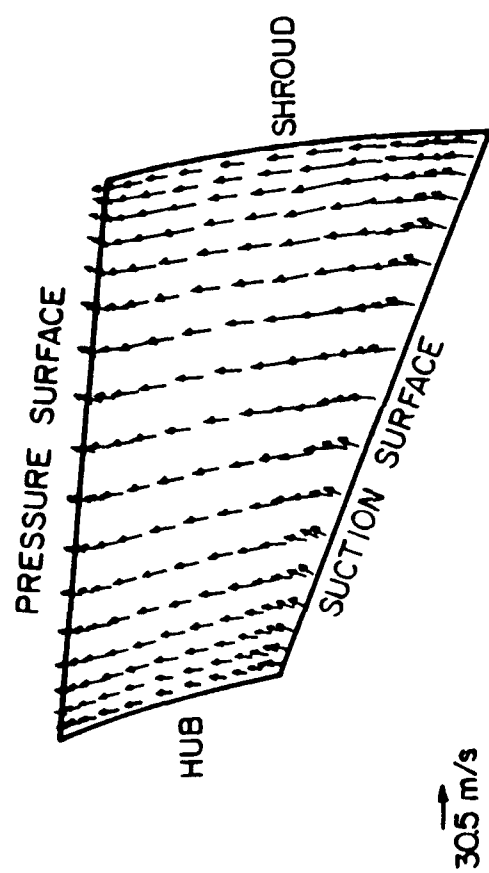


Figure 5.87 Secondary Velocity Vector Plot - Viscous Prediction
Design Point - Plane 2

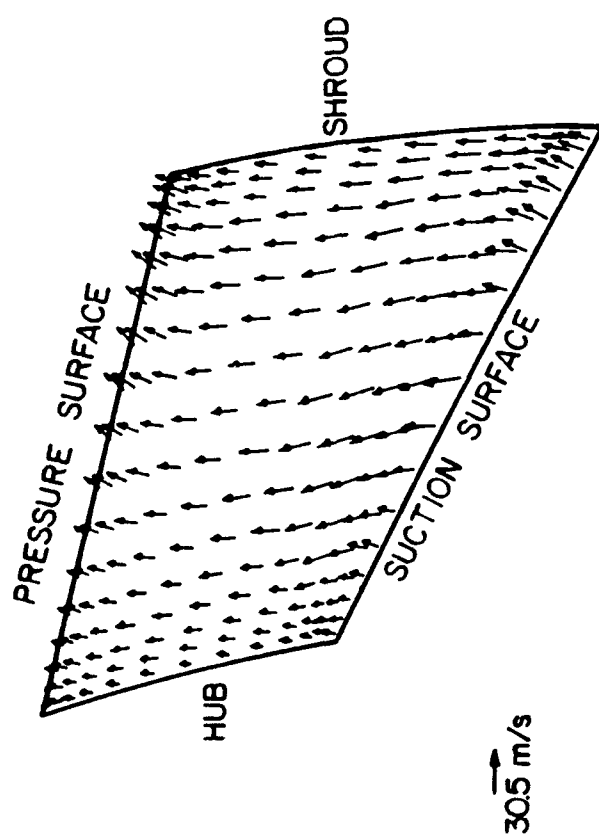


Figure 5.88 Secondary Velocity Vector Plot - Viscous Prediction
Design Point - Plane 3

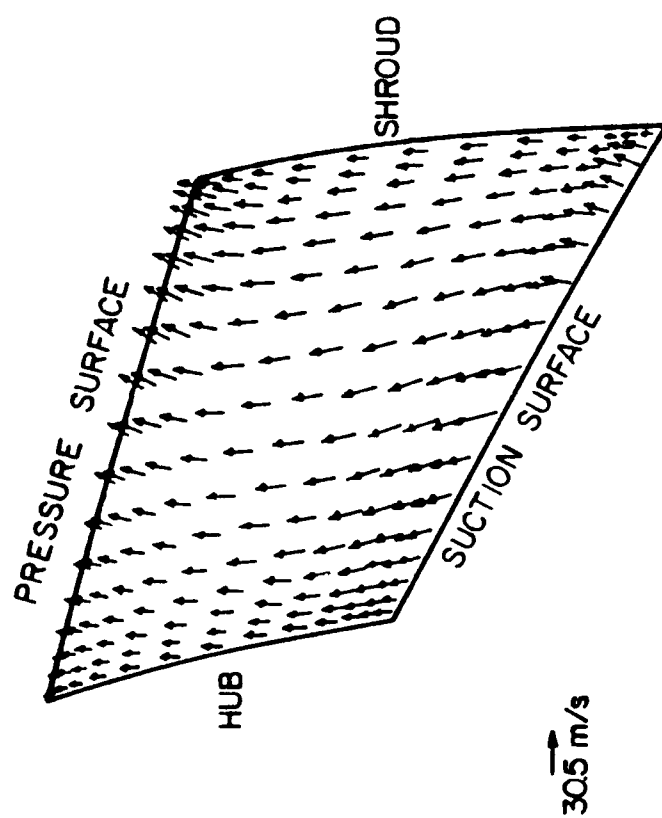


Figure 5.89 Secondary Velocity Vector Plot - Viscous Prediction
Design Point - Plane 4

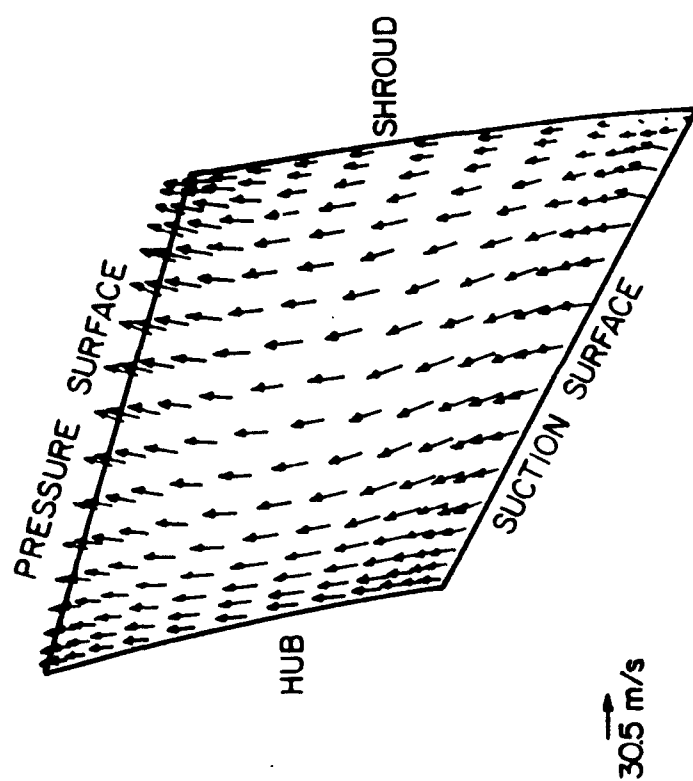


Figure 5.90 Secondary Velocity Vector Plot - Viscous Prediction
Design Point - Plane 5

shroud direction oriented outwardly is predicted along the pressure surface at the shroud suction surface. The region of predicted reverse flow is also evident in the secondary velocity vector results at Plane 5.

5.3.3 Correlation with Experimental Data

The inviscid predictions of the impeller flow field are not at all similar to the measured flow field due to difficulties encountered in applying the inviscid model. The primary difficulty was a discontinuity at the leading edge of the impeller blade. Although these difficulties may not be indicative of a fundamental problem with the model, the inability to correct this problem resulting in a lack of correlation of the predictions with the experimental data significantly limit its value as a design tool. Additionally, the experimental results clearly indicate the viscous nature of the flow. Consequently, the applicability of an inviscid code for this flow field is severely limited.

The predictions from the viscous code capture the flow phenomena but show poor correlation with the data. The code predicts the jet-wake region observed in the experimental data. However, the code does not accurately predict the streamwise position where the wake region starts nor the position of the maximum velocity deficit in the measurement planes. Although the start of the wake region is clearly observed at Plane 3 in the LDV results, this phenomenon is first seen in the predictions at Plane 4. The model also predicts that the wake region is located in the shroud suction corner, which is inconsistent with the LDV results. Finally, the model predicts a high velocity region in the passage which is not observed in the experimental results.

CHAPTER 6 - SUMMARY AND CONCLUSIONS

A series of experiments was performed to provide internal three-dimensional flow field data in the passages of centrifugal compressors and to describe the flow phenomena characteristic of the flow at the point of incipient rotating stall. These experiments entailed the acquisition and analysis of LDV data in the impeller passages of the Purdue Research Centrifugal Compressor at two compressor operating points: (1) the design operating point and (2) the incipient stall operating point. Additionally, the nature of rotating stall in the compressor was quantified by the acquisition and analysis of unsteady pressure data at the impeller inlet and at circumferentially distributed locations at the impeller exit. Finally, predictions at the compressor design point from contemporary internal flow models were used for comparison with the LDV data.

The Purdue Research Centrifugal Compressor is a low speed turbomachine which features a mixed-flow impeller with 23 backswept blades and a vaned radial diffuser operated at 1,790 rpm. Optical access was provided by a plexiglass shroud attached to the impeller. Errors due to finite LDV probe volume are negligible due to the large size of the impeller.

The LDV data taken at both operating points show the traditional jet-wake structure observed in many centrifugal compressors. This structure is characterized by a local velocity deficit region near the blade suction surface along the shroud. At the design point, the wake was observed along the shroud 70% of the length from the pressure to suction surface. At the incipient stall point, the wake was located in the shroud suction corner. The trends observed in the data are consistent with the trends suggested by the nondimensional Rosby number, with the rotational effect dominating the streamline curvature effect and the wake moving to the suction surface as the mass flow rate (and Rosby number) is reduced. However, the critical value of Rosby number is higher in the shrouded impeller of the Purdue Research Centrifugal Compressor than

has been observed in unshrouded impellers. This suggests that tip leakage in unshrouded impellers stabilizes the flow, delaying the onset of rotating stall. It was also observed that the extent of the wake region from the impeller exit, backwards through the passage, was the same at both operating points.

The unsteady pressure data show three distinct modes of rotating stall in the compressor dependent upon the mass flow rate. Mode 1 is characterized by two stall patterns rotating concurrently with relative rotational speeds below 15% of the impeller rotational speed. This mode occurs at the highest mass flow rate and is strongest at the impeller inlet. Modes 2 and 3 occur at reduced mass flow rates and are characterized by single rotating stall patterns. The patterns in both modes rotate with relative rotational speeds exceeding 90% of the impeller rotational speed, with the patterns strongest at the diffuser inlet. Modes 2 and 3 are more stable than Mode 1. Since the rotating stall is observed at both the impeller inlet and exit, all three modes are impeller rotating stall. However, it is evident the character of the stall differs significantly between the modes, with different rotational speeds and locations of greatest strength.

Application of a contemporary inviscid flow model for prediction of the compressor flow field had little success. The predicted impeller inlet flow was not smooth, sufficiently disturbing the flow field to affect it through the remainder of the passage. However, the experimental results clearly indicate the viscous nature of the flow. Consequently, an inviscid code would not be expected to predict the flow field regardless of this problem. Better success was achieved with the viscous flow model. It predicted the major phenomena in the flow field, specifically the wake structure near the end of the passage. However, the viscous model showed poor correlation with the data. It predicted that the wake was located in the shroud suction corner different from the LDV results at the design operating point. It also predicted a high velocity region in the core flow which was not observed in the experimental data. These results suggest that although current models can now predict phenomena associated with viscous regions in the impeller passage as well as the structure in the potential region of the flow, further development is required before modelling can be used to accurately predict the internal flow field.

These investigations have shown the three-dimensional flow field and the nature of the rotating stall in the Purdue Research Centrifugal Compressor is similar to that in much smaller high speed turbomachines. The large scale and low rotational speed of this facility makes it ideal for fundamental research.

LIST OF REFERENCES

LIST OF REFERENCES

1. Krain, H., "Experimental Observations of the Flow in Impellers and Diffusers", von Karman Institute for Fluid Dynamics Lecture Series 1984-07, May 1984.
2. Eckardt, D., "Detailed Flow Investigations Within a High-Speed Centrifugal Compressor Impeller", ASME Journal of Fluids Engineering, Vol. 98, 1976, pp. 390-402.
3. Elder, R. and Forster, C., "Measurements in Centrifugal Compressors", von Karman Institute for Fluid Dynamics Lecture Series 1987-01, January 1987.
4. Johnson, M. and Moore, J., "The Influence of Flow Rate on the Wake in a Centrifugal Impeller", ASME Paper 82-GT-45, 1982.
5. Adler, D. and Levy, Y., "A Laser-Doppler Investigation of the Flow Inside a Backswept, Closed, Centrifugal Impeller", Journal Mechanical Engineering Science, Vol. 21, 1979, pp. 1-6.
6. Durao, F.G., Goulas, A., and Whitelaw, J.H., "Measured Velocity Characteristics of the Flow in the Impeller of a Centrifugal Compressor", ASME Paper 79-HT-32, 1979.
7. Stenning, A., "Rotating Stall and Surge", ASME Journal of Fluids Engineering, Vol. 102, 1980, pp. 14-20.
8. Van Den Braembussche, R., "Surge and Stall in Centrifugal Compressors", von Karman Institute for Fluid Dynamics Lecture Series 1984-07, May 1984.
9. Senoo, Y. and Kinoshita, Y., "Limits of Rotating Stall and Stall in Vaneless Diffusers of Centrifugal Compressors", ASME Paper 78-GT-19, 1978.
10. Frigne, P. and Van Den Braembussche, R., "Distinction Between Different Types of Impeller and Diffuser Rotating Stall in a Centrifugal Compressor with Vaneless Diffuser", ASME Paper 83-GT-61, 1983.
11. Kammer, N. and Rutenberg, M., "An Experimental Investigation of Rotating Stall Flow in a Centrifugal Compressor", ASME Paper 82-GT-82, 1982.
12. Haupt, U., Chen, Y.N., and Rutenberg, M., "The Vortex-Filament Nature of the Reverse Flow on the Verge of Rotating Stall", ASME Paper 88-GT-120, 1988.
13. Mizuki, S., Hattori, T., Ariga, I., and Watanabe, I., "Reversed Flow Phenomena within Centrifugal Compressor Channels at Lower Flow Rate", ASME Paper 76-GT-86, 1986.
14. Jansen, W., "Rotating Stall in a Radial Vaneless Diffuser", ASME Journal of Basic Engineering, Vol. 86, No. 4, Dec. 1964, pp. 750-758.
15. Abdelhamid, A. N., "Analysis of Rotating Stall in Vaneless Diffusers of Centrifugal Compressors", ASME Paper 80-GT-184, 1984.
16. Moore, F.K., "Weak Rotating Flow Disturbances in a Centrifugal Compressor with a Vaneless Diffuser", ASME Paper 88-GT-76, 1988.

17. Bryan, W.B., and Fleeter, S., "The Effect of Prewirl on the Internal Aerodynamics and Performance of a Mixed Flow Centrifugal Compressor", USAAVSCOM Technical Report TR-87-C-35, 1987.
18. Schlichting, H., Boundary-Layer Theory, New York: McGraw-Hill, 1979.
19. Maxwell, B.R. and Seasholtz, R.G., "Velocity Lag of Solid Particles in Oscillating Gases and in Gases Passing Through Normal Shock Waves", NASA TN-D7490, 1974.
20. Roesler, T.C., Stevenson, W.H., and Thompson, H.D., "Investigation of Bias Errors in Laser Doppler Velocimetry Measurements", Air Force Report AFWAL-TR-80-2105, 1980.
21. Walraven, R., "Digital Filters", Proceedings of the Digital Equipment Computer Users Society, San Diego, 1980.
22. McNally, W.D. and Sockol, P.M., "Review - Computational Methods for Internal Flows With Emphasis on Turbomachinery", ASME Journal of Fluids Engineering, Vol. 107, March 1985, pp. 6-21.
23. Denton, J.D., "An Improved Time Marching Method for Turbomachinery Flow Calculation", ASME Paper 82-GT-239, 1982.
24. Rhie, C.M., "Basic Calibration of a Partially-Parabolic Procedure Aimed at Centrifugal Impeller Analysis", AIAA Paper 83-0260, 1983.
25. Wilcox, D.C. and Chamber, T.L., "Streamline Curvature Effects on Turbulent Boundary Layers, AIAA Journal, Vol. 15, 1977.

APPENDICES

Appendix A - Ray Tracing

Laser Doppler Velocimetry measurements within the blade passage of the Purdue Research Centrifugal Compressor requires imaging of the probe volume through the plexiglass impeller shroud. A standard technique for finding the beam intersection and the probe volume half angle when imaging through windows is to perform a ray trace of the axial ray of each illumination beam. For simple geometries such as planar or cylindrical windows, an analytical solution for finding the beam intersection and probe volume half angle is easily derived and solved. For this research the complex geometry of the impeller shroud which functions as an access window complicates the problem. A three-dimensional reverse ray trace model has been developed to locate and orient the probe volume within the blade passage of the centrifugal compressor. The model allows the user to input the measurement location and direction and returns the axis settings for the final optics assembly.

I. Optical Model

The ray tracing model is based upon geometric optics and performs an exact ray trace by applying the law of reflection and Snell's law, Equations A1 and A2 respectively. The angle conventions are shown in Figure A1. For this model Equations A1 and A2 are applied to rays in three-dimensional space.

$$\theta_i = \theta_r \quad (.11)$$

$$n_i \sin \theta_i = n_t \sin \theta_t \quad (.12)$$

θ_i - incidence angle

θ_r - reflection angle

θ_t - refraction angle

n_i, n_t - indices of refraction

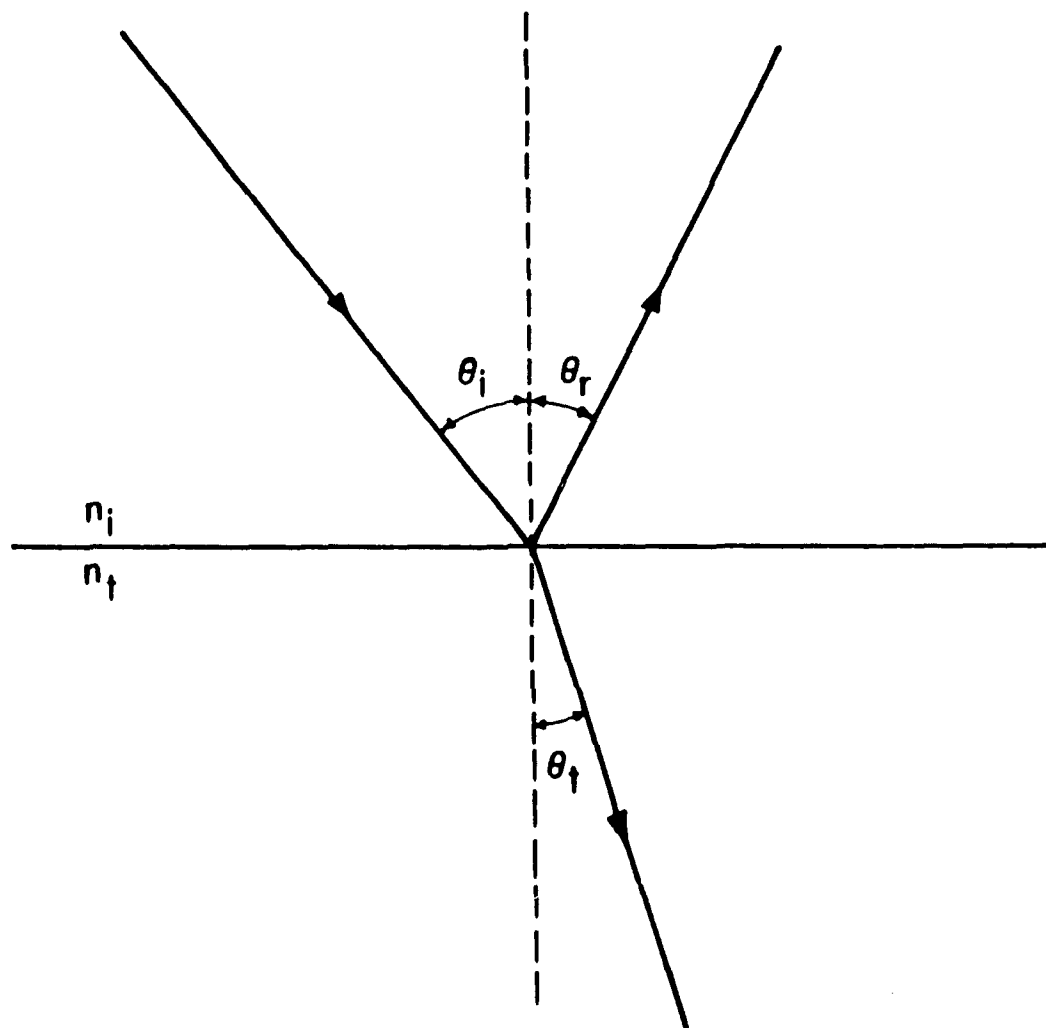


Figure A.1 Ray Trace Angle Conventions

II. Impeller Shroud

The optical surface of interest for the reverse ray trace is the impeller shroud (the LDV focussing lens is treated as an ideal lens where all infinite conjugate rays pass through the focal point). The shroud is modeled as a constant thickness window with the inside surface matching the tip profile of the impeller blades. A meridional section of the inside shroud surface is described by a cubic spline, Equation A3.

$$r(z) = r_0 + c_1 d + c_2 d^2 + c_3 d^3 \quad (A3a)$$

$$d = z - z_0 \quad (A3b)$$

In order to describe the surface in three-dimensional space, the spline is rotated about the axis of the machine resulting in a surface of revolution, Equation A4. The outside surface of the shroud is modeled in the meridional plane as a grid of points that are located equidistance from the inside surface along the local normal. The geometry is shown in Figure A2. The surface location and normal direction between points is found by linear interpolation between the values at each endpoint. The surface location in three-dimensional space is found by rotating each segment about the machine axis.

$$x^2 + y^2 = [r(z)]^2 \quad (A4)$$

III. Reverse Ray Trace

Using the three-dimensional ray trace and impeller shroud models, a forward ray trace can be performed to find the measurement location, direction, and effective half angle for given axis settings of the LDV positioning system. However, it is desirable to specify the measurement location and direction and find the required axis settings. This is accomplished by using a reverse ray trace.

The reverse ray trace algorithm requires input of the measurement location and direction as well as the axial direction of the illumination beams. For use in the blade passages of the centrifugal compressor, the axial direction is determined by the blade angles to minimize beam blockage. The algorithm traces the axial rays of the two

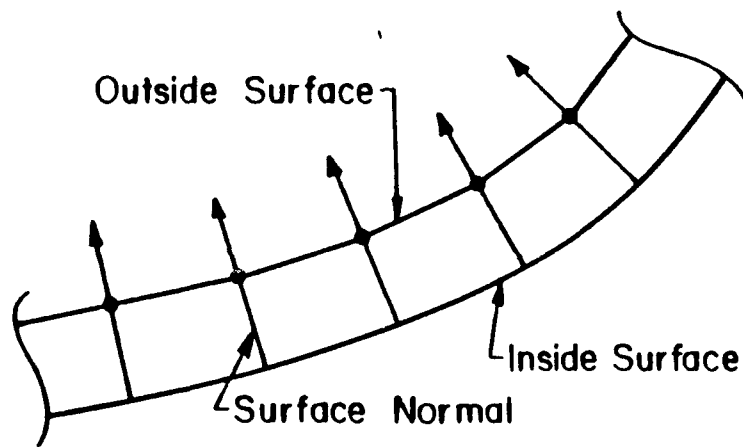


Figure A.2 Ray Trace Impeller Shroud Model

illumination beams with a specified probe volume half angle and the required measurement direction, Figure A3. A reverse ray trace is performed finding the path of the rays from the probe volume through the shroud. The angle between the beams at the lens is calculated and compared to the focussing lens half angle. The probe volume half angle is iterated until the beams have the proper lens half angle. The axis settings for the six axis positioning system are subsequently calculated.

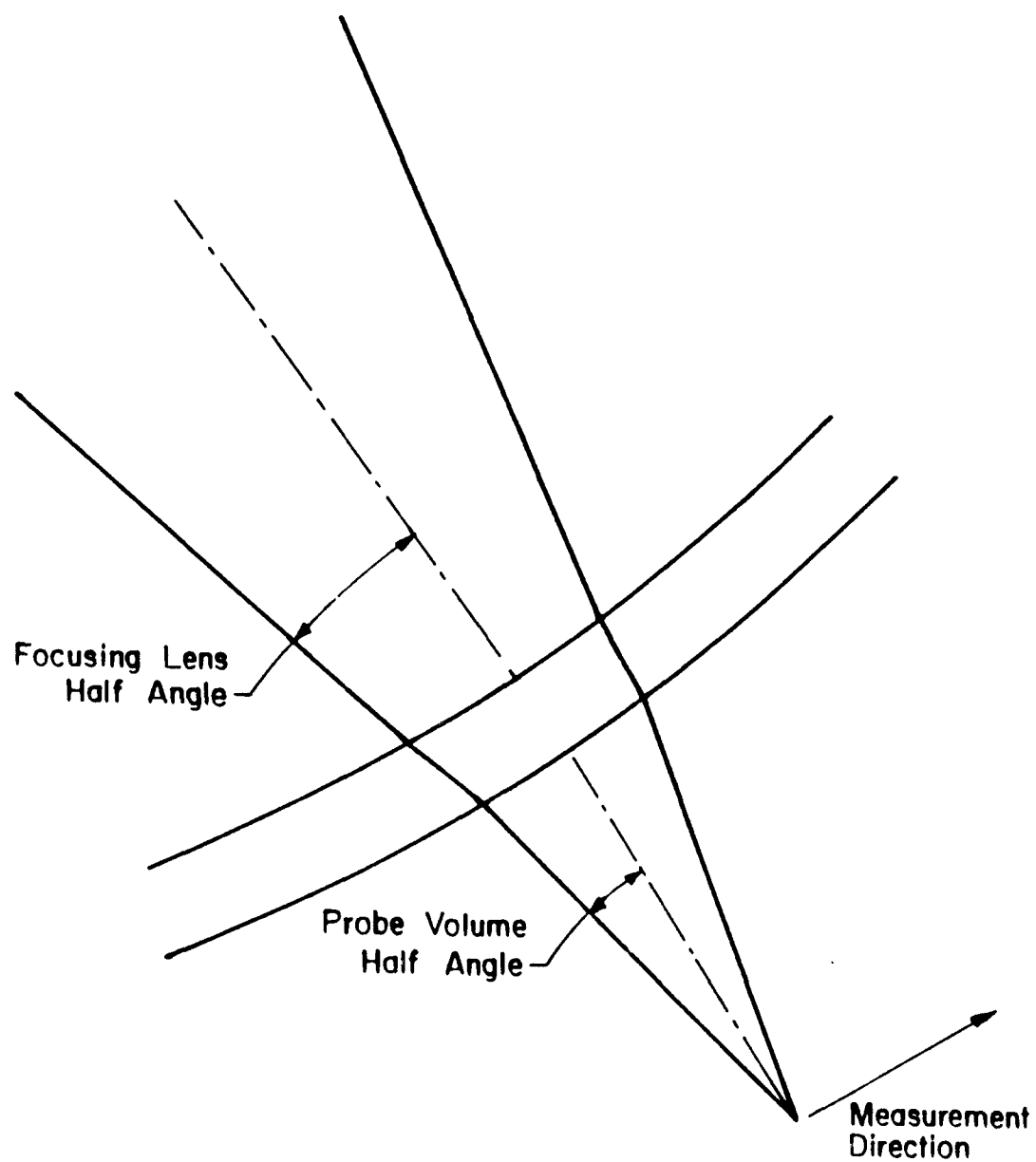


Figure A.3 Ray Trace Through the Impeller Shroud

Appendix B - Error Estimation

The following analysis gives an estimation of the uncertainty involved in determining the mean flow velocity vector from a typical set of measurements made with a one-dimensional LDV in the Purdue Research Centrifugal Compressor. An important factor in these estimates is the uncertainty in the determination of the probe volume location and geometry from the ray trace model. Although the ray trace is exact, within the limits of the application of geometric optics to this problem, the model describing the shroud surface is idealized. The uncertainty due to this factor is estimated at 10% of the difference between the value of the parameter given by the ray trace model and the undeviated value (the value of the parameter if the shroud did not deviate the illumination beams). A location in the first data plane (15% passage) is used for this analysis. The important parameters and experimental results are given in Table B1.

I. Probe Volume Location

The uncertainty in determining the exact location of the probe volume has contributions from three sources. These include: 1) inaccuracies of the ray trace modeling; 2) accuracy limits of the six axis positioning system; and 3) accuracy in referencing the positioning system. The uncertainty for this measurement due to inaccuracy in the ray trace model is less than .010 cm (.004 in) for the vertical (x) axis and .003 cm (.001 in) for the horizontal and axial (y and z) axes. The movement precision of each axis of the six axis positioning system is given in Table 3.2. The linear axes have a movement precision of .003 cm (.001 in). The 25.0 cm (9.843 in) focal length lens used for these measurements extends the probe volume 19.474 cm (7.667 in) from the center of the mirror making the inaccuracy due to the mirror rotation much larger than the translation error. The mirror tilt has a movement precision of 0.45 degrees, and results in beam deviation of 0.90 degrees. At 19.474 cm the movement precision is .306 cm (.120 in) in the plane of the mirror tilt and normal to the illumination beam axis. The tilt axis drive has been adjusted to remove any lash and its accuracy (or repeatability) is within .064 degrees which gives a positional accuracy of .022 cm (.009

Table B.1 Experimental Parameters and Results

Mass Flow Rate: 3.34 kg/s (7.35 lbm/s)
 Axial Position: 3.871 cm (1.524 in)
 Radial Position: 22.611 cm (8.902 in)
 Time Window: 20

Direction	A			B			C		
Frequency (mHz)	Mean		11.316	(-.2203, -.4905, .8431)		(-.0003, .4898, .8718)		(.2185, -.0007, .9758)	
	Error		.01295			.01061		.01461	
	Standard Deviation		.3623			.2934		.4025	
Half Angle (radians)			.099465			.099441		.099461	

in). The most significant contribution is due the inaccuracy in referencing the positioning system. The system is referenced by using the linear axes to locate the probe volume at a reference position after zeroing the angular axes. In the horizontal and axial directions the inaccuracy of the reference position is of the order of the probe volume diameter which is .013 cm (.005 in). Because the probe volume length is an order of magnitude larger than the diameter, care is taken to center the probe volume at the reference point. The accuracy along the vertical axis is better than half the probe volume length or .063 cm (.025 in). Even with additive errors the inaccuracy in probe volume position is less than .038 cm (.015 in) along the axial and horizontal axes and less than .076 cm (.030 in) along the vertical axis.

II. Velocity Measurement Accuracy

The analysis of the measurement accuracy is done in two steps. First the uncertainty for each of the directional measurements is estimated. Subsequently, the uncertainty is calculated for the orthogonal velocity components.

The mean velocity for each measurement is calculated from Equation 3.13. The uncertainty for the measurement is given by Equation B1. The total uncertainty for the measurement is due to three sources as demonstrated by the above equation. The values for each term of Equation B1 for the three measurement directions is given in Table B2. The first term on the right hand side of the equation is the contribution due to the finite bandwidth of the laser. The laser has a specified bandwidth of 20 GHz which corresponds to an uncertainty in wavelength of 2.206×10^{-12} m. For this measurement the wavelength term is negligible compared to the other terms of Equation B1. The wavelength term is nearly constant for all data and will be subsequently neglected. The second term on the right hand side of Equation B1 is due to uncertainty in the half angle at the probe volume. The conventions used for this analysis estimate the half angle uncertainty at 10% of the deviation caused by refraction at the shroud surfaces. The third term on the right hand side of Equation B1 is due to the uncertainty in estimating the mean from the experimental data based upon a normal distribution. The uncertainty for each of the measurements is less than .15%.

$$d\bar{U}_A = \left(\frac{\partial \bar{U}_A}{\partial \lambda} \right) d\lambda + \left(\frac{\partial \bar{U}_A}{\partial k_A} \right) dk_A + \left(\frac{\partial \bar{U}_A}{\partial \bar{v}_{DA}} \right) d\bar{v}_{DA} \quad (B.1)$$

The total uncertainty for the measurement is due to three sources as demonstrated by the above equation. The values for each term of Equation B1 for the three measurement directions is given in Table B2. The first term on the right hand side of the equation is the contribution due to the finite bandwidth of the laser. The laser has a specified bandwidth of 20 GHz which corresponds to an uncertainty in wavelength of 2.206×10^{-12} m. For this measurement the wavelength term is negligible compared to the other terms of Equation B1. The wavelength term is nearly constant for all data and will be subsequently neglected. The second term on the right hand side of Equation B1 is due to uncertainty in the half angle at the probe volume. The conventions used for this analysis estimate the half angle uncertainty at 10% of the deviation caused by refraction at the shroud surfaces. The third term on the right hand side of Equation B1 is due to the uncertainty in estimating the mean from the experimental data based upon a normal distribution. The uncertainty for each of the measurements is less than .15%.

The orthogonal velocity components are determined from velocity measurements made in non-orthogonal directions. The relation is given by Equation 3.12. As a consequence, the uncertainty for each of the velocity components depend upon the angular separation of the measurement directions and the measurement uncertainties. The analysis is further complicated due to uncertainties in the actual measurement directions. This part of the analysis is done in two steps. The mean velocity components and uncertainties along each of the orthogonal axes are calculated with the measurement directions calculated from the ray trace model. In a subsequent step, the calculations are repeated using the measurement directions for the axis settings based upon no refraction of the beams by the shroud surfaces. The mean velocities for the two cases are compared to set an upper limit for the velocity uncertainties due to an error in determining the measurement direction. All the results are presented in Table B3. Only for the velocity along the x-axis (radial direction) is the additive error above 1%. It is not surprising the error is largest in this direction because optical access to the passage severely limits the angle between the measurements for resolution of the hub-to-tip component which is

Table B.2 Experimental Uncertainty Due to Individual Sources

	A	B	C
$\frac{\partial U_A}{\partial \lambda} d\lambda$ (m/s)	1.257×10^{-4}	neglect	neglect
$\frac{\partial U_A}{\partial k_A} dk_A$ (m/s)	5.876×10^{-3}	6.694×10^{-3}	7.474×10^{-3}
$\frac{\partial U_A}{\partial \nu_{DA}} d\nu_{DA}$ (m/s)	3.355×10^{-2}	2.749×10^{-2}	3.785×10^{-2}
Total (m/s)	3.955×10^{-2}	3.418×10^{-2}	4.532×10^{-2}
Error	.13%	.10%	.12%

Table B.3 Measurement Direction Uncertainty

	Calculated Direction			No Distortion		
	Velocity	Uncertainty		Δ Velocity		
	m/s	m/s	%	m/s	m/s	%
X	4.674	± 0.014	0.3	.166		3.6
Y	2.029	± 0.007	0.3	-.013		-0.6
Z	37.172	± 0.74	0.2	-.036		-0.1

nearly radial for this position. Additionally, the error due to uncertainty in the measurement direction is much higher (one order in magnitude) than other sources of error. The analysis of that error is very conservative and could likely be reduced by a factor of 3-5.

III. Conclusions

This analysis is not an attempt to rigorously calculate the uncertainty for the results. It is an attempt find the magnitude of the error for a typical measurement. The results demonstrate that the uncertainty in position is small compared to the passage dimensions. It is also seen that the uncertainty in determining the mean velocity is not larger than the uncertainty in setting and controlling the mass flow rate through the machine which is estimated at 2-3%.

Appendix C - L2F Evaluation

The laser two-focus velocimeter (L2F) was designed in response to the signal-to-noise limitations of the laser Doppler velocimeter. Table C1 compares and contrasts the important characteristics of the two systems. Similar to the laser Doppler velocimeter, the laser two-spot velocimeter collects light scattered from particles convected by the flow. However, the time-of-flight of the particles between two focused laser spots is measured rather than the Doppler frequency shift. In principle, this increases the signal-to-noise ratio and also enables measurements to be made closer to boundaries. In contrast to the laser Doppler velocimeter, the laser two-focus velocimeter is a statistical based measurement system. Therefore, the temporal fluctuations of the flow can not be measured and, although the variance and higher order moments can be estimated from the frequency distribution, turbulent spectral information can not be determined.

I. Instrument Design

The operating principle for the laser two-spot velocimeter is extremely simple. A start and stop gate are formed by two small light beams that each focus to a convergent-divergent cross-section with a fixed separation in space. A high speed clock times the period of a particle passing from one beam to the other, and the velocity is calculated. Because the photodetectors do not need to resolve the Doppler frequency, but only the passage of the particle, the required signal-to-noise ratio is reduced. The optical path for the Polytec L2F used for these measurements is shown in Figure C1.

II. L2F Experimental Technique

The dimensions of the optics housing for the L2F are 105 cm x 48 cm x 15 cm (41 in x 19 in x 6 in). This relatively large physical size of the L2F system restricts the locations in the compressor flow path where L2F measurements can be made. L2F measurements were taken in the compressor inlet, in the first 25% of the impeller blade passage flow channel, and in the radial diffuser. L2F measurements were also taken at 40% and 60% of the impeller blade passage flow path. However, the extent of these

Table C.1 LDV and L2F Comparison

LDV	L2F
Light Scattered by Small Particles Convected by the Flow	Light Scattered by Small Particles Convected by the Flow
Doppler Frequency Shift is Measured	Time-of-Flight of the Particles is Measured
Measures Instantaneous Velocity at a Point in the Flow Field	Statistical-Based Measurement System
One-Dimensional Measurement System	Two-Dimensional Measurement System

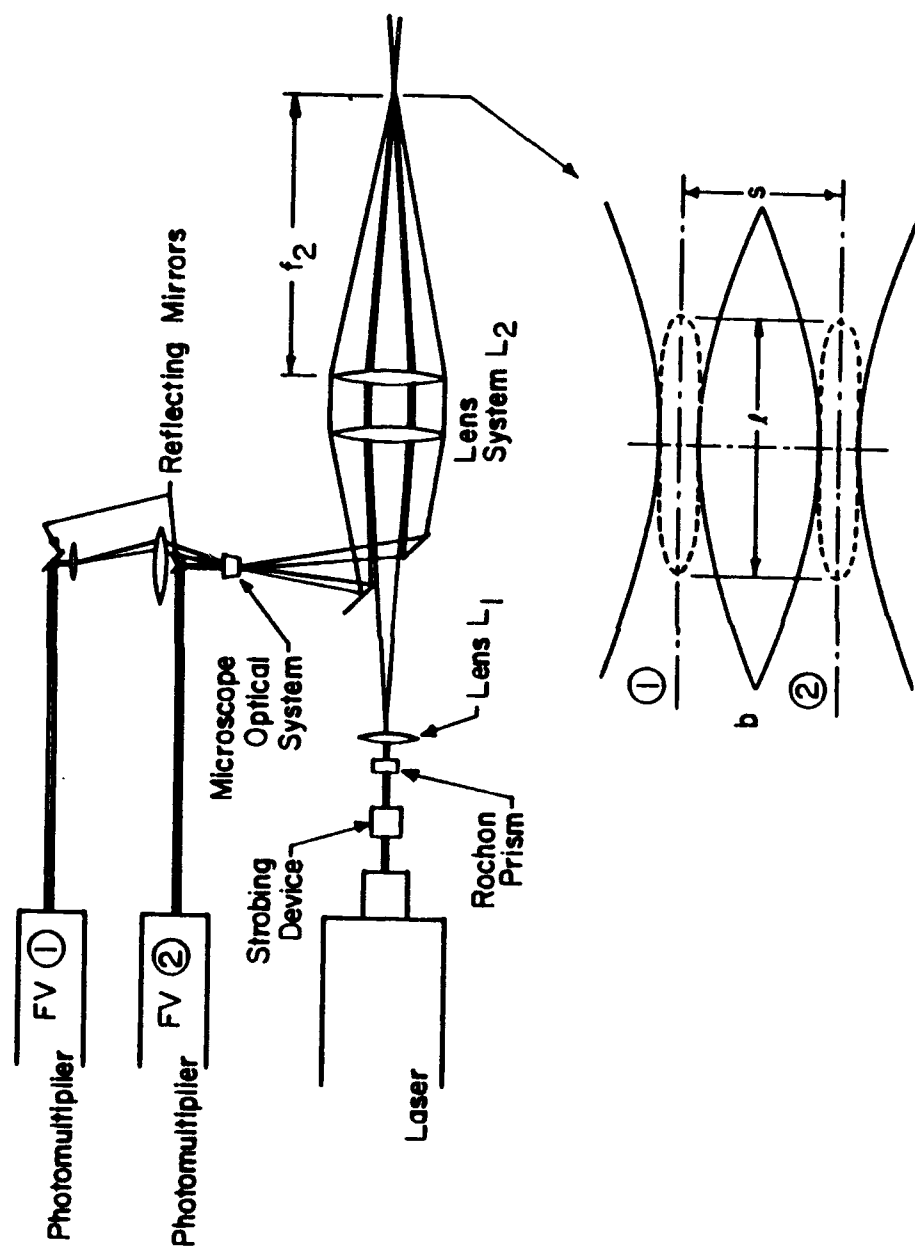


Figure C.1 L2F Optical Path

latter two measurement planes is limited because the geometry of the impeller blades at these planes prohibits L2F optical access. The orientation of the L2F with respect to the impeller is depicted in Figure C2.

The L2F makes a measurement by sweeping the two focused laser beams through a range of angles about the mean flow direction in a plane with a normal along the axis of the illumination beam propagation. The measurements are synchronized to the impeller rotation impeller by instrumentation internal to the L2F system. Measurements can be taken in a single impeller blade passage or averaged over all the passages. Additionally, the laser can be strobed with a Bragg cell to eliminate the saturation of the photodetectors by reflections from the impeller blades.

a. Optical Corrections

To make L2F measurements in the impeller, the illumination beams as well as the scattered light must pass through a plexiglass window with a complex contour. These measurements are affected by positional deviation as well as geometric distortion of the measurement volume. Thus, L2F measurements through a curved window are more sensitive to beam misalignment than corresponding LDV measurements. As a result, it is necessary to verify the L2F measurement volume location and geometry. This is accomplished by developing an algorithm to determine the effect on the measurement volume geometry of illuminating the L2F measurement volume through a thin window of arbitrary geometry.

The output beam of the laser operating in its fundamental mode TEM_{00} has a Gaussian intensity distribution. A Gaussian beam has the characteristics that the wavefront is planar at the beam waist and has a spherical wavefront along the beam not near the waist. To model the L2F illumination beams, the Gaussian beam equations are used to find the theoretical wavefront, i.e. the beam radius and radius of curvature at the focal lens of the illumination beams for the measurement volume geometry specified by the beam waist diameters, locations and beam separation. The wavefront is replaced

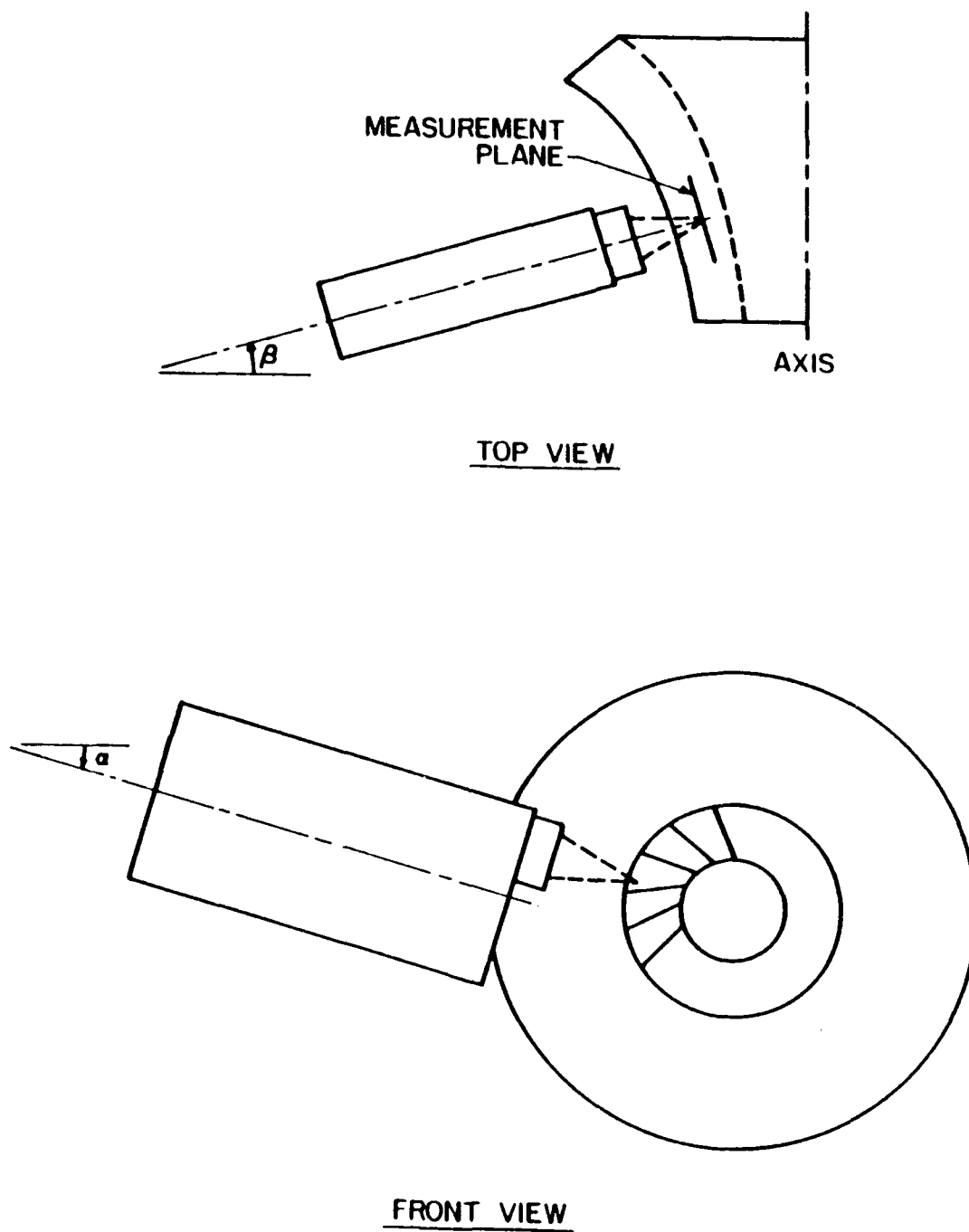


Figure C.2 L2F Measurement Access

with a finite number of rays propagating towards the beam waist. An exact ray trace is used to track each ray an equivalent optical path length through the window. The geometry is shown in Figure C3.

The basis of this model is that the window causes a perturbation to the original Gaussian beams resulting in new Gaussian beams with unique geometry. Assuming the distance from the beam waist to the window is much larger than the Rayleigh length, a new spherical wavefront can be estimated from the endpoints of each ray. A set of equations equal to the number of rays is then generated. If there are only four rays, the system can be solved exactly for the center position and radius of the sphere. However, four rays are not adequate to model the distortion to the beam by the window. The required additional relations result in an over-specified system of nonlinear equations. An optimum solution is found by using a small perturbation analysis to linearize the equations, with a least squares solution determined. A detailed mathematical development of this model is given by Fagan and Fleeter [1].

b. Flow Field Results

L2F and LDV data are obtained to quantify the flow field throughout the flow path of the Purdue Research Centrifugal Compressor. The experimental data are then correlated with appropriate predictions from three-dimensional inviscid and viscous flow models.

Inlet Flow Field

The compressor inlet flow field was measured 6.83 cm (2.69 in) upstream of the leading edge of the impeller blades with the L2F. The inlet flow field is essentially uniform, as seen in Figure C4 which presents the inlet axial and circumferential velocity components as a function of radial position.

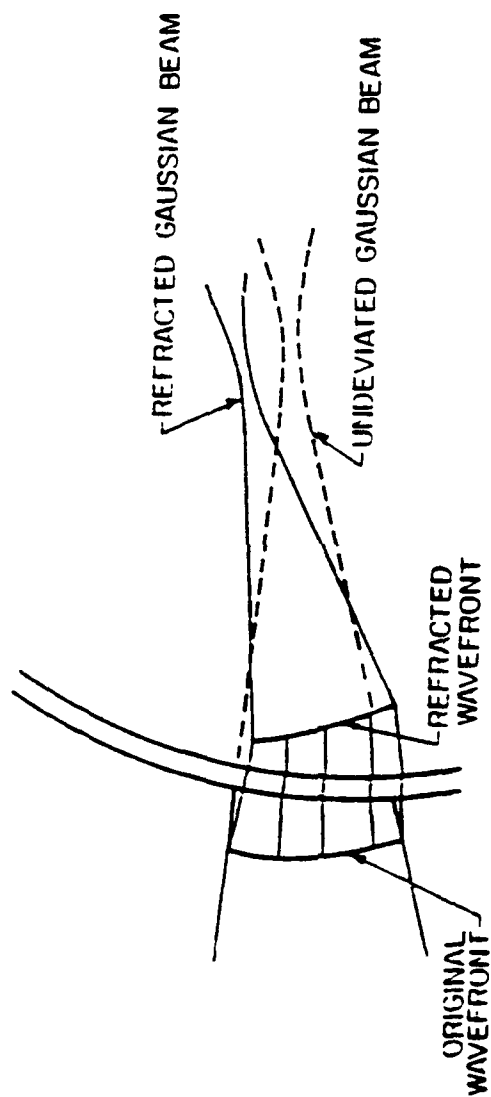


Figure C.3 Optical Correction Geometry

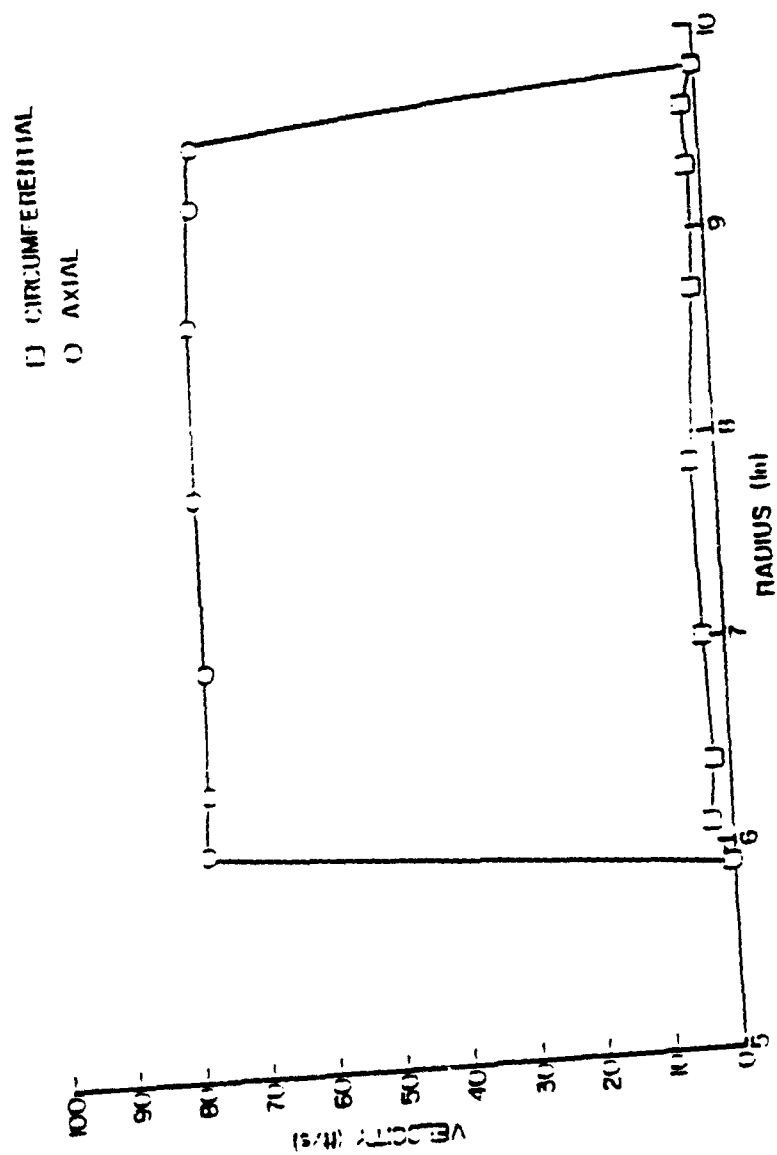


Figure C.4 Impeller Inlet Flow Field

Impeller Blade Passage

L2F and LDV data were taken at two axial planes in the impeller blade passage: 3.81 cm (1.5 in) and 6.73 cm (2.65 in) downstream of the leading edge of the impeller blades. Figures C5 through C8 present these throughflow velocity data together with the corresponding inviscid and viscous predictions.

The L2F and LDV at the measurement plane defined by $z = 3.81$ cm show similar hub-to-tip blade loading, Figure C5. In the tip region, the throughflow velocity magnitude data are approximately equal. In the hub region, however, the L2F velocity data are approximately 10% higher than the corresponding LDV data. As a result, the L2F determined throughflow velocity is somewhat higher at the hub than at the tip. This contrasts with both the LDV data and the viscous flow prediction. The viscous model also predicts similar blade loading to the experimental results whereas the inviscid predictions indicate that the blades are unloaded in the tip region.

For the measurement plane defined by $z = 6.73$ cm, the L2F and LDV data are similar, with the LDV data showing a higher loading in the tip region. Again, the L2F data indicate that the throughflow velocity is increasing slightly near the hub, in contrast to the LDV data. The viscous model predicts blade loading and hub-to-tip velocity gradients which are similar to the experimental data. However the viscous prediction indicates a high velocity region on the suction surface near the tip which is not indicated by the data. The inviscid prediction indicates positive loading along the entire section, but with much higher loading than measured.

With regard to the flow predictions, two items should be noted. The input data for the code is impeller design data. However, due to manufacturing limitations, the fabricated impeller and the design have some differences. For example, instead of tapered blades intersecting a tapered cylindrical hub surface, the passage is smoothed and rounded. Consequently, geometrical variations between blade passages as well as a reduced passage area are introduced. The data presented herein are interpolated onto the same grid as used for the numerical models. As a result, the predicted velocity is approximately 10-15% low and interpolation errors can be high at the points along the

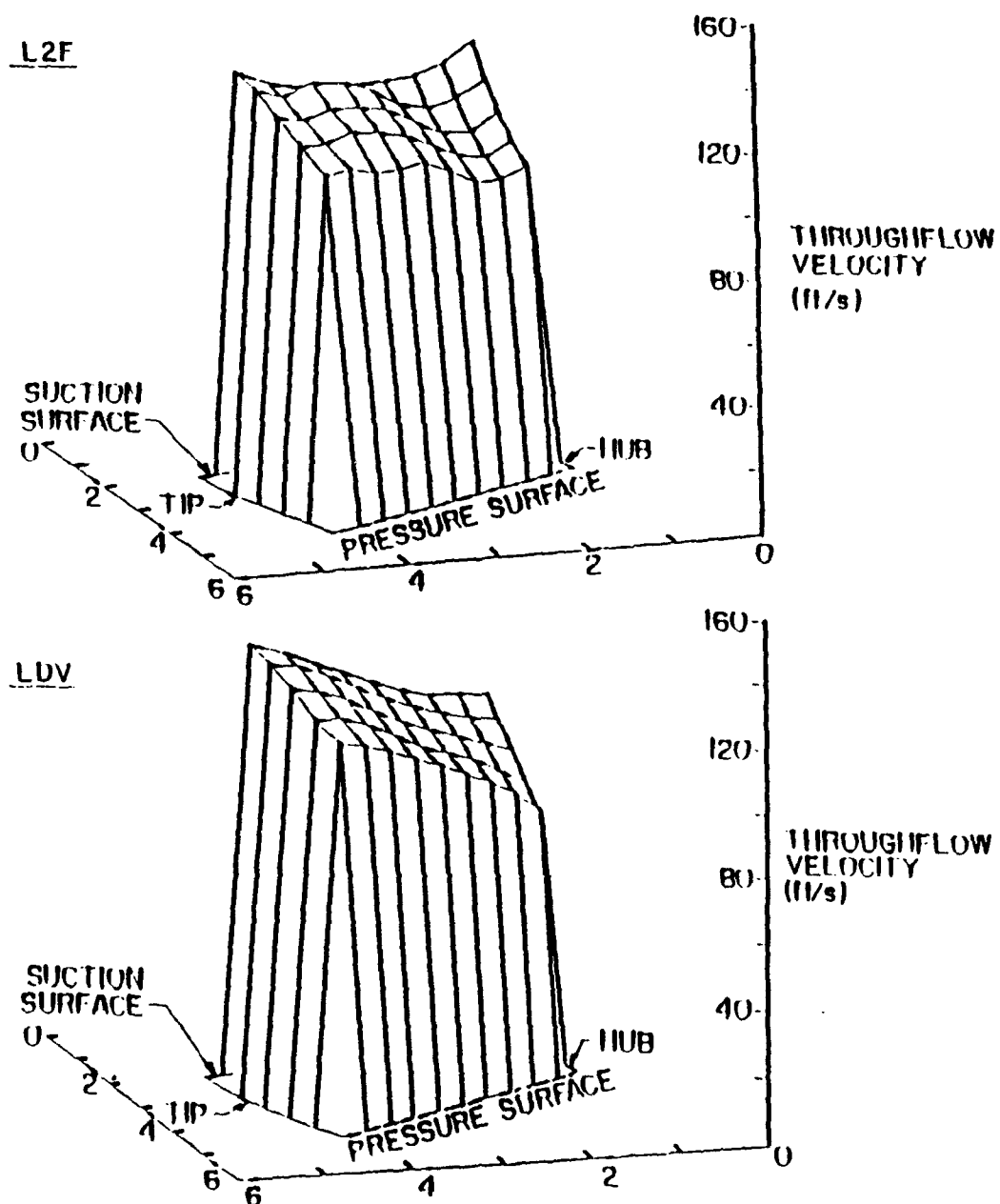


Figure C.5 LDV and L2F Throughflow Velocity Data ($z=3.8$ cm)

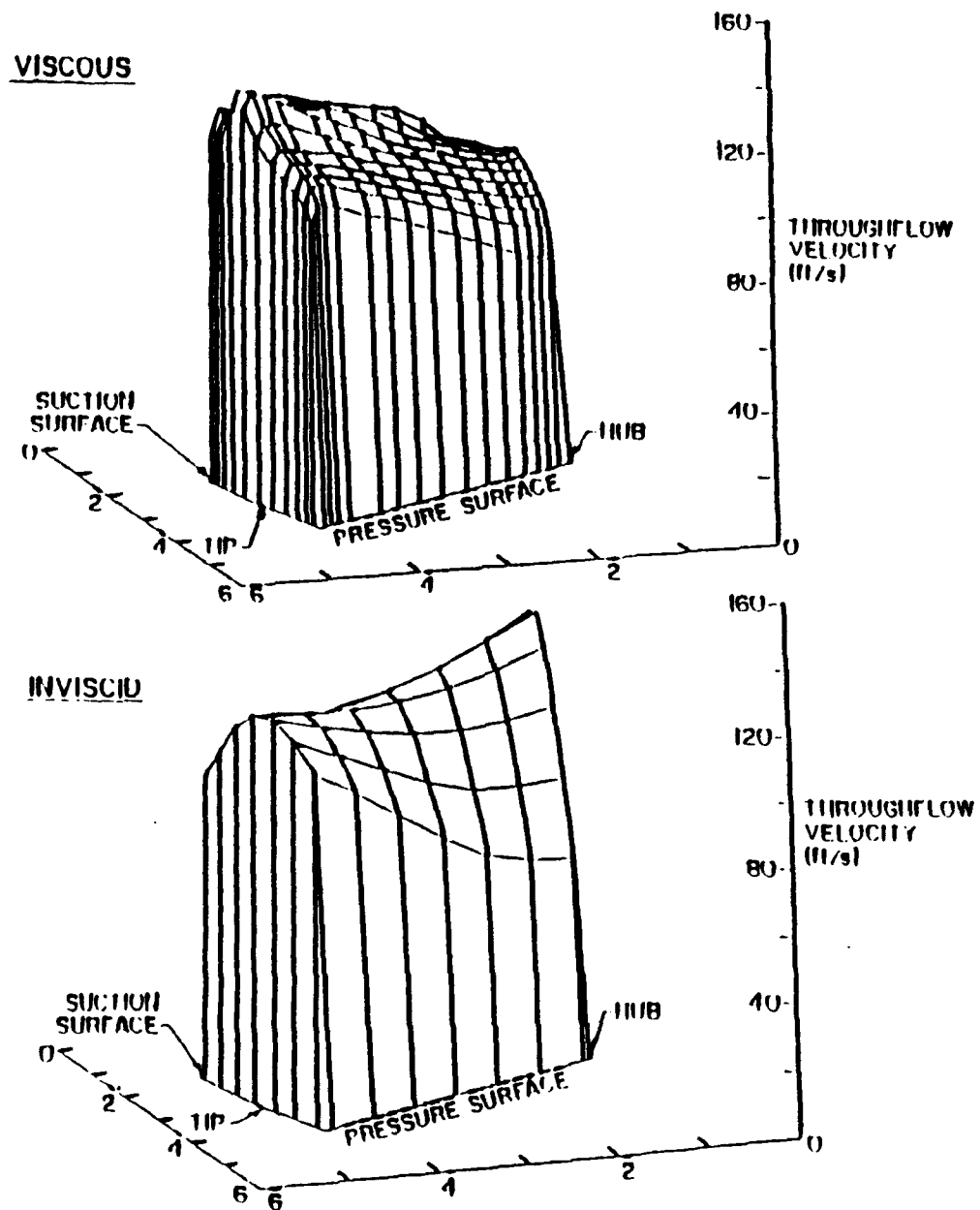


Figure C.6 Inviscid and Viscous Prediction of Throughflow Velocity ($z=3.8$ cm)

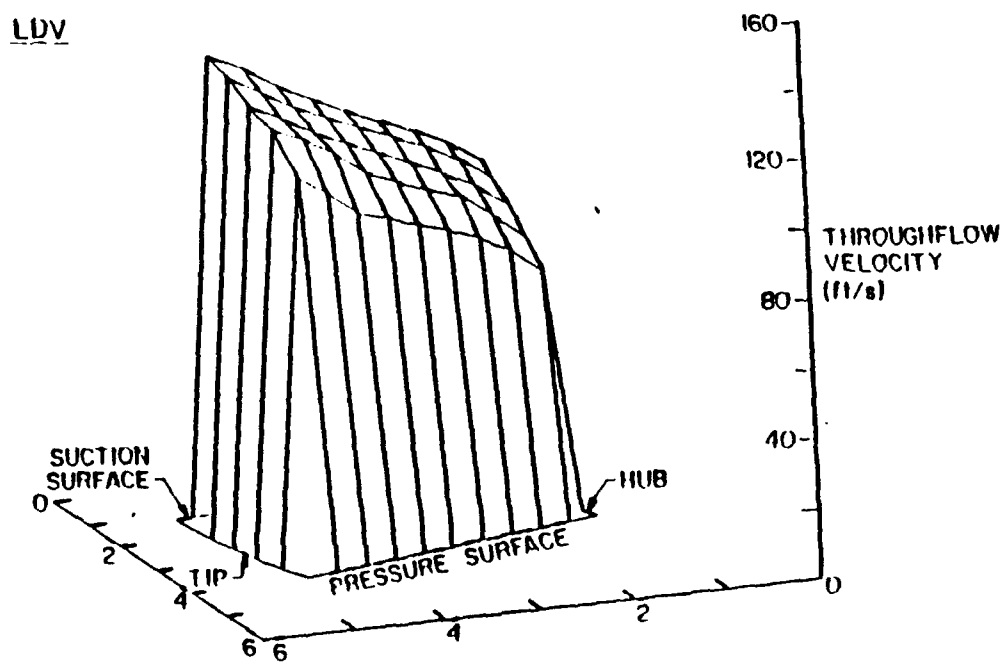
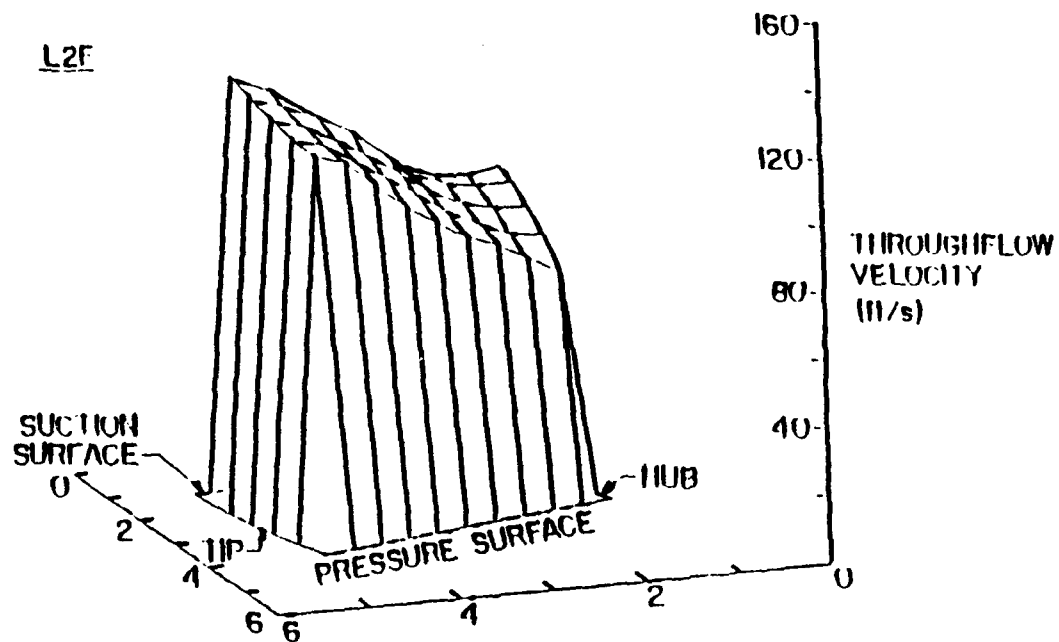


Figure C.7 LDV and L2F Throughflow Velocity Data ($z=6.7$ cm)

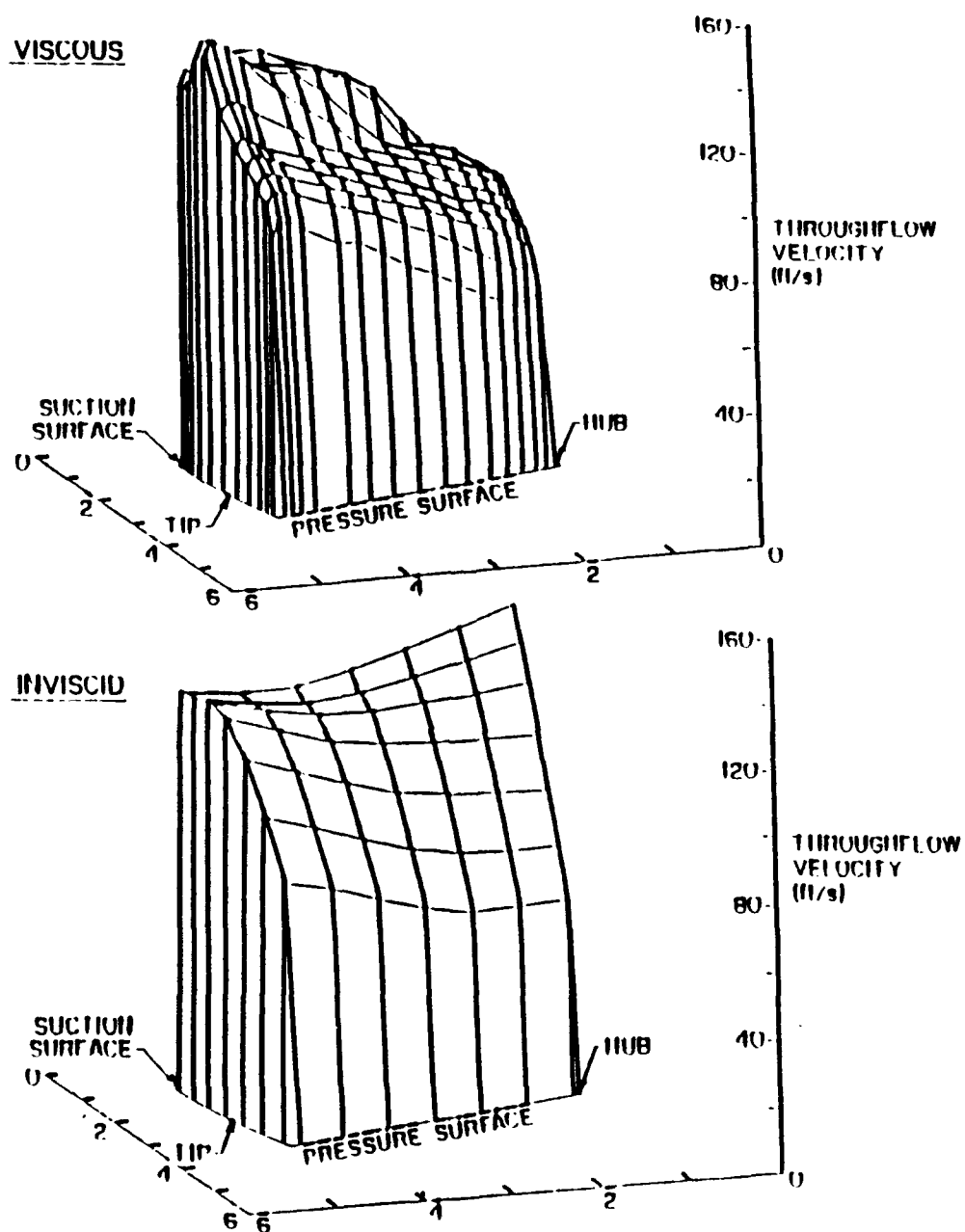


Figure C.8 Inviscid and Viscous Prediction of Throughflow Velocity ($z=6.7$ cm)

blade surfaces in the hub region where the data is sparse. The second item is that the Denton inviscid predictions in the first 25% of the blade passage are very sensitive to the leading edge cusp. This sensitivity may be the reason that the trends shown by the inviscid results are significantly different than both the viscous predictions and the data.

III. L2F - LDV Comparison

The L2F and LDV data show analogous large scale flow field behavior in agreement with a previous work on more fundamental flow fields, Rabe and Dancey [2]. Thus, the L2F could be a valuable tool for turbomachinery applications if it satisfies one of the following criteria: (1) the L2F is capable of measurements not possible with the LDV; (2) L2F is sufficiently easy to use that measurement can be made with little set-up and analysis time; or (3) data acquisition times are significantly shorter than for the LDV, thereby reducing the operational time of the experimental facility. The following discussion relates the experiences of these experiments to these issues.

a. Signal-to-Noise Ratio

In principle, the L2F can make measurements closer to solid boundaries and in noisier environments than an LDV for two reasons. The L2F illumination beam is focused to a much smaller spot, resulting in higher beam intensity. Also, the required L2F signal-to-noise ratio is smaller because only the presence of the particle, not the Doppler frequency, must be determined. This is particularly important for measurements in turbomachinery as such measurements are generally made in the backscatter mode and at orientations nearly normal to the hub surface and the optical access window.

Measurements made in the diffuser region where the window is nearly flat and the passage boundaries are stationary clearly demonstrate this concept. L2F data were acquired $.076 \pm .025$ cm ($0.030 \pm .010$ in) from the front window and $.127 \pm .025$ cm (0.050 ± 0.010 in) from the back wall. Corresponding LDV data have been acquired as close as $.508$ cm (0.200 in) from the front window. Although it is likely an LDV

measurement can be made nearer to the window by using a field stop or through the application of fluorescence techniques, the L2F clearly has some advantage for this geometry.

Measurements in the impeller blade passage lead to the opposite conclusion. LDV data were acquired nearer to both the window, i.e. the rotating shroud, and the hub wall than were L2F data. There appear to be two independent causes for this behavior.

Primarily, the rotating surfaces tend to reflect light that is collected by the L2F optical system and imaged on the photodetectors. Imperfections in these surfaces produce a detectable L2F signal. In fact, when the measurement volume is sufficiently near the surface, it is the wall velocity that is measured by the L2F. As the measurement volume is moved away from the wall, there is a measurement region where events are detected from both particles passing through the measurement volume and from wall surface reflections. Since the wall velocity is the asymptotic velocity of the fluid as the wall is approached, events from the wall can undetectably contribute to the velocity histogram thereby biasing the L2F velocity and turbulence data.

A second factor is associated with the difficulties in acquiring L2F data through curved windows. The scattered light from particles passing through the L2F measurement volume are imaged on the photodetectors. When the measurement is deep in the passage and the window curvature effects are large, it is very difficult to adjust the L2F optics for good imaging over the range of angles, making L2F measurements nearly impossible. As a consequence, the application of the L2F is limited for measurements very near rotating surfaces and through curved windows.

b. Sample Rate

The L2F makes a two-dimensional flow field measurement whereas the LDV is a one-dimensional measurement system. As a result, the determination of the two-dimensional flow field with an LDV requires either two independent measurements or a simultaneous LDV measurement, for example a two-color LDV system. In either case a simple measurement can be made more quickly with the L2F. This is due to the

portability of the L2F system and the relatively simple optical set-up. Additionally, the L2F system used in these experiments includes the hardware for synchronizing to shaft rotation for measurements in the rotating frame of reference. However, the actual data acquisition rate is much lower for the L2F and the LDV.

To discuss the sample rate, some terminology must be defined. For the L2F it is important to distinguish between a sampled event, which occurs when the system is in the ready mode and a particle passes through the start beam, and a correlated event. A correlated event statistically occurs when a single particle passes through both the start and the stop beam and contributes to building the velocity probability density distribution. The rate at which events can be sampled with the L2F is limited because the mean particle separation in the flow must be much larger than the beam spacing. For velocities on the order of 50 m/s, the sampling rate is limited to approximately 500 Hz. Even in regions of low turbulence intensity, less than 10% of the sampled events are correlated and, thus, contribute to the probability density distribution when the beams are swept over a reasonable range of angles. The percentage of correlated events decreases as the turbulence intensity increases, with approximately only 5% of the sampled events correlated for these measurements. As a result, the effective L2F sampling rate has an upper limit of approximately 25 Hz ($500 \text{ Hz} \times 0.05$). In contrast, a reasonable sample rate for the LDV is 700 Hz. As a result of the internal LDV validation circuitry, most bad measurements are rejected by the processor and not passed as an event. In a post processor LDV analysis, any velocity measurement outside of four standard deviations from the mean value is rejected. The number of rejected LDV measurements typically makes up less than 1% of the total, resulting in an effective sampling rate of 690 Hz.

c. Marginal Distributions

In theory the L2F builds the two-dimensional velocity probability density distribution from the time-of-flight histograms collected at each angular position. However, the Polytec instrument does not build the complete two-dimensional velocity probability density distribution because of data storage limitations in the multi-channel

analyzer. Rather, two marginal distributions are constructed: (1) a time-of-flight histogram which is independent of angular position, and (2) a histogram of the number of correlated events versus the angular position which independent of the time-of-flight measurement. The mean velocity and the turbulence intensities are calculated from these two distributions. This introduces several potential problems. No rigorous mathematical treatment has been developed quantifying the error introduced by modeling the two-dimensional velocity probability density distribution with the marginal distributions. As a result, the magnitude of the experimental error can not be calculated directly. Also, employing the marginal distributions yields a streamwise turbulence intensity and an angular turbulence intensity. However, no relation between the angular turbulence intensity and the transverse turbulence intensity, the standard fluid mechanics definition, has been developed. If the two-dimensional velocity probability density distribution is built, the turbulence intensity in any direction can be easily calculated. Finally, no angle dependent measurement volume geometry correction can be applied in a post data acquisition step when the marginal distributions are used.

d. Other Considerations

It was found in these experiments that the optimal seed particle diameter for the L2F was between 0.1 and 0.5 μm with a seeding fluid of propylene glycol thinned with ethanol. This is an order of magnitude smaller than the particles used for the corresponding LDV measurements. Smaller particles are advantageous when making measurements in regions with steep velocity gradients, high frequency flow oscillations, or velocity jumps such as shock waves. Although none of these conditions are relevant to measurements in the Purdue Research Centrifugal Compressor, it could be important in a high speed turbomachine.

The L2F is limited as a research instrument because it does not provide spectral information and can only be used in regions of relatively low turbulence intensity. This inability to provide spectral information is not a serious limitation because an instrument capable of easily measuring the mean flow velocity and turbulence intensity for turbomachinery flow fields is of great value. However the turbulence intensity limitation

of the L2F is significant. This is because important flow regions in high speed turbomachines often have turbulence intensities above the limits of the L2F, with the literature and these experiments suggesting an upper limit of approximately 15%.

The Polytec L2F system is well packaged for making measurements synchronized to shaft rotation. A once-per-revolution or once per-blade-passage signal is input to the system and it automatically bins data according to circumferential position across the passage for ensembled data over all the passages or for data from a single passage. However, the data collection circuitry does not count data for individual bins. If there is a large variation in the velocity across the passage, it is difficult to obtain adequate sampling in all circumferential bins. This is particularly important in wake regions where the local mass flow is significantly reduced and, consequently, the number of particles per time passing through the measurement volume is reduced.

IV. L2F-LDV Conclusions

Results of this experimental program raise a number of points about both the fundamental operating principles of laser two-focus velocimetry and the details of its implementation in the Polytec system. It is important to distinguish between the two because the first provides fundamental limits for the L2F whereas the latter can be changed to make a more useful instrument.

The L2F is fundamentally limited because it does not have the capability to make measurements in flows with turbulence intensities greater than approximately 15%. Since this is well within the range of values found in high speed turbomachinery, the L2F is not a general instrument for turbomachinery flow field measurements. However, the L2F does have the ability to make measurements much closer to normal stationary surfaces than does the LDV. This is likely a great advantage for turbomachine applications. Unfortunately, the L2F can not make measurements as close to rotating surfaces as an LDV.

The other fundamental limitation of the L2F is the achievable sampling rate. Considering that the L2F accumulates correlated events at a rate an order of magnitude slower than the LDV and that it takes more data to build the L2F two-dimensional velocity probability density distribution than the two one-dimensional distributions required for the comparable LDV measurement, actual L2F sample times are much longer. It should be noted, however, that the two-dimensional distribution does provide more information than the two one-dimensional distributions. In contrast, the actual experimental run and data acquisition times are often small compared to the instrumentation set-up and preparation times, and the LDV requires two measurements to obtain the same data as the L2F.

With regard to the particular L2F system utilized in these experiments, there are two items which should be altered to provide a more useful instrument. First, the complete two-dimensional distribution should be accumulated and analyzed rather than the two one-dimensional distributions. Assuming the data density is sufficiently high to neglect discretization errors, this would enable the mean velocity and turbulence intensity as well as uncertainty limits to be determined using standard mathematical formulations. Implementation should be relatively simple because the data link currently exists to pass the data to a microcomputer for analysis. With proper interfacing the increase in data acquisition time would be negligible because the data transfer rate is very much faster than the data acquisition rate. A modification should also be introduced to guarantee a minimum data count in each circumferential bin before incrementing the measurement orientation angle. Although this would likely require a hardware change, it would guarantee a reliable measurement throughout the passage given significant circumferential velocity variations.

With the implementation of the above modifications, the L2F could be a useful tool for application to turbomachinery. Its primary benefit would be to: (1) make measurements near stationary boundaries where other optical techniques have difficulty; and (2) make a limited number of measurements with minimum set-up time.

V. List Of References

1. Fagan, J.R. and Fleeter, S., "Measurement of Turbomachinery Flow Fields by Laser Two-Focus Velocimetry", USAAVSCOM Technical Report TR-89-10, 1989.
2. Rabe, D.C. and Dancey, C.L., "Comparison of Laser Transit and Laser Doppler Anemometer Measurements in Fundamental Flows", AIAA Paper 86-1650, 1986.